A Finite Element Approach To Inverse Scattering Problems

PROYECTO FIN DE CARRERA

ESCUELA DE INGENIERÍA Y ARQUITECTURA DE ZARAGOZA
INGENIERÍA DE TELECOMUNICACIÓN

Escuela de
Ingeniería y Arquitectura
Universidad Zaragoza

AUTOR: ENRIQUE MASGRAU RITE
DIRECTOR: GIUSEPPE VECCHI
PONENTE: ENRIQUE MASGRAU GÓMEZ

22 de noviembre de 2012

Agradecimientos

Durante este último año he vivido una de las mejores experiencias vitales de mi vida. Torino es el lugar que ha sido mi casa durante todo este tiempo, y de donde yo me llevaré fantásticos amigos para siempre. En este país, me he sentido como uno más, además de recibir un gran afecto por parte de toda su gente. Realmente, Torino estará siempre dentro de mí cuando esta aventura termine.

Torino además es el lugar donde yo decidí terminar mis estudios universitarios, incluido este trabajo. Quiero dar las gracias al Politecnico di Torino por darme esta posibilidad. Estudiar en el extranjero me ha hecho crecer realmente como persona.

Ahora es el momento de dar las gracias a todas las personas que me han apoyado a lo largo de este tiempo a realizar mi Proyecto Fin de Carrera. Gracias también al Istituto Superiore Mario Boella, lugar donde he desarrollado mi proyecto final de carrera. En el ISMB yo he podido disfrutar de un ambiente agradable de trabajo. Me gustaría dar mis más sínceras gracias al pofesor Giuseppe Vecchi por darme la oportunidad de realizar el PFC con él y a Elia A.Attardo por todo su apoyo, esfuerzo y paciencia durante todos estos meses.

Del mismo modo, me gustaría mostrar mi gratitud a mi familia por su guía y apoyo a lo largo de estos años. Sin ellos, esta experiencia no podría haber sido posible.

Finalmente, quisiera dar las gracias a mis amigos de España, Italia y Erasmus en general que me han ayudado a disfrutar de mi trabajo, estudios y de los buenos momentos.

De verdad, gracias a todos.

Resumen

En este proyecto se desarrolla una aplicación basada en "Microwave Imaging" (MWI), implementada con el propósito de obtener las propiedades materiales desconocidas de un determinado objeto. Este método consta de dos partes fundamentales: El *Problema Directo* y el *Algoritmo Inverso*.

La primera etapa, el *Problema Directo*, implica la medición del campo eléctrico disperso a lo largo de un dominio material. El *Objeto de Interés* (OI) representa un cuerpo material desconocido que se encuentra dentro de un tanque, rodeado por un conjunto de antenas que iluminan el escenario y almacenan los datos experimentales de las mediciones relacionadas con el campo eléctrico. Además, se introduce un medio adaptador dentro del recinto cerrado, el cual es denominado como "background".

Con el objetivo de simular los datos experimentales, se desarrolla el *Método de los Elementos Finitos*. FEM representa una técnica matemática e ingenieril muy potente que nos permite resolver un conjunto de ecuaciones lineales que describen el comportamiento electromagnético. De este modo, podremos generar los datos sintéticos referidos a las variables nodales, que definen el escenario de imagen simulado mediante un simulador de FEM, denominado GiD y desarrollado por la UPC.

Después de resolver el *Problema Directo*, se aborda el "Contrast Source Inversion Method" (CSIM) con el propósito de reconstruir los parámetros físicos originales que definen el OI. Haciendo uso de este algoritmo de inversión será viable alcanzar el error mínimo global entre los datos reales y los reconstruidos. Cuando este método iterativo converja, los resultados reconstruidos serán analizados con el objeto de identificar los materiales implicados en el "Imaging Domain".

En este trabajo se describen los diferentes experimentos relacionados con el *Problema Directo* y *Algoritmo Inverso*, obteniendo diversas conclusiones sobre el funcionamiento de FEM-CSIM. En concreto, se analizan los conductores eléctricos perfectos, la distribución de las fuentes de corriente, las própiedades dieléctricas del "background" y la influencia de la frecuencia. Del mismo modo, los resultados de reconstrucción serán comparados en diferentes experimentos, obteniendo información sobre la resolución del método y las limitaciones del algoritmo.

Finalmente es importante destacar las simulaciones realizadas con medios con y sín pérdidas, y los experimentos de biomedicina que tratan de representar posibles experimentos reales de imagen médica. Observaremos como CSIM proporciona una calidad alta en los resultados cómo para poder detectar la posicion y características de los objetivos. En las mejores situaciones de reconstrucción obtendremos errores en torno al 25%, que aunque puedan parecer discretos, son suficientes en muchas aplicaciones de imagen médica.

Índice

1 Introducción **15**

1.1 Ámbito de la Aplicación . . . 15
1.2 Motivación . . . 16
1.3 Definición del problema . . . 16
1.4 Solución propuesta . . . 17
1.5 Contenido del Proyecto . . . 17

2 Conceptos Electromagnéticos **19**

2.1 Ecuaciones de Maxwell . . . 19
2.2 Condiciones de Contorno . . . 20
2.3 Ecuación de Helmholtz . . . 21
2.4 Ecuaciones Para Ondas Escalares . . . 21

3 El Problema Directo **23**

3.1 Punto de Partida . . . 23
3.2 Ondas Electromagnéticas . . . 24
3.3 Métodos de Simulación . . . 25

4 El Método De Los Elementos Finitos **27**

4.1 Conceptos Básicos de FEM . . . 27
4.2 Discretización del Dominio . . . 28
4.3 Funciones Base . . . 29
4.3.1 Funciones Base Nodales . . . 30
4.3.2 Funciones Base Vectoriales . . . 31
4.4 Problemas Escalares . . . 32

4.4.1 Problema de Valores en la Frontera en 2D . . . 33
4.4.2 Resolviendo BVP Usando el Método de Garlerkin . . . 33
4.5 Problemas Vectoriales . . . 36
4.5.1 La Ecuación "Curl-Curl" y Los Elementos Vectoriales . . . 36
4.6 Absorbiendo Condiciones de Contorno . . . 37
4.6.1 "The Perfectly Matched Layer" en 2D . . . 38
4.7 Implementación de la Matriz FEM . . . 41
4.8 Simulaciones . . . 41
4.8.1 Recinto Circular . . . 41
4.8.2 Recinto Triangular . . . 46
4.8.3 Recinto Cuadrado . . . 47

5 Resolución de Problemas Inversos de Dispersión Electromagnética 49
5.1 El Algoritmo de Inversión . . . 49
5.2 Operadores Matriciales de Inversión . . . 50
5.3 The Contrast Source Inversion Method . . . 51
5.3.1 Normas y Productos Internos . . . 52
5.3.2 Estimación Inicial de FEM-CSIM . . . 53
5.4 Simulaciones . . . 53

6 Resultados y Conclusiones 61
6.1 Limítaciones del CSIM . . . 61
6.1.1 Influencía del Contraste . . . 61
6.1.2 Frecuencia . . . 64
6.2 Recintos PEC . . . 67
6.3 Elección del "Background" . . . 69
6.3.1 Medios Con Pérdidas . . . 69
6.3.2 Medios Sin Pérdidas . . . 72
6.4 Aplicaciones Biomédicas . . . 74
6.5 Conclusiones . . . 78
6.6 Trabajos Futuros . . . 79

Apéndice 85

A Documento original de la tesis 85

Lista de Figuras

1.1 Resultados de una aplicación MWI 16

1.2 Descripción del proceso 17

3.1 Permitividad relativa (línea azul) y conductividad (línea roja) para glycerine-water 80:20 de 300MHz hasta 3GHz 24

3.2 Sistema de Imagen Cerrado. 24

3.3 (a) Protótipo de un sístema MWT (b) Lectura de tomografía 25

3.4 (a) modelo MWI 2D (b) modelo MWI 3D 26

4.1 Elementos diferentes para discretización del dominio en 1D, 2D y 3D 28

4.2 Error de discretización derivado del uso de triángulos o cuadrados. 29

4.3 Malla adaptativa de una geometría en 2D. 29

4.4 Numeración de los nodos locales de cada elemento e. 30

4.5 Elemento triangular basado en elementos vectoriales 32

4.6 MWI application results 37

4.7 PML encerrando un dominio infinito 40

4.8 Problema Directo resuelto con FEM usando funciones nodales: $\epsilon'_r = 20$, (Xs,Ys)=(0.5,0), (a)(b) $|E|$ y $\angle E$ para $\sigma = 0.0005$ S/m (c)(d) $|E|$ y $\angle E$ para $\sigma = 0.5$ S/m. 42

4.9 Problema Directo resuelto con FEM usando funciones nodales: $\epsilon'_r = 20$ (a)(b) $|E|$ y $\angle E$ para $\sigma = 0.0005$ [S/m] con fuentes (Xs,Ys)=([0.05 0],[0 -0.05]), (c)(d) $|E|$ y $\angle E$ para $\sigma = 0.0005$ [S/m] con fuentes (Xs,Ys)=([-0.05 0.05],[-0.05 0.05]). 42

4.10 Problema Directo resuelto con FEM usando funciones nodales: $\epsilon'_r = 80$ (a)(b) $|E|$ y $\angle E$ para $\sigma = 0.0005$ [S/m] con (Xs,Ys)=(0.05,0), (c)(d) $|E|$ para $\sigma = 0.0005$ [S/m], con (Xs,Ys)=(0.02,0) y (Xs,Ys)=(0.07,0). 43

4.11 (a)(b) Escenarios Inhomogéneos (c)(d) $|E|$ correspondiente a fuentes localizdas a (Xs,Ys)=(0,-0.05). 44
4.12 $\epsilon'_r = 10$, $\sigma = 0.03$ [S/m], (a) $|E|$ a $f_o = 700MHz$, (b) $|E|$ a $f_o = 1GHz$, (c) $|E|$ a $f_o = 1.5GHz$, (d) $|E|$ a $f_o = 2GHz$ 45
4.13 r= 0.1m, $\epsilon'_r = 10$, $\sigma = 0.03$ [S/m], (a)(b) $|E|$ a $f_o = 700MHz$ y $f_o = 2GHz$ respectivamente. 46
4.14 Triangular 2D: $\epsilon'_r = 20$, (a) $|E|$ para $\sigma = 0.02$ [S/m] con (Xs,Ys)=(0,0), (c) $|E|$ para $\sigma = 0.5$ [S/m] con (Xs,Ys)=(0,0) 46
4.15 (a) Simple fuente eléctrica (b) Tres fuentes eléctricas 47

5.1 (a) Parte real permitividad relativa ϵ'_r (b) Conductividad σ 53
5.2 Estimación Inicial: (a) Prop.Dieléctricas (ϵ'_r,σ) (b) Contraste Inicial $\chi_{t,0}$ 54
5.3 (a) Reconst.prop.dieléctricas (b) True Re(χ) and Im(χ) (c) Reconst. Re(χ) and Im(χ) 55
5.4 Total, state and domain functional cost; Err: Error vs Iterations 55
5.5 d= 0.09m (a) Parte real permitividad relativa ϵ'_r (b) Conductividad σ 56
5.6 d= 0.09m ((a) Reconst.prop.dieléctricas (b) True Re(χ) and Im(χ) (c) Reconst. Re(χ) and Im(χ) 56
5.7 d= 0.02m (a) Reconst. diel. properties (b) Reconst. Re(χ) and Im(χ) 56
5.8 d= 0.09m (a) Parte real permitividad relativa ϵ'_r (b) Conductividad σ 57
5.9 d= 0.06m (a) Reconst.prop.dieléctricas (b) True Re(χ) and Im(χ) (c) Reconst. Re(χ) and Im(χ) 57
5.10 Total, state and domain functional cost; Err: Error vs Iterations 58
5.11 U-Shape profile: (a) Parte real permitividad relativa ϵ'_r (b) Conductividad σ 58
5.12 U-Shape profile: (a) Reconst.prop.dieléctricas (b) True Re(χ) and Im(χ) (c) Reconst. Re(χ) and Im(χ) 59
5.13 U-Shape profile: Total, state and domain functional cost; Err: Error vs Iterations 59

6.1 $|\chi| < 1$: (a) Parte real permitividad relativa ϵ'_r (b) Conductividad σ. 62
6.2 $|\chi| < 1$: (a) Reconst.prop.dieléctricas (b) True Re(χ) and Im(χ) (c) Reconst. Re(χ) and Im(χ). 62
6.3 $re(\chi) < 0$: (a) Reconst.prop.dieléctricas (b) True Re(χ) and Im(χ) (c) Reconst. Re(χ) and Im(χ). 63
6.4 $|\chi| > 1$: (a) Parte real permitividad relativa ϵ'_r (b) Conductividad σ. 63
6.5 $|\chi| > 1$: (a) Reconst.prop.dieléctricas (b) True Re(χ) and Im(χ) (c) Reconst. Re(χ) and Im(χ). 64
6.6 (R/λ_{bk}) análisis (a) Prop.Dieléctricas (ϵ'_r,σ) (b) Resultados Reconst. r= 0.21m (c) Resultados Reconst. r= 0.28m. 65

6.7 (R/λ_{bk}) análisis (a) True χ (b) Reconst.χ r= 0.21m (c) Reconst.χ r= 0.28m 65
6.8 f_o = 500MHz: (a) Reconst. prop. dieléctricas (b) True Re(χ) and Im(χ) (c) Reconst. Re(χ) and Im(χ) 66
6.9 Estudio del PEC: (a) Prop.Dieléctricas (b) Contraste Verdadero 67
6.10 Circular: (a) Escenario (b) reconst.prop.dieléc. (c) reconst.contraste 67
6.11 Cuadrada: (a) Escenario (b) reconst.prop.dieléc. (c) reconst.contraste 68
6.12 Triangular: (a) Escenario (b) reconst.prop.dieléc. (c) reconst.contraste 68
6.13 Cuadrados: a) True prop.dieléc. (b) Reconst. prop.diléc. (c) Estimación Inicial. 69
6.14 Cuadrados: a) True χ (b) Reconst. χ (c) Estimación Inicial 70
6.15 Cuadrados: Total, state and domain functional cost; Err: Error vs Iterations 70
6.16 E-phantom: a) True prop.dieléc. (b) Reconst. prop.diléc. (c) Estimación Inicial. . . . 71
6.17 E-phantom: a) True χ (b) Reconst. χ (c) Estimación Inicial 71
6.18 E-phantom: Total, state and domain functional cost; Err: Error vs Iterations 72
6.19 Medios sin pérdidas I: a) True prop.dieléc. (b) Reconst. prop.diléc. (c) Estimación Inicial. 72
6.20 Medios sin pérdidas I: a) True χ (b) Reconst. χ (c) Estimación Inicial 73
6.21 Medios sin pérdidas I: Total, state and domain functional cost; Err: Error vs Iterations . 73
6.22 Medios sin pérdidas II: (a) Reconst.Prop.Dieléctricas (b) Reconst.Contraste 74
6.23 Medios sin pérdidas II: Total, state and domain functional cost; Err: Error vs Iterations . 74
6.24 Antebrazo: (a) Parte real permitividad relativa ϵ_r' (b) Conductividad σ 75
6.25 Antebrazo: (a) True Contrast (b) Reconst.Contrast 75
6.26 Antebrazo: Total, state and domain functional cost; Err: Error vs Iterations 76
6.27 Cerebro: (a) Propiedades Dieléctricas (b) True Contrast 76
6.28 Cerebro: (a) Reconst.Diel.Properties (b) Reconst.Contrast 77
6.29 Cerebro: Total, state and domain functional cost; Err: Error vs Iterations 77

Lista de Tablas

4.1 Numeración de aristas para un elemento triangular 32
4.2 Costes Computacionales 48

6.1 Comparación entre las 3 simulaciones 66
6.2 Comparación entre PECs 69
6.3 Definición antebrazo 75
6.4 Modelo Cerebral 77
6.5 CSIM Resultados 79

Capítulo 1

Introducción

En este trabajo se diseña e implementa una herramienta matemática e ingenieril para aplicaciones biomédicas, denominada FEM-CSIM. Posteriormente, se evalúan e interpretan los resultados. Se desarrollan conceptos electromágneticos usados para resolver los posibles escenarios, y se presentan técnicas que nos permitirán optimizar este proceso.

1.1 Ámbito de la Aplicación

"Microwave Imaging" (MWI) es una de los más importantes campos de estudio dentro de la teoría de imagen para microondas en biomedicina (tomografía o detección de tumores son algunas posibles aplicaciones biomédicas basadas en MWI). Esta puede ser definida como el proceso en el cuál se descubre la estructura interna de un objeto empleando métodos electromagnéticos. Nosotros analizaremos un método basado en MWI que nos permitirá reconstruir las propiedades diléctricas de un determinado objetivo que a priori, son desconocidas. Este cuerpo que representa nuestro objetivo, es conocido como *Objeto de Interés* (OI), el cual será descrito profundamente durante el Capítulo 3.

El *Problema Directo* es una de las dos principales etapas que constituyen la aplicación. El OI es radiado mediante instrumentación electromagnética (antenas) y los resultados son utilizados como entrada en el algoritmo inverso, que constituye la segunda parte del proceso. A lo largo de este trabajo, el método inverso y la manera con la que los resultados electromagnéticos son computados (método de los elementos finitos) se describirán detalladamente.

1.2 Motivación

El *Problema Directo* y el *Método Inverso* serán implementados y evaluados separadamente para obtener un método global que nos permite conocer las propiedades materiales de un blanco desconocido, que puede estar localizado dentro de un cuerpo conocido. Conociendo estas propiedades del material es posible entender qué tipo de material se está analizando. Esta situación implica un gran beneficio en la ingenería biomédica, y más exactamente, en el tratamiento de imagen en el ámbito de la medicina. Por ejemplo, la tomografía nos permite establecer elcamino a la detección de tumores de mama, diagnosis de huesos y otro tipo de enfermedades.

Estos problemas reflejan las razones de la elección de este proyecto. MWI tiene un importante impacto en la ingenería médica y es innegable lo adecuado de este tipo de estudios para el desarrollo de la medicina. Por ello, la ingenería debe investigar en el campo de la medicina. Es un orgullo participar en el estudio e investigación de aplicaciones de bioingenería que resultan tan importantes para la mejora de la vida.

1.3 Definición del problema

Esta sección presenta una descripción del escenario en el que se desarrolla este trabajo. Supóngase que existe un cuerpo con unas cualidades determinadas y desconocidas, y estas propiedades son el objeto del estudio e investigación. Es necesario entender el comportamiento de este material para poder establecer conclusiones que pueden ser de gran importancia para el éxito de la investigación. Por ejemplo para diagnosticar un posible problema de salud (cáncer de mama).

En la Fig.1.1 se muestra un escenario médico, una detección de cáncer de mama. En este caso las propiedades materiales del pecho son conocidas, y si se aplica un correcto análisis, será posible detectar la existencia de cuerpos extraños que podrían representar un pequeño tumor.

Hay que tener muy en cuenta que el análisis del OI requiere que se aplique un método que nos permita descubrir las propiedades dieléctricas del cuerpo desconocido, sin ser alterado y mucho menos, ser dañado durante el proceso.

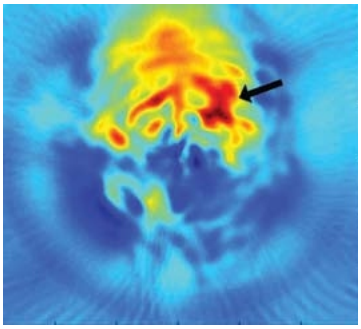

Figura 1.1: Resultados de una aplicación MWI

1.4 Solución propuesta

Existen diferentes caminos y métodos para solventar este problema. En este proyecto el método usado para resolver este problema biomédico es conocido como FEM-CSIM (FEM-Contrast Source Imaging Method). FEM será uno de los principales objetos de estudio, ya que permite computar de forma muy eficaz los parámetros electromagnéticos, además de representar un método muy popular para analizar escenarios en infinidad de aplicaciones ingenieriles como diseño de estructuras y análisis de temperatura. Si FEM-CSIM es implementado correctamente, se obtendrán las propiedades dieléctricas del OI con un pequeño error. Más tarde, estos resultados tendrán que ser analizados e interpretados por especialistas para determinar posibles problemas de salud.

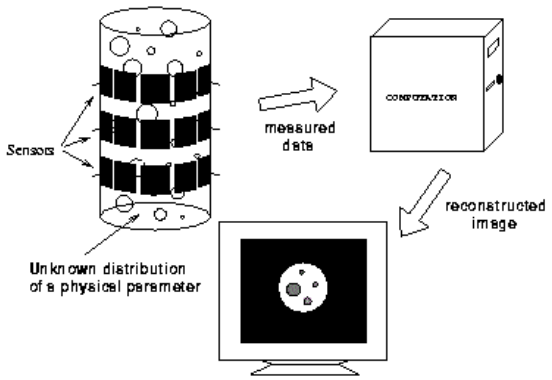

Figura 1.2: Descripción del proceso

Como ya fue mencionado anteriormente, podemos dividir la aplicación en dos partes: *Problema Directo*, resuelto mediante la implementación de FEM, y el *Algoritmo Inverso*. Gracias al método iterativo CSIM podremos obtener las propiedades eléctricas del OI. En la Fig.1.2, se describe el esquema general del proceso.

1.5 Contenido del Proyecto

Esta memoria esta compuesta por seis capítulos, siendo el objetivo del autor describir correctamente el método, los conceptos implicados en el proceso y, obviamente, los resultados y correspondientes conclusiones de la aplicación.

El Capítulo 2 aborda los conceptos electromagnéticos que han sido considerados durante este proyecto, principalmente los principios del electromagnetismo y la formulación de las ecuaciones de Maxwell. Además es necesario explicar otros conceptos imprescindibles en este trabajo como el estudio de las

condiciones de contorno.

El *Problema Directo* es presentado en el Capítulo 3, describiendo el escenario de MWI y cómo este problema es resuelto en experimentos reales, comparándolo con los escenarios simulados mediante FEM, que es el objeto de estudio del capítulo siguiente.

En el Capítulo 4 se describe detalladamente el Método de los Elementos Finitos (FEM). La complejidad de este método implica un estudio en profundidad y una importante comprensión del funcionamiento e implementación. También se describen sus aspectos matemáticos y geométricos centrados en los escenarios 2D. Sin embargo, se incluye una explicación breve sobre los problemas en 3D.

El problema de dispersión inversa es objeto de estudio en el Capítulo 5, donde se desarrolla e implementa FEM-CSIM y se evalúan los resultados obtenidos. Durante el Capítulo 6 se presentarán más resultados y conclusiones de determinados experimentos con el propósito de comprender más detalladamente el comportamiento de la aplicación.

Finalmente, también en el Capítulo 6, se abordan los posibles trabajos futuros que pueden ser llevados a cabo con el objeto de observar la amplitud del campo de estudio que suponen las aplicaciones MWI basadas en problemas inversos.

Capítulo 2

Conceptos Electromagnéticos

El electromagnetismo ha representado una parte indispensable de muchos estudios científicos e ingenieriles desde que J.C.Maxwell completase la teoría del electromagnetismo en 1873 [1]. Como es bien sabido, el problema del análisis electromagnético consiste en la resolución de un conjunto de ecuaciones de Maxwell sujetas a unas condiciones de contorno determinadas. En este capítulo se revisa la formulación matemática necesaria para implementar la aplicación de MWI. De este modo, revisaremos brevemente algunos conceptos básicos de la teoría electromagnética que se usarán en este trabajo. La formulación descrita considera tanto los casos en dos dimensiones (2D) para problemas escalares como los correspondientes a configuraciones vectoriales.

2.1 Ecuaciones de Maxwell

Las ecuaciones de Maxwell explican el comportamiento del fenómeno electromagnético y pueden ser expresadas mediante formas diferenciales e integrales. El conocimiento de estas ecuaciones es esencial para una correcta compresión del estudio desarrollado en este proyecto. Las ecuaciones de Maxwell, en su correspondiente forma diferencial, se derivan de su versión integral mediante el uso de los teoremas de Strokes y Gauss.

$$\nabla \times \vec{E}(\vec{r},t) = -\frac{\partial \vec{B}(\vec{r},t)}{\partial t} \tag{2.1}$$

$$\nabla \times \vec{H}(\vec{r},t) = \frac{\partial \vec{D}(\vec{r},t)}{\partial t} + \vec{J}(\vec{r},t) \tag{2.2}$$

$$\nabla \cdot \vec{D}(\vec{r},t) = \rho(\vec{r},t) \tag{2.3}$$

$$\nabla \cdot \vec{B}(\vec{r},t) = 0 \tag{2.4}$$

$$\nabla \cdot \vec{J}(\vec{r},t) = -\frac{\partial \rho}{\partial t} \tag{2.5}$$

donde los vectores espaciales $\vec{E}$, $\vec{H}$, $\vec{D}$, $\vec{B}$ and $\vec{J}$ son respectivamente, el campo eléctrico [V/m], la intensidad del campo magnético [A/m], el flujo de densidad eléctrica $[C/m^2]$, el flujo de densidad magnética $[Wb/m^2]$ y finalmente la densidad de corriente eléctrica $[A/m^2]$, en la ecuacione (2.3) la variable ρ se refiere a la carga eléctrica.
La densidad de corriente eléctrica $\vec{J}$ es la suma de dos contribuciones diferentes: la densidad de corriente de conducción $\vec{J_c}$, que implica la capacidad del medio para conducir corriente eléctrica, y la densidad de corriente impuesta $\vec{J_i}$, debida a las fuentes de corriente impuestas sobre el medio. Así,

$$\vec{J}(\vec{r},t) = \vec{J_c}(\vec{r},t) + \vec{J_i}(\vec{r},t) \tag{2.6}$$

Además es necesario introducir algunas ecuaciones adicionales para presentar correctamente la teoría desarrollada por Maxwell. Para medios isotrópicos, homogéneos y no dispersivos algunas relaciones de interés a considerar son las siguientes:

$$\vec{D}(\vec{r},t) = \epsilon_o \epsilon_r(\vec{r})\vec{E}(\vec{r},t) \tag{2.7}$$

$$\vec{B}(\vec{r},t) = \mu_o \mu_r(\vec{r})\vec{H}(\vec{r},t) \tag{2.8}$$

$$\vec{J_c}(\vec{r},t) = \sigma_o(\vec{r})\vec{E}(\vec{r},t) \tag{2.9}$$

En estas expresiones aparecen parámetros relacionados con las propiedades materiales como la permitividad en el vacío ϵ_o , la permitividad relativa compleja ϵ_r , la permeabilidad en el vacío μ_o, la permeabilidad relativa μ_r y la conductividad σ_o.

2.2 Condiciones de Contorno

Las ecuaciones diferenciales expuestas en la Sección 2.1 pueden ser resultas si se consideran las correspondientes condiciones de contorno de los medios presentes. En otras palabras, es necesaria una completa descripción de las interfaces entre medios con el objeto de obtener soluciones reales. Algunas condiciones de frontera usadas en la práctica son descritas:

$$\hat{n} \times (\vec{E_1}(\vec{r}) - \vec{E_2}(\vec{r})) = 0 \tag{2.10}$$

$$\hat{n} \times (\vec{H_1}(\vec{r}) - \vec{H_2}(\vec{r})) = 0 \tag{2.11}$$

$$\hat{n} \times (\vec{D_1}(\vec{r}) - \vec{D_2}(\vec{r})) = 0 \tag{2.12}$$

$$\hat{n} \times (\vec{B_1}(\vec{r}) - \vec{B_2}(\vec{r})) = 0 \tag{2.13}$$

En las expresiones (2.11) y (2.12), tanto la densidad de corriente eléctrica superficial como la carga eléctrica superficial son consideradas nulas. En el caso de que este supuesto no se cumpla, las expresiones son,

$$\hat{n} \times (\vec{H_1}(\vec{r}) - \vec{H_2}(\vec{r})) = \vec{J_s} \tag{2.14}$$

$$\hat{n} \times (\vec{D_1}(\vec{r}) - \vec{D_2}(\vec{r})) = \rho_s \tag{2.15}$$

2.3 Ecuación de Helmholtz

En esta aplicación es necesario resolver ecuaciones diferenciales parciales (PDE) del campo eléctrico $\vec{E}$. Para obtener la siguiente expresión es necesario eliminar la componente magnética $\vec{H}$,

$$\nabla \times \nabla \times \vec{E}(\vec{r}) - w^2 \mu_o \epsilon_o(\vec{r}) \vec{E}(\vec{r}) = -jw\mu_o \vec{J_i}(\vec{r}) \tag{2.16}$$

En la expresión (2.16) se han asumido dos condiciones: (i) no existen cargas eléctricas (ρ=0), (ii) la permeabilidad relativa es nula (problemas no magnéticos) $\mu_r = 1$. La ecuación (2.16) es conocida como la ecuacion de Helmholtz. Durante la descripción de FEM para problemas vectoriales veremos como se refiere a ella con el nombre de "curl-curl equation".

2.4 Ecuaciones Para Ondas Escalares

En el análisis electromagnético, siempre que sea posible, se utiliza una formulación simplificada de los problemas haciendo uso de modelos en 2D como aproximación a los problemas en 3D. Podemos definir el escenario escalar de la siguiente manera,

$$\nabla^2 E_z + k_o^2 \epsilon_r E_z = jw\mu_o J_z \tag{2.17}$$

también conocida como *ecuación para ondas escalares inhomogéneas*. Esta expresión será usada durante el Capítulo 4 para describir los problemas escalares en 2D correspondientes al caso de una polarización TM-z.

Capítulo 3

El Problema Directo

"Microwave Imaging" (MWI) es de interés para diversas aplicaciones, como estudios geofísicos e imágenes médicas. En la aplicación de MWI considerada en este proyecto se trata de reconstruir cuantitativamente las propiedades eléctricas (i.e. permitividad y conductividad), en su mayor parte desconocidas, de un objeto de interés (OI) que está sumergido en un medio "background" de propiedades diléctricas conocidas [9]. Como se comentó en el Capítulo 1, para resolver una aplicación de MWI es necesario implementar el *Problema Directo* con el propósito de obtener las distribución del campo eléctrico. En este capítulo, describiremos como se realiza la resolución del *Problema Directo* en aplicaciones experimentales reales en comparación a las apliaciones basadas en problemas simulados.

3.1 Punto de Partida

Antes de explicar como se implementa el *Problema Directo* mediante simulación, es interesante y beneficioso para una mayor compresión del problema explicar cómo se realiza dicho proceso en aplicaciones médicas reales como detección de tumores o diagnósticos de huesos. Se considera un escenario de microondas en donde la región de imagen esta rodeada por una superficie eléctrica conductora. Esta superficie trabaja como una interfaz protectora de las interferencias exteriores y como contenedor de un medio adaptador que debe evitar las reflexiones producidas en las paredes. En la Fig.3.1. (extraida de [6]) se puede observar un liquído común en muchas aplicaciónes MWI basada en una solución de glicerina-agua al 80:20 por ciento.

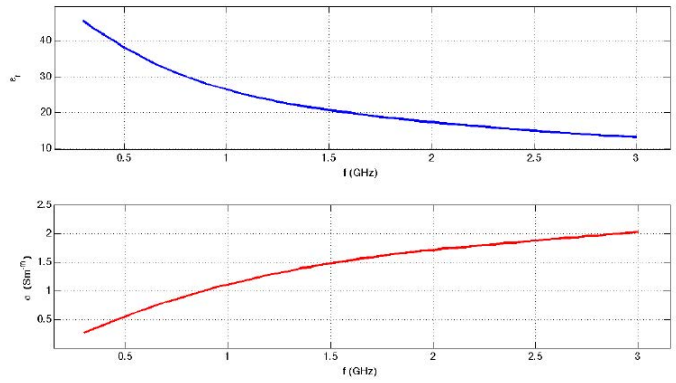

Figura 3.1: Permitividad relativa (línea azul) y conductividad (línea roja) para glycerine-water 80:20 de 300MHz hasta 3GHz

Un conjunto de antenas que rodean el OI, que trabajan tanto como emisores como receptores, iluminan el escenario con el objetivo de captar las mediciones EM. El OI se encuentra localizado en la región $\mathcal{D}$ junto con parte del "background" homogéneo (permitividad denotada como ϵ_b).

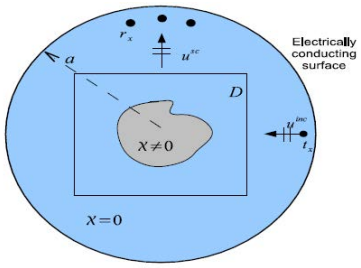

Figura 3.2: Sistema de Imagen Cerrado.

En la Fig.3.2 [10] se puede visualizar el esquema general de la aplicación. En este caso, el recinto cerrado es un tanque cilíndrico. Nótese que durante este proyecto denotaremos las propiedades dieléctricas como

$$\epsilon = \epsilon' + j\epsilon'' = \epsilon_o\epsilon_r = \epsilon_o\left(\epsilon_r' + j\epsilon_r''\right) = \epsilon_o\left(\epsilon_r' + j\frac{\sigma}{w\epsilon_o}\right) \tag{3.1}$$

Algunas posibles aplicaciones basadas en obtención de imágenes se observan en la Fig.3.3.

3.2 Ondas Electromagnéticas

Cuando hablamos sobre el análisis EM en el *Problema Directo*, necesitamos diferenciar entre los posibles casos que pueden darse. En un medio, la propagación de una onda puede ser onda transversal electromagnética caracterizada por $E_z = H_z = 0$, lo cual implica que las componentes transversales son

(a) (b)

Figura 3.3: (a) Protótipo de un sístema MWT (b) Lectura de tomografía

nulas. Otra posiblidad es el caso de ondas TE. Esta propagación implica que $E_z = 0$, de forma que la unica componente transversal existente es la magnética, $H_z \neq 0$. Finalmente, existe un caso EM basado en la presencia de una componente eléctrica no nula, $E_z \neq 0$, mientras que la componente tranversal magnética cumple, $H_z = 0$. En el ambiente de aplicaciones de imagen para microondas, la formulación 2D corresponde a la polarización TM. Este problema será resuelto con solvencia mediante el uso de elementos nodales.

3.3 Métodos de Simulación

El objeto de esta sección es la obtención de técnicas de simulación capaces de proporcionar un modelo sintético de posibles experimentos reales basados en MWI. De ellos se podría extraer los parámetros EM del escenario. La técnica elegida en este proyecto es denomidada como *método de los elementos finitos*, que implica la resolución de una ecuación matricial donde los coeficientes eléctricos que definen el campo eléctrico en nuestro escenario, pueden ser computados mediante la generación de una matriz global, conocida como *matriz FEM*. Esta matriz relaciona la geometría del escenario con las correspondientes propiedades eléctricas propias de éste. Esta ecuación matricial viene dada por la siguiente expresión,

$$\mathbf{Az} = \mathbf{b} \tag{3.2}$$

Nuestra simulación directa involucra un método iterativo en el que una determinada antena funciona como emisor mientras el resto de antenas trabajan como receptores. Posteriormente, otra antena será la transmisora, de forma que el Tx de la anterior medición trabaja como Rx junto al resto de antenas. Obviamente, a mayor número de antenas mayor cantidad de información será recolectada por lo que la solución será más proxima a la real. En la Fig.3.4 (imágenes obtenidas de [3]), se definen los escenarios en 2D y 3D.

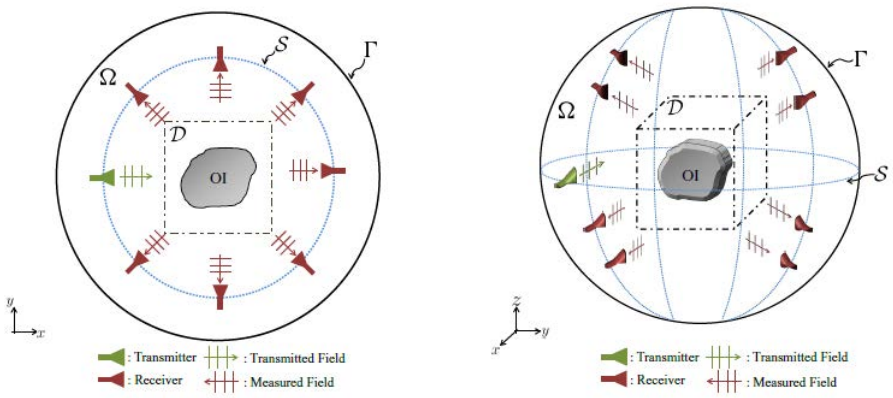

(a) (b)

Figura 3.4: (a) modelo MWI 2D (b) modelo MWI 3D

Debido a que nosotros trabajaremos con datos sintéticos, es necesario generar un posible escenario en dos o tres dimensiones que describa un posible escenario real. Existen un gran abanico de simuladores que nos permiten generar este tipo de datos. En nuestro caso, el simulador elegido es GiD, obviamente basado en FEM (más información en la web oficial de GiD http://gid.cimne.upc.es/).

Finalmente, es necesario aclarar que FEM representa una manera diferente de computar el campo electromagnético respecto a la teoría tradicional basada en las funciones de Green, teoría denominada como la *Formulación de Integración*.

Capítulo 4

El Método De Los Elementos Finitos

En este capítulo se presenta el método de los elementos finitos modelado para imagen en microondas. Debido a la importancia de FEM durante la realización de este proyecto, representa uno de los principales objetos de estudio. Se tratarán temas como los conceptos básicos que definen esta técnica, así como las posibles aplicaciones del método, los requisitos necesarios para su correcto funcionamiento, aspectos relacionados con la creación de las mallas, la implementación de las matrices implicadas en el proceso y, obviamente, cómo esta herramienta se utiliza para resolver el *Problema Directo*. Además, serán tratadas cuestiones como los problemas de contorno (BVP), especificándolas tanto para problemas escalares (2D) como para problemas vectoriales (3D).

4.1 Conceptos Básicos de FEM

En esta sección se presentan los principios básicos del método de los elementos finitos (FEM). El método de los elementos finitos es una herramienta muy utilizada para la resolución de ecuaciones diferenciales en muchas disciplinas. Por ejemplo, en electromagnetismo, mecánica de sólidos y estructuras, dinámica de fluidos, acústica y conducción térmica, entre otras. En esta sección se presenta el método FEM en el ámbito del electromagnetismo, donde las ecuaciones de Maxwell se encuentran involucradas. A continuación se enumeran los pasos necesarios para realizar con éxito la resolución de FEM para una determinada geometría en 2D. Obviamente, para 3D los pasos serían equivalentes pero aplicando la geometría y funciones correspondientes a los problemas vectoriales.

1. Discretización del dominio en 2D.

2. Derivación de la formulación de la ecuación diferencial.

3. Derivación de los elementos matriciales y vectoriales.

4. Implementación de la matriz global que define el sistema.

5. Imposición de las condiciones de frontera.

6. Resolución de la ecuación matricial global.

7. Posterior procesado de los resultados.

La ventaja principal por la que FEM es el método favorito en muchas aplicaciones ingenieriles es la capacidad del método para ser aplicado en geometrías muy complejas. Normalemente, este proceso se realiza mediante el uso de mallas no estructuradas basadas en triángulos para 2D y tetrahedros en 3D, aunque otros elementos pueden ser usados para construir la malla. Sin embargo, existe una desventaja importante en comparación con otros métodos, como se comentó en la Sección 2. En lugar de resolver la formulación explícita de los campos en el dominio temporal la computación de estos requieren la resolución de un conjunto de ecuaciones lineales. Debido a ello, para un mismo número de variables, FEM requiere mayores recursos de computación, en términos de tiempo y memoria.

4.2 Discretización del Dominio

Un paso fundamental en la ejecución de FEM, y quizas el más importante, es el problema atribuido a la definición del dominio computacional. El objeto del análisis es una determiniada región Ω, y para una correcta definición, es necesario discretizar el dominio; es decir, la region Ω es dividida en subelementos. Este proceso tiene tanta importancia debido a que la manera con la que se realice la discretización afectará a aspectos tan esenciales como el coste computacional o la precisión de los resultados numéricos.

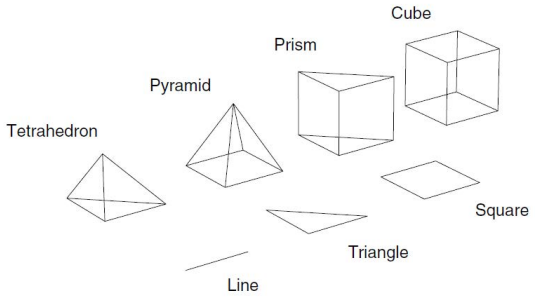

Figura 4.1: Elementos diferentes para discretización del dominio en 1D, 2D y 3D

Otra cuestión importante es el tipo de elementos usados durante la discretización, Mientras que en 1D los elementos usados se basan en líneas curvas o rectas que pueden conectar dos nodos diferentes, en los casos de 2D los elementos comunmente utilizados son triángulos o cuadriláteros como cuadrados. Es preferible el uso de triángulos debido a que su geometría le permite adaptarse mejor a geometrías

complejas (por ejemplo contornos con curvas) evitando un error de discretización grande. En la fig.4.2 [4], podemos observar el error producido por ambos subelementos. En un problema en 3D, se hace uso de tetrahedros o prismas. En la Fig.4.1 se muestran diferentes posibilidades.

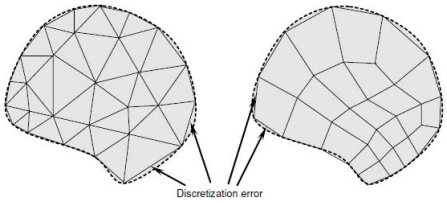

Figura 4.2: Error de discretización derivado del uso de triángulos o cuadrados.

Nos centraremos en el caso de dos dimensiones, donde los triángulos serán los elementos usados para nuestra malla. Se deberán respetar las siguientes propiedades, (i) dentro del dominio, los elementos no deben solaparse y los elementos comparten nodos y aristas, (ii) los triángulos deberían ser lo más próximos a triangulos equiláteros y (iii) su tamaño debe ser definido como función de la longitud de onda y del gradiente de la solución. Debido a la tercera condición, aparecen las mallas adaptativas, definidas por la cualidad de presentar un mayor número de subelementos para aquellas regiones o zonas donde la variabilidad de la geometría es mayor.

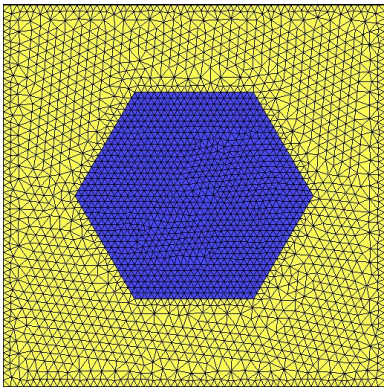

Figura 4.3: Malla adaptativa de una geometría en 2D.

Para obetener resultados correctos es necesario que la longitud de las aristas que definen los elementos de la malla para cada región del dominio seá inferior a $\lambda_g/15$ donde $\lambda_g = \frac{\lambda_o}{\sqrt{\epsilon_r \mu_r}}$.

4.3 Funciones Base

El método de elementos finitos permite computar el campo electromagnético utilizando unas funciones espaciales denominadas como *Funciones Base*. Estas interrelacionan las propiedades electromagnéticas

con las cualidades físicas del dominio computacional. Recordemos la ecuación matricial global dada por FEM introducida en el Capítulo 3:

$$\underline{\underline{A}} \cdot \underline{x} = \underline{b} \tag{4.1}$$

Es posible resolver la expresión (4.1) aproximando el campo eléctrico de la siguiente forma,

$$\mathbf{E} \cong \sum_i e_i \mathbf{W_i} \tag{4.2}$$

donde e_i representa a los coeficientes eléctricos y $\mathbf{W_i}$ a las funciones de base.

Como hemos comentado anteriormente, existen los problemas escalares y también los vectoriales. A cada uno de ellos se le asocia un tipo diferente de *funciones base*. Podemos definir las *Funciones Base Nodales* y las *Fuciones Base Vectoriales*. En las siguientes secciones se describen ambos tipos, determinando sus ventajas y desventajas y obviamente asociándolas a los problemas escalares o vectoriales.

4.3.1 Funciones Base Nodales

Las funciones base locales son denotadas por $\varphi_i^e(x, y)$, donde el superíndice etiqueta el elemento (e = 1,..., Ne) y el subíndice se refiere al número del nodo local dentro de ese elemento (i = 1, 2, 3). De forma que cada función base local se asocia a cada nodo de nuestro elemento, en nuestro caso, a cada nodo que forma el triángulo. En la Fig.4.4 se describe la numeración y etiquetado de cada elemento triangular.

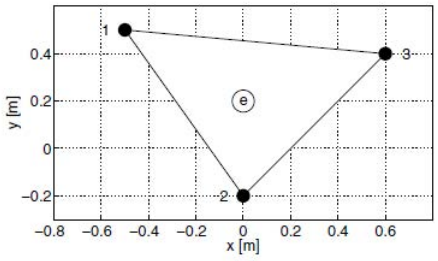

Figura 4.4: Numeración de los nodos locales de cada elemento e.

Vemos como cada nodo se asocia a dos etiquetas: un número local, que indica la posición dentro del elemento triangular y un número global, que indica su posición relativa dentro de la malla. Nótese que los nodos son numerados en dirección opuesta a las agujas del reloj para evitar áreas negativas en la posterior integración.

Dentro de cada triángulo e, la variable viene definida como,

$$u^e(x,y) = \sum_{i=1}^{3} u_i^e \varphi_i^e(x,y) \tag{4.3}$$

Las funciones base presentan las siguientes propiedades:

- Dentro de cada elemento, son lineales en x e y,

$$\varphi_i^e(x,y) = \frac{1}{2A^e}\left(a_i^e + b_i^e x + c_i^e y\right) \tag{4.4}$$

- Son iguales a uno en un nodo y se desvanencen en el resto:

$$\varphi_i^e\left(x_i^e, y_i^e\right) = 1, \qquad \varphi_i^e\left(x_j^e, y_j^e\right) = 0, \forall i \neq j \tag{4.5}$$

Véase en la versión original [A.1] la Sección 4.3.1 exp.(4.6), para mejor comprensión del proceso de obtención de los parámetros a, b y c de la ecuación (4.4).

En algunos tipos de geometrías, como en escenarios en 3D, las funciones nodales aproximan soluciones incorrectas, conocidas como soluciones no físicas, debido a modos falsos asociados a problemas vectoriales. Este fenómeno puede ser solventado mediante el uso de *Funciones Base Vectoriales*.

4.3.2 Funciones Base Vectoriales

Como acabamos de comentar, la resolución de problemas vectoriales mediante FEM usando variables nodales provoca algunos inconvenientes como las soluciones falsas. Afortunadamente, una aproximación revolucionaria fue descubierta para solucionar estos problemas. Este nuevo planteamiento se basa en el uso de las denominadas funciones base vectoriales o elementos vectoriales que asignan un mayor grado de libertad frente a las funciones nodales. Los elementos vectoriales permiten eliminar esas soluciones no físicas que introducen un error en la computación del campo EM. Definimos los elementos vectoriales para dos dimensiones mediante la siguiente expresión:

$$\vec{E}^e(\vec{r}) = \sum_{j=1}^{3} E_j^e \vec{N}_j^e(\vec{r}) \tag{4.6}$$

donde E_j^e denota el campo tangencial a lo largo de la arista jth.

Los nodos del elemento triangular se encuentran unidos por tres aristas. Cada una de las aristas de la malla están identificadas por dos etiquetas: un número local para indicar su posición en un determinada triángulo y un número global para indicar su localización respecto a la malla total.

Tabla 4.1: Numeración de aristas para un elemento triangular

Edge No.i	Node i_1	Node i_2
1	1	2
2	2	3
3	3	1

Cada uno de esas aristas esta asociada a una función base vectorial:

$$\vec{N}_j^e(\vec{r}) = l_i^e \left(\varphi_{i_1}^e \vec{r} \nabla \varphi_{i_2}^e \vec{r} - \varphi_{i_2}^e \vec{r} \nabla \varphi_{i_1}^e \vec{r}\right) \tag{4.7}$$

donde l_i^e denota la longitud de la arista i, $\varphi_{i_1}^e \vec{r}$ and $\varphi_{i_2}^e \vec{r}$ son las funciones nodales descritas en la expresión (4.4) de cada uno de los nodos que forman la arista e.

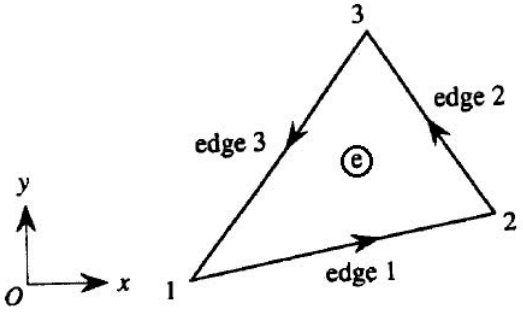

Figura 4.5: Elemento triangular basado en elementos vectoriales

4.4 Problemas Escalares

Es el momento de introducir FEM en la resolución de algunos posibles problemas en dos dimensiones relacionados a problemas escalares. Básicamente, un problema escalar se encuentra definido por una variable que debe ser determinada, por ejemplo, una polariazación TM-z. Esta sección se centra en este caso particular ya que define nuestro marco de estudio en este trabajo. Introduciendo las condiciones de contorno descritas en el Capítulo 2 surge el problema de valores de frontera (BVP) en nuestro enfoque. En definitiva, en esta sección, la formulación FEM asociada al desarrollo de las ecuaciones matriciales será utilizada para la resolución de problemas escalares.

4.4.1 Problema de Valores en la Frontera en 2D

En la Sección 2.4 se introdujo la expresión (2.17), que denominamos como *ecuación de onda inhomogénea*. Ahora tratamos de analizarla para geometrías en 2D. Nótese que las aplicaciones MWI están sujetas a un recinto basado en un PEC. Esto requiere que las condiciones de frontera seán consideradas en la formulación y computación de FEM. De esta forma, nuestro escenario escalar en 2D quedará correctamente definido por la siguiente ecuación

$$-\nabla \cdot (\alpha \nabla u) + \beta u = g \tag{4.8}$$

y las condiciones de contorno

$$u = p \qquad on \ \ \Gamma_1 \tag{4.9}$$

$$\hat{n} \cdot (\alpha \nabla u) + \gamma u = q \qquad on \ \ \Gamma_2 \tag{4.10}$$

donde u es la función desconocida, α y β son los parámetros conocidos asociados a las propiedades físicas del dominio Ω, y g es la fuente o función de excitación. Acorde con las condiciones de frontera, Γ_1 define la condición de contorno de "Dirichlet" mientras Γ_2 se refiere a la de Robin, con $\Gamma_1 + \Gamma_2 = \Gamma$. Γ denota la interfaz que encierra el área Ω. γ, p y q son los parámetros conocidos asociados con las propiedades físicas de la frontera. Cuando $\gamma = 0$ la condición de frontera de Robin se convierte en un caso especial denominado como la frontera Neumman.

4.4.2 Resolviendo BVP Usando el Método de Garlerkin

La expresión general de BVP en 2D que aparece en (4.8) puede ser reescrita de la siguiente forma equivalente

$$\frac{\partial}{\partial x}\left(\alpha_x \frac{\partial u}{\partial x}\right) + \frac{\partial}{\partial y}\left(\alpha_y \frac{\partial u}{\partial y}\right) + \beta u = g \tag{4.11}$$

y las condiciones de contorno

$$u = p \qquad on \ \ \Gamma_1 \tag{4.12}$$

$$\left(\alpha_x \frac{\partial u}{\partial x} \cdot \hat{x} + \alpha_y \frac{\partial u}{\partial y} \cdot \hat{y}\right) \cdot \hat{n} + \gamma u = q \qquad on \ \ \Gamma_2 \tag{4.13}$$

donde α_x, α_y y β son constantes. La formulación necesaria para este problema puede obtenerse construyendo el residuo ponderado de la expresión (4.11) para un simple elemento con dominio Ω^e

$$r^e = \frac{\partial}{\partial x}\left(\alpha_x \frac{\partial u}{\partial x}\right) + \frac{\partial}{\partial y}\left(\alpha_y \frac{\partial u}{\partial y}\right) + \beta u - g \tag{4.14}$$

Este elemento residual sería idealmente cero, lo cual implicaría que la solución numérica obtenida de u es igual a la solución exacta. Sin embargo, este no es el caso, de forma que por general, el elemento residual r^e es no nulo. Para minimizar el residuo, primero debemos multiplicar todos los términos de la expresión por los pesos w, y posteriormente integrar la expresión resultante a lo largo del área del elemento en cuestión, y finalmente fijarla a cero.

$$\int\int_{\Omega_e} w\left[\frac{\partial}{\partial x}\left(\alpha_x \frac{\partial u}{\partial x}\right) + \frac{\partial}{\partial y}\left(\alpha_y \frac{\partial u}{\partial y}\right) + \beta u - g\right] dxdy = 0 \tag{4.15}$$

Haciendo uso de la *Formulación Variacional* para elementos finítos y del *Teorema de Divergencia* podemos desarrollar la expresión (4.15) hasta reducir la formulación débil de la ecuación diferencial a la siguiente expresión (Para más detalles en la obtención de la expresión (4.16) analizar ecuaciones (4.19)-(4.27) del elemento original [A.1]),

$$\begin{aligned} &-\int\int_{\Omega_e}\left[\alpha_x \frac{\partial w}{\partial x}\frac{\partial u}{\partial x} + \alpha_y \frac{\partial w}{\partial y}\frac{\partial u}{\partial y}\right] dxdy + \int\int_{\Omega_e} \beta\, w\, u\, dxdy = \int\int_{\Omega_e} w\, g\, dxdy \\ &-\oint_{\Gamma^e} w\left(\alpha_x \frac{\partial u}{\partial x}\hat{x} + \alpha_y \frac{\partial u}{\partial y}\hat{y}\right) dl \end{aligned} \tag{4.16}$$

Asumiendo el planteamiento de Garlerkin, la función de pesos w debe ser relacionada al mismo conjunto de funciones espaciales que interpolan la incognita principal, u. Esta incognita es interpolada usando los polinomios de Lagrange que aparecen en la expresión (4.3). Es decir,

$$u = \sum_{j=1}^{n} u_j^e N_j \tag{4.17}$$

donde N_j es la correspondiente función espacial basada en elementos nodales y n es el número total de nodos que forman el dominio Ω_e (caso general, en nuestro caso $n = 3$). Imponiendo $w = N_i$ con $i = 1, 2, 3...N_e$ y substituyendo en (4.16) obtenemos,

$$
\begin{aligned}
&-\int\int_{\Omega_e}\left[\alpha_x\left(\frac{\partial N_i}{\partial x}\right)\left(\sum_{j=1}^{N_e}u_j^e\frac{\partial N_j}{\partial x}\right)+\alpha_y\left(\frac{\partial N_i}{\partial y}\right)\left(\sum_{j=1}^{N_e}u_j^e\frac{\partial N_j}{\partial y}\right)\right]dxdy\\
&+\int\int_{\Omega_e}\beta\,N_i\left(\sum_{j=1}^{N_e}u_j^eN_j\right)dxdy=\int\int_{\Omega_e}N_i\,g\,dxdy-\oint_{\Gamma^e}N_i\left(\alpha_x\frac{\partial u}{\partial x}\hat{x}+\alpha_y\frac{\partial u}{\partial y}\hat{y}\right)dl,
\end{aligned}
\tag{4.18}
$$

$for\ \ i=1,2,3...N_e$

La ecuación (4.18) en forma matricial resulta

$$
\begin{bmatrix}M_{11}^e & M_{12}^e & \cdots & M_{1n}^e\\ M_{21}^e & M_{22}^e & \cdots & M_{2n}^e\\ \vdots & \vdots & \ddots & \vdots\\ M_{n1}^e & M_{n2}^e & \cdots & M_{nn}^e\end{bmatrix}\begin{Bmatrix}u_1^e\\u_2^e\\\vdots\\u_n^e\end{Bmatrix}+\begin{bmatrix}T_{11}^e & T_{12}^e & \cdots & T_{1n}^e\\ T_{21}^e & T_{22}^e & \cdots & T_{2n}^e\\ \vdots & \vdots & \ddots & \vdots\\ T_{n1}^e & T_{n2}^e & \cdots & T_{nn}^e\end{bmatrix}\begin{Bmatrix}u_1^e\\u_2^e\\\vdots\\u_n^e\end{Bmatrix}=\begin{Bmatrix}f_1^e\\f_2^e\\\vdots\\f_n^e\end{Bmatrix}+\begin{Bmatrix}p_1^e\\p_2^e\\\vdots\\p_n^e\end{Bmatrix}
\tag{4.19}
$$

donde

$$
M_{ij}^e=-\int\int_{\Omega_e}\left[\alpha_x\left(\frac{\partial N_i}{\partial x}\right)\left(\frac{\partial N_j}{\partial x}\right)+\alpha_y\left(\frac{\partial N_i}{\partial y}\right)\left(\frac{\partial N_j}{\partial y}\right)\right]dxdy \tag{4.20}
$$

$$
T_{ij}^e=\int\int_{\Omega_e}\beta\,N_i\,N_j\,dxdy \tag{4.21}
$$

$$
f_i^e=\int\int_{\Omega_e}N_i\,g\,dxdy \tag{4.22}
$$

$$
p_i^e=-\oint_{\Gamma^e}N_i\left(\alpha_x\frac{\partial u}{\partial x}\hat{x}+\alpha_y\frac{\partial u}{\partial y}\hat{y}\right)dl \tag{4.23}
$$

Es posible implentar un sístema matricial más compacto,

$$
\begin{bmatrix}K_{11}^e & K_{12}^e & \cdots & K_{1n}^e\\ K_{21}^e & K_{22}^e & \cdots & K_{2n}^e\\ \vdots & \vdots & \ddots & \vdots\\ K_{n1}^e & K_{n2}^e & \cdots & K_{nn}^e\end{bmatrix}\begin{Bmatrix}u_1^e\\u_2^e\\\vdots\\u_n^e\end{Bmatrix}=\begin{Bmatrix}b_1^e\\b_2^e\\\vdots\\b_n^e\end{Bmatrix}
\tag{4.24}
$$

donde

$$
\begin{aligned}
K_{ij}^e&=M_{ij}^e+T_{ij}^e\\
b_i^e&=f_i^e+p_i^e
\end{aligned}
\tag{4.25}
$$

La matriz $\mathbf{K^e}$ es la matriz FEM de cada elemento. Para implementar la matriz FEM es necesario sumar la matriz de Stiffness (4.20) y la matriz de Mass (4.21), mientras que $\mathbf{M^e}$ depende de las condiciones de frontera del dominio, y $\mathbf{T^e}$ depende de las propiedades dieléctricas del dominio elemental Ω_e.

Tras el desarrollo llevado a cabo en el documento original (A.1), ecuaciones (4.36)-(4.41), podemos obtener una nueva versión de la ecuación (4.23) dada por,

$$p_i^e = -\int_{\Gamma_2} N_i \left(q - \gamma\, u\right) dl \tag{4.26}$$

La integral de línea en (4.26) existe solamente para los elementos de contorno, y ésta debe ser evaluado solo para las aristas localizadas a lo largo de Γ_2. Para las interiores, la contribución es nula.

4.5 Problemas Vectoriales

Aunque los problemas escalares definen el escenario de nuestro proyecto, creemos que es beneficioso introducir la formulación asociada a la teoría vectorial en electromagnetismo. A diferencia de los problemas escalares, los vectoriales se encuentran definidos por dos o más variables.

4.5.1 La Ecuación "Curl-Curl" y Los Elementos Vectoriales

El campo electromagnético es presentado como la ecuación de Helmholtz, generando una ecuación particular que es conocida como la ecuación "curl-curl" para el campo $\vec{E}$.

$$\nabla \times \left(\mu^{-1} \nabla \times \vec{E}(\vec{r})\right) - \left(w^2 \epsilon' - jw\sigma\right) \vec{E}(\vec{r}) = -jw\vec{J}_s(\vec{r}) \qquad on \;\; S \tag{4.27}$$

y las condiciones de contorno

$$\hat{n} \times \vec{E}(\vec{r}) = \vec{p}(\vec{r}) \qquad on \;\; \Gamma_1 \tag{4.28}$$

$$\hat{n} \times (\mu^{-1} \nabla \times \vec{E}(\vec{r})) + \gamma(\vec{r}) \hat{n} \times (\hat{n} \times \vec{E}(\vec{r})) = \vec{q}(\vec{r}) \qquad on \;\; \Gamma_2 \tag{4.29}$$

El siguiente paso es seguir el planteamiento de Garlerkin pero utlizando elementos vectoriales. La formulación débil de integración viene dada por

$$\begin{aligned} &\int_S \left[\mu^{-1} \left(\nabla \times \vec{W}_i\right) \cdot \left(\nabla \times \vec{E}\right) - \left(w^2 \epsilon' - jw\sigma\right) \vec{W}_i \cdot \vec{E}\right] dS \\ &+ \int_{\Gamma_2} \vec{W}_i \cdot \left(\vec{q} - \gamma \hat{n} \times \hat{n} \times \vec{E}\right) dl = -jw \int_S \vec{W}_i \cdot \vec{J}_s \, dS \end{aligned} \tag{4.30}$$

Expandiendo la solución $\vec{E}(\vec{r})$ en términos de las nuevas funciones base,

$$\vec{E}(\vec{r}) = \sum_{j=1}^{N_e} E_j \mathbf{N_j} \tag{4.31}$$

donde E_j es el campo tangencial a lo largo de la arista j-simo, Ne es el número de elementos vectoriales e imponiendo $\vec{W}_i = \mathbf{N_i}$, substituimos en (4.30) obteniendo un sístema lineal de ecuaciones $\mathbf{Az} = \mathbf{b}$ con

$$\begin{aligned} A_{ij} = &\int_S \left[\mu^{-1} \left(\nabla \times \mathbf{N_i}\right) \cdot \left(\nabla \times \mathbf{N_j}\right) - \left(w^2\epsilon' - jw\sigma\right) \mathbf{N_i} \cdot \mathbf{N_j}\right] dS \\ &+ \int_{\Gamma_2} \gamma \left(\hat{n} \times \mathbf{N_i}\right) \cdot \left(\hat{n} \times \mathbf{N_j}\right) dl \end{aligned} \tag{4.32}$$

$$z_j = E_j \tag{4.33}$$

$$b_i = -jw \int_S \mathbf{N_i} \cdot \mathbf{J_s}\, dS - \int_{\Gamma_2} \mathbf{N_i} \cdot \mathbf{q}\, dl \tag{4.34}$$

4.6 Absorbiendo Condiciones de Contorno

La mayor parte de los problemas de dispersión descritos durante este trabajo se resuelven en espacios finitos de espacio físico. Sin embargo, existen aplicaciones de electromagnetismo donde el emplazamiento se realiza en espacio abierto. Imagínese una aplicación de medición de los parámetros de una determinada antena o la interacción de una onda incidente en una determinada estrucura. En ambos casos el campo radiado se propaga a través del espacio libre. En otras palabras, las condiciones de frontera deberían encontrarse en el infinito.

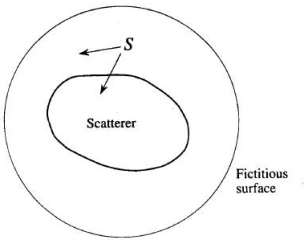

Figura 4.6: MWI application results

En la Sección 4.3 vimos como la principal desventaja del FEM son los costes computacionales necesarios para computar los datos electromagnéticos. De forma que el caso de una aplicación en espacio abierto implicaría unos requerimientos computacionales no aceptables. Por ello, será necesario truncar mediante barreras artificiales la region exterior con el propósito de limitar el tamaño del dominio computacional. Esta frontera deberá aparecer tan transparente como sea posible para el campo dispersivo/radiado. Es

decir, las reflexiones producidas en la frontera artificial deberán ser minimizadas. Este cambio de estudio es conocido como Absorbiendo Condiciones de Contorno (ABCs).

ABCs simulan o reemplazan el espacio infinito que rodea un dominio computacional finito. Esta operación nunca es perfecta, de forma que la solución computada dentro del ABC es solo una estimación de la solución real. Algunas propiedades de estas regiones artificiales deben ser:

1. ABC debe estar tan cercano como sea posible a la estructura, de forma que el dominio computacional sea lo más pequeño posible. Esto permitirá computar una cantidad de datos suficientemente aceptables.

2. Los cambios del escenario original deben ser prácticamente inapreciables con el objeto de obtener resultados lo más reales posibles.

3. Si ABC sólo puede absorber ondas planas homogéneas, ésta deberá ser colocada fuera de la región evanescente que rodea la fuente electromagnética (antena, guía de ondas).

4. Si ABC puede absorber campos evanescentes, esta deberá ser colocada lo más cercana posible a la fuente para reducir el dominio computacional.

La teoría tradicional sobre el fenómeno de ABC analiza una serie de posibles implementaciones basadas en aproximaciones de Taylor de orden n-simo. Básicamente, se describe la curva del coeficiente de reflexión de nuestra interfaz y se manipula de forma que este coeficiente sea nulo para determinados ángulos de incidencia. Sin embargo, este método presenta una gran desventaja, ya que sólo para una única frecuencia obtendremos el propósito que buscamos. Este problema fue solucionando cuando en 1994 Berenger [5] propusó el concepto del "perfectly matched layer" (PML).

4.6.1 "The Perfectly Matched Layer" en 2D

Una "perfectly matched layer" (PML) es una interfaz que no refleja una onda plana para ninguna frecuencia, ni ángulo de incidencia. Al mismo tiempo, permite truncar el dominio infinito a un tamaño de coste computacional aceptable. El planteamiento principal se basa en la introducción de unos parámetros conocidos como factores de estiramiento: s_x, s_y and s_z (Coordenadas de estiramiento). Además, es importante presentar un nuevo operador, ∇_s, que se usa para la correspondiente modificación de las ecuaciones de onda.

$$\nabla_s = \hat{x}\frac{1}{s_x}\frac{\partial}{\partial x} + \hat{y}\frac{1}{s_y}\frac{\partial}{\partial y} + \hat{z}\frac{1}{s_z}\frac{\partial}{\partial z} \tag{4.35}$$

de forma que

$$\mathbf{k_s} = \hat{x}\frac{k_x}{s_x} + \hat{y}\frac{k_y}{s_y} + \hat{z}\frac{k_z}{s_z} \tag{4.36}$$

la nueva formulación de las ecuaciones de Maxwell viene dada por,

$$\nabla_s \times \vec{E}(\vec{r}) = -jw\mu\vec{H}(\vec{r}) \tag{4.37}$$

$$\nabla_s \times \vec{H}(\vec{r}) = jw\epsilon\vec{E}(\vec{r}) \tag{4.38}$$

Definamos las coordenadas de estiramiento, (formulación extraida de [5])

$$s_x = 1 + \frac{\sigma_x}{jw\epsilon_o} \qquad s_x^* = 1 + \frac{\sigma_x^*}{jw\mu_o} \tag{4.39}$$

$$s_y = 1 + \frac{\sigma_y}{jw\epsilon_o} \qquad s_y^* = 1 + \frac{\sigma_y^*}{jw\mu_o} \tag{4.40}$$

En conclusion, es posible eliminar las reflexiones entre un medio y el PML para todos los ángulos de incidencia y rango de frecuencias imponiendo igualdad en las coordenadas de estiramiento transversales de los dos medios y forzando las coordendas longitudinales (Ver documento original para más detalles del proceso) a ser iguales a la siguiente expresión [7]:

$$s_x(x) = s_o(x)\left[1 - j\frac{\sigma_x(x)}{w\epsilon'}\right] \qquad with \;\; \epsilon' = \epsilon_r'\epsilon_o \tag{4.41}$$

$$s_o(x) = 1 + s_m\left(\frac{\pi}{\delta}\right)^2 \tag{4.42}$$

$$\sigma_x(x) = sin^2\left(\frac{\pi x}{2\delta}\right) \tag{4.43}$$

donde δ es la espesor del amortiguador y s_m es el coeficiente que depende de la longitud de onda del medio.
Otra posibilidad se obtiene de [1] como

$$s_x(x) = 1 - j\left(\frac{x-\delta}{\delta}\right)^2 \delta_{max} \tag{4.44}$$

$$\delta_{max} = \frac{\sigma_{max}}{w\epsilon_o} \qquad or \qquad \delta_{max} \approx w^{-1} \tag{4.45}$$

y una buena elección para la espesor del amortiguador podría ser $\delta = \lambda/4$.

En la Fig.4.7 puede visualizarse un ejemplo de implementación de interfaz PML para limitar el dominio computacional de una aplicación en región abierta. Como podemos observar, es necesario colocar un región basada en PML en cada una de las posibles fronteras.

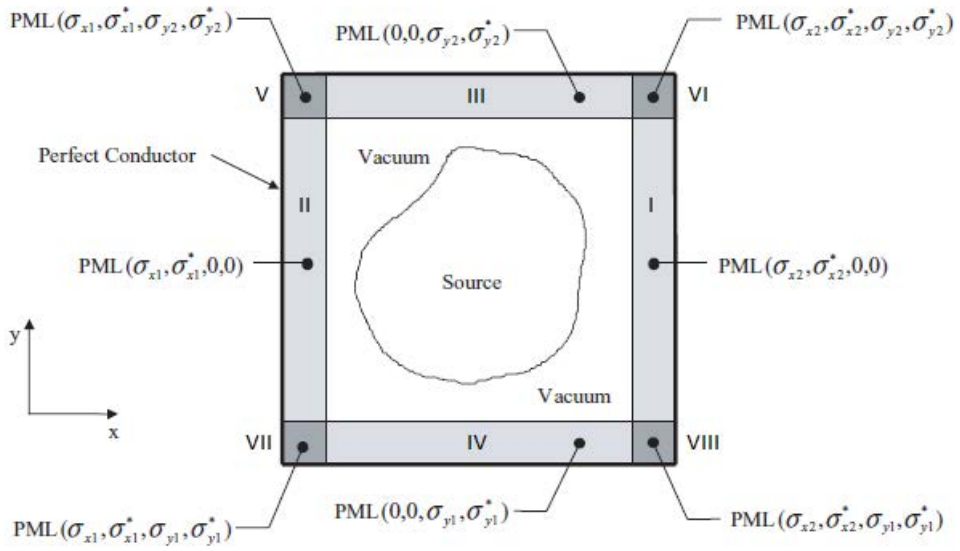

Figura 4.7: PML encerrando un dominio infinito

Finalmente, las distintas regiones descritas en la figura anterior quedarían definidas por los siguientes factores de estiramiento:

1. Region Ω. $s_x = s^*_x = 1 \wedge s_y = s^*_y = 1$
2. Region I. $s_x = (4.44) \wedge s_y = 1$
3. Region II. $s_x = (4.44) \wedge s_y = 1$
4. Region III. $s_x = 1 \wedge s_y = (4.44)$
5. Region IV. $s_x = 1 \wedge s_y = (4.44)$
6. Region V. $s_x = s_y = (4.44)$
7. Region VI. $s_x = s_y = (4.44)$
8. Region VII. $s_x = s_y = (4.44)$
9. Region VIII. $s_x = s_y = (4.44)$

Es necesario mencionar que durante las simulaciones se comprobó que el escenario descrito en la Fig.4.7 no funciona correctamente implementándose con funciones nodales. Es decir, debido a la complejidad del escenario se requiere el uso de elementos vectoriales para obtener soluciones reales.

4.7 Implementación de la Matriz FEM

En el Capítulo 3 comprobamos cómo el *Problema Directo* podía ser resuelto evaluando el campo eléctrico dispersado por el OI al ser iluminado por un conjunto de antenas. En el caso de escenarios simulados como el nuestro, es necesario resolver la ecuación matricial descrita en (3.2). Esta puede ser desarrollada acorde a la formulación presentada en la Sección 4.4.2 para problemas escalares o la formulación descrita en la Sección 4.5.1 para problemas vectoriales. En ambos casos, es imprescindible implementar la matriz global FEM. Para la implementación de dicha matriz se debe determinar la contribución de cada uno de los elementos que forman la malla. Una vez calculadas cada una de las matrices locales FEM, debemos relacionar los índices locales de los nodos con sus correspondientes índices globales para construir con exito la matriz global.
Detalles del proceso: documento original [A.1] en la Sección 4.7 y la obtención de los elementos que forman la matriz FEM puede analizarse en el apéndice [A.1] y [A.2] del documento original.

4.8 Simulaciones

Finalmente, esta sección presenta diversas simulaciones basadas en geometrías en 2D con el objetivo de visualizar los resultados de computación del FEM. Todos los casos que se tratan son problemas escalares, de forma que el *Problema Directo* se ha ejecutado mediante el uso de funciones nodales. Estudiaremos el método para diferentes escenarios en cuanto a sus propiedades dieléctricas así como la influencia de las cargas de corriente y de la frecuencia de trabajo utilizada.

4.8.1 Recinto Circular

En esta sección analizamos un PEC circular cuyo radio del tanque es igual a 0.1m. El propósito de estas simulaciones es analizar las consecuencias que implican diferentes propiedades diléctricas, frecuencias y localización de las fuentes de corriente. Primero, fijamos la frecuencia a 500MHz. Las siguientes simulaciones se caracterizan por un medio con $\epsilon_r' = 20$ y diferentes valores de conductividad. Consideramos una simple carga localizada en las coordenadas (Xs,Ys)=(0.5,0)

Los resultados se muestran en la Fig.4.8: dependiendo de la relación entre la conductividad y la permitividad relativa (tangente de pérdidas), el número de reflexiones existentes en el medio es mayor o menor. En el caso donde la conductividad es considerablemente grande, y por tanto la relación es más grande, se observa cómo la intensidad del campo computado se localiza en el punto de la fuente, mientras que en el otro caso, donde la conductividad es suficientemente pequeña y la tangente de pérdidas es demasiado pequeña, que las reflexiones no se atenuan y provocan picos de intensidad en zonas donde no hay cargas eléctricas.

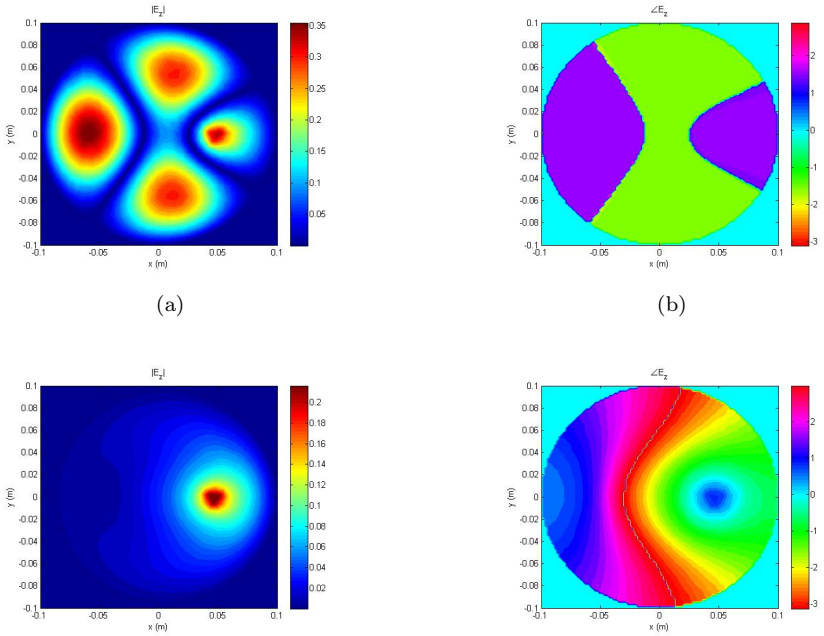

(a) (b)

(c) (d)

Figura 4.8: Problema Directo resuelto con FEM usando funciones nodales: $\epsilon'_r = 20$, (Xs,Ys)=(0.5,0), (a)(b) $|E|$ y $\angle E$ para $\sigma = 0.0005$ S/m (c)(d) $|E|$ y $\angle E$ para $\sigma = 0.5$ S/m.

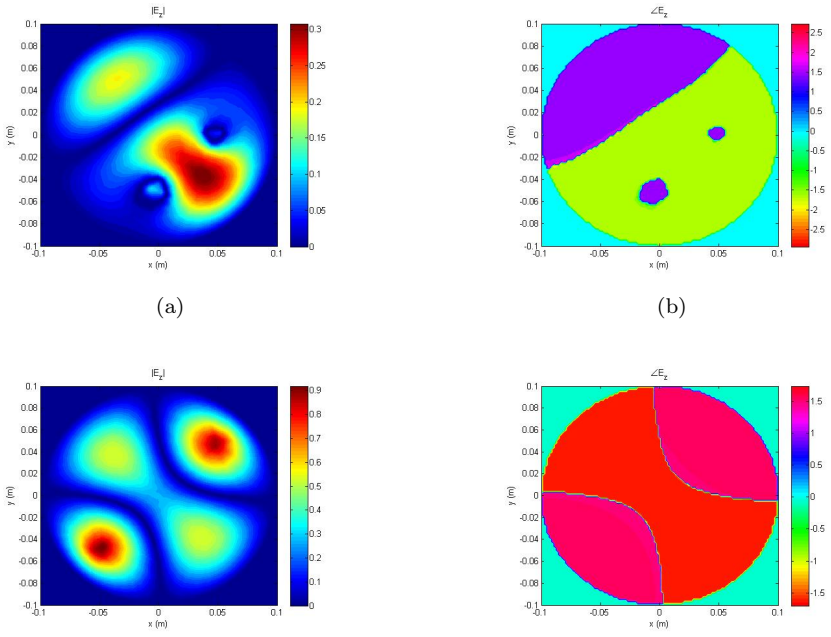

(a) (b)

(c) (d)

Figura 4.9: Problema Directo resuelto con FEM usando funciones nodales: $\epsilon'_r = 20$ (a)(b) $|E|$ y $\angle E$ para $\sigma = 0.0005$ [S/m] con fuentes (Xs,Ys)=([0.05 0],[0 -0.05]), (c)(d) $|E|$ y $\angle E$ para $\sigma = 0.0005$ [S/m] con fuentes (Xs,Ys)=([-0.05 0.05],[-0.05 0.05]).

Hablamos de medios con pérdidas cuando la tangente de pérdidas es suficientemente grande, mientras que si esta relación es despreciable, hablaremos de medios sín pérdidas. Un determinado medio se le considerará como buen conductor o medio con pérdidas cuando se cumpla $\sigma/(w_o\epsilon') >> 1$. En la Fig.4.9(a) se considera otra combinación de fuentes electromagnéticas. Es posible detectar cómo aparece solapamiento entre las dos cargas debido a la "pequeña" distancia en términos de longitud de onda entre ellas (problema de resolución tratado en Capítulo 5). Esto no ocurre en el caso (c), con cargas más distantes entre sí.

Consideremos un nuevo escenario caracterizado por una permitividad mayor, $\epsilon'_r = 80$. En Fig.4.10(a)(b), es posible observar como el número de reflexiones producidas en el PEC es mayor debido a que las pérdidas en el medio son menores.

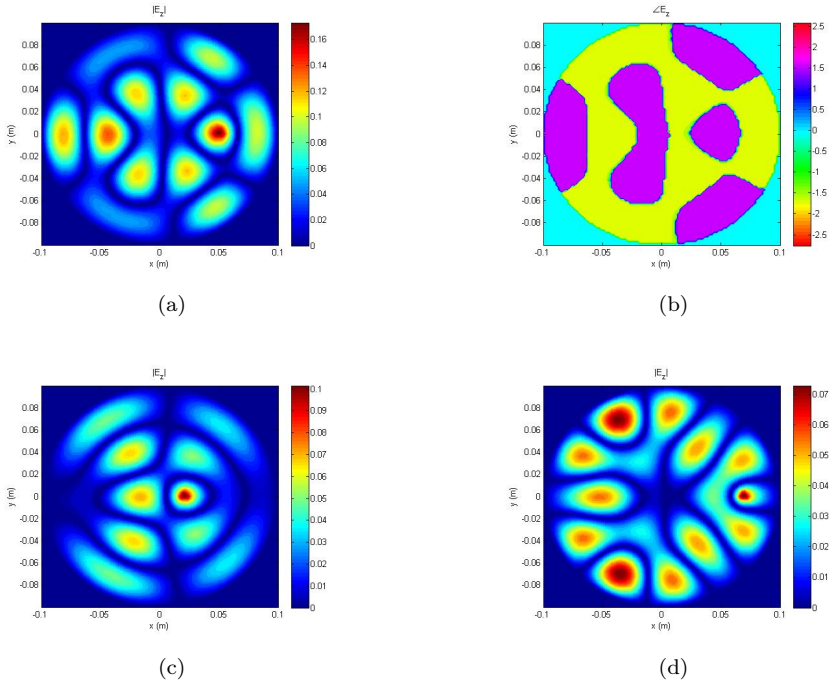

Figura 4.10: Problema Directo resuelto con FEM usando funciones nodales: $\epsilon'_r = 80$ (a)(b) $|E|$ y $\angle E$ para $\sigma = 0.0005$ [S/m] con (Xs,Ys)=(0.05,0), (c)(d) $|E|$ para $\sigma = 0.0005$ [S/m], con (Xs,Ys)=(0.02,0) y (Xs,Ys)=(0.07,0).

Además, en la Fig.4.10.(c-d) se comparan los resultados para un emplazamiento de las fuentes más lejano o cercano al PEC por lo que la atenuación experimentada por las ondas reflectadas es mayor o inferior debido a la distancia de propagación, lo que implica un menor o mayor número de reflexiones que alteran nuestra medición electromagnética.

Hemos analizado medios homogéneos, pero en las aplicaciones reales las propiedades dieléctricas varían a lo largo de la superficie, es decir, son medios inhomogéneos. En la Fig.4.11(a)(b), se presentan dos escenarios inhomogéneos en 2D.

- Superficie Verde $\Rightarrow \epsilon_r' = 20$; $\sigma = 0.0005$;
- Superficie Amarilla $\Rightarrow \epsilon_r' = 80$; $\sigma = 0.02$;
- Superficie Azul $\Rightarrow \epsilon_r' = 6$; $\sigma = 0.1$;

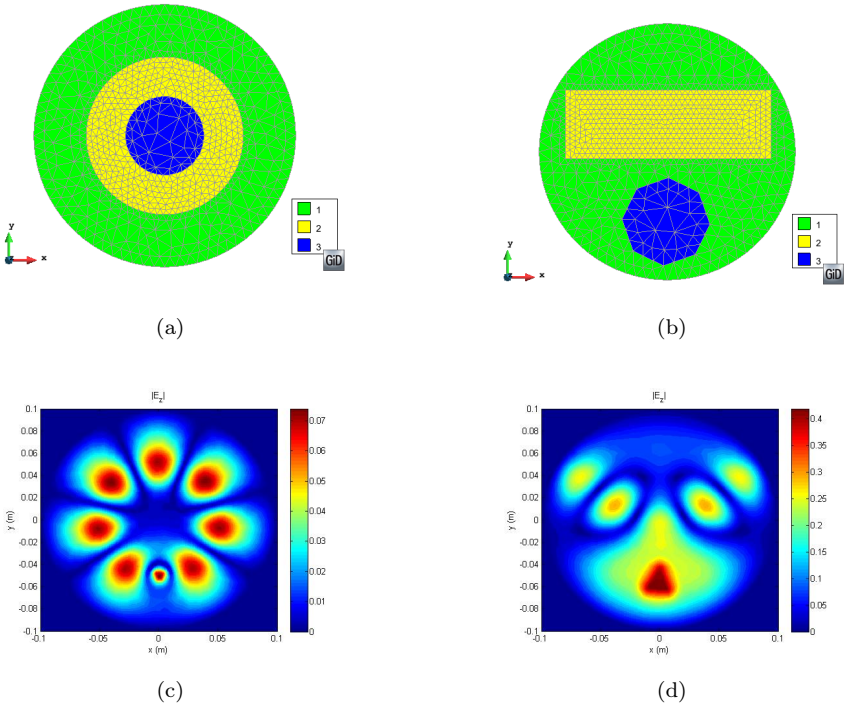

(a) (b)

(c) (d)

Figura 4.11: (a)(b) Escenarios Inhomogéneos (c)(d) $|E|$ correspondiente a fuentes localizdas a (Xs,Ys)=(0,-0.05).

Podemos comprobar cómo en la Fig.4.11(a)(c) aparecen reflexiones muy intensas a lo largo de la región verde donde la tangente de pérdidas es menor y la carga está localizada. Parte de las reflexiones alcanzan la zona amarilla donde las pérdidas no son tampoco suficientemente grandes, sin embargo, en la zona azul no aparecen picos de intensidad. En la Fig.4.11(b)(d) el comportamiento es diferente, ya que la fuente se encuentra en la zona donde las pérdidas son mayores (comportamiento similar a Fig.4.8(c)). Por ello, sólo aparece campo en esa zona y em algunas regiones de la superficie verde.

Ahora fijemos las propiedades dieléctricas con el próposito de computar el campo eléctrico en función de la frecuencia de trabajo, de forma que entendamos su influencia en los resultados. Consideremos un

recinto circular de radio 0.3m y un escenario homogéneo ($\epsilon'_r = 10$, $\sigma = 0.03$), la fuente eléctrica esta localizada en (Xs,Ys)=(0,0.1m).

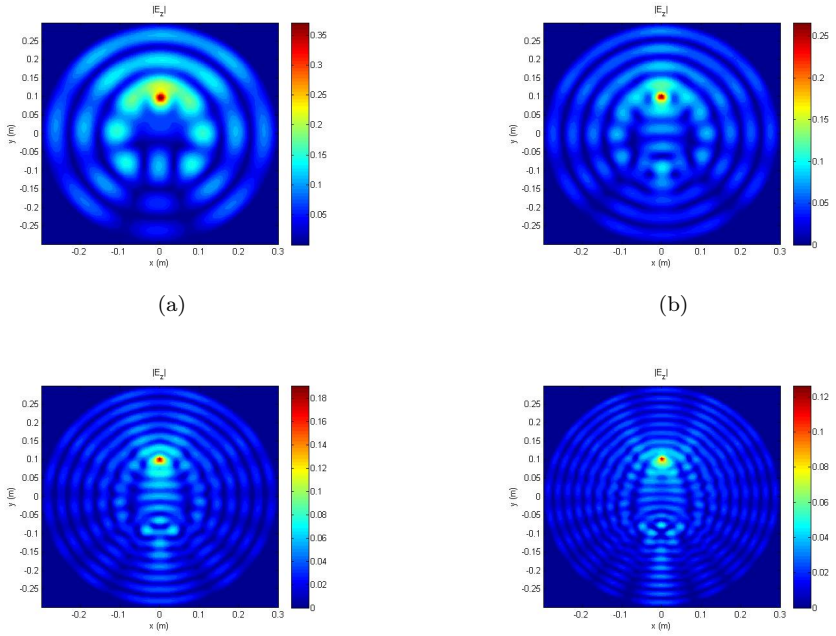

(a) (b)

(c) (d)

Figura 4.12: $\epsilon'_r = 10$, $\sigma = 0.03$ [S/m], (a) $|E|$ a $f_o = 700MHz$, (b) $|E|$ a $f_o = 1GHz$, (c) $|E|$ a $f_o = 1.5GHz$, (d) $|E|$ a $f_o = 2GHz$

En la Fig.4.12 es posible visualizar cómo, incrementando la frecuencia de trabajo, se generan una mayor número de líneas de campo debido a las reflexiones. Al aumentar la frecuencia estamos reduciendo considerablemente las pérdidas en el medio por lo que las reflexiones experimentan una menor atenuación. Sin embargo, podemos observar como la intensidad de las reflexiones es menor que en casos anteriores, debido, principalmente, a que el recinto es más grande en términos de longtud de onda (radio 3 veces mayor y una permitividad más baja). Ello implica una mayor atenuación de las ondas reflejadas en el PEC, que recorren una mayor distancia.

Para comprobar la veracidad de la segunda conclusión, comparamos los resultados visualizados en las Fig.4.12(a)(d) con sus equivalentes en un recinto cicular más pequeño, r= 0.1m. En la Fig.4.13 se puede comprobar cómo el número de reflexiones e intesidad de dichos picos es mayor debido a una menor dimensión del medio en términos de longitud de onda.

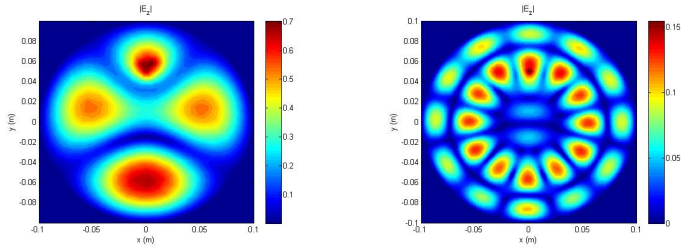

(a) (b)

Figura 4.13: r= 0.1m, $\epsilon'_r = 10$, $\sigma = 0.03$ [S/m], (a)(b) $|E|$ a $f_o = 700MHz$ y $f_o = 2GHz$ respectivamente.

4.8.2 Recinto Triangular

En esta sección utilzamos un recinto triangular con lado igual a 0.15m para entender mejor las consecuencias de utilizar un tipo de PEC u otro. Las simulaciones expuestas a continuación se refieren a una frecuencia de 500MHz. En la Fig.4.14 se observa el mismo comportamiento, respecto a la tangente de pérdidas en el medio, que en los casos con recinto circular. (a) Al presentar una conductividad que implica bajas pérdidas se solapan una mayor cantidad de reflexiones; para (b), las conductividades son suficientemente grandes para que la atenuación presente impida la propagación de reflexiones producidas en el PEC.

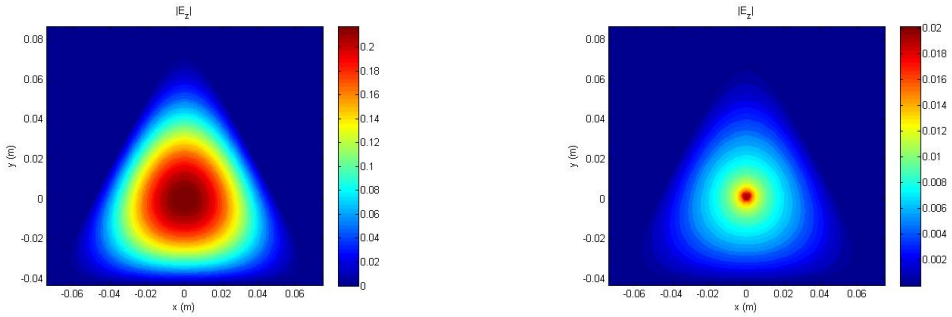

(a) (b)

Figura 4.14: Triangular 2D: $\epsilon'_r = 20$, (a) $|E|$ para $\sigma = 0.02$ [S/m] con (Xs,Ys)=(0,0), (c) $|E|$ para $\sigma = 0.5$ [S/m] con (Xs,Ys)=(0,0)

La razón por la que no se visualizan picos de intensidad, debido a reflexiones en las paredes conductoras, reside en la propia geometría del recinto triangular; es decir, la posición y orientación de los lados de un triángulo equilatero provocan que las reflexiones se acumulen en torno al circuncentro del triángulo. Para mayor comprensión obsérvese el experimento que se muestra en la Fig.4.15.

En la Fig.4.15(a) se presenta un escenario triangular con un medio homogéneo de propiedades $\epsilon'_r = 20$ y $\sigma = 0.02$ Una simple carga es ubicada en (Xs,Ys)=(0,0.05), remarcando su posición con un círculo rojo. Comprobamos cómo, estando situada en uno de los vértices del triángulo, la intensidad del campo eléctrico surge de nuevo en el circuncentro del escenario triangular.

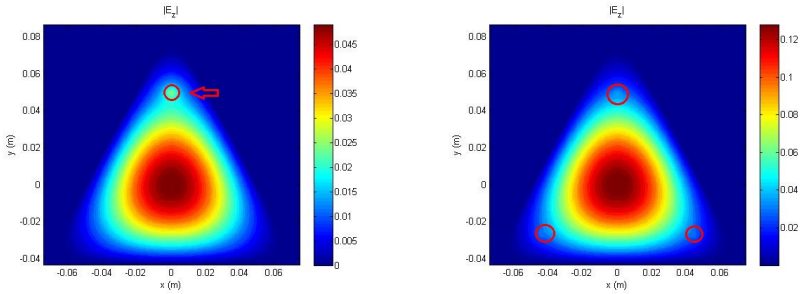

(a) (b)

Figura 4.15: (a) Simple fuente eléctrica (b) Tres fuentes eléctricas

Comparemos la simulación comentada con el mismo escenario pero donde, en lugar de forzar una única carga, colocamos tres fuentes de corriente en cada uno de los vértices del triángulo (Fig.4.15(b)), cada una de ellas indicada con un círculo rojo. Las coordenadas de cada una de las fuentes son (Xs,Ys)=([0,-0.045,0.045],[0.05,-0.026,-0.026]).

Los resultados visuales parecen iguales. Sin embargo, si analizamos los valores numéricos, podemos apreciar cómo, para el caso con mayor número de fuentes de corriente, la intensidad del campo es aproximadamente 3 veces mayor debido a que presenta el triple de cargas. Mientras que en (a) el máximo valor es de 0.045V, en (b) es de aproximadamente 0.12V.

4.8.3 Recinto Cuadrado

Esta sección esta dedicada a simulaciones con recinto cuadrado. Sin embargo, en lugar de describir los resultados EM, utilizaremos estas simulaciones para analizar los costes computacionales del *Problema Directo*. Es importante mencionar que dichos costes solo se refieren a la la implementación de la matriz global FEM. Las simulaciones durante este proyecto se han realizado con un procesador Intel(R) Core(TM) i7-2630QM CPU 2.00GHz con una memoria RAM de 6.00GB.

El escenario esta basado en un cuadrado de lado 0.2m, y una simple carga localizada en (Xs,Ys)=(0,0). Los costes computacionales para diversas simulaciones, donde las propiedades diléctricas y la frecuencia de trabajo son distintas, son mostrados en la Tabla.4.2.

Finalmente, es importante aclarar que este experimento supone simulaciones más o menos sencillas (geometría simple y una única carga). Por ello, los costes son aceptables. Sin embargo, en las simulaciones

Tabla 4.2: Costes Computacionales

Frequency [GHz]	Permittivity	Edge Size [m]	Num.Nodes	Num.Elem.	Time [s]
0.4	10	0.0158	210	366	0.220609
0.8	20	0.0056	1534	2922	4.004716
1.5	12	0.0038	3295	6376	15.41539
2	30	0.0018	14356	28266	270.684261
2.5	40	0.0013	27370	54122	1000.769933
3.2	40	9.8821e-004	47375	93940	3349.545703

del FEM-CSIM realizadas en los siguientes capítulos, el coste computacional se incrementa rápidamente debido a que el *Problema Directo* deberá ser resuelto para cada uno de los transmisores además de la correspondiente posterior resolución del algoritmo inverso. Y ello sin olvidar que los escenarios analizados son de una complejidad mayor.

Capítulo 5

Resolución de Problemas Inversos de Dispersión Electromagnética

En este capítulo se presenta el objetivo fundamental de este trabajo, el denominado *Algoritmo Inverso*. Para la realización de imágenes médicas se requiere la inversión de la ecuación de onda que describe nuestro escenario electromagnético. Es decir, los resultados numéricos obtenidos durante la resolución del *Problema Directo* mediante FEM deben ser aplicados a un proceso de inversión con el propósito de reconstruir el origen físico que los ha generado.
El método de inversión desarrollado durante este proyecto se denomina como "Contrast Source Inversion Method" (CSIM), el cual trabaja iterativamente actualizando dos variables: la fuente de contraste y las variables de constraste. Minimizando iterativamente una función, que describiremos más adelante, llegaremos a obtener las propiedades dieléctricas del OI analizado.

5.1 El Algoritmo de Inversión

Una vez obtenidos los datos asociados a la dispersión electromagnética de un determinado escenario en 2D, almacenados para cada uno de los posibles transmisores y receptores que iluminan el OI (Fig. 3.2), estos se utilizan como inicialización del proceso de inversión. Pero antes, definamos la correspondiente variable de contraste para un determinado escenario,

$$\chi(r) = \frac{\epsilon_r(r) - \epsilon_b(r)}{\epsilon_b(r)} \tag{5.1}$$

donde $\epsilon_b(r)$ es la permitividad relativa compleja del "background", de forma que, $\chi(r) = 0 \forall r \notin \mathcal{D}$. Como se comentó en el Capítulo 3, el Dominio Imagen $\mathcal{D}$ es iluminado por uno de los Tx de los Ntx trans-

misores/receptores existentes, generando el campo incidente E_t^{inc}, modelado por la siguiente ecuación escalar de Helmholtz,

$$\nabla^2 E_t^{inc}(r) + k_b^2 E_t^{inc}(r) = jw\mu_o J_t(r) \tag{5.2}$$

donde $k_b(r) = w\sqrt{\mu_o \epsilon_o \epsilon_b(r)}$ es el vector de ondas del "background".
La siguiente medición se basa en introducir el OI en el recinto cerrado, generando el campo eléctrico total E_t, para cada transmisor. Satisface la siguiente ecuación escalar,

$$\nabla^2 E_t(r) + k^2 E_t(r) = jw\mu_o J_t(r) \tag{5.3}$$

En este caso, $k(r) = w\sqrt{\mu_o \epsilon_o \epsilon_r(r)}$. Entoces podemos definir el campo disperso como $E_t^{sct}(r) \equiv E_t(r) - E_t^{inc}(r)$, referido a

$$\nabla^2 E_t^{sct}(r) + k_b^2 E_t^{sct}(r) = -k_b^2(r) w_t(r) \tag{5.4}$$

donde la fuente de constraste, $w_t(r) = \chi(r) E_t(r)$, describe la variable de contraste en términos del campo eléctrico total generado por las fuentes. La siguiente ecuación matricial relaciona las matrices FEM referidas a cada uno de los nodos que forman la malla con el campo disperso,

$$[\mathbf{S} - \mathbf{T_b}]\, E_{t,\Omega}^{sct} = \mathbf{T_b} w_{t,\Omega} \tag{5.5}$$

mientras $\mathbf{S} \in \mathbb{C}^{N\times N}$ es la matriz de Stiffness que depende de las BCs, $\mathbf{T_b} \in \mathbb{C}^{N\times N}$, la matriz de Mass que define las propiedades del "background", los vectores $E_{t,\Omega}^{sct} \in \mathbb{C}^N$ y $w_{t,\Omega} \in \mathbb{C}^N$ son, respectivamente, los valores de dispersión EM y de las fuentes de contraste para cada Tx en el dominio Ω.
Hay que aclarar que, debido al funcionamiento del FEM-CSIM, fue necesario modificar la implementación de la matriz FEM, ya que el método requiere la definición de las propiedades diléctricas nodo a nodo en lugar de elemento a elemento (Documento original [A.1] apéndice [B.1].

5.2 Operadores Matriciales de Inversión

Para la correcta definición del FEM-CSIM es necario introducir algunos operadores matriciales. El primer operador es denotado como $\mathcal{M}_\mathbf{s} \in \mathbb{C}^{R\times N}$, donde R es el número de receptores. Este operador nos permite transformar los N valores nodales del campo disperso relacionados con el dominio Ω con los

R fuentes puntuales. El segundo operador es representado como $\mathcal{M}_{\mathcal{D}} \in \mathbb{C}^{I\times N}$, donde I es el número de nodos definidos en el Dominio Imagen $\mathcal{D}$ y selecciona los valores de campo de los I nodos del dominio imagen. De esta forma podemos obtener el vector fuente de constraste para toda la malla como

$$w_{t,\Omega} = \mathcal{M}_{\mathcal{D}}^{T} w_t \tag{5.6}$$

Usando (5.6) en la ecuación matricial (5.5), obtenemos un nuevo operador, $\mathcal{L} \in \mathbb{C}^{N\times I}$, dado como

$$E_{t,\Omega}^{sct} = \mathcal{L}[w_t] = \left[\mathbf{S} - \mathbf{T_b}\right]^{-1} \mathbf{T_b} \mathcal{M}_{\mathcal{D}}^{T} [w_t] \tag{5.7}$$

5.3 The Contrast Source Inversion Method

CSIM reliza la actualización de las variables de contraste y de las fuentes de contraste, minimizando la siguiente función de coste,

$$\begin{aligned} \mathcal{F}(\chi, w_t) &= \mathcal{F}^{S}(w_t) + \mathcal{F}^{D}(\chi, w_t) \\ &= \frac{\sum_t \|f_t - \mathcal{M}_{\mathbf{s}}\mathcal{L}[w_t]\|_S^2}{\sum_t \|f_t\|_{\mathcal{S}}^2} + \frac{\sum_t \left\|\chi \odot E_t^{inc} - w_t + \chi \odot \mathcal{M}_{\mathcal{D}}\mathcal{L}[w_t]\right\|_D^2}{\sum_t \left\|\chi \odot E_t^{inc}\right\|_{\mathcal{D}}^2} \end{aligned} \tag{5.8}$$

Aquí, $f_t \in \mathbb{C}^R$ es el campo disperso medido en las R posiciones de las fuentes para cada transmisor. Recuérdese que necesitamos convertir los datos medidos para todo el dominio Ω, a los equivalentes en el Dominio Imagen $\mathcal{D}$ usando $E_t^{inc} = \mathcal{M}_{\mathcal{D}} E_{t,\Omega}^{inc}$.

Como primer paso, en el algoritmo CSI actualizamos las fuentes de contraste w_t con el método del gradiente conjugado (CG) con las direcciones de búsqueda Polak Ribière (formulación desarrollada en [9]), asumiendo constantes las variables de contraste χ. En el segundo paso, w_t se considera constante, y la función de coste $\mathcal{F}^{D}(\chi, w_t)$ es minimizada. Ambas operaciones se realizan secuencialmente en cada iteración.

$$w_{t,n} = w_{t,n-1} + \alpha_{t,n} d_{t,n} \tag{5.9}$$

donde $\alpha_{t,n}$ es el paso de actualización para el transmisor t en la iteración n, $d_{t,n}$ son las direcciones Polak Ribière. El paso viene definido como [9]

$$\alpha_{t,n} = \frac{\eta^{\mathcal{S}} \left\langle \rho_{t,n-1}, \mathcal{M}_s\mathcal{L}[d_{t,n}]\right\rangle_{\mathcal{S}} + \eta_n^{\mathcal{D}} \left\langle r_{t,n-1}, d_{t,n} - \chi_{n-1} \odot \mathcal{M}_{\mathcal{D}}\mathcal{L}[d_{t,n}]\right\rangle_{\mathcal{D}}}{\eta^{\mathcal{S}} \left\|\mathcal{M}_s\mathcal{L}[d_{t,n}]\right\|_{\mathcal{S}}^2 + \eta_n^{\mathcal{D}} \left\|d_{t,n} - \chi_{n-1} \odot \mathcal{M}_{\mathcal{D}}\mathcal{L}[d_{t,n}]\right\|_{\mathcal{D}}^2} \tag{5.10}$$

donde $\eta^{\mathcal{S}}$ y $\eta_n^{\mathcal{D}}$ son los factores de normalización,

$$\begin{aligned}\eta^{\mathcal{S}} &= \left(\sum_t \|f_t\|^2_{\mathcal{S}}\right)^{-1} \\ \eta^{\mathcal{D}}_n &= \left(\sum_t \left\|\chi \odot E^{inc}_t\right\|^2_{\mathcal{D}}\right)^{-1}\end{aligned} \tag{5.11}$$

y los términos de error $\rho_{t,n-1}$ y $r_{t,n-1}$ son

$$\begin{aligned}\rho_{t,n-1} &= f_t - \mathcal{M}_s\mathcal{L}[w_{t,n-1}] \\ r_{t,n-1} &= \chi \odot E^{inc}_t - w_{t,n-1} + \chi_{n-1} \odot \mathcal{M}_{\mathcal{D}}\mathcal{L}[w_{t,n-1}]\end{aligned} \tag{5.12}$$

Las direcciones de búsqueda de Polak Ribière $d_{t,n}$ son calculadas por la siguiente fórmula [9],

$$d_{t,n} = -g_{t,n} + \frac{\langle g_{t,n}, g_{t,n} - g_{t,n-1}\rangle_{\mathcal{D}}}{\|g_{t,n-1}\|^2_{\mathcal{D}}} d_{t,n-1} \tag{5.13}$$

donde $d_{t,0}$ es fijada a cero y $g_{t,n}$ es el gradiente de la función de coste $F(\chi, w_t)$ respecto a $w_{t,n}$, y puede ser aproximado por, (formulación extraída de [9])

$$g_{t,n} = -2\eta^{\mathcal{S}}\mathbf{T}^{-1}_{\mathcal{D}}\mathcal{L}^H\mathcal{M}^H_s\rho_{t,n-1} - 2\eta^{\mathcal{D}}_n\mathbf{T}^{-1}_{\mathcal{D}}\left(\mathbf{I} - \mathcal{L}^H\mathcal{M}^T_{\mathcal{D}}\mathbf{X}^H_{n-1}\right)\mathbf{T}_{\mathcal{D}}r_{t,n-1} \tag{5.14}$$

Donde $\mathbf{I} \in \mathbb{R}^{I\times I}$ es una matriz de identidad y $\mathbf{X}_{n-1}$ es la matriz diagonal cuyos elementos de la diagonal son los valores de χ_{n-1}.
Después de actualizar las fuentes de contraste, χ es evaluada minimizando $\mathcal{F}^D(\chi, w_t)$ donde w_t es considerada constante. χ_n puede obtenerse resolviendo la siguiente igualdad matricial,

$$\left(\sum_t \mathbf{E}^H_{t,n}\mathbf{T}_{\mathcal{D}}\mathbf{E}_{t,n}\right)\chi = \sum_t \mathbf{E}^H_{t,n}\mathbf{T}_{\mathcal{D}}w_{t,n} \tag{5.15}$$

donde $\mathbf{E}_{t,n} \in \mathbb{C}^{I\times I}$ es la matriz diagonal definida por el vector $\mathbf{E}_{t,n} = \mathbf{E}^{inc}_t + \mathcal{M}_{\mathcal{D}}\mathcal{L}[w_{t,n}]$.

5.3.1 Normas y Productos Internos

En este sección definimos algunos operadores y símbolos que aparecen durante la formulación anterior. La norma-L2 y el producto interior son calculados como,

$$\|x\|^2_{\mathcal{D}} = x^H\mathbf{T}_{\mathcal{D}}x \qquad \text{and} \qquad \langle x, y\rangle_{\mathcal{D}} = y^H\mathbf{T}_{\mathcal{D}}x \tag{5.16}$$

siendo x e y vectores de tamaño I, y $\mathbf{T}_{\mathcal{D}} \in \mathbb{R}^{I \times I}$ es la matriz de Mass para los nodos pertenecientes al Dominio Imagen $\mathcal{D}$, definida como

$$\mathbf{T}_{\mathcal{D}} = \int_{\mathcal{D}} \lambda_i \cdot \lambda_j ds \tag{5.17}$$

Para la norma-L2 y el producto interior en Ω, con vectores de tamaño R, se define como

$$\|x\|_{\mathcal{S}}^2 = x^H x \qquad \text{and} \qquad \langle x, y \rangle_{\mathcal{S}} = y^H x \tag{5.18}$$

5.3.2 Estimación Inicial de FEM-CSIM

No podemos incializar el método iterativo fijando la iteración inicial a cero porque la función de coste quedaría indefinida tras la primera iteración. De [3] y [9] extraímos la formulación óptima para la estimación inicial. La expresión (5.19) se obtiene aplicando el método de "steepest descent" a $\mathcal{F}^S(w_t)$.

$$w_{t,0} = \frac{\mathrm{Re}\left\langle \mathcal{M}_s \mathcal{L}[\mathcal{G}^{\mathcal{S}} f_t], f_t \right\rangle_{\mathcal{S}}}{\|\mathcal{M}_s \mathcal{L}[\mathcal{G}^{\mathcal{S}} f_t]\|_{\mathcal{S}}^2} \mathcal{G}^{\mathcal{S}} f_t \tag{5.19}$$

donde el operador $\mathcal{G}^{\mathcal{S}} = -2\eta^{\mathcal{S}} \mathbf{T}_{\mathcal{D}}^{-1} \mathcal{L}^H \mathcal{M}_s^H$.

5.4 Simulaciones

En esta sección se presentan brevemente algunos resultados de simulaciones basadas en FEM-CSIM. Dado un determinado perfil, se utilizan los resultados electromagnéticos obtenidos tras la ejecucion de FEM para procesar el método de inversión. Se analizan una serie de experimentos donde determinaremos algunas conclusiones sobre la problemática de la aplicación. Para más detalles de cada simulación y experimento leer el documento original [A.1].

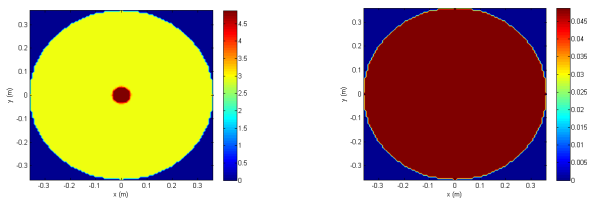

(a) (b)

Figura 5.1: (a) Parte real permitividad relativa ϵ'_r. (b) Conductividad σ

Comenzaremos presentando un escenario simple basado en un OI circular de r= 0.02m con $\epsilon_r = 5.0000 - j1.2839$. El OI se encuentra iluminado por 16 Txs a $f_o = 700MHz$ equiespaciados con un r= 0.3m, mientras que el PEC circular tiene un radio igual a 0.36m, El "background" elegido está caracterizado por $\epsilon_b = 3.0000 - j1.2839$. Se muestra el escenario en la Fig.5.1.

Para visualizar más fácilmente la calidad de las reconstrucciones obtenidas, calculamos el error entre el perfil reconstruido y el original. El error se define en términos relativos como,

$$Err = \frac{\|\chi_{exact} - \chi_{reconst}\|_{\mathcal{D}}}{\|\chi_{exact}\|_{\mathcal{D}}} \tag{5.20}$$

Para comenzar el método iterativo hacemos uso del método de "backpropagation" [9] con el propósito de obtener la éstimación inicial. En la siguiente figura podemos observar $\chi_{t,0}$ y el correspondiente perfil dieléctrico.

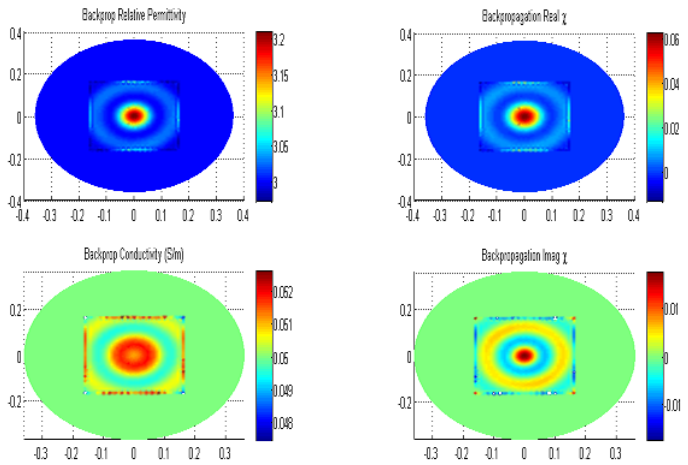

(a) (b)

Figura 5.2: Estimación Inicial: (a) Prop.Dieléctricas (ϵ'_r,σ) (b) Contraste Inicial $\chi_{t,0}$

En las siguientes figuras se presentan los resultados de la reconstrucción después de 400 iteraciones. Podemos observar como las reconstrucciones son bastante cercanas al perfil exacto. El OI es localizado e identificado. Los mayores problemas se visualizan a lo largo de las interfaces entre regiones debido a la asignación de parámetros físicos entre nodos pertenecientes a ambas regiones.
En la Fig.5.4 se puede observar cómo la función de coste es minimizada hasta aproximadamente 10^{-4}. Considerando que el resultado óptimo podría encontrase en torno al 10^{-5}, el algoritmo ha funcionado correctamente. Se alcanza un error del 45.2%. La función $\mathcal{F}^S(w_t)$, hace referencia al error normalizado de los datos electromagnéticos mientras que $\mathcal{F}^D(\chi, w_t)$, indica el error normalizado correspondiente a la

reconstrucción del Dominio Imagen $\mathcal{D}$.

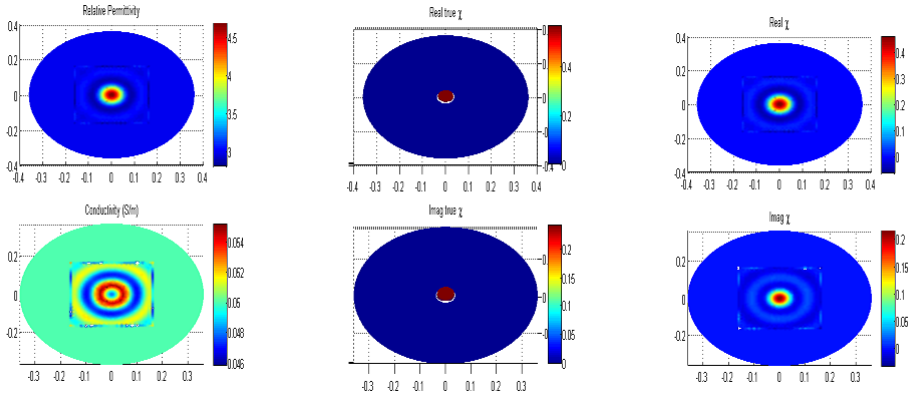

(a) (b) (c)

Figura 5.3: (a) Reconst.prop.dieléctricas (b) True Re(χ) and Im(χ) (c) Reconst. Re(χ) and Im(χ)

Aunque el error obtenido puede considerarse alto, para este tipo de aplicaciones es suficiente. El propósito de la imagen médica es el de detectar cuerpos extraños o posibles patologías. No se busca obtener resultados con la máxima definición, si no determinar la posición y naturaleza de las distintas regiones involucradas.

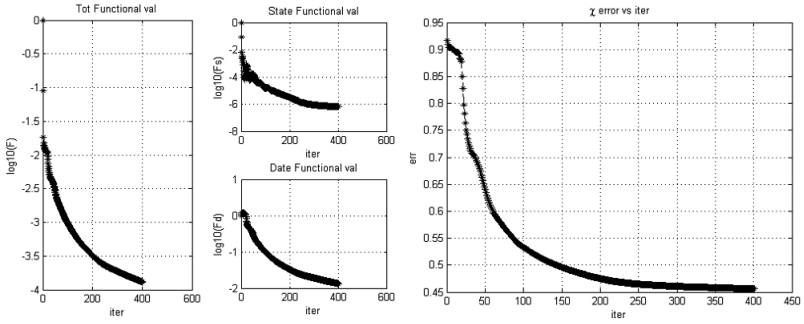

Figura 5.4: Total, state and domain functional cost; Err: Error vs Iterations

En el documento original [A.1] se realiza un experimento con este mismo escenario, tratando de determinar las limitaciones del algoritmo [13].

El siguiente experimento trata de definir la resolución de FEM-CSIM. Para ello, simulamos un escenario donde hay presentes dos OIs circulares de permitividad relativa compleja, $\epsilon_r = 10 - j1.7975$ a $f_0 = 500MHz$, separados por una distancia, d= 0.09m. Se introduce en un recinto circular PEC, de radio igual a 0.31m, con un "background" de $\epsilon_{bk} = 6 - j2.876$. Posteriormente, reducimos la distancia hasta d= 0.02m. Comparemos resultados.

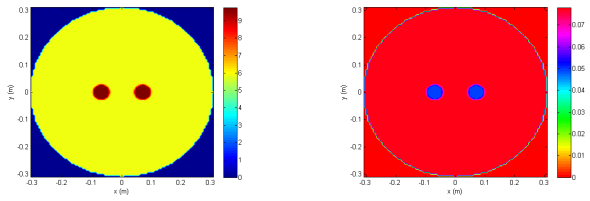

(a) (b)

Figura 5.5: d= 0.09m (a) Parte real permitividad relativa ϵ'_r (b) Conductividad σ

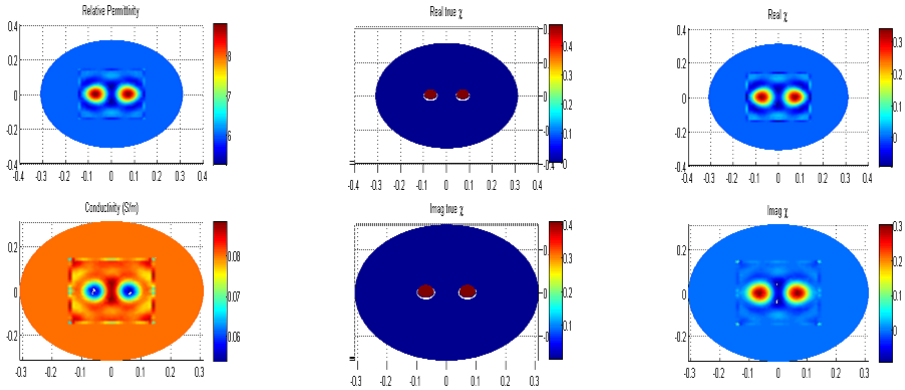

(a) (b) (c)

Figura 5.6: d= 0.09m ((a) Reconst.prop.dieléctricas (b) True Re(χ) and Im(χ) (c) Reconst. Re(χ) and Im(χ)

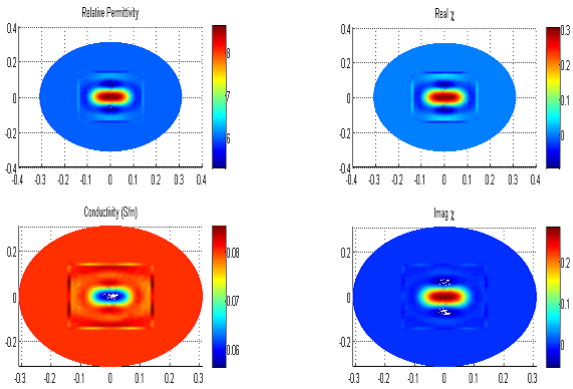

(a) (b)

Figura 5.7: d= 0.02m (a) Reconst. diel. properties (b) Reconst. Re(χ) and Im(χ)

Miestras que para una distancia mayor (Fig.5.9), ambos OIs son identificados con éxito, para la segunda simulación (Fig.5.10), se observa un solapamiento entre las superficies. Este hecho ocurre debido a que la segunda distancia es inferior a la resolución de la aplicación, definida como la mínima distancia entre dos posibles objetivos para poder ser identificados sin solapamiento. La distancia mínima viene dada por $dmin = \lambda_g/4$.

Consideremos un escenario basado en un OI de características diléctricas inhomogéneas. Existe un primer círculo de radio igual a 0.25m con permitividad relativa, $\epsilon_r = 12 - j0.674$. Dentro de este cuerpo circular hay presentes dos más pequeños de permitividad relativa, $\epsilon_r = 16 - j1.573$ a 800MHz. El PEC circular de radio 0.312m contiene un "background" definido por $\epsilon_b = 8 - j2.246$. Ejecutamos el CSIM durante 850 iteraciones, usando 16 antenas localizadas a lo largo de un círculo de 0.25m.

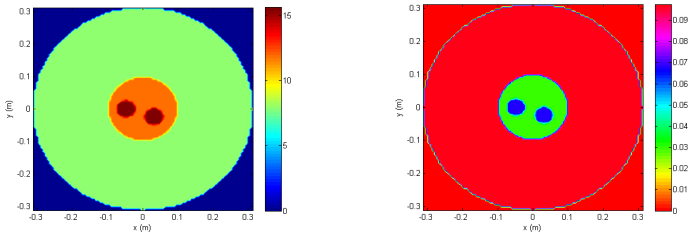

(a) (b)

Figura 5.8: d= 0.09m (a) Parte real permitividad relativa ϵ_r' (b) Conductividad σ

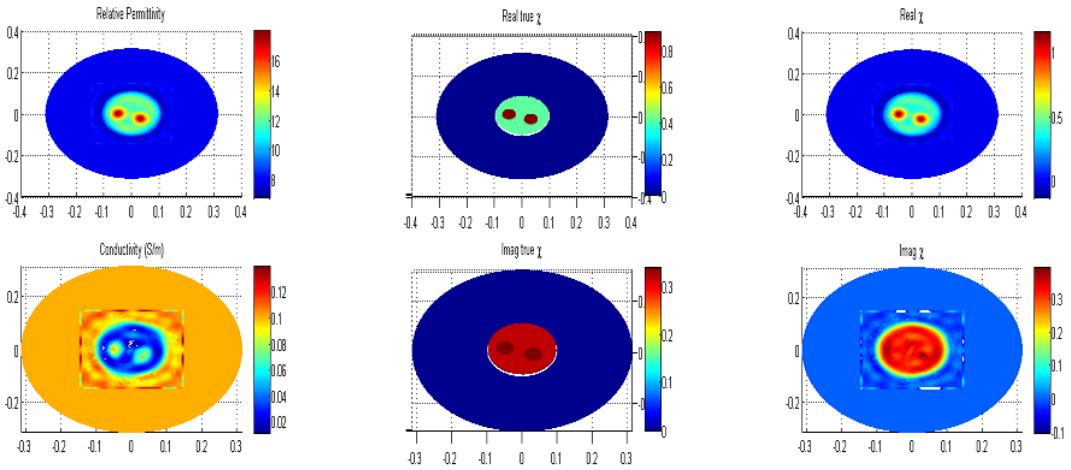

(a) (b) (c)

Figura 5.9: d= 0.06m (a) Reconst.prop.dieléctricas (b) True Re(χ) and Im(χ) (c) Reconst. Re(χ) and Im(χ)

En la Fig.5.9 se pueden observar como los valores reconstruidos son muy próximos a los verdaderos. Nótese que el medio elegido presenta pérdidas, que como demostraremos en el Capítulo 6, implica un mejor funcionamiento de la aplicación.

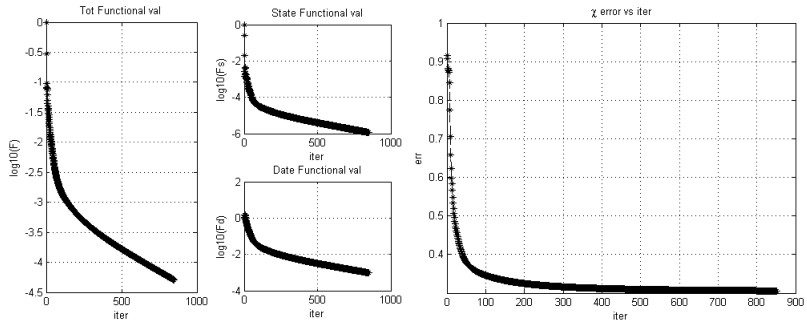

Figura 5.10: Total, state and domain functional cost; Err: Error vs Iterations

En la figura anterior se pueden analizar los resultados numéricos obtenidos en términos del error presentado. Dicho error se mantiene estable sobre 0.3. Lo cual, sugiere que la reconstrucción ha sido ejecutada con mucho éxito. El error en las medición de los datos ha sido minimizado hasta 10^{-6}, lo que sugiere una correcta sintetización de los datos, mientras que la función que describe el error en la reconstrucción en el dominio imagen alcanza un valor de 10^{-3}. (Estimación inicial mediante "backpropagation" descrita en el documento original [A.1]).

La siguiente simulación es un experimento de imagen en microondas muy popular. Consideramos el perfil Uumlaut (Ü), [3][9][10][12] cuyas propiedades diléctricas se muestran en la Fig.5.11. La distintas superficifes que componen el OI presentan una permitividad, $\epsilon_r = 24 - j0.9986$, dentro de un "background" con bajas pérdidas caracterizado por $\epsilon_{bk} = 16 - j1.7975$ a $f_o = 0.9$GHz.

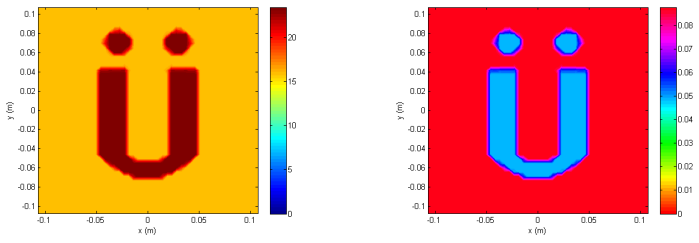

(a) (b)

Figura 5.11: U-Shape profile: (a) Parte real permitividad relativa ϵ_r' (b) Conductividad σ

El dominio de inversión $\mathcal{D}$ está basado en un cuadrado de lado igual a 0.2m representado por 2668 nodos. El número total de nodos es de 10441. Los resultados después de 700 iteraciones nos proporcionan una aproximación del perfil en cuestión.

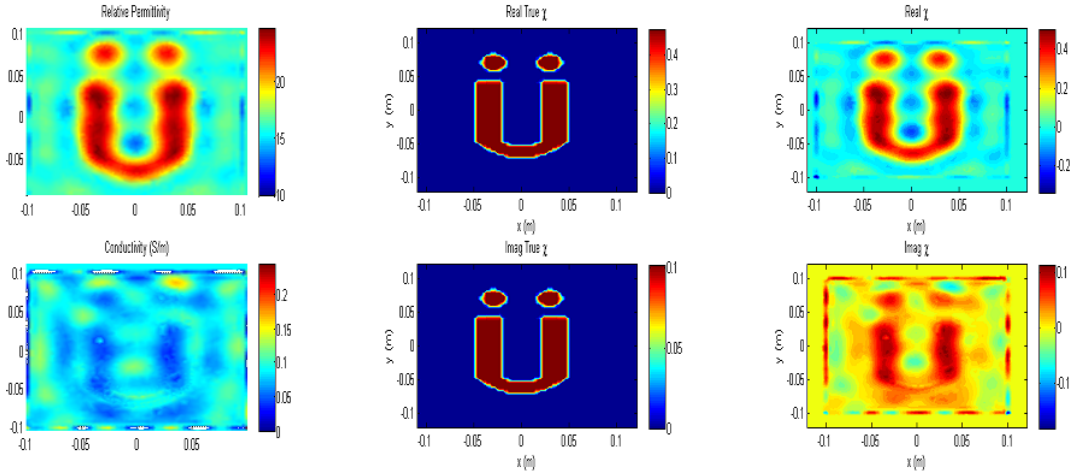

(a) (b) (c)

Figura 5.12: U-Shape profile: (a) Reconst.prop.dieléctricas (b) True Re(χ) and Im(χ) (c) Reconst. Re(χ) and Im(χ)

Podemos observar cómo en el espacio existente entre las superficies circulares y la U, aparacen valores numéricos distintos a los correspondientes del "background". Esto sucede debido a que la distancia no es suficientemente grande en términos de longitud de onda.

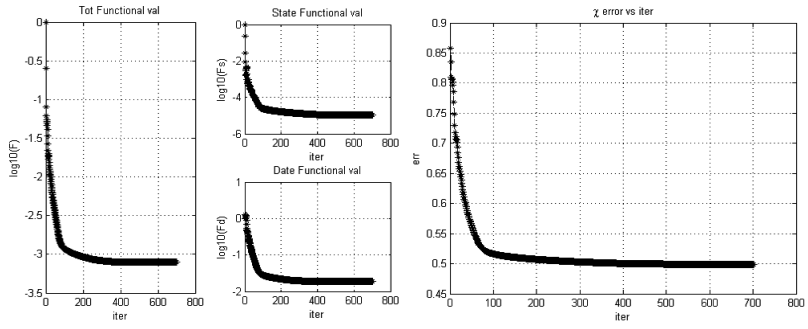

Figura 5.13: U-Shape profile: Total, state and domain functional cost; Err: Error vs Iterations

Alcanzamos un error igual al 49% para un escenario de perfil complejo. Podemos detectar como la función de estado se mantiene estable para un valor suficientemente bajo. Sin embargo, la función asociada a los datos deja de decrecer para $10^{-1.8}$, lo que significa que mientras lo datos obtenidos tras la resolución del *Problema Directo* presentan poco ruido, la inversión no consigue reconstruir correctamente las fuentes que generan dichos datos, principalmente, la reconstrucción de los parámetros no reales.

Capítulo 6

Resultados y Conclusiones

Durante este capítulo se describirán diversos experimentos con el propósito de analizar determinados poblemas asociados a FEM-CSIM así como las posibles limítaciones del método, se analizarán distintos tipos de PECs y se compararán los resultados para medios con y sin pérdidas. También se simularán escenarios médicos. Finalmente, presentaremos posibles futuros trabajos relacionados con la Imagen Médica en microondas, con la idea de ampliar la investigación acerca de aplicaciones MWI.

6.1 Limítaciones del CSIM

En esta sección se simularán una serie de problemas en 2D que intentan determinar el comportamiento del *Algoritmo Inverso* para diferentes situaciones donde la inversión no es aceptable, incluso puede ser no legible.

6.1.1 Influencía del Contraste

Uno de los príncipales parámetros que definen el Dominio Imagen $\mathcal{D}$, es la variable contraste χ. El valor de dicha variable indica la relación existente entre el OI y el medio adaptativo. En [13] se realiza una interpretación de los resultados numéricos para diversas simulaciones analizando las limítaciones asociadas a χ.

En primer lugar, se analiza el escenario presentado en la Fig.6.1 para diferentes condiciones de la variable contraste, comparando los resultados de la inversión. Se considera un dominio imagen definido por un cuadrado de lado igual a 0.32m donde el OI es un triángulo de lado l= 0.23m. Las permitividades relativas para cada medio son, $\epsilon_b = 3 - j0.8988$ y $\epsilon_r = 5 - j0.8988$ a 1GHz. A lo largo de una circunferencia de r= 0.3m se han posicionado 16 antenas. El número de nodos implicados en el Dominio Imagen, $\mathcal{D}$, es de 1963 de los N= 7994 totales.

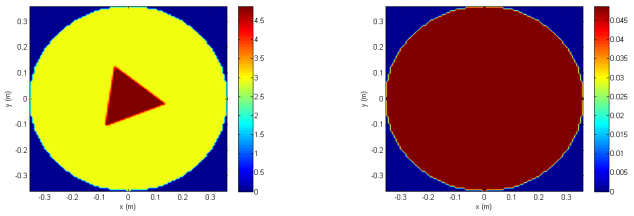

(a) (b)

Figura 6.1: $|\chi| < 1$: (a) Parte real permitividad relativa ϵ'_r (b) Conductividad σ.

Usando la expresión (5.1), se puede determinar que $|\chi| < 1$. Comparemos los resultados obtenidos en la Fig.6.2 con los correspondientes a la Fig 6.3, simulación realizada con el mismo escenario pero en la cual se ha forzado la parte real del constraste a ser negativa.

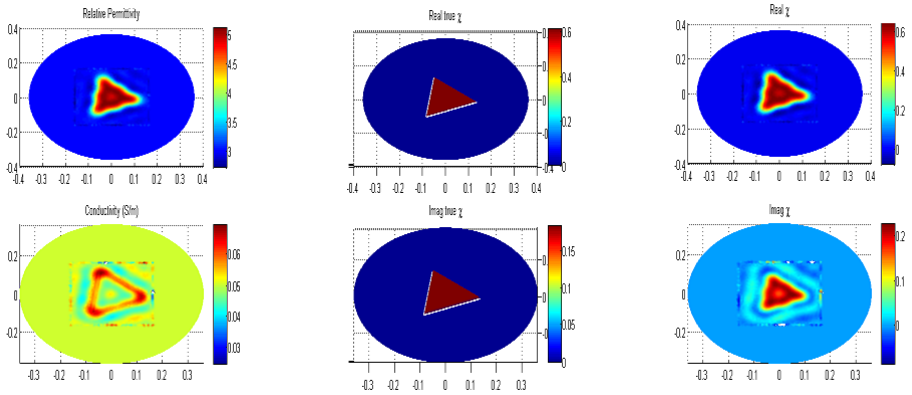

(a) (b) (c)

Figura 6.2: $|\chi| < 1$: (a) Reconst.prop.dieléctricas (b) True Re(χ) and Im(χ) (c) Reconst. Re(χ) and Im(χ).

Claramente, los resultados para $|\chi| < 1$ presentan una mayor calidad. Mientras que la primera simulación genera un error igual al 30%, la simulación con contraste negativo implica un error próximo al 45% tras 200 iteraciones. Aunque no representa un error excesivo, en la Fig.6.3 se aprecia como la geometría no está correctamente definida.

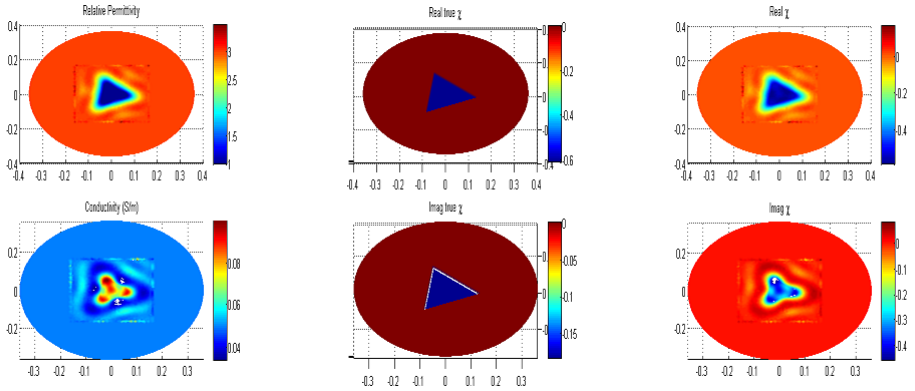

(a) (b) (c)

Figura 6.3: $re(\chi) < 0$: (a) Reconst.prop.dieléctricas (b) True Re(χ) and Im(χ) (c) Reconst. Re(χ) and Im(χ).

La siguiente simulación abordada proporciona peores resultado que el caso de $re(\chi) < 0$. El escenario elegido utiliza la misma geometría que en los anteriores casos pero está caracterizado por $|\chi| > 1$. Esta condición implica resultados totalmente erróneos. La permitividad del "background" y del OI son, respectivamente, $\epsilon_b = 2 - j0.8988$ y $\epsilon_r = 15 - j0.8988$ a 1GHz. El error obtenido es del 99% y la función de coste alcanza un valor de $10^{-0.7}$, mientras que para $|\chi| < 1$ se alcanza $10^{-3.5}$ para el mismo número de iteraciones.

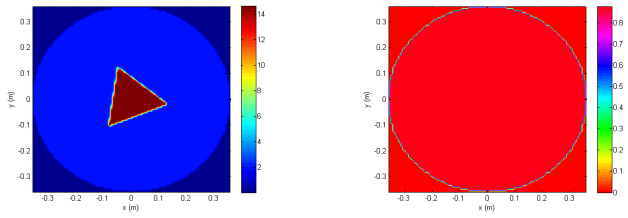

(a) (b)

Figura 6.4: $|\chi| > 1$: (a) Parte real permitividad relativa ϵ'_r (b) Conductividad σ.

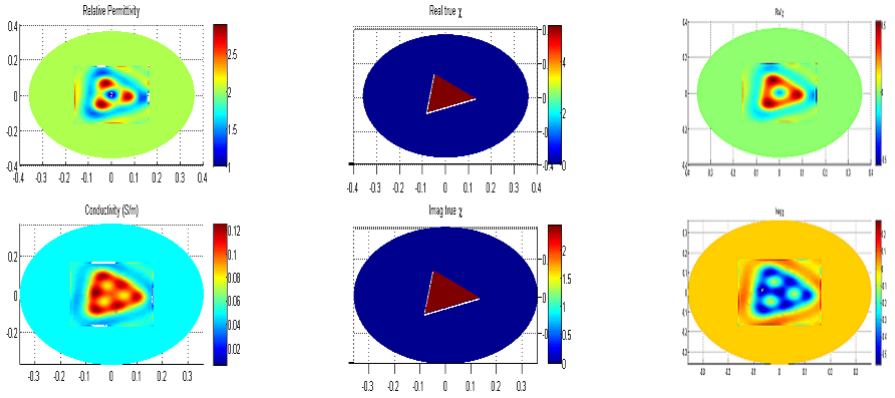

(a) (b) (c)

Figura 6.5: $|\chi| > 1$: (a) Reconst.prop.dieléctricas (b) True Re(χ) and Im(χ) (c) Reconst. Re(χ) and Im(χ).

Nótese que la elección del medio es fundamental para una correcta inversión, debiéndose adaptar al objeto de estudio. Para visualizar las distintas funciones de error y coste puede consultarse el documento original [A.1].

6.1.2 Frecuencia

Se deben considerar otros parámetros de simulación que implican consecuencias en los resultados, como la frecuencia de trabajo. Como ya se vio en el Capítulo 4, una frecuencia suficientemente grande puede acarrear una costosa discretización en términos de computación debido a la presencia de un mayor número de variables nodales. Sin embargo, tratamos de determinar las consecuencias que afectan a la calidad de la reconstrucción al usar una frecuencia u otra.

Para ello, se ejecutan 3 simulaciones diferentes. Primero, un determinado dominio imagen es introducido en dos recintos circulares de diferente dimensionado, pero igual "background", $\epsilon_b = 8 - j0.719$. El primero de los PEC presenta un r= 0.21m, mientras que el segundo, r= 0.28m. Las propiedades dieléctricas del OI quedan definidas por $\epsilon_r = 11.6 - j0.539$ a $f_o = 1$GHz. Nótese las diferencias del radio para cada uno de los dos casos. Si se denota el radio R en términos de la longitudes de onda, la primera computación es igual a $2\lambda_{bk}$ mientras que en la segunda es de $2.75\lambda_{bk}$.

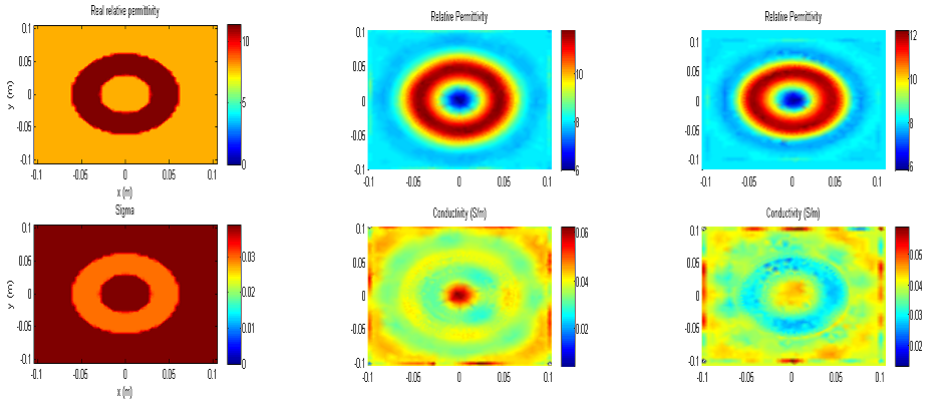

(a) (b) (c)

Figura 6.6: (R/λ_{bk}) análisis (a) Prop.Dieléctricas (ϵ_r', σ) (b) Resultados Reconst. r= 0.21m (c) Resultados Reconst. r= 0.28m.

En la Fig.6.6(a) el perfil original es comparado con los resultados de la reconstrucción para ambos casos. De la misma manera, en la Fig.6.7 se puede contemplar la variable contraste original junto a las reconstrucciones realizadas para ambas simulaciones.

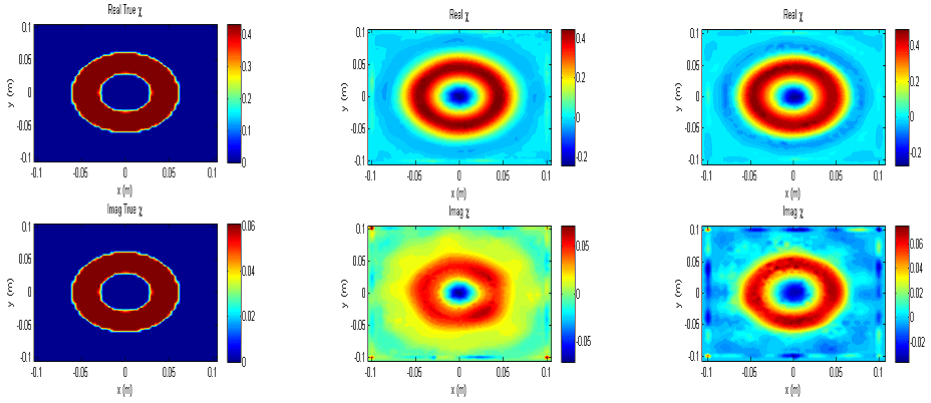

(a) (b) (c)

Figura 6.7: (R/λ_{bk}) análisis (a) True χ (b) Reconst.χ r= 0.21m (c) Reconst.χ r= 0.28m

Finalmente, se realiza la tercera simulación, consistente en el recinto circular de r= 0.21m donde se introduce el mismo perfil dieléctrico que en la Fig.6.6(a) pero a una frecuencia menor, $f_o = 500$MHz. De este modo, las permitividades relativas presentan un valor de $\epsilon_r = 11.6 - j1.0785$ y $\epsilon_b = 8 - j1.438$ para el "background".

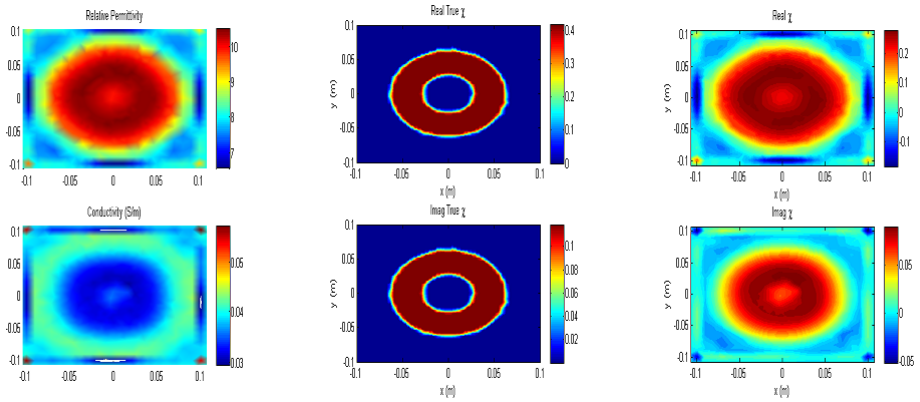

(a) (b) (c)

Figura 6.8: f_o = 500MHz: (a) Reconst. prop. dieléctricas (b) True Re(χ) and Im(χ) (c) Reconst. Re(χ) and Im(χ)

En la tabla 6.1 se muestran los términos de error para cada simulación después de 200 iteraciones. Se puede observar como la tercera computación genera los peores resultados mientras que la segunda presenta la mejor calidad de reconstrucción. En el caso de la primera y segunda simulación se está utilizando un medio con las mismas pérdidas. Sin embargo, la relación R/λ_{bk} es mayor para el segundo caso, lo que implica una mayor atenuación en las ondas reflectadas en el PEC, y en consecuencia, presenta una mejor calidad. En cuanto al tercer caso, a pesar de que presenta la mayor tangente de pérdidas, R/λ_{bk} es demasiado baja, lo que implica una baja atenuación de las reflexiones, provocando fallos durante la resolución del *Problema Directo*. La conclusión que se puede extraer de las simulaciones descritas en esta sección es que para realizar una correcta medición durante la realización del *Problema Directo*, es necesario establecer un compromiso entre la tangente de pérdidas que define a nuestro medio adaptador y las dimensiones del recinto para permitir una atenuación lo suficientemente grande, y de esta forma, evitar las reflexiones que representan ruido en nuestra aplicación.

Tabla 6.1: Comparación entre las 3 simulaciones

f_o [GHz]	$\lvert\chi\rvert$	R_PEC [m]	R/λ_{bk}	$\frac{\epsilon_b''}{\epsilon_b'}$	err(%)
1	0.448	0.21	2	0.089	43.8
1	0.448	0.28	2.75	0.089	42
0.5	0.445	0.21	1	0.179	55

6.2 Recintos PEC

En esta sección se pretende determinar la mejor opción posible para el recinto conductor. Hasta el momento, hemos utilizado siempre PEC circulares; ahora analizaremos un mismo perfil para tres formas distintas del PEC. Imaginemos que se dispone de tres cilindros de dimensiones iguales pero fabricados con diferentes materiales. Sin embargo, desconocemos la identidad de cada uno de ellos. Para determinar la identidad del material de cada cilindro, se realiza el estudio de la sección transversal de los tres OIs, localizándolos equiespaciadamente.

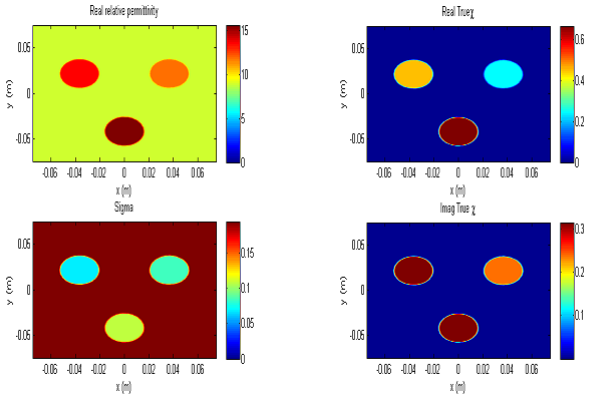

(a) (b)

Figura 6.9: Estudio del PEC: (a) Prop.Dieléctricas (b) Contraste Verdadero

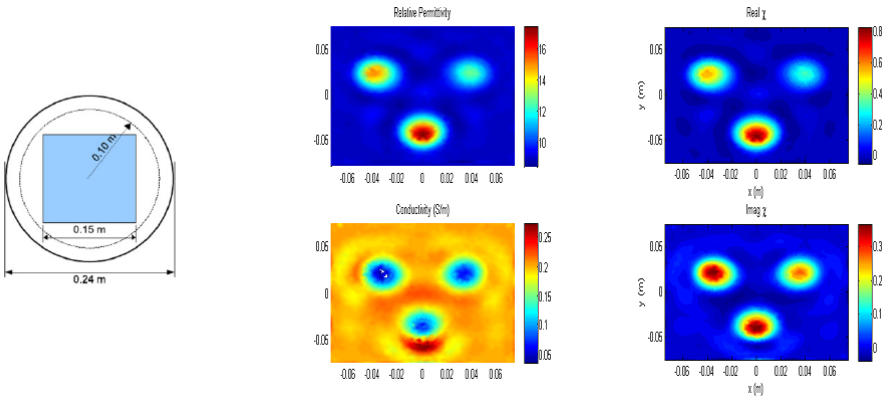

(a) (b) (c)

Figura 6.10: Circular: (a) Escenario (b) reconst.prop.dieléc. (c) reconst.contraste

En la Fig.6.9 se describen las propiedades dieléctricas y la variable contraste del Dominio Imagen $\mathcal{D}$. Las permititividades relativas de cada unade las regiones son: $\epsilon_{sc1} = 14 - j0.8988$; $\epsilon_{sc2} = 12 - j1.0913$; $\epsilon_{sc3} = 16 - j1.4123$ a $f_o = 1.4$GHz.

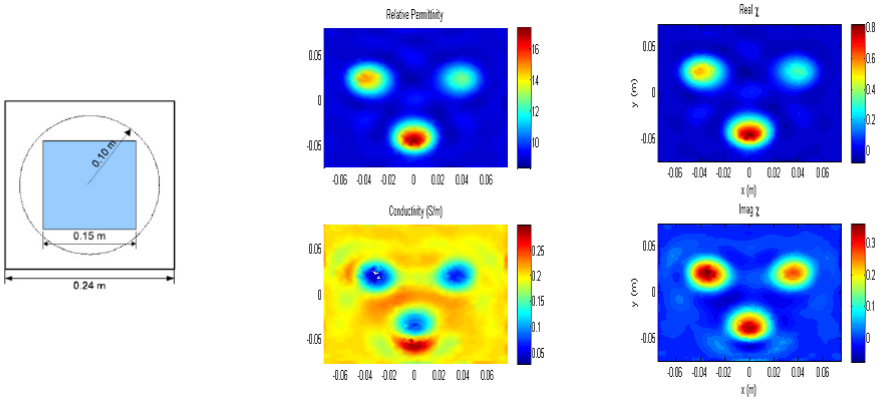

(a) (b) (c)

Figura 6.11: Cuadrada: (a) Escenario (b) reconst.prop.dieléc. (c) reconst.contraste

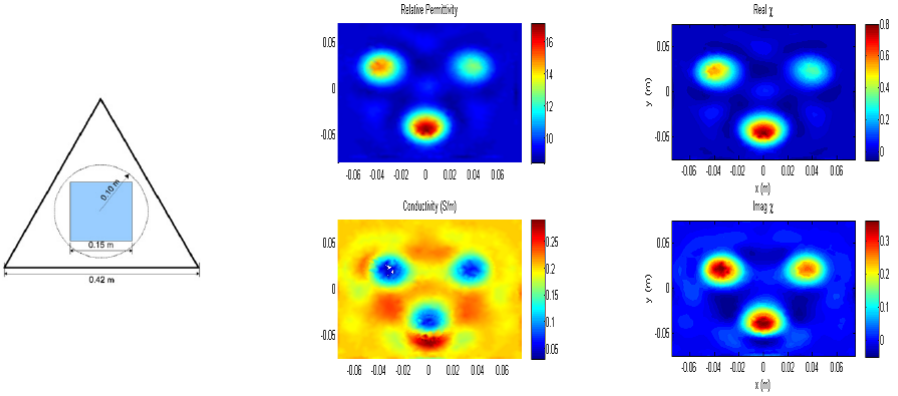

(a) (b) (c)

Figura 6.12: Triangular: (a) Escenario (b) reconst.prop.dieléc. (c) reconst.contraste

Como se comentó anteriormente, el dominio imagen es introducido en tres recintos con formas distintas: un círculo de radio 0.12m Fig.6.10(a), un cuadrado de lado 0.24m Fig.6.11(a) y un triángulo equilatero de lado 0.42m Fig.6.12(a). Para todas las simulaciones, se utilizó un "background" con pérdidas ($\epsilon_b = 9 - j2.568$ a 1.4GHz). El OI fue iluminado por 24 antenas emplazadas a un radio de 0.1m. El dominio de inversión se basa en un cuadrado de lado 0.15m. En los tres casos el número de nodos era entre 5000 y 6000 nodos. En la Tabla 6.2 se muestran los resultados numéricos tras 550 iteraciones.

Tabla 6.2: Comparación entre PECs

Simulación	err(%)	$log_{10}(F)$	$log_{10}(F_s)$	$log_{10}(F_d)$
Circular	51	-3.61	-5.5	-1.8
Cuadrada	52	-3.375	-5.4	-1.7
Tirangular	52.5	-3.65	-5.7	-1.5

Se puede observar como los resultados de reconstrucción son similares para todas las simulaciones, de forma que podemos entender que no exiten consecuencias importantes en utilizar un tipo de recinto u otro, siempre y cuando las áreas en términos de longitud de onda seán más o menos equivalentes.

6.3 Elección del "Background"

Hemos comprobado como la elección del medio donde el OI es sumergido requiere la consideración de las limitaciones del contraste. Igualmente, el "background" implica un mejor o peor funcionamiento de FEM-CSIM en cuanto a las pérdidas que este medio presenta, esencial en la atenuación de las reflexiones.

6.3.1 Medios Con Pérdidas

Presentamos un escenario inhomogéneo basado en un OI cuadrado de lado 0.07m dentro de otro más grande de lado, l= 0.12m. El más pequeño tiene una permitividad compleja igual a $\epsilon_r = 12 - j0.449$, mientras la permitividad del grande, $\epsilon_r = 8 - j1.123$. Introducimos el dominio imagen dentro de un "background" definido por, $\epsilon_b = 6 - j1.7975$ a 800MHz. A continuación se muestra el perfil original junto a las correspondientes reconstrucciones y estimaciones iniciales.

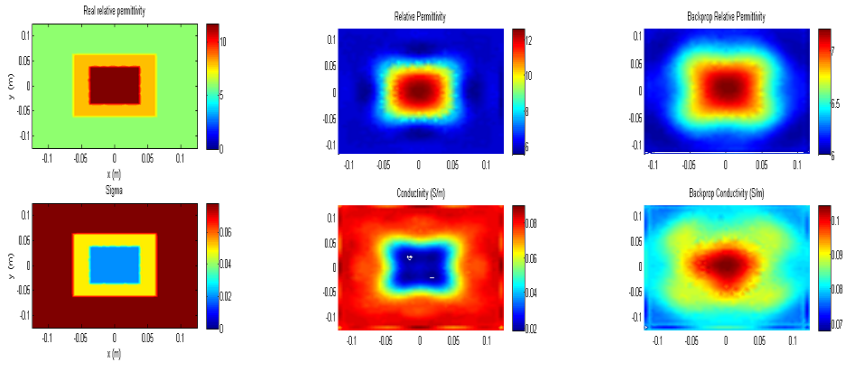

(a) (b) (c)

Figura 6.13: Cuadrados: a) True prop.dieléc. (b) Reconst. prop.diléc. (c) Estimación Inicial.

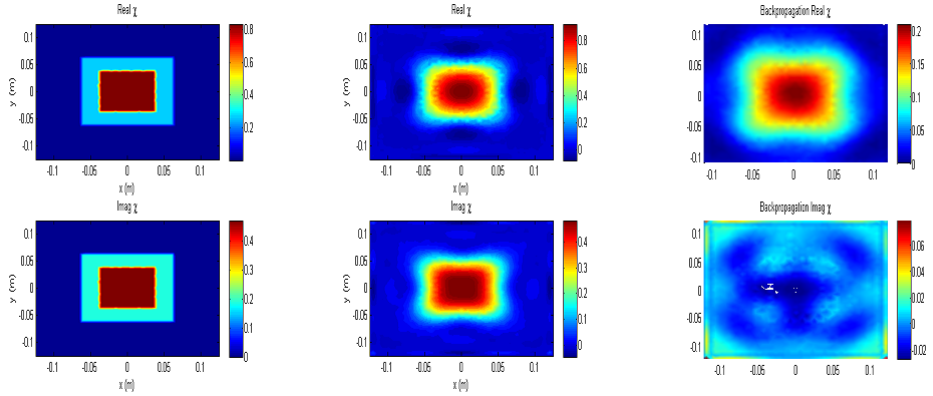

(a) (b) (c)

Figura 6.14: Cuadrados: a) True χ (b) Reconst. χ (c) Estimación Inicial

Los resultados obtenidos tras 220 iteraciones son óptimos, con un error del 25%, lo que significa que el error ha decrecido rapidamente desde la iteración inicial. Se ha podido minizar la función hasta $10^{-4.5}$, un valor muy cercano a la minimización óptima, 10^{-5}. En la Fig.6.15 se muestran los resultados en términos de error.

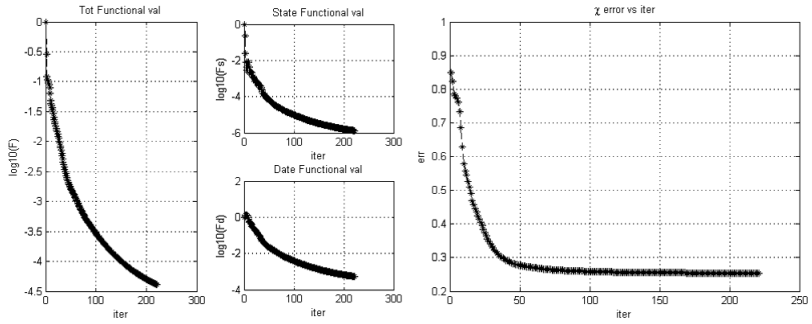

Figura 6.15: Cuadrados: Total, state and domain functional cost; Err: Error vs Iterations

La siguiente simulación se basa en un perfil muy popular en imagen conocido como E-phantom. En este caso suponemos un medio con bajas pérdidas con una permitividad relativa, $\epsilon_b = 16 - j1.8$ a $f_o = 1.2GHz$. El E-phantom esta basado en superficies inhomogéneas donde, la mayor parte de la superficie presenta $\epsilon_r = 33 - j2$, mientras que la pequeña inclusión circular y el rasgo de más a la derecha quedan definidos por $\epsilon_r = 33 - j8.33$. El radio elegido para el PEC es igual a 0.17m.

En las imágenes expuestas a continuación se muestran las propiedades dieléctricas del dominio imagen, y junto a ellas, se presentan los correspondientes resultados de reconstrucción. Del mismo modo, podemos observar tanto los datos como los resultados obtenidos para la variable contraste en la Fig.6.17.

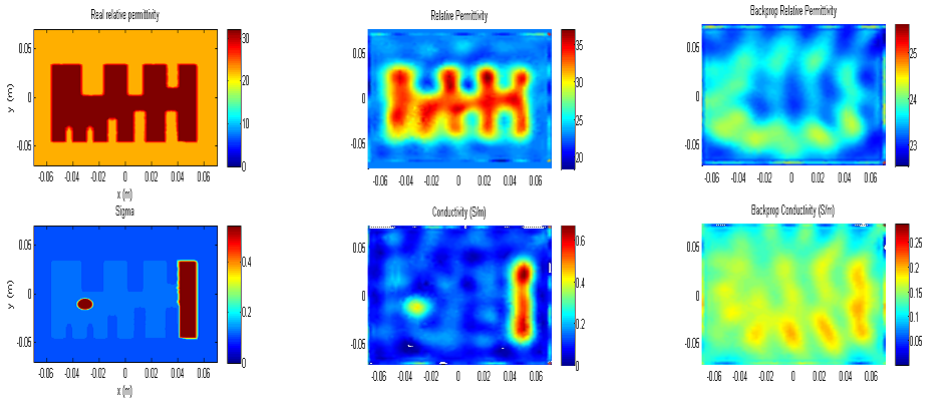

(a) (b) (c)

Figura 6.16: E-phantom: a) True prop.dieléc. (b) Reconst. prop.diléc. (c) Estimación Inicial.

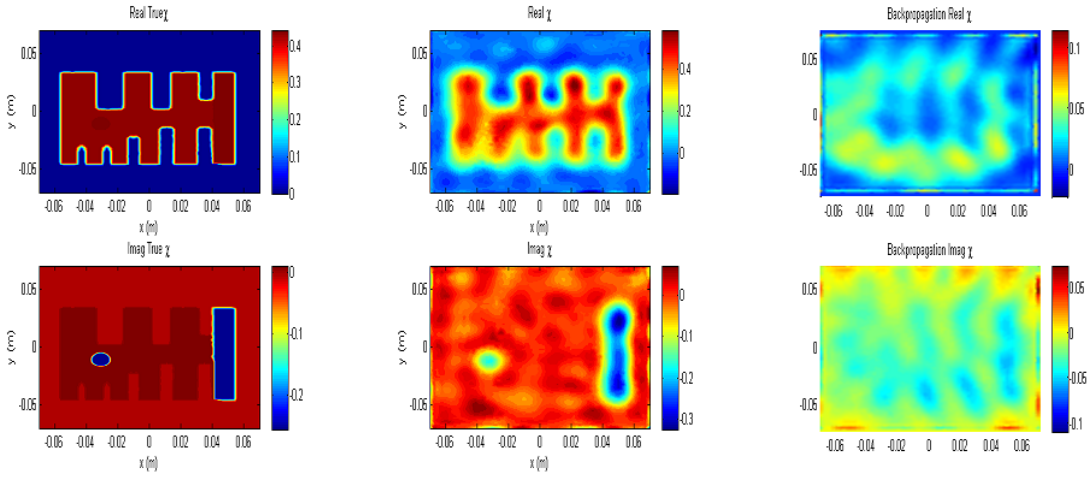

(a) (b) (c)

Figura 6.17: E-phantom: a) True χ (b) Reconst. χ (c) Estimación Inicial

Es posible identificar cada una de las superficies que constituyen el OI, lo que indica alta calidad en el proceso de inversión. Sin embargo, debido a la resolución del algoritmo, en la zona donde las líneas se encuentran más próximas, los resultados nos muestran una zona difusa donde las partes no se identifican correctamente. El error obtenido tras 751 iteraciones, estimación inicial incluida, es del 38.1%. Si se analiza las funciones de estado y datos, se puede apreciar que los datos sintéticos presentan poco ruido, lo que ha permitido obtener un buen resultado de la reconstrucción en comparación con los datos reales.

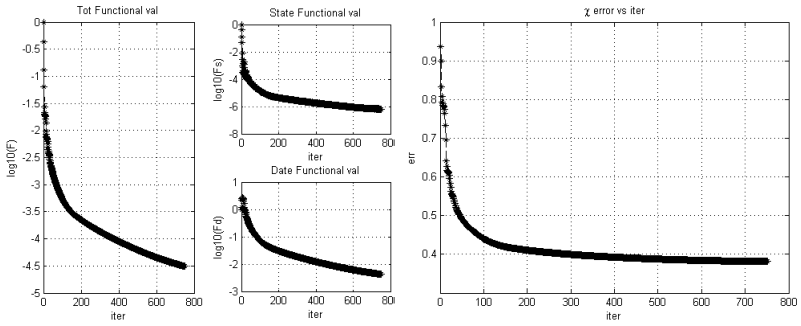

Figura 6.18: E-phantom: Total, state and domain functional cost; Err: Error vs Iterations

6.3.2 Medios Sin Pérdidas

A continuación se presentan los resultados de inversión usando medios sin pérdidas, donde se observa cómo la calidad de la reconstrucción es claramente inferior a los resultados equivalentes con medios con pérdidas. La razón reside en la ausencia de pérdidas durante la propagación de las ondas reflejadas en las paredes, lo cual provoca que aparezcan problemas en la sintetización de los datos simulados tras el *Problema Directo* debido a las reflexiones que iluminan el dominio imagen. Este hecho genera soluciones no reales; es decir, FEM-CSIM genera reconstrucciones de objetivos que no representan el auténtico OI. Esta situación podría entenderse como otra limitación de la aplicación en escenarios simulados.

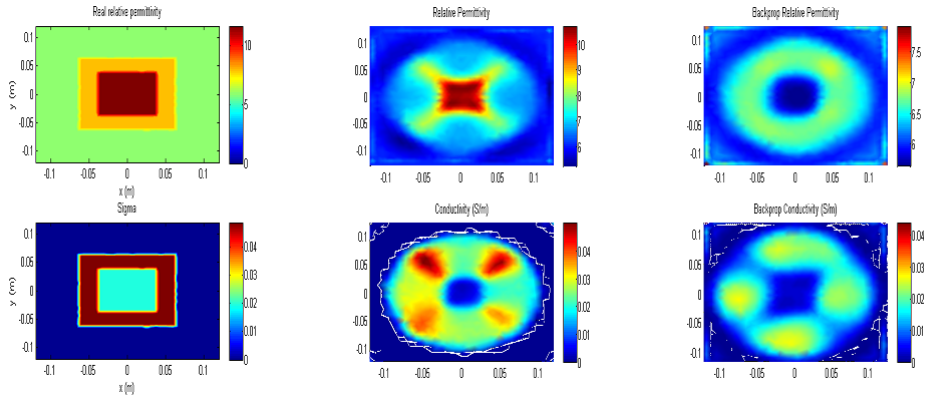

(a) (b) (c)

Figura 6.19: Medios sin pérdidas I: a) True prop.dieléc. (b) Reconst. prop.diléc. (c) Estimación Inicial.

Ahora, se simula el mismo perfil dieléctrico que en Fig.6.13(a) dentro de un "background" sin pérdidas, $\epsilon_b = 6$ a 800MHz. Recordad que el OI inhomogéneo se basaba en dos superficies cuadradas de permitividad, respectivamente, $\epsilon_r = 12 - j0.449$ y $\epsilon_r = 8 - j1.123$.

Podemos observar como los resultados de la Fig.6.19, obtenidos presentan valores numéricos cercanos a los originales pero las localizaciones de las regiones y las formas no están bien definidas.

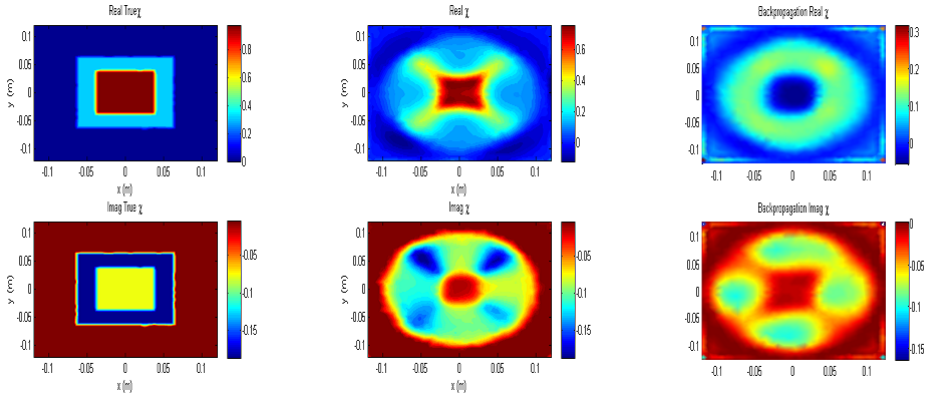

(a) (b) (c)

Figura 6.20: Medios sin pérdidas I: a) True χ (b) Reconst. χ (c) Estimación Inicial

Analicemos ahora los resultados asociados a la variable constraste. Estos resultan ser similares a los anteriores, apareciendo extrañas formas que no permiten identificar correctamente la geometría del dominio imagen. Esos errores se deben a los problemas asociados a las reflexiones y soluciones no reales.

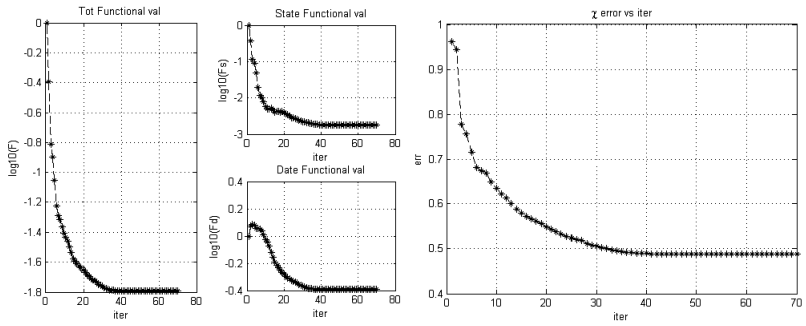

Figura 6.21: Medios sin pérdidas I: Total, state and domain functional cost; Err: Error vs Iterations

El error en la variable de contraste es del 49%. Observese la escasa minimización realizada por el algoritmo en las funciones de coste en comparación con su equivalente con pérdidas en el medio. Vemos como la inversión obtenida en la función de datos ha sido demasiado pobre.

Realicemos de nuevo una comparación respecto a los "backgrounds" utilizados, basada en la misma geometría del E-phantom definida en la Fig.6.16(a). Consideremos un OI homogéneo con una permitividad relativa igual a $\epsilon_r = 5.9 - j1.7975$, sumergido en un "background" de permitividad $\epsilon_b = 4.2$ a $f_o = 800$MHz.

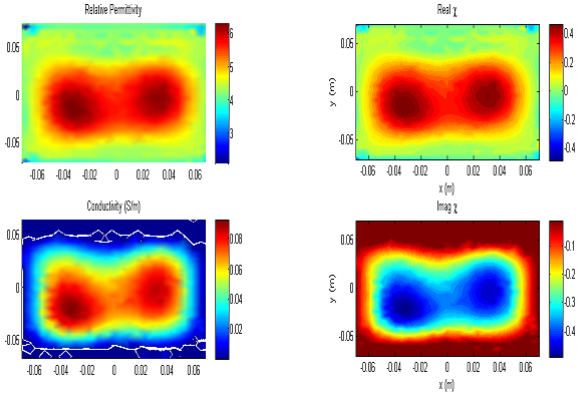

(a) (b)

Figura 6.22: Medios sin pérdidas II: (a) Reconst.Prop.Dieléctricas (b) Reconst.Contraste

Los resultados no son aceptables debido principalmente a la resolución, $\lambda_b/4$ es demasiado grande para definir correctamente la geometría de E-phantom. El error alcanza el 49.5% después de 400 iteraciones mientras que las funciones de coste han sido minimizadas a niveles aceptables, es decir, se han detectado las variables a reconstruir, pero no la forma y localización del OI.

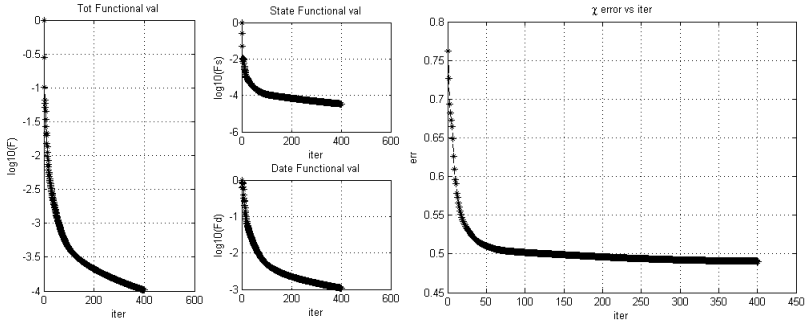

Figura 6.23: Medios sin pérdidas II: Total, state and domain functional cost; Err: Error vs Iterations

6.4 Aplicaciones Biomédicas

Por último, se simulan posibles experimentos reales en biomedicina. Uno de los problemas principales, que se experimentaron durante las computaciones de estos escenarios, fue el coste computacional gigante que implican debido a la complejidad de los escenarios, que requieren de una discretización potente. Primero se presenta un análisis común de la salud de los huesos. Para ello se simula la sección transversal de un antebrazo. En la Tabla 6.3 se define cada una de las regiones que conforman el OI. El medio adaptativo se caracteriza por $\epsilon_b = 76.56 - j15$ a 1GHz. Se utilizaron 16 antenas y un recinto de r= 0.14m.

Tabla 6.3: Definición antebrazo

Piel	Músculo	Huesos
$46 - j15$	$55 - j16$	$13 - j2.3$

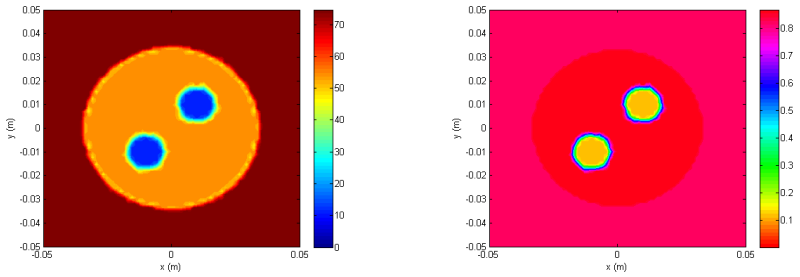

(a) (b)

Figura 6.24: Antebrazo: (a) Parte real permitividad relativa ϵ'_r (b) Conductividad σ

En la Fig.6.25 el contraste reconstruido se compara con el contraste verdadero. Se puede identificar el hueso pero, sin embargo, la piel no se detecta. Aunque podemos adelantar que no implicará un grave error debido a la pequeña proporción de la piel frente al dominio total.

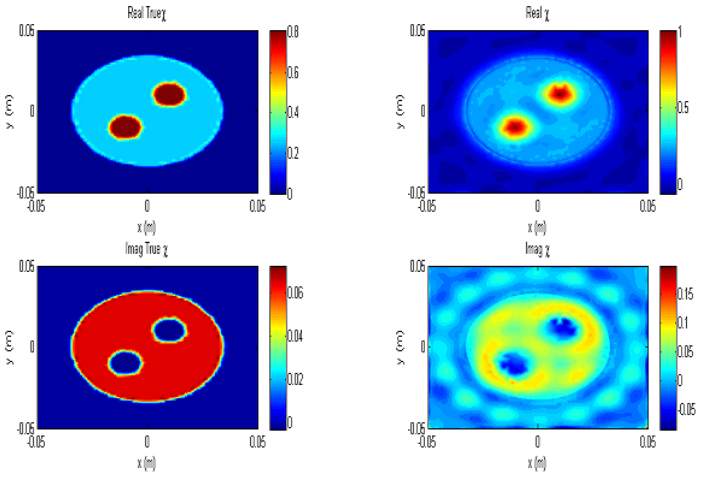

(a) (b)

Figura 6.25: Antebrazo: (a) True Contrast (b) Reconst.Contrast

El error obtenido tras 415 iteraciones es de 0.338, es decir, FEM-CSIM ha funcionado correctamente en este experiomento médico.

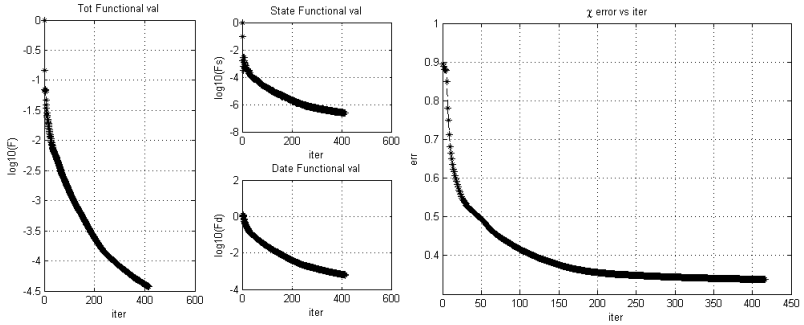

Figura 6.26: Antebrazo: Total, state and domain functional cost; Err: Error vs Iterations

El segundo experimento trata de reconstruir un modelo cerebral que presenta síntomas de un pequeño derrame cerebral. Este modelo consiste de diferente regiones: piel, cráneo, fluido cerebral espinal (CSF), materia gris (GM) y materia blanca (WM). La región asociada al derrame está representada por un coágulo localizado en el lado izquierdo de la materia blanca. Todas las propiedades materiales están expuestas en la Tabla 6.4. Además, el medio presenta una permitividad, $\epsilon_b = 35 - j13$ a 1GHz. El recinto PEC se basa en un círculo de radio 0.28m.

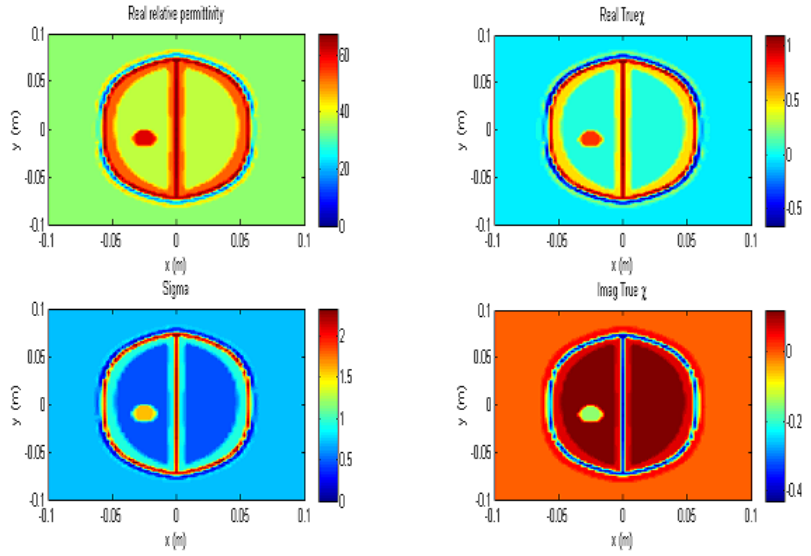

(a) (b)

Figura 6.27: Cerebro: (a) Propiedades Dieléctricas (b) True Contrast

Tabla 6.4: Modelo Cerebral

Piel	Cráneo	CSF	GM	WM	Derrame
$46 - j15$	$40 - j2.4$	$69.3 - j42.8$	$52.8 - j16.9$	$38.6 - j9$	$61.1 - j28.5$

Los resultados se muestran en las figuras siguientes. Se puede observar facílmente como la calidad de la reconstrucción es inaceptable. No se localizan ni identifican las distintas superficies que constituyen nuestro OI, obteniendo un error inaceptable de 0.9465 y una minimización del $10^{-0.1}$. Claramente, FEM-CSIM no ha podido ejecutar correctamente esta aplicación biomédica debido a su complejidad.

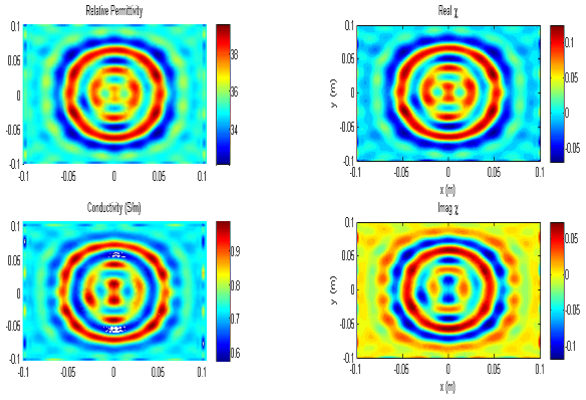

(a) (b)

Figura 6.28: Cerebro: (a) Reconst.Diel.Properties (b) Reconst.Contrast

Estos resultados erróneos se deben a la presencia de una gran cantidad de ruido en la medición. Visualizando la función de coste del estado determinamos que no es decreciente, lo que implica que los datos sintéticos contienen ruido y no representan una solución real.

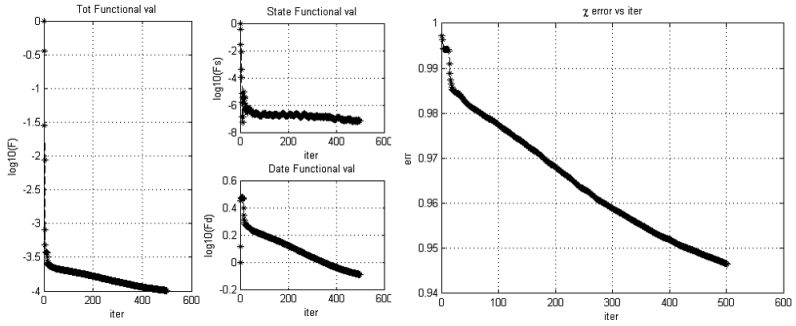

Figura 6.29: Cerebro: Total, state and domain functional cost; Err: Error vs Iterations

Es importante añadir que, disponiendo de un procesador más potente, se podría realizar una discretización más idónea con el propósito de obtener mayor precisión en los datos sintéticos. En nuestro caso, la computación del *Problema Directo* costó sobre 8 horas mientras que la ejecución del CSIM aproximandamente 14 horas.

6.5 Conclusiones

En esta sección se exponen las principales conclusiones derivadas de este trabajo, tanto para el Problema Directo como para el *Algoritmo Inverso*.

Se ha comprobado cómo FEM permite la resolución de las ecuaciones de Helmholtz, proporcionando ventajas como la eficacia con escenarios complejos y presentando desventajas, principalmente, el coste computacional.

Se ha determinado que los problemas escalares deben quedar definidos mediante el uso de *funciones base nodales*, mientras que para problemas vectoriales es necesario utilizar *funciones vectoriales*.

Tras las simulaciones del *Problema Directo*, concluimos que es necesario la utilización de medios que presenten una atenuación suficientemente grande para evitar problemas en la iluminación del OI debido a las reflexiones producidas en el PEC.

Mientras que en aplicaciones de MWI reales las mediciones se realizan mediante instrumental adecuado, en experimentos basados en datos sintéticos las simulaciones presentan diversas limitaciones en la computación.

En la ejecución de CSIM se ha comprobado que el criterio de estimación inicial requerido por el algoritmo de inversión, basado en el método de "backpropagation" y obtenido aplicando el método de "steepest descent", trabaja adecuadamente. Este proceso nos permite alcanzar el mínimo global de una función de coste que debe ser minimizada para una correcta reconstrucción. Sin embargo, existen algunas desventajas: la convergencia del método se obtiene de formar lenta y en algunos casos, no se garantiza.

Se han determinando las limitaciones de la aplicación y su comportamiento, analizando su resolución, la influencia de la frecuencia de tabajo así como la del medio adaptativo. Además se han estudiado diferentes recintos basados en PECs, por no olvidar un detallado estudio sobre el problema asociado a las reflexiones. Finalmente, analizamos dos experimentos de biomedicina, obteniendo éxito en uno de ellos y reconstruyendo una solución no real para el otro debido a la presencia de ruido y a la complejidad del escenario. El nivel de precisión necesario requiere de una potencia de cálculo que excedía en mucho la disponible en el equipo utilizado. En la Tabla 6.5 se resumen parte de los experimentos realizados durante este trabajo.

Tabla 6.5: CSIM Resultados

Simulación	N nodos	I nodos	Iteraciones	err(%)	$log_{10}(F)$	$log_{10}(F_s)$	$log_{10}(F_d)$
Círculo $\|\chi\| < 1$	4831	1352	400	45.5	-3.9	-6.1	-1.9
OI circular inhomogéneo	8553	2853	850	30	-4.25	-6	-3.1
Ü perfil	10441	2668	700	49	-3.1	-4.9	-1.85
Triángulo $\|\chi\| < 1$	7794	1963	200	31	-3.5	-5.5	-2.1
Cuadrados con pérdidas	6759	1590	250	25	-4.4	-5.98	-3.6
E-phantom con pérdidas	13051	2936	750	38.1	-4.5	-6	-2.85
Cuadrados sin pérdidas	4988	1146	70	49	-1.8	-2.85	-0.4
E-phantom sin pérdidas	3480	818	400	49	-4	-4.5	-3
Aplicación bio: Antebrazo	19707	3984	415	33.8	-4.45	-6.4	-3.25

6.6 Trabajos Futuros

En este trabajo se han realizado y analizado una gran cantidad de simulaciones de CSIM, obteniendo resultados esperados para escenarios sintéticos. Sin embargo, existen técnicas más avanzadas que permiten mejorar los resultados de reconstrucción, reduciendo el error hasta el 20%, como son las denominadas *Regularización Multiplicativa* (MR FEM-CSIM) o *Regularización Multiplicativa Balanceada* (BMR FEM-CSIM), que podrían implementarse en un futuro trabajo.

Además, sería interesante realizar otros experimentos: comparar el método de "backpropagation" con otros criterios para la estimación inicial o comparar FEM-CSIM con la técnica tradicional, IE-CSIM.

Dentro del campo de estudio de esta investigación, el paso siguiente sería extender los experimentos a escenarios en 3D donde sería necesario el uso de elementos vectoriales así como de una discretización correcta. Finalmente, se habría que abordar experimentos reales con el intrumental de imagen necesario para aplicaciones de imagen médica.

Bibliografía

[1] Jianming Jin, *The Finite Element Method in Electromagnetics.*
A Wiley-Interscience Publication, John wiley & Sons, Inc. 2nd Edition, 2002.

[2] A.Bondenson, T.Rylander, P.Ingelström, *Computational Electromagnetics.* Springer.
June 27,2005.

[3] Amer Zakaria, *The Finite-Element Contrast Source Inversion Method for Microwave Imaging Applications.* A Thesis submitted to the Faculty of Graduate Studies of The University of Manitoba. 2012.

[4] Anastasis C.Polycarpou, *Introduction to the Finite Element Method in Elecromagnetics.*
Morgan & Claypool Publishers. First Edition, 2006.

[5] Jean-Pierre Berenger, *Perfectly Matched Layer (PML) for Computational Electromagnetics.*
Morgan & Claypool Publishers. First Edition, 2007.

[6] Elia A.Attardo, *Computational Methods for Microwave Imaging: Biomedical Applications.*
PhD Thesis, Politecnico di Torino. May 2011.

[7] Jiayuan Fang, Zhonghua Wu, *Generalized Perfectly Matched Layer-An Extension of Berenger's Perfectly Matched Layer Boundary Condition.*
IEEE Microwave And Guided Wave Letters, VOL. 5, NO. 12. December 1995.

[8] David M.Pozar, *Microwave Engineering.*
John wiley & Sons, Inc. Second Edition, 1998.

[9] A.Zakaria, C.Gilmore and J.LoVetri, *Finite-Element Contrast Source Inversion Method for Microwave Imaging.*
Article IOPscience. September 2010.

[10] C.Gilmore and J.LoVetri, *Enhancement of Microwave Tomography Through The Use of Electrically Conducting Enclosures.*
Article IOPscience. April 2008.

[11] International Center for Numerical Methods in Engineering, http://gid.cimne.upc.es/support/manuals
CINME,UPC.

[12] Microwave Imaging Laboratory Website, http://www.ece.umanitoba.ca/EM_Imaging_Lab/index.html
University of Manitoba.

[13] M.D'Urso, T.Isernia, and Andrea F.Morabito, *On the Solution of 2-D Inverse Scattering Problems via Source-Type Integral Equations.*
IEEE TRANSACTIONS ON GEOSCIENCE AND REMOTE SENSING, VOL.48, NO.3, March 2010.

[14] A.Zakaria and J.LoVetri, *Application of Multiplicative Regularization to the Finite-Element Contrast Source Inversion Method.*
IEEE TRANSACTIONS ON ANTENNAS AND PROPAGATION, VOL. 59, NO. 9, September 2011.

[15] C.J.Reddy, Manohar D.Deshpande, C.R.Cockrell, and Fred B.Beck *Finite Element Method for Eigenvalue Problems in Electromagnetics.*
NASA Technical Paper 3485, December 1994.

[16] Jianming Jin and W.C. Chew *Combining PML and ABC for Finite Element Analysis of Scattering Problems.*
Article of University of Illinois at Urbana-Champaign,

[17] J.Fang and Z.Wu *Generalized Perfectly Matched Layer for the Absorption of Propagating and Evanescent Waves in Lossless and Lossy Media.*
IEEE TRANSACTIONS ON MICROWAVE THEORY AND TECHNIQUES, VOL. 44, NO.12 December 2012

[18] P.Mojabi and J.LoVetri *Eigenfunction Contrast Source Inversion for Circular Metallic Enclosures.*
IOP PUBLISHING. INVERSE PROBLEMS. 12 January 2010

Apéndice

Apéndice A

Documento original de la tesis

A Finite Element Approach To Inverse Scattering Problems

MASTER'S DEGREE PROJECT

POLITECNICO DI TORINO

TELECOMMUNICATIONS ENGINEERING

AUTOR: ENRIQUE MASGRAU RITE

TUTOR: GIUSEPPE VECCHI

November 22, 2012

Acknowledgements

During this last year I have lived one of the best vital experiences of my life. Torino has been my home for all this time, and from where I will take amazing friends forever. In this country, I have felt like one more, and I have received a great affection by all its people. I really will have Torino inside me when this adventure will finish.

Furthermore, Torino is the place where I decided to finish my university studies, including this work. I want to thank Politecnico di Torino for giving me this possibility. Study abroad has made me grow as a person.

Now, I want to thank all the people that support me along this time to perform this research work. Thank to Istituto Superiore Mario Boella, the place where I have been doing my master's project. In the ISMB I've been able to enjoy a friendly atmosphere of work. I would like to sincerely show my gratitude to professor Giuseppe Vecchi for letting me make the thesis with him and for Elia A.Attardo for all his support, effort and patience during these months.

In the same way, I would like to show gratitude to my family. For years of guidance and support. Without them, this experience would not have been possible.

Finally, I would like to thank my friends from Spain, Italy and Erasmus in general that have helped me to enjoy the work, the studies and good moments.

Grazie a tutti, davvero.

Abstract

During this research work we develop a Microwave Imaging (MWI) application that is used to obtain the unknown material properties of a certain target. This method is based on two different parts: The *Forward Problem* and the *Inversion algorithm*.

The first stage, the *Forward Problem*, performs the measurament of a scattered electric field along a material domain. The *Object of Interest* (OI) represents the unknown target, it is surronded inside a tank by a set of antennas that illuminate it and collect experimental data about electric measuraments. A matching medium is inserted inside the enclosure, it is called as background.

With the aim of simulate the experimental data, we develop the *Finite Element Method*. FEM is a powerful mathematical and engineering technique that lets us to solve the Helmholtz Equations that describe the behaviour of electromagnetics. On this way, we could generate synthetic data that are related to the real experimental data. To create the scenario that represents the MWI application we use a triangular meshing with nodal basis functions using a FEM simulator, called as GiD.

After solving the *Forward Problem*, the Contrast Source Inversion Method (CSIM) is introduced to reconstruct the original physical parameters that define our OI. Using this inversion algoritm is possible to minimize the error function close to its minima global with the measuraments obtained during FP solver. When the iterative method finishes, the reconstructed results are analyzed in order to identificate the materials involved in the Imaging Domain.

In this research work we will describe different experiments related to the *Forward Problem* and Constrast results. Several conclusions about FEM results are obtained from simulations. We will talk about PEC concepts, current source distribution, background dielectric properties and frequency influence during the FP solver.

However, the main results are related to CSIM simulations for different scenarios are explained. Results will be compared in several experiments, concluding concepts about method resolution, limitations in the algorithm and analyzing results according to dimensions in terms of wavelength.

Finally, it is important to mention simulations related to lossy and lossless mediums, and biomed-

ical experiments that perform real MWI experiments. We will observe how the CSIM will provide enough quality for material reconstructions in order to be able to detect the position of targets inside a MWI scenario. In best reconstructed results we will obtain an error over 25%, that is enough for many biomedical applications.

Contents

1 Introduction **17**

1.1 Scope . . . 17

1.2 Motivation . . . 18

1.3 Problem Definition . . . 18

1.4 Proposed Solution . . . 19

1.5 Thesis Overview . . . 20

2 Electromagnetic Concepts **23**

2.1 Maxwell's Equations . . . 23

2.2 Boundary Conditions . . . 25

2.3 Helmholt Equation . . . 26

2.4 Scalar Wave Equations . . . 27

3 The Forward Problem **29**

3.1 Starting Point . . . 29

3.2 Electromagnetic Waves . . . 31

3.3 Simulation Methods . . . 32

4 The Finite Element Method **35**

4.1 FEM basic concepts . . . 35

4.2 Domain Discretization . . . 37

4.3 Basis Functions . . . 39

4.3.1 Nodal Basis Funtions . . . 40
4.3.2 Edge Basis Functions . . . 42
4.4 Scalar Problems . . . 43
4.4.1 2D Boundary-Value Problem . . . 43
4.4.2 Solving BVP via Garlerkin's Method . . . 44
4.5 Vector Problems . . . 50
4.5.1 The Curl-Curl Equation And Edge Elements . . . 50
4.6 Absorbing Boundary Conditions . . . 52
4.6.1 The Perfectly Matched Layer on 2D . . . 53
4.7 Assembling FEM Matrix . . . 60
4.8 Simulations . . . 62
4.8.1 Circular Enclosure . . . 62
4.8.2 Triangular Enclosure . . . 69
4.8.3 Square Enclosure . . . 70

5 Solving Inverse Scattering Problems 73
5.1 The Inversion Algorithm . . . 74
5.2 Inversion FEM Matrix Operators . . . 75
5.3 The Contrast Source Inversion Method . . . 76
5.3.1 Norms And Inner Products . . . 78
5.3.2 FEM-CSIM Initial Guess . . . 78
5.4 Simulations . . . 79

6 Results And Conclusions 93
6.1 Constraints of CSIM . . . 93
6.1.1 Contrast Source Influence . . . 93
6.1.2 Frequency . . . 99
6.1.3 Section Conclusion . . . 102
6.2 PEC Enclosures . . . 102
6.3 Background Choice . . . 105
6.3.1 Lossy Mediums . . . 106
6.3.2 Lossless Mediums . . . 109

6.4 Biomedical Issues 112
6.5 Conclusions 117
6.6 Future Works 119

Appendix **123**

A Assembly of FEM Global Matrices **123**

A.1 Scalar Problems 123
A.2 Vector Problems 128

B FEM-CSIM **129**

B.1 Scalar Problems: Two-Dimensional Case 129
B.2 Incident Field in Conductive Enclosures 130

Lista de Figuras

1.1 MWI application results 19
1.2 Process description 20

2.1 Interface between two media. 26

3.1 Relative permittivity (blue line) and conductivity (red line) for glycerine-water 80:20 from 300MHz up to 3GHz 30
3.2 The enclosed imaging system. 30
3.3 (a) MWT prototype system (b) Tomography reading 31
3.4 (a) 2D MWI model (b) 3D MWI model 32

4.1 Different elements to discretize a certain 1D, 2D or 3D geometry 37
4.2 Discretization error obtained using triangular or quadrilateral elements 38
4.3 2D geometry based on two different regions 38
4.4 The numbering of local nodes for the element e. 40
4.5 Triangular element divided into three sub-triangles. 41
4.6 Triangular edge element. 43
4.7 (a) Interior edge shared by two neighboring triangles. (b) The outward unit vectors normal to the common edge point in opposite directions 49
4.8 Fictitious Boundary 52
4.9 Incident, reflected and trasmitted waves 56
4.10 The PML ABC on a plane boundary 57
4.11 Concave surface enclosing the domain 58

4.12 2D meshing for $\epsilon'_r = 20$. 62
4.13 Forward Problem solved by FEM using nodal functions: $\epsilon'_r = 20$, (Xs,Ys)=(0.5,0), (a)(b) $|E|$ and $\angle E$ field for $\sigma = 0.0005$ S/m (c)(d) $|E|$ and $\angle E$ field for $\sigma = 0.5$ S/m. 63
4.14 Forward Problem solved by FEM using nodal functions: $\epsilon'_r = 20$ (a)(b) $|E|$ and $\angle E$ field for $\sigma = 0.0005$ [S/m] and for current sources (Xs,Ys)=([0.05 0],[0 -0.05]), (c)(d) $|E|$ and $\angle E$ field for $\sigma = 0.0005$ [S/m] and for current sources (Xs,Ys)=([-0.05 0.05],[-0.05 0.05]). 64
4.15 Forward Problem solved by FEM using nodal functions: $\epsilon'_r = 80$ (a)(b) $|E|$ and $\angle E$ field for $\sigma = 0.0005$ [S/m] and for current sources (Xs,Ys)=(0.05,0), (c)(d) $|E|$ field for $\sigma = 0.0005$ [S/m], current sources (Xs,Ys)=(0.02,0) and (Xs,Ys)=(0.07,0). 65
4.16 (a)(b) Inhomogeneous 2D Scenarios (c)(d) $|E|$ fields for current source at (Xs,Ys)=(0,-0.05). 66
4.17 Forward Problem solved by FEM using nodal functions: $\epsilon'_r = 10$, $\sigma = 0.03$ [S/m], (a) $|E|$ field for $f_o = 700MHz$, (b) $|E|$ field for $f_o = 1GHz$, (c) $|E|$ field for $f_o = 1.5GHz$, (d) $|E|$ field for $f_o = 2GHz$ 68
4.18 (a)(b) $|E|$ field for $f_o = 700MHz$ and $f_o = 2GHz$ respectively. 68
4.19 Triangular 2D: $\epsilon'_r = 20$, (a)(b) $|E|$ and $\angle E$ for $\sigma = 0.02$ [S/m] and (Xs,Ys)=(0,0), (c)(d) $|E|$ and $\angle E$ for $\sigma = 0.5$ [S/m] and (Xs,Ys)=(0,0) 69
4.20 (a) One current source (b) Three current sources 70

5.1 (a) Real relative permittivity ϵ'_r (b) Conductivity σ 79
5.2 Initial Guess: (a) Diel.Properties (ϵ'_r,σ) (b) Initial Constrast $\chi_{t,0}$ 80
5.3 (a) Reconst. diel. properties (b) True Re(χ) and Im(χ) (c) Reconst. Re(χ) and Im(χ) 81
5.4 (a) Total, state and domain functional cost (b) Error vs Iterations 82
5.5 $|\chi| > 1$: (a) True Re(χ) and Im(χ) (b) Reconstructed Re(χ) and Im(χ) 84
5.6 $Re(\chi) < 0$:(a) True Re(χ) and Im(χ) (b) Reconstructed Re(χ) and Im(χ) . . . 85
5.7 d= 0.09m (a) Real relative permittivity ϵ'_r (b) Conductivity σ 86
5.8 d= 0.09m (a) Reconst. diel. properties (b) True Re(χ) and Im(χ) (c) Reconst. Re(χ) and Im(χ) 86

5.9 d= 0.02m (a) Reconst. diel. properties (b) Reconst. Re(χ) and Im(χ) 87
5.10 Inhomogeneous Profile (a) Real relative permittivity ϵ_r' (b) Conductivity σ . . . 87
5.11 Inhomogeneous Profile (a) Reconst. diel. properties (b) True Re(χ) and Im(χ) (c) Reconst. Re(χ) and Im(χ) 88
5.12 Total, state and domain functional cost; Err: Error vs Iterations 88
5.13 Initial Guess: (a) Diel.Properties (ϵ_r',σ) (b) Initial Constrast $\chi_{t,0}$ 89
5.14 U-Shape profile: (a) Real relative permittivity ϵ_r' (b) Conductivity σ 90
5.15 U-Shape profile: (a) Reconst. diel. properties (b) True Re(χ) and Im(χ) (c) Reconst. Re(χ) and Im(χ) 90
5.16 U-Shape profile: Total, state and domain functional cost; Err: Error vs Iterations 91

6.1 $|\chi| < 1$: (a) Real relative permittivity ϵ_r' (b) Conductivity σ 94
6.2 $|\chi| < 1$: (a) Reconst. diel. properties (b) True Re(χ) and Im(χ) (c) Reconst. Re(χ) and Im(χ) 95
6.3 $re(\chi) < 0$: (a) Reconst. diel. properties (b) True Re(χ) and Im(χ) (c) Reconst. Re(χ) and Im(χ) 95
6.4 $|\chi| > 1$: (a) Real relative permittivity ϵ_r' (b) Conductivity σ 96
6.5 $|\chi| > 1$: (a) Reconst. diel. properties (b) True Re(χ) and Im(χ) (c) Reconst. Re(χ) and Im(χ) 96
6.6 $|\chi| < 1$ (a) Total, state and domain functional cost (b) Error vs Iterations . . 97
6.7 $re(\chi) < 0$ (a) Total, state and domain functional cost (b) Error vs Iterations . 98
6.8 (R/λ_{bk}) analysis (a) Diel.Properties (ϵ_r',σ) (b) reconst.results r= 0.21m (c) reconst.results r= 0.28m 99
6.9 (R/λ_{bk}) analysis (a) True χ (b) Reconst.χ r= 0.21m (c) Reconst.χ r= 0.28m . . 100
6.10 f_o = 500MHz: (a) Reconst. diel. properties (b) True Re(χ) and Im(χ) (c) Reconst. Re(χ) and Im(χ) 101
6.11 PEC study profile: (a) Dielec.Properties (b) True Contrast Source 103
6.12 Circle: (a) Enclosure shape (b) reconst.dielectric prop. (c) reconst.contrast source 103
6.13 Square: (a) Enclosure shape (b) reconst.dielectric prop. (c) reconst.contrast source 104

6.14 Triangle: (a) Enclosure shape (b) reconst.dielectric prop. (c) reconst.contrast source 104
6.15 Squares: a) True diel. properties (b) Reconst. diel. properties (c) Initial guess 106
6.16 Squares: a) True χ (b) Reconstructed χ (c) Initial guess 107
6.17 Squares: Total, state and domain functional cost; Err: Error vs Iterations 107
6.18 E-phantom: a) True diel. properties (b) Reconst. diel. properties (c) Initial guess 108
6.19 E-phantom: a) True χ (b) Reconstructed χ (c) Initial guess 108
6.20 E-phantom: Total, state and domain functional cost; Err: Error vs Iterations . . 109
6.21 Lossless I: a) True diel. properties (b) Reconst. diel. properties (c) Initial guess 110
6.22 Lossless I: a) True χ (b) Reconstructed χ (c) Initial guess 110
6.23 Lossless I: Total, state and domain functional cost; Err: Error vs Iterations . . . 111
6.24 Lossless II: (a) Reconst.Dielectric Properties (b) Reconst.Contrast Source 112
6.25 Lossless II: Total, state and domain functional cost; Err: Error vs Iterations . . . 112
6.26 Forearm: (a) Real relative permittivity ϵ_r' (b) Conductivity σ 113
6.27 Forearm: (a) True Contrast (b) Reconst.Contrast 114
6.28 Forearm: Total, state and domain functional cost; Err: Error vs Iterations 114
6.29 Brain: (a) Dielectric properties (b) True Contrast 115
6.30 Brain: (a) Reconst.Diel.Properties (b) Reconst.Contrast 116
6.31 Brain: Total, state and domain functional cost; Err: Error vs Iterations 116

A.1 (a) Linear triangular element in the xy-plane. (b) Linear triangular element (master element) in the $\xi\eta$-plane 124

Lista de Tablas

4.1 Edge Numbering for a Triangular Element 42
4.2 Computational Costs 71

6.1 Comparision between 3 simulations 101
6.2 Comparision between PEC shapes 105
6.3 Forearm properties 113
6.4 Brain Model 115
6.5 CSIM Results 118

Chapter 1

Introduction

In this research work a biomedical application is described and designed, to do this, a mathematical and engineering method is implemented with the purpose of being evaluated to extract conclusions about the results. On the one hand, this method presents important electromagnetic concepts that are used to solve this medical scenario (among many other possibilities), and on the other hand engineering techniques are mixed with those concepts to optimize the method that is researched.

1.1 Scope

Nowadays Microwave Imaging (MWI) is one of the most important research fields in biomedial imaging (tomography and breast detection are some biomedial applications based on MWI), it can be defined as discovering the internal structure of an object by illuminating it with electromagnetic methods. Inverse Scattering problem is a MWI application, the aim of this research work is based on describing the method to solve it in the correct way.

MWI can be based on several methods according to the medical or engineering application, in this case the method works with electromagnetic concepts mixed with engineering and mathematical techniques to know the dielectric properties of a certain target that is unknown but can be reconstructed, this target is known as Object of Interest (OI) and it will be described more deeply in Chapter 3 during the description of the *Forward Problem*.

The *Forward Problem* is one of the two main steps that form this method, the target is radiated by electromagnetic devices (antennas) and the results are used like an input of the Inverse Scattering method, that is the second part of the process.
Along this research work the inverse method and the way to compute the electromagnetic results (Finite Element Method) will be described deeply.

1.2 Motivation

Forward Problem and Inverse method will be implemented and evaluated separately to obtain a global method that lets us to known the dielectric properties of a unknown object that can be placed inside of a known body, knowing these material properties is possible to understand what type of material is analyzing, this idea has a great benefit in biomedical engineering, more exactly in medical imaging, for example, the tomography gives us a way to detect breast tumors, problems in bones and other type of diseases.
These problems are the reasons why this research work was choosen and correctly developed, MWI has an important impact in medical engineering, it is undeniable that such studies are necessary in the development of medicine, so that, engineering must research about medical applications and methods to improve it. Is proud to be part of the study of these bio-engineering applications so important in the real life.

1.3 Problem Definition

This section presents a description of the scenario that is involved in this research work. Imagine that there is a body with certain unknown properties, these unknown properties are the target of a study or investigation, It's necessary to understand the behaviour of this material to be able to determine some conclusions that are very important from the point of view of the investigation, for example a medical analysis to diagnosticate a possible proplem (breast cancer detection). Then, we have a target that part is known and a part is unknown, as mentioned in section before, this unknown body is called as *Object of Interest*, in the future we will always refer to this target as OI.
In Fig.1. a possible medical scenario is shown, a breast cancer detection, in this case the material properties of the breast are known, so with the correct anaylis is possible to detect some strange

bodies in the breast that could be a little tumor. In final results of the diagnostic would be possible to observe a total surface or volume where different dielectric properties are involved and obviously some of them means a dangerous object.
Other possibility could be an analysis of an object formed by two parts, firstly the known region called as background medium whose dielectric porperties are known, secondly the Imaging Domain that is formed by the OI and a part of the total background medium (known material) , the total region is the sum of both regions although the Imaging Domain is the aim of this MWI application. For the study of the OI is necessary to implement and design a method that lets us to obatin those properties of the unknown body such that the target must not be altered, much less damaged by the method.

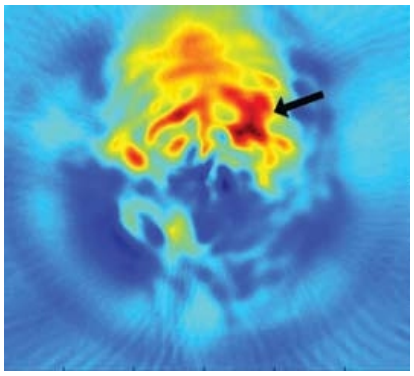

Figure 1.1: MWI application results

1.4 Proposed Solution

There are different ways and methods to solve this problem, in this project the global method that performs this type of biomedical applications is known as FEM-CSIM (FEM-Contrast Source Imaging Method). FEM means Finite Element method, it will be one of the targets of study more important in this research work, this method lets to compute very efficiently electromagnetic parameters in a certain scenario, it is a popular method to analyze an object or target that is used in a lot of engineering fields such as structure designs, temperature analysis of objects... FEM will be described in Chapter 4 to understand how this method works and how is implemented. If FEM-CSIM is implemented correctly, it will provide the dielectric properties of the OI (object of interest) with a little error like in all engineering applications, later these results could be

interpreted by specialists to determine a certain disease as tumors. As mentioned at Scope Section this method will be divided in two main steps, the *Forward Problem* that requires to illuminate the target with radiating devices as antennas to obtain the electromagnetic field distribution among the surface or volume of study, these results are recorded and computed by FEM techniques, later the Inverse Scattering problem is performed. The iterative method (CSIM) is implemented to obtain the dielectric properties of the OI, in Fig.1.2. a global method scheme is shown. Finally, as commented above, the results has to be analysed by specialists in medicine in the case of a medical scenario or in the case of an ingeneering study (material investigation) by corresponding specialists.

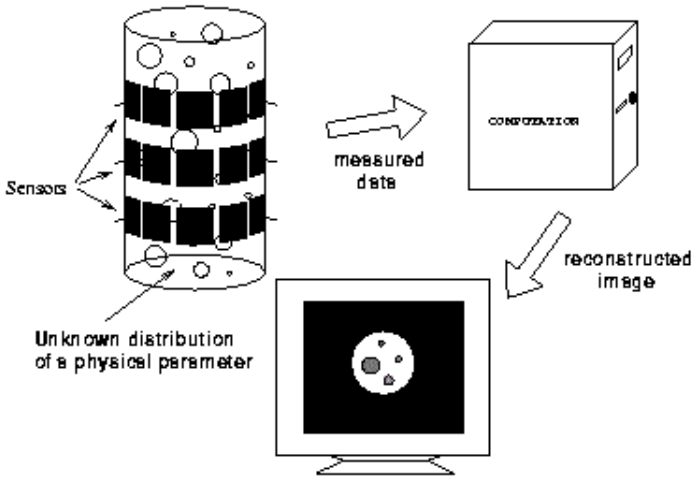

Figure 1.2: Process description

1.5 Thesis Overview

This research work is composed by six chapters, the aim of the author is to describe correctly the method, concepts that are involved in this process and obviously the results of the implementation with the corresponding conclusions.

Chapter 2 is based on the basic electromagnetic concepts that have been considered during this project, mainly the principles of electromagnetism are focus in Maxwell's studies as formulation

known as Maxwell's equations, furthermore is necessary to explain other concepts that are very important to study like boundary conditions.

The Forward Problem is presented in Chapter 3, we will talk about the MWI scenario and how experimental solvers work, comparing them against simulated scenarios as FEM that is the main target of study in next chapter.

Chapter 4 describes deeply the Finite Element Method (FEM), the complexity of this method has implied a detailed study and effort to understand how it works and how it must be implemented, both geometrical and mathemathical formulation is described. This description focuses in 2D scenarios, however a short theorically description of 3D problems in FEM is considered in the chapter.

The Inverse Scattering problem is the target of study in Chapter 5 where the FEM-CSIM is developed and implemented, results of possible simulations are evaluated. Thus, in Chapter 6 results and conclusions after problem simulations are presented with the aim of obtain a correct global idea of the application that is involved in this research work.

Finally in Chapter 6, future possible works are introduced with the purpose of observe the wide field of study that suppose MWI applications based on scattering problems.

Chapter 2

Electromagnetic Concepts

Electromagnetic analysis has been an indespensable part of many engineering and scientific studies since J.C.Maxwell completed the electromagnetic theory in 1873 [1]. The problem of electromagnetic analysis is actually a problem of solving a set of Maxwell's equations subject to given boundary conditions. In this chapter mathematical formulation necessary to implement our MWI application is described, this formulation is based on electromagnetism theory, so we review briefly some basic concepts and equations of electromagnetic theory that are used in this research work

The formulation is shown for twodimensional (2D) for scalar problems as well as vector configurations (3D). For 2D cases there are two possible problems, the trasnverse magnetic (TM) and the transverse electric (TE), during this research work the TM case has been chosen.

The correspoding formulation for each case is derived from Maxwell's equations.

2.1 Maxwell's Equations

Maxwell's equations is the name with which we refer to a set of equations that explains the electromagnetic phenomena, these equations can be written in both differential and integral forms, differential ones are presented during this section. The next expressions mean the basic concepts of electromagnetism, this is the reason why describe these ideas is essential to understand correctly the purpose of the project.

Differential Maxwell's equations are derived from integral forms using Strokes and Gauss theorems.

$$\nabla \times \vec{E}(\vec{r},t) = -\frac{\partial \vec{B}(\vec{r},t)}{\partial t} \tag{2.1}$$

$$\nabla \times \vec{H}(\vec{r},t) = \frac{\partial \vec{D}(\vec{r},t)}{\partial t} + \vec{J}(\vec{r},t) \tag{2.2}$$

$$\nabla \cdot \vec{D}(\vec{r},t) = \rho(\vec{r},t) \tag{2.3}$$

$$\nabla \cdot \vec{B}(\vec{r},t) = 0 \tag{2.4}$$

$$\nabla \cdot \vec{J}(\vec{r},t) = -\frac{\partial \rho}{\partial t} \tag{2.5}$$

where the spatial vectors $\vec{E}$, $\vec{H}$, $\vec{D}$, $\vec{B}$ and $\vec{J}$ are respectively, the electromagnetic field [V/m], the magnetic field intensity [A/m], the electric flux density $[C/m^2]$, the magnetic flux density $[Wb/m^2]$ and finally the electric current density $[A/m^2]$, in equations (2.3) the variable ρ refers to the electric charge density.
The electric current density $\vec{J}$ is the sum based on two different contributions, the conduction current density $\vec{J}_c$ that is the medium's ability to conducte electric current and the impressed current density $\vec{J}_i$, due to the given current sources.

$$\vec{J}(\vec{r},t) = \vec{J}_c(\vec{r},t) + \vec{J}_i(\vec{r},t) \tag{2.6}$$

In addition it's necessary to introduce some more expressions to present correctly the theory about Maxwell's equations, if we consider an isotropic, homogenous and non dispersive medium some realtions will be avalaible.

$$\vec{D}(\vec{r},t) = \epsilon_o \epsilon_r(\vec{r}) \vec{E}(\vec{r},t) \tag{2.7}$$

$$\vec{B}(\vec{r},t) = \mu_o \mu_r(\vec{r}) \vec{H}(\vec{r},t) \tag{2.8}$$

$$\vec{J}_c(\vec{r},t) = \sigma_o(\vec{r}) \vec{E}(\vec{r},t) \tag{2.9}$$

In expressions that appear above there are some parameters that refer to the material properties, they are the permittivity in vacuum ϵ_o , the relative permittivity ϵ_r (formed by real relative permittivity and complex permittivity), permeability in vacuum μ_o, relative permeability μ_r and the conductivity σ_o.

The Maxwell's equations are assumed to have a time-harmonic dependecy of e^{jwt}, according to this assumption the equations (2.1)-(2.5) become

$$\nabla \times \vec{E}(\vec{r}) = -jw\vec{B}(\vec{r}) \tag{2.10}$$

$$\nabla \times \vec{H}(\vec{r}) = jw\vec{D}(\vec{r}) + \vec{J}(\vec{r}) \tag{2.11}$$

$$\nabla \cdot \vec{D}(\vec{r}) = \rho(\vec{r}) \tag{2.12}$$

$$\nabla \cdot \vec{B}(\vec{r}) = 0 \tag{2.13}$$

$$\vec{J}(\vec{r}) = \vec{J}_c(\vec{r}) + \vec{J}_i(\vec{r}) \tag{2.14}$$

2.2 Boundary Conditions

The differential equations presented in Section 2.1 can be solved if the corresponding boundary conditions of the involved mediums are considered, in other words, a complete description of the medium at boundaries is necessary to obtain a real solution. In this section a set of boundary conditions that can be used in many practical scenarios are presented.

$$\hat{n} \times (\vec{E_1}(\vec{r}) - \vec{E_2}(\vec{r})) = 0 \tag{2.15}$$

$$\hat{n} \times (\vec{H_1}(\vec{r}) - \vec{H_2}(\vec{r})) = 0 \tag{2.16}$$

$$\hat{n} \times (\vec{D_1}(\vec{r}) - \vec{D_2}(\vec{r})) = 0 \tag{2.17}$$

$$\hat{n} \times (\vec{B_1}(\vec{r}) - \vec{B_2}(\vec{r})) = 0 \tag{2.18}$$

Where $\hat{n}$ is the unit vector normal in the interface from medium 1 to medium 2, as can be observed in Fig.2.1

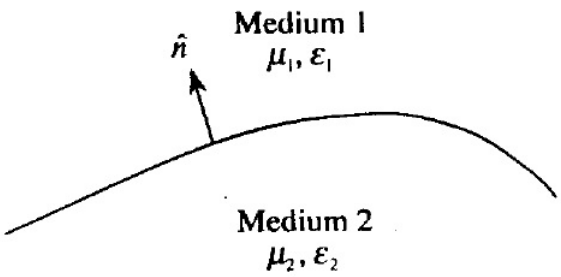

Figure 2.1: Interface between two media.

In expressions (2.16) and (2.17) both surface electric current density and surface electric charge density have been considered zero, in the case where this assumption is not considered the expresions would be,

$$\hat{n} \times (\vec{H_1}(\vec{r}) - \vec{H_2}(\vec{r})) = \vec{J_s} \tag{2.19}$$

$$\hat{n} \times (\vec{D_1}(\vec{r}) - \vec{D_2}(\vec{r})) = \rho_s \tag{2.20}$$

2.3 Helmholt Equation

In the application that is developed during this work is important to solve partial difference equations (PDE) where the $\vec{E}$ field is involved, remove $\vec{H}$ is necessary to obtain the next expression, obviously this assumption implies consequences in most of the equations commented until this moment.

$$\nabla \times \nabla \times \vec{E}(\vec{r}) - w^2 \mu_o \epsilon(\vec{r}) \vec{E}(\vec{r}) = -jw\mu_o \vec{J_i}(\vec{r}) \tag{2.21}$$

Two conditions have been assumed, (i) there aren't electric charges (ρ=0), (ii) the relative permeability is null (non-magnetic problems) $\mu_r = 1$.
Equation (2.21) is known as Helmholtz Equation, in particular, FEM is generally used to solve the frequency domain form of the curl-curl equation, sometimes referred to as the vector Helmholtz equation.

2.4 Scalar Wave Equations

In electromagnetic analysis, whenever possible problems are simplified by using a 2D model to approximate a 3D problem. Assume that the fields has not variation with respect to one Cartesian coordinate (z-coordinate), we treat a scalar scenario that is defined by

$$\nabla^2 E_z + k_o^2 \epsilon_r E_z = jw\mu_o J_z \tag{2.22}$$

also called as *inhomogeneous scalar wave equation*, this expression will be used in Chapter 4 to describe the 2D scalar problem given by TM and z-polarization case.

Chapter 3

The Forward Problem

Microwave imaging (MWI) is of interest for various applications such as geophysical surveying and medical imaging. In the form of MWI considered herein, one attempts to quantitatively reconstruct the, mostly unknown, electrical properties (i.e. permittivity and/or conductivity) of an object of interest (OI) which is immersed in a background medium of known electrical properties [9]. As mentioned in Scope Section in Chapter 1, to solve a MWI application as is developed during this research work is necessary firstly implement the *Forward Problem* with the aim of obtain the electric distribution of the electromagnetic field along the OI, after the electromagnetic field is computed, the next step is based on the *Inverse Algorithm* that is presented in Chapter 5. This chapter represents a briefly introduction to the *Forward Problem* in the context of our biomedical application, the chosen method used to compute the electric field is totally defined for 2D geometries in Chapter 4. However, along this chapter we talk about this method, describing how it is executed in real experimental applications in order to understand the differences between experimental and synthetic.

3.1 Starting Point

Before explaining how is implemented the Forward Problem based on simulating, we think that could be profitable to understand how MWI is performed in real medical applications such as breast detection or bone tissue analysis. To get this, a description of real experiments based on MWI is developed during this section. We consider microwave scenarios where the imaging region is surrounded by an electrically conducting surface, this surface is denoted as PEC.

In real MWI applications the OI is placed inside a tank, the conductive surface serves as both the container for any possible matching fluid and a shield from outside interference as commented before. Obviously, the inclusion of the conducting enclosure considerably changes the distribution of the EM energy as compared to an open region. The matching medium should be as optimal as possible to avoid possible wave reflection from the walls, in Fig.3.1 extracted from [6] we can observe a common used liquid medium based on 80:20 percent glycerine-water solution.

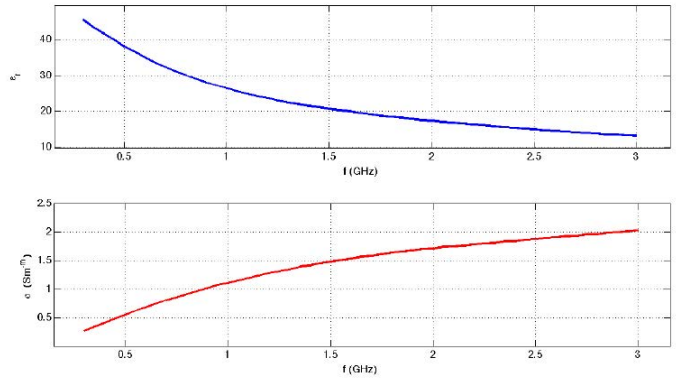

Figure 3.1: Relative permittivity (blue line) and conductivity (red line) for glycerine-water 80:20 from 300MHz up to 3GHz

Surrounding the OI inside the tank, a set of antennas, that work both Tx and Rx electromagnetic devices, illuminate the OI with the aim of storing the scattering electric field. The scatterer is located entirely within the region $\mathcal{D}$ and is embedded in a homogenous background medium (matching medium) with a background permittivity whose dielectric properties are denoted as ϵ_b.

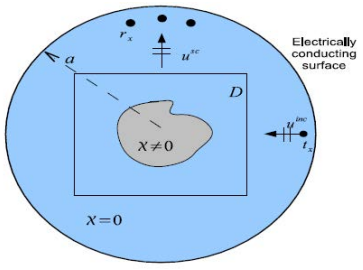

Figure 3.2: The enclosed imaging system.

In Fig.3.2[10] a general scheme is shown. In this case the enclosure is based on a cylinder tank. Notice that during this project the dielectric properties are denoted as

$$\epsilon = \epsilon' + j\epsilon'' = \epsilon_o\epsilon_r = \epsilon_o\left(\epsilon'_r + j\epsilon''_r\right) = \epsilon_o\left(\epsilon'_r + \frac{\sigma}{jw\epsilon_o}\right) \tag{3.1}$$

Now, some possible real MWI scenarios are shown in the next figure.

(a) (b)

Figure 3.3: (a) MWT prototype system (b) Tomography reading

3.2 Electromagnetic Waves

When we talk about analyse the electromagnetic wave in the *Forward Problem*, we need to differentiate between all possible EM cases. In this section a general discussion of the different types of wave propagation that can exist is presented. Maybe in a medium the wave propagation could be based on tranverse electromagnetic waves characterized by $E_z = H_z = 0$, this implies that tranverse field components are zero. Other possible case is the TE waves, this propagation means that $E_z = 0$, so the unique transverse component is the magnetiz field $H_z \neq 0$. Finally, there is a wave propagation case based on a non zero electric tranverse component, $E_z \neq 0$, instead the magnetic tranverse field is null, $H_z = 0$. In microwave terminology, the 2D formulation corresponds to TM polarization. This 2D problem is readily solved using nodal elements and is the object of this performed electromagnetic study along the research work. TM scenarios are described by the Maxwell's equations defined in Chapter 2 and precisely in Section 2.4.

3.3 Simulation Methods

The purpose of this research work is to simulate a real MWI experiment using a method that let us to compute the scattered electric field, there are different used techniques along the history to get it. One of them is called as *the finite element method* that will be described deeply in Chapter 4, it is the chosen method to solve the *Forward Problem* in our MWI application. Basically, this method implies to solve a matrix equation where the electric coefficients that define the electric field can be obtained generating with FEM, a global matrix called as *FEM matrix* that is related to the geometry and properties of our scenario (OI + background). This matrix equation will be detailed developed in Chapter 4 and is given by

$$\mathbf{Az} = \mathbf{b} \tag{3.2}$$

Our forward simulation involve an iterative method where a given antenna from the set of antennas, that are surronding the OI, works as a trasnsmitter, i.e., in each iteration one different of the total antennas is the trasmitter while the others work as receivers, later that antenna will work as receiver while other antenna will be the new transmitter. Obviously, if the number of antennas used in the method is higher, the quantity of information will be wider. In Fig.3.4 (images from [3])a 2D and 3D approach is defined, observe how one of the antennas works as Tx while the others are Rx devices.

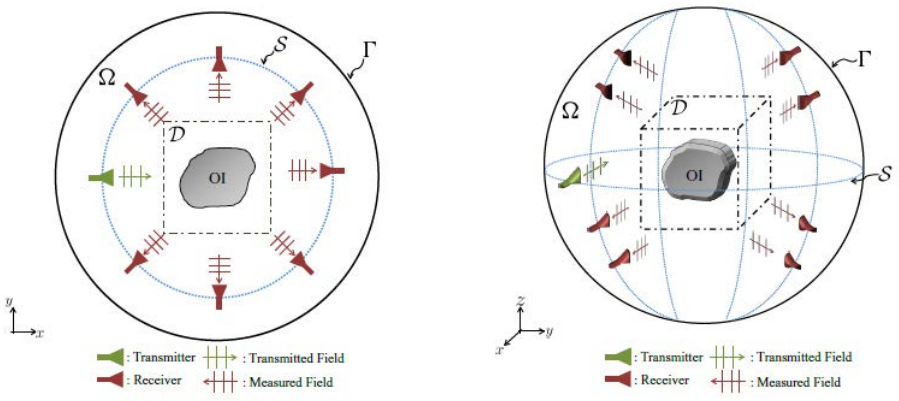

(a) (b)

Figure 3.4: (a) 2D MWI model (b) 3D MWI model

As we work with synthetic data, it is also necessary to generate a possible 2D or 3D geometry that describe a certain scenario as the defined in last section. There are a lot of simulators that let us to create several surfaces or volumes. In our case, the software is called as GiD, obviously it is based on the FEM (more information on GiD website http://gid.cimne.upc.es/).

Finally, it is important to clarify that FEM represents a different way to compute the EM field than the traditional theory based on Green's function that is called as the Intregral Formulation, in [9] a deeply comparision between both methods is performed.

Chapter 4

The Finite Element Method

This chapter presents a finite element method modeling for Microwave Imaging tomography, due to the importance of FEM in this project it represents one of the main targets of study during this research work. We will talk about the basic concepts of this technique, possible applications for using this method, the requirements that the FEM design need to perform correct results, the elements used to build the possible meshing, the assembling matrix and obviously how FEM is used to solve the Forward Problem.
Furthermore other problems are solved such as the boundary-value problems (BVP) in 2D geometries for scalar and vector problems (3D), and scenarios where a certain type of structures called as Absorbing Boundary Conditions like Perfect Matched Layers (PMLs) are considered in the design and computational simulation. The finite element method to solve the Forward Problem has been implemented using MatLab and GiD programmes that are respectively a very popular mathemathical simulator based on matrix processing and a powerful structure designer and simulator using the finite element method.

4.1 FEM basic concepts

This section presents the basic principles of the finite element method (FEM), the first practical use for FEM began in the 1950s for aircraft design; however it's first use in electrical engineering was not until 1965 when Winslow used it to solve for the magnetic field on an irregular mesh [3]. The finite element method is a standard tool for solving differential equations in many disciplines, e.g., electromagnetics, solid and structural mechanics,fluid dynamics, acous-

tics, and thermal conduction. This section gives an introduction to the finite element method where Maxwell's equations are involved. Such problems usually involve a second-order differential equation of a single dependent variable that is subject to a set of boundary conditions as described in Chapter 2, these boundary conditions could be of the Dirichlet type, the Neumann type, or a mixed type.

Mainly, a 2D geometry is deeply described, so at the beggining a domain of the problem is a 2D geometry with an arbitrary shape. Thus, a correct discretization of the domain using the most appropriate shape of basic elements called the finite elements is necessary to obtain an accurate representation of the domain in the context of the FEM. A 3D geometry short description will be introduced in the chapter, describing vector problems and edge functions.

A good FEM scenario should perform the next major steps in a general finite element method applied to 2D geometry:

1. Discretization of the 2-D domain.
2. Derivation of the weak formulation of the governing differential equation.
3. Derivation of the element matrices and vectors.
4. Assembly of the global matrix system.
5. Imposition of boundary conditions.
6. Solution of the global matrix system.
7. Postprocessing of the results.

A very strong advantage of the FEM and the main reason why it is the favorite method in many branches of engineering, is its ability to deal with complex geometries. Typically, this is done using unstructured grids, which are commonly known as (unstructured) meshes. These meshes usually consist of triangles in 2D and tetrahedra in 3D, althoung other elements can be used to build the mesh. However, an important disadvantage of the FEM, compared to other methods, is that explicit formulas for updating the fields in time-domain simulations cannot be derived in the general case. Instead, a linear system of equations has to be solved in order to update the fields. Due to this, provided that the same number of cells are used for the two methods, the FEM requires more computer resources, both in terms of CPU time and memory.

4.2 Domain Discretization

An essential step in solving a problem using FEM, and perhaps the most important, is how the problem domain is defined. A certain region, Ω, is the target of analysis, to define correctly this surface or volume in 3D cases is necessary to discretize it, this means that the region Ω is divided to build a mesh of triangles or quadrilateral elements. This step of FEM is so important because the manner in which the domain is discretized will affect the computer storage requirements, the computation time and the accuracy of numerical results.

Basically, dicretize the domain problem is based on the next process, the total domain Ω is divided in a certain number of subdomains that are known as elements and denoted as $\Omega^e = 1, 2, 3, ..., M$ where M is the number of elements, the type of elements used to design and build the mesh depend on the type of geometry that we want to discretize, in one-dimensional cases the elements are curved or straight lines that connect two different nodes. In 2D geometries the commonly elements are the triangles or quadrilaterals as squares, but the triangular elements are the most important geometry for 2D cases because unlike squares, the triangular elements can be used for more complex geometries, where they can model curved boundaries easily and the squares can't present accuracy in results, this means that the discrezitation error is smaller using triangles, we can observe what is the discretization error in Fig.4.2 [4]. In a 3D solution, the domain may be subdivided into tetrahedra, triangular prisms or rectangular bricks. In Fig.4.1 the different possibilities for dividing a total domain are shown, the image has been extrated from [2]

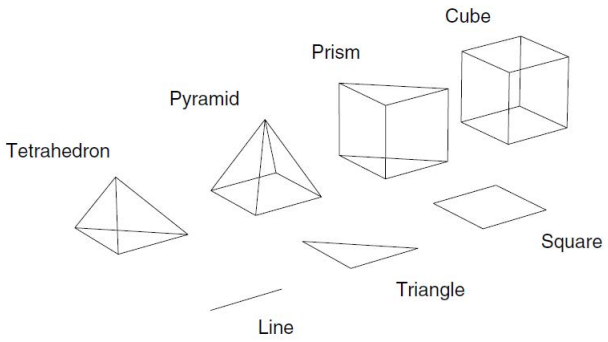

Figure 4.1: Different elements to discretize a certain 1D, 2D or 3D geometry

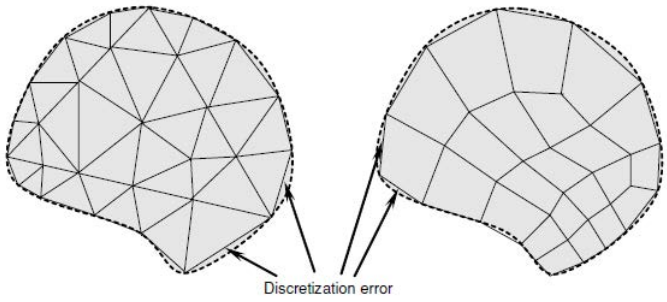

Figure 4.2: Discretization error obtained using triangular or quadrilateral elements

Two-dimensional geometries is the main target of the different possibilities in this project, we will divide the total domain Ω into triangular elements that should present the next properties, (i) within the domain, the elements must not overlap and must have no gaps between them. The triangles are interconnected, and sharing nodes and edges, (ii) they should be as close to equilateral triangles as possible and (iii) their size should be defined as a function of the local wavelength and the gradient of the solution. Due to the third condition appears an adapted mesh to discretize Ω, the number of subelemets is different in each region depending of the variability, so if the solution gradient is expected to be high at a certain region of Ω, the density will be higher in that region.

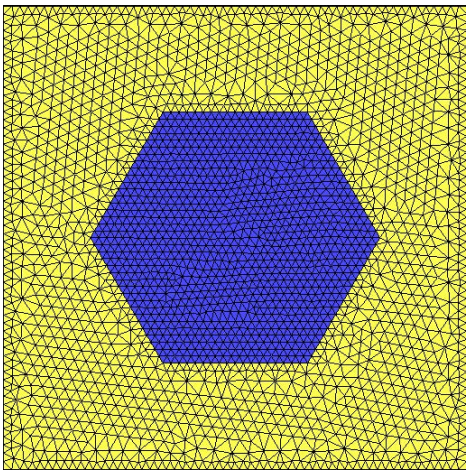

Figure 4.3: 2D geometry based on two different regions

In Fig.4.3 a possible adapted mesh method is presented, there is a square surface formed by two regions, these regions are different because their dielectric properties are not equal, so the

size of triangular elements are also different in each region because the size is proportional to the wavelength, normally, to obtain good results is necessary to implement a edge size smaller than $\lambda_g/15$ where $\lambda_g = \frac{\lambda_o}{\sqrt{\epsilon_r \mu_r}}$. We can observe how in regions with more variability the density of elements is higher.

4.3 Basis Functions

The finite element method lets us to compute the electromagnetic field for a given spatial domain using certain functions called as *Basis Functions*, they link the electromagnetic properties with the physical behaviour of the computational domain. Thanks to basis functions is possible to solve the matrix equation described in Chapter 3 given by

$$\underline{\underline{A}} \cdot \underline{x} = \underline{b} \tag{4.1}$$

during this research work we approximate the electromagnetic field solving (4.1) using

$$\mathbf{E} \cong \sum_i e_i \mathbf{W_i} \tag{4.2}$$

where e_i are the electromagnetic coefficients and $\mathbf{W_i}$ are the basis funtions.

In this MWI application there are two different types of problems that can be analysed, scalar and vector problems depending on the number of variables that are involved in the computation. Obviously, the type of basis functions will be different for each of the two problems. They are called as *Nodal Basis Functions* and *Edge Basis Functions*. In this section the two kinds of basis functions are described and related with scalar or vector equations, including the advantages or disadvantages that they could present. As discussed in Chapter 3, we consider the case of a TM and z-polarization wave, then our problem is based on scalar problems, it's important to note that despite analyze the particular case of a TM and z-polarization wave during this research work, the other type of basis functions used for vector problems have been implemented to understand better their benefits.

4.3.1 Nodal Basis Funtions

The local basis functions are denoted by $\varphi_i^e(x, y)$, where the superindex labels the element (e = 1,..., Ne) and the subindex the local node number (i = 1, 2, 3). There is one local basis function associated with each node of the element, in our case each triangle is defined by three nodes as depicted Fig 4.4. After the mesh is created, the unknown variable u (represents the electromagnetic field) is approximated within each triangular element.

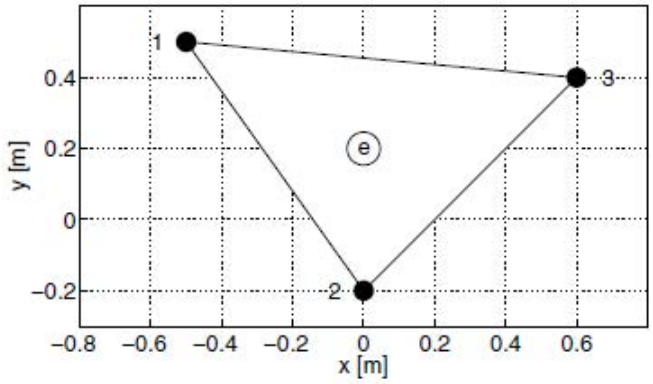

Figure 4.4: The numbering of local nodes for the element e.

Each node in the mesh is associated with two labels: a local number to indicate its location in a given triangle and a global number to indicate its location relative to the entire mesh. Notice that nodes are locally numbered in a counter-clockwise direction to avoid negative areas. Within a triangular element e, the unknown variable is given by

$$u^e(x, y) = \sum_{i=1}^{3} u_i^e \varphi_i^e(x, y) \tag{4.3}$$

The basis functions have the following properties:

- Inside each element, they are linear in x and y,

$$\varphi_i^e(x, y) = \frac{1}{2A^e} \left(a_i^e + b_i^e x + c_i^e y\right) \tag{4.4}$$

- They equal unity on one node and vanish on the others:

$$\varphi_i^e \left(x_i^e, y_i^e\right) = 1, \quad \varphi_i^e \left(x_j^e, y_j^e\right) = 0, \forall i \neq j \tag{4.5}$$

Now we divide the element e into three triangles as shown in Fig.4.5. While, A^e is the area of the triangular element, A_i^e is the area of the subtriangle i defined in (A.35), then $A^e = A_1^e + A_2^e + A_3^e$

The basis functions $\varphi_i^e(x, y)$ can be formulated by means of the area coordinates A_i^e as

$$\varphi_i^e(x,y) = \frac{A_i^e}{A^e} = \frac{1}{2A^e}\left[\hat{z}\left(\vec{r}_{i-1}^{\,e} - \vec{r}_{i+1}^{\,e}\right) \times \left(\vec{r} - \vec{r}_{i+1}^{\,e}\right)\right] \tag{4.6}$$

Expression (4.6) is equal to (4.4), for example assuming $i = 1$

$$\varphi_1^e(x,y) = \frac{1}{2A^e}\left[(x_2^e y_3^e - y_2^e x_3^e) + (y_2^e - y_3^e)\,x + (x_3^e - x_2^e)\,y\right] \tag{4.7}$$

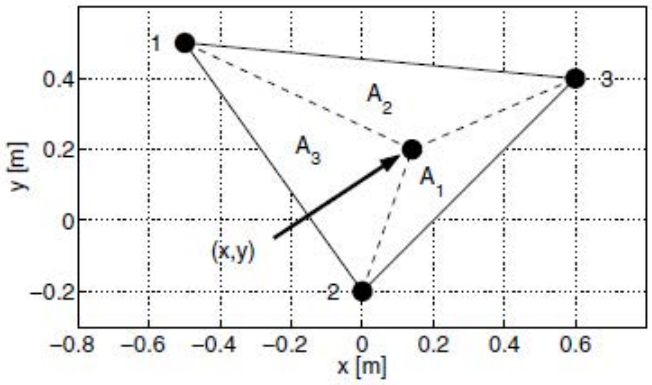

Figure 4.5: Triangular element divided into three sub-triangles.

it is clear that comparing the two expressions for $i = 1$ that

$$a_1^e = x_2^e y_3^e - y_2^e x_3^e \tag{4.8}$$

$$b_1^e = y_2^e - y_3^e \tag{4.9}$$

$$c_1^e = x_3^e - x_2^e \tag{4.10}$$

Using Nodal Basis Functions we can assemble the FEM matrix adding each of the contributions of each element, notice that is essential to relate the local index of each node with the global index of nodes in the global matrix. However, it turns out that such an approach leads to nonphysical solutions, referred to as spurious modes for vector problems, this situation can be solved using other type of basis functions known as Edge Basis Functions.

Tabla 4.1: Edge Numbering for a Triangular Element

Edge No.i	Node i_1	Node i_2
1	1	2
2	2	3
3	3	1

4.3.2 Edge Basis Functions

For solving vectorial problems using FEM, the use of nodal-based elements exhibits shortcomings as spurious solutions, fortunately, a revolutionary approach was discovered. This approach uses so-called vector basis or vector elements that assign degrees of freedom to the edges rather than to the nodes of the elements. Edge elements eliminate spurious modes that can introduce errors in field calculations for near-field problems. In this section we introduce edge elements in two dimensions. Thanks to edge elements the electric field in each triangular element can be approximated by the next expression:

$$\vec{E^e}(\vec{r}) = \sum_{j=1}^{3} E_j^e \vec{N}_j^e(\vec{r}) \tag{4.11}$$

where E_j^e denotes the tangential field along the jth edge.

The nodes of the triangular element are joined together by three edges. Each edge in the mesh is identified with two labels: a local number to indicate its location in a given triangle and a global number to indicate its location with respect to the entire mesh. Each edge of the triangle is associated with a vector-basis function:

$$\vec{N}_j^e(\vec{r}) = l_i^e \left(\varphi_{i_1}^e \vec{r} \nabla \varphi_{i_2}^e \vec{r} - \varphi_{i_2}^e \vec{r} \nabla \varphi_{i_1}^e \vec{r}\right) \tag{4.12}$$

where l_i^e denotes the length od the edge i, $\varphi_{i_1}^e \vec{r}$ and $\varphi_{i_2}^e \vec{r}$ are the nodal basis functions described in expression (4.4) of each node that forms edge e.

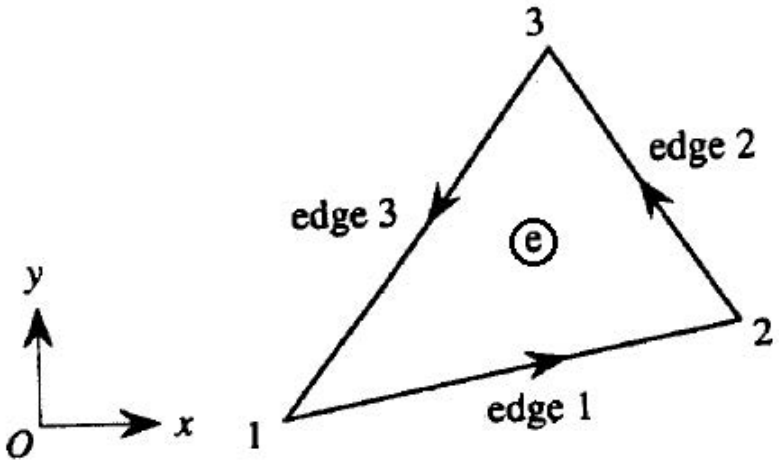

Figure 4.6: Triangular edge element.

4.4 Scalar Problems

Once the finite element method has been described is necessary to introduce the method to solve possible problems, in Chapter 2 scalar and vector wave equations were commented. Now we develop FEM for two-dimensional scenarios in electromagnetics that are defined by scalar problems, basically a scalar problem is represented by a variable wich must be measured, for example, a TM z-polarization case. This section is focus on TM, z-polarization and two-dimensional case that are the main characteristics that define our stage in this research work. In Chapter 2 the boundary conditions in electromagnetic theory were also presented, here introducing these concepts in scalar equations the Boundary-Value Problem arises in our approach, a particular method called as Garlerkin's method is deeply described to solve scalar problems and obviously how nodal basis functions are used in these applicatios. In conlusion, during this section FEM formulation based on processing matrix equations is used to solve scalar problems

4.4.1 2D Boundary-Value Problem

In Section 2.4 a second-order PDE that defines scalar problems was introduced, expresion (2.22) was named as *inhomogeneous scalar wave equation*, now we analyse it for 2D geometries. It is important to notice that MWI applications are focused on PEC enclosure, this means that BC must be considered during the performed formulation and computation using the finite element method. Then some boundary conditions are involved in this second-order PDE to define

correctly the scalar problem of our application, in 2D geometry this approach is known as 2D Boundary-Value Problem (BVP). These new conditions must be considered in order to implement with accuracy the formulation that will determine the assembling process, so the boundary-value problem under consideration is defined by the next second order differential equation

$$-\nabla \cdot (\alpha \nabla u) + \beta u = g \tag{4.13}$$

and the boundary conditions

$$u = p \qquad on\ \ \Gamma_1 \tag{4.14}$$

$$\hat{n} \cdot (\alpha \nabla u) + \gamma u = q \qquad on\ \ \Gamma_2 \tag{4.15}$$

where u is the unknown function, α and β are the known parameters associated with the physical propoperties of the domain Ω, and g is the source or excitation function. According to boundary conditions, Γ_1 defines the Dirichlet boundary while Γ_2 refers to the Robin boundary, with $\Gamma_1 + \Gamma_2 = \Gamma$, Γ denotes the contour enclosing the area Ω. γ, p and q are the knwon parameters associated with the physical propperties of the boundary, when $\gamma = 0$ the Robin BC is a special case called as Neumman boundary.

As we explained in Section 2.4, in scalar problems we assume that the fields has not variation with respect to one Cartesian coordinate, for example z coordinate. Our problem depends only on one variable, this is the case of TM and z-polaraization wave, so the expression (4.13) can be written as given in (2.22).

4.4.2 Solving BVP via Garlerkin's Method

The generic 2D BVP considered in expression (4.13) in this section could be expressed by a second-order partial differential equation given by

$$\frac{\partial}{\partial x}\left(\alpha_x \frac{\partial u}{\partial x}\right) + \frac{\partial}{\partial y}\left(\alpha_y \frac{\partial u}{\partial y}\right) + \beta u = g \tag{4.16}$$

and the boundary conditions

$$u = p \qquad on\ \ \Gamma_1 \tag{4.17}$$

$$\left(\alpha_x \frac{\partial u}{\partial x} \cdot \hat{x} + \alpha_y \frac{\partial u}{\partial y} \cdot \hat{y}\right) \cdot \hat{n} + \gamma u = q \qquad on\ \ \Gamma_2 \tag{4.18}$$

where α_x, α_y and β are constants. The weak formulation of this problem can be obtained by first constructing the weighted residual of (4.16) for a single element with domain Ω^e

$$r^e = \frac{\partial}{\partial x}\left(\alpha_x \frac{\partial u}{\partial x}\right) + \frac{\partial}{\partial y}\left(\alpha_y \frac{\partial u}{\partial y}\right) + \beta u - g \tag{4.19}$$

This element residual is ideally zero, provided that the numerical solution u to be obtained is identical to the exact solution. However, this is not the case, and therefore, the element residual r^e is, in general, nonzero. Our objective is to minimize this element residual in a weighted sense. To achieve this, we must first multiply r^e with a weight function w, then integrate the result over the area of the element, and finally, set the integral to zero.

$$\int\int_{\Omega_e} w\left[\frac{\partial}{\partial x}\left(\alpha_x \frac{\partial u}{\partial x}\right) + \frac{\partial}{\partial y}\left(\alpha_y \frac{\partial u}{\partial y}\right) + \beta u - g\right] dxdy = 0 \tag{4.20}$$

A new formulation called as *The Variational Formulation* is introduced to develop the mathematical expression (4.20), this new formulations is given by the next identities

$$\frac{\partial}{\partial x}\left(w\alpha_x \frac{\partial u}{\partial x}\right) = \frac{\partial w}{\partial x}\left(\alpha_x \frac{\partial u}{\partial x}\right) + w\frac{\partial}{\partial x}\left(\alpha_x \frac{\partial u}{\partial x}\right) \tag{4.21}$$

rearranging the identity as

$$w\frac{\partial}{\partial x}\left(\alpha_x \frac{\partial u}{\partial x}\right) = \frac{\partial}{\partial x}\left(w\alpha_x \frac{\partial u}{\partial x}\right) - \frac{\partial w}{\partial x}\left(\alpha_x \frac{\partial u}{\partial x}\right) = \frac{\partial}{\partial x}\left(w\alpha_x \frac{\partial u}{\partial x}\right) - \alpha_x \frac{\partial w}{\partial x}\frac{\partial u}{\partial x} \tag{4.22}$$

obviously with the term relationed to α_y in integral (4.20) occurs the same that with α_x, substituting expression (4.22) into (4.20) results

$$\int\int_{\Omega_e}\left[\frac{\partial}{\partial x}\left(w\alpha_x\frac{\partial u}{\partial x}\right)+\frac{\partial}{\partial y}\left(w\alpha_y\frac{\partial u}{\partial y}\right)\right]dxdy-\int\int_{\Omega_e}\left[\alpha_x\frac{\partial w}{\partial x}\frac{\partial u}{\partial x}+\alpha_y\frac{\partial w}{\partial y}\frac{\partial u}{\partial y}\right]dxdy \\ +\int\int_{\Omega_e}\beta\,w\,u\,dxdy=\int\int_{\Omega_e}w\,g\,dxdy \tag{4.23}$$

using the divergence theorem

$$\int\int_{\Omega_e}\left(\nabla\cdot\vec{A}\right)dA=\oint_{\Gamma^e}\vec{A}\cdot\hat{a_n}\,dl \tag{4.24}$$

that means

$$\int\int_{\Omega_e}\left(\frac{\partial A_x}{\partial x}+\frac{\partial A_y}{\partial y}\right)dxdy=\oint_{\Gamma^e}(\hat{a_x}A_x+\hat{a_y}A_y)\cdot\hat{a_n}\,dl \tag{4.25}$$

and applying the divergence theorem to the first integral of expression (4.23), results to

$$\int\int_{\Omega_e}\left[\frac{\partial}{\partial x}\left(w\alpha_x\frac{\partial u}{\partial x}\right)+\frac{\partial}{\partial y}\left(w\alpha_y\frac{\partial u}{\partial y}\right)\right]dxdy=\oint_{\Gamma^e}w\left(\alpha_x\frac{\partial u}{\partial x}\hat{x}+\alpha_y\frac{\partial u}{\partial y}\hat{y}\right)dl \tag{4.26}$$

Substituting this expression into (4.23), the weak form of the differential equation reduces to

$$-\int\int_{\Omega_e}\left[\alpha_x\frac{\partial w}{\partial x}\frac{\partial u}{\partial x}+\alpha_y\frac{\partial w}{\partial y}\frac{\partial u}{\partial y}\right]dxdy+\int\int_{\Omega_e}\beta\,w\,u\,dxdy=\int\int_{\Omega_e}w\,g\,dxdy \\ -\oint_{\Gamma^e}w\left(\alpha_x\frac{\partial u}{\partial x}\hat{x}+\alpha_y\frac{\partial u}{\partial y}\hat{y}\right)dl \tag{4.27}$$

According to the Garlerkin approach, the weight function w must be relationed to the same set of shape functions that are used to interpolate the main unknown, u. This unknown is interpolated using a set of Lagrange polynomials as in (4.3). Thus,

$$u=\sum_{j=1}^{n}u_j^eN_j \tag{4.28}$$

where N_j is the corresponding shape functions based on nodal elements (in expression (4.3) is denoted as $\varphi_i^e(x,y)$) and n is the total number of nodes that form the element domain Ω_e. Imposing $w = N_i$ with $i = 1, 2, 3...N_e$ and substituting into (4.27)

$$\begin{aligned} &-\int\int_{\Omega_e}\left[\alpha_x\left(\frac{\partial N_i}{\partial x}\right)\left(\sum_{j=1}^{N_e}u_j^e\frac{\partial N_j}{\partial x}\right)+\alpha_y\left(\frac{\partial N_i}{\partial y}\right)\left(\sum_{j=1}^{N_e}u_j^e\frac{\partial N_j}{\partial y}\right)\right]dxdy \\ &+\int\int_{\Omega_e}\beta\,N_i\left(\sum_{j=1}^{N_e}u_j^eN_j\right)dxdy=\int\int_{\Omega_e}N_i\,g\,dxdy-\oint_{\Gamma^e}N_i\left(\alpha_x\frac{\partial u}{\partial x}\hat{x}+\alpha_y\frac{\partial u}{\partial y}\hat{y}\right)dl, \\ &for\ \ i=1,2,3...N_e \end{aligned} \tag{4.29}$$

Notice that the primary unknown u in the contour integral of (4.29) has not been replaced by interpolation functions given by (4.28), this integral will be treated separately. Equation (4.29) can be expressed in a matrix form given by

$$\begin{bmatrix} M_{11}^e & M_{12}^e & \cdots & M_{1n}^e \\ M_{21}^e & M_{22}^e & \cdots & M_{2n}^e \\ \vdots & \vdots & \ddots & \vdots \\ M_{n1}^e & M_{n2}^e & \cdots & M_{nn}^e \end{bmatrix}\begin{Bmatrix} u_1^e \\ u_2^e \\ \vdots \\ u_n^e \end{Bmatrix}+\begin{bmatrix} T_{11}^e & T_{12}^e & \cdots & T_{1n}^e \\ T_{21}^e & T_{22}^e & \cdots & T_{2n}^e \\ \vdots & \vdots & \ddots & \vdots \\ T_{n1}^e & T_{n2}^e & \cdots & T_{nn}^e \end{bmatrix}\begin{Bmatrix} u_1^e \\ u_2^e \\ \vdots \\ u_n^e \end{Bmatrix}=\begin{Bmatrix} f_1^e \\ f_2^e \\ \vdots \\ f_n^e \end{Bmatrix}+\begin{Bmatrix} p_1^e \\ p_2^e \\ \vdots \\ p_n^e \end{Bmatrix} \tag{4.30}$$

where

$$M_{ij}^e=-\int\int_{\Omega_e}\left[\alpha_x\left(\frac{\partial N_i}{\partial x}\right)\left(\frac{\partial N_j}{\partial x}\right)+\alpha_y\left(\frac{\partial N_i}{\partial y}\right)\left(\frac{\partial N_j}{\partial y}\right)\right]dxdy \tag{4.31}$$

$$T_{ij}^e=\int\int_{\Omega_e}\beta\,N_i\,N_j\,dxdy \tag{4.32}$$

$$f_i^e=\int\int_{\Omega_e}N_i\,g\,dxdy \tag{4.33}$$

$$p_i^e=-\oint_{\Gamma^e}N_i\left(\alpha_x\frac{\partial u}{\partial x}\hat{x}+\alpha_y\frac{\partial u}{\partial y}\hat{y}\right)dl \tag{4.34}$$

Is possible to implement a more compact matrix system,

$$\begin{bmatrix} K_{11}^e & K_{12}^e & \cdots & K_{1n}^e \\ K_{21}^e & K_{22}^e & \cdots & K_{2n}^e \\ \vdots & \vdots & \ddots & \vdots \\ K_{n1}^e & K_{n2}^e & \cdots & K_{nn}^e \end{bmatrix} \begin{Bmatrix} u_1^e \\ u_2^e \\ \vdots \\ u_n^e \end{Bmatrix} = \begin{Bmatrix} b_1^e \\ b_2^e \\ \vdots \\ b_n^e \end{Bmatrix} \tag{4.35}$$

where

$$\begin{aligned} K_{ij}^e &= M_{ij}^e + T_{ij}^e \\ b_i^e &= f_i^e + p_i^e \end{aligned} \tag{4.36}$$

Matrix $\mathbf{K^e}$ is the FEM Matrix in each element. FEM Matrix is based on the basis functions that our method is using to represent the corresponding contribution and its relation respect the electromagnetic field. To assemble the FEM Matrix is neccesary to sum Stiffness Matrix (4.31) and Mass Matrix Matrix (4.32), on one hand $\mathbf{M^e}$ depends on the boundary conditions of the domain, and on the other hand $\mathbf{T^e}$ depends on the dielectric properties of the element domain Ω_e.

The contour integral in (4.34) must be evaluated along the closed boundary of each element in the domain, imagine that the finite element mesh is based on triangular elements, in this case the contour integral should be evaluated along the three edges of each triangle in a counter-clockwise direction. However, it is important to realize that a nonboundary edge belongs to two neighboring triangles, as shown in Fig.4.7(a). Evaluating the line integral in (4.34) for element e_1 in Fig.4.7(b) along the edge from node 1 to node 2 is exactly the same result but opposite sign than evaluating the same line integral for element e_2 along the edge from node 3 to node 1.

The opposite sign stems from the fact that the unit vector normal of the common edge point in opposite directions.

$$\hat{a}_{n1} = -\hat{a}_{n2} \tag{4.37}$$

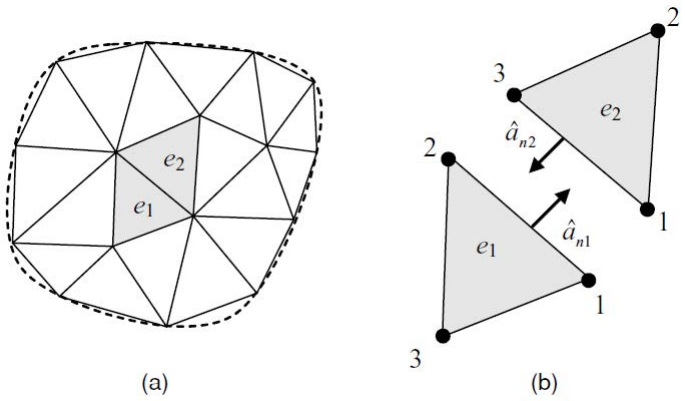

Figure 4.7: (a) Interior edge shared by two neighboring triangles. (b) The outward unit vectors normal to the common edge point in opposite directions

To give an example, we compute the contribution to the global entry of the vector $\vec{p}$ by local node 1 of element e_1 and local node 1 of element e_2, as the integration in (4.34) is evaluated along the common edge to the two triangles: the contribution to the global entry by local node 2 of element e_1 and local node 3 of element e_2 is also evaluated.

$$p_{1-1} = -\int_{1\to 2} N_1^{(e_1)} \left(\alpha_x \frac{\partial u}{\partial x} \hat{x}^{(e_1)} + \alpha_y \frac{\partial u}{\partial y} \hat{y}_{(e_1)} \right) dl - \int_{3\to 1} N_1^{(e_2)} \left(\alpha_x \frac{\partial u}{\partial x} \hat{x}^{(e_2)} + \alpha_y \frac{\partial u}{\partial y} \hat{y}_{(e_2)} \right) dl \tag{4.38}$$

$$p_{2-3} = -\int_{1\to 2} N_2^{(e_1)} \left(\alpha_x \frac{\partial u}{\partial x} \hat{x}^{(e_1)} + \alpha_y \frac{\partial u}{\partial y} \hat{y}_{(e_1)} \right) dl - \int_{3\to 1} N_3^{(e_2)} \left(\alpha_x \frac{\partial u}{\partial x} \hat{x}^{(e_2)} + \alpha_y \frac{\partial u}{\partial y} \hat{y}_{(e_2)} \right) dl \tag{4.39}$$

Substituting (4.37) in the expressions above, and using the fact that

$$N_1^{(e_1)} = N_1^{(e_1)} \wedge N_2^{(e_1)} = N_3^{(e_2)} \tag{4.40}$$

along the path of integration, it is evident that the two integrals cancel each other out. Consequently, the contribution of the line integral in (4.34) to the global right-hand-sive vector

$\vec{p}$ is zero for all interior edges. It is nonzero for edges that belong to the domain boundary Γ. For boundary edges that belong to Γ_1, where a Dirichlet boundary condition is to be imposed, the contribution of the line integral in (4.34) will be discarded. Thus, the only contribution of the line integral (4.34) is attributed only to boundary edges that reside on Γ_2.

Substituting the boundary condition in expression (4.15) into (4.34), the line integral becomes

$$p_i^e = -\int_{\Gamma_2} N_i \left(q - \gamma\, u\right) dl \tag{4.41}$$

The line integral in (4.41) exists only for boundary elements, it must be evaluated only along boundary edges that reside on Γ_2. For interior edges, as commented before, the contribution is zero.

4.5 Vector Problems

In this section vector problems are briefly described, due to scalar problems define our application they represent most of this research work, nevertheless we consider that it is important to develop vector theory in electromagnetics. While scalar problems are defined by a single magnitude, vector equations describe the behaviour of two or more variables. In Section 2.3 the Helmholtz Equations was introduced for electric fields, now we use that formulation as the curl-curl equation of electromagnetics.

4.5.1 The Curl-Curl Equation And Edge Elements

To deal with vector quantities, such as the electric field, a first attempt might be to expand each vector component separately in nodal basis functions. It turns out that such an approach leads to nonphysical solutions, referred to as spurious modes. This can be avoided by using edge elements (Section 4.3.2), which are very well suited for approximating electromagnetic fields. The electromagnetic field is introduced as Helmholtz equation, performing a particular partial equation that is known as the curl-curl equation for $\vec{E}$ field.

$$\nabla \times \left(\mu^{-1} \nabla \times \vec{E}(\vec{r})\right) - \left(w^2 \epsilon' - jw\sigma\right) \vec{E}(\vec{r}) = -jw\vec{J}_s(\vec{r}) \qquad on\ \ S \tag{4.42}$$

and the boundary conditions

$$\hat{n} \times \vec{E}(\vec{r}) = \vec{p}(\vec{r}) \qquad on\ \ \Gamma_1 \tag{4.43}$$

$$\hat{n} \times (\mu^{-1} \nabla \times \vec{E}(\vec{r})) + \gamma(\vec{r}) \hat{n} \times (\hat{n} \times \vec{E}(\vec{r})) = \vec{q}(\vec{r}) \qquad on\ \ \Gamma_2 \tag{4.44}$$

The next step is to follow the Garlerkin's method developed during the last section, introducing the test or weigthed function into the residual expression and using the edge basis functions, the integral weak form is given by

$$\begin{aligned} &\int_S \left[\mu^{-1} \left(\nabla \times \vec{W}_i\right) \cdot \left(\nabla \times \vec{E}\right) - \left(w^2 \epsilon' - jw\sigma\right) \vec{W}_i \cdot \vec{E}\right] dS \\ &+ \int_{\Gamma_2} \vec{W}_i \cdot \left(\vec{q} - \gamma \hat{n} \times \hat{n} \times \vec{E}\right) dl = -jw \int_S \vec{W}_i \cdot \vec{J}_s \, dS \end{aligned} \tag{4.45}$$

We expand the solution $\vec{E}(\vec{r})$ in terms of the basis functions, the edges are labeled by integers 1, 2,..., Ne.

$$\vec{E}(\vec{r}) = \sum_{j=1}^{N_e} E_j \mathbf{N_j} \tag{4.46}$$

where E_j is the tangential electric field along the jth edge, choosing $\vec{W}_i = \mathbf{N_i}$ and substituting in (4.45) we obtain a linear system of equations $\mathbf{Az} = \mathbf{b}$ with

$$\begin{aligned} A_{ij} = &\int_S \left[\mu^{-1} \left(\nabla \times \mathbf{N_i}\right) \cdot \left(\nabla \times \mathbf{N_j}\right) - \left(w^2 \epsilon' - jw\sigma\right) \mathbf{N_i} \cdot \mathbf{N_j}\right] dS \\ &+ \int_{\Gamma_2} \gamma \left(\hat{n} \times \mathbf{N_i}\right) \cdot \left(\hat{n} \times \mathbf{N_j}\right) dl \end{aligned} \tag{4.47}$$

$$z_j = E_j \tag{4.48}$$

$$b_i = -jw \int_S \mathbf{N_i} \cdot \mathbf{J_s} \, dS - \int_{\Gamma_2} \mathbf{N_i} \cdot \mathbf{q} \, dl \tag{4.49}$$

Notice that during this section we refer to ϵ' as the real part of the permittivity, assuming that $\epsilon = \epsilon' + j\epsilon'' = \epsilon_o \epsilon_r = \epsilon_o \left(\epsilon'_r + j\epsilon''_r\right)$.

4.6 Absorbing Boundary Conditions

Most of the scattering problems described during this research work are solved on a part of the physical space, reduced to a surface or a region of space, depending on the problem. However there are electromagnetic applications that happen in free-space, consider for instance two typical problems of numerical electromagnetics, first the calculation of the radiation pattern of an antenna, second the interaction of an incident wave with a scattering structure. In both cases the radiated field propagates toward the free space surrounding the structure of interest; in other words the physical boundary conditions should be placed at infinity.

In Section 4.1 (FEM Concepts) we saw that the main disadvantage of the finite element method is the computational requirements to solve the linear system of equations because FEM requires more computer resources than other forward methods, both in terms of CPU time and memory, then when solving open-region scattering/radiation problem using the FEM, the infinite region exterior to the scatterer/radiator must be truncated with an artificial boundary to limit the size of the computational domain. Consequently, a boundary condition must be introduced at this artificial boundary for an unique finite solution. Boundary should appears as transparent as possible to the scattered/radiated field, this means that the nonphysical reflections from the boundary must be minimized, this field of study is called as Absorbing Boundary Conditions (ABCs).

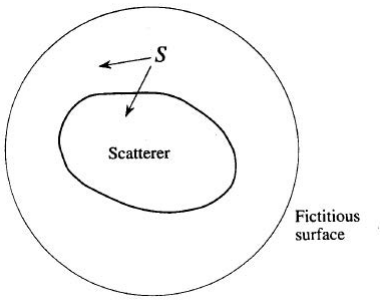

Figure 4.8: Fictitious Boundary

The ABCs simulate or replace the infinite space that surrounds a finite computational domain. The replacement is never perfect, so the solution computed within an ABC is only an estimate to the solution that would be computed within a really infinite domain.

In this section of the chapter, we discuss the properties and the corresponding implementation of ABC for 2D scattering and antenna applications in free-space. Finally, we describe a new type of ABC called as the Perfectly Matched Layer (PML). Some properties that absorbing boundary conditions should present are:

1. An ABC placed as close as possible to the structure is needed so as to replace the infinite free space and allow the overall domain to be as small as possible. This permits the computational resources to be devoted to the use of a discretization of the structure as fine as possible.

2. Changes in real scenario induced by the ABC must be almost negligible due to the request of obtain simulated results as similar as possible.

3. If the ABC is only able to absorb homogeneous plane waves, itmust be placed out of the evanescent region surrounding the source (antenna, scattering structure, waveguide).

4. If the ABC is able to absorb evanescent fields, it can be placed close to the source, in the evanescent region. In that case, the overall computational domain is significantly smaller.

In [1] some ABC formulation is described, they are based on using nth-order Taylor approximation, depending on the order used, the implementations is easier or more difficult. Basically, a reflection coefficient curve is presented, where if the order is bigger, the approximation will be better, it's known that for a certain angle of wave incidence the reflection is the lowest, so these type of ABCs are implemented to obtain the minimum reflection for the anlge of incidende of the wave that the ficticious layer should absorb. However, these ABCs present a disadvantage, they only work for a single wave frequency, as a result, they can not be applied to a wide frequency band without redesign. This problem was solved in 1994 when Berenger [5] proposed the concept of a perfectly matched layer (PML).

4.6.1 The Perfectly Matched Layer on 2D

A perfectly matched layer (PML) is an interface that does not reflect a plane wave for all frequencies and all angles of incidence and polarizations. The loss of the wave is in the direction normal to the interface. Obviously, PML also truncates the computational domain for numerical solutions of partial differential equations. We will describe the situation based on PML-medium,

a necessary condition to be a PML medium is called as the matching condition, the impedance of a plane wave in the medium equals the impedance in a vacuum.

$$\frac{\sigma}{\epsilon} = \frac{\sigma^*}{\mu} \tag{4.50}$$

where the wave impedance is

$$\eta = \frac{|\mathbf{E}|}{|\mathbf{H}|} = \sqrt{\frac{\mu}{\epsilon}} \tag{4.51}$$

which indicates that the stretching factors do not affect the wave impedance.
There are two different but equivalent formulations for PML approach, the first formulation is known as *derivation based on Coordinate Stretching*, where a new partial operator is introduced, ∇_s, it can be considered as the standard ∇ operator in Cartesian coordinates where x, y and z axes are stretched by a factor s_x, s_y and s_z (Stretching Coordinates). ∇_s is given by

$$\nabla_s = \hat{x}\frac{1}{s_x}\frac{\partial}{\partial x} + \hat{y}\frac{1}{s_y}\frac{\partial}{\partial y} + \hat{z}\frac{1}{s_z}\frac{\partial}{\partial z} \tag{4.52}$$

and we can define

$$\mathbf{k_s} = \hat{x}\frac{k_x}{s_x} + \hat{y}\frac{k_y}{s_y} + \hat{z}\frac{k_z}{s_z} \tag{4.53}$$

that gives the dispersion relation

$$\left(\frac{k_x}{s_x}\right)^2 + \left(\frac{k_y}{s_y}\right)^2 + \left(\frac{k_z}{s_z}\right)^2 = k^2 \tag{4.54}$$

The obvious solution to this equation is

$$k_x = ks_x sin\theta cos\varphi \tag{4.55}$$

$$k_y = ks_y sin\theta sin\varphi \tag{4.56}$$

$$k_z = ks_z cos\theta \tag{4.57}$$

and the new formulation that is called as modified Maxwell's equations can be expressed as

$$\nabla_s \times \vec{E}(\vec{r}) = -jw\mu\vec{H}(\vec{r}) \tag{4.58}$$

$$\nabla_s \times \vec{H}(\vec{r}) = jw\epsilon\vec{E}(\vec{r}) \tag{4.59}$$

where $\mu = \mu' + \frac{\sigma^*}{jw}$ and $\epsilon = \epsilon' + \frac{\sigma}{jw}$, σ^* is a nonphysical parameter that allows the absorption of the magnetic field to be symmetrized with respect to the absorption of the electric field. From now, 2D geometries are the considered scenarios during this section, let us define the stretching coordinates in 2D

$$s_x = 1 + \frac{\sigma_x}{jw\epsilon_o} \quad s_x^* = 1 + \frac{\sigma_x^*}{jw\mu_o} \tag{4.60}$$

$$s_y = 1 + \frac{\sigma_y}{jw\epsilon_o} \quad s_y^* = 1 + \frac{\sigma_y^*}{jw\mu_o} \tag{4.61}$$

Imagine a plane wave in a certain medium that incides against a PML interface (see Fig.4.9 and Fig.4.10) placed in y-axes, the plane of the scenario is the XY plane ($\theta = \frac{\pi}{2}$) and the medium is the vacuum, so it's characterized by ϵ_o and μ_o, to obtain the reflection coefficient we describe the incident and reflected wave equations

$$\mathbf{E^i} = \mathbf{E_0} e^{-j\mathbf{k^i}\cdot\mathbf{r}} = \mathbf{E_0} e^{-j(k_x x + k_y y)} \tag{4.62}$$

$$\mathbf{E^r} = R\mathbf{E_0} e^{-j\mathbf{k^r}\cdot\mathbf{r}} = \mathbf{E_0} e^{-j(-k_x x + k_y y)} \tag{4.63}$$

$$\mathbf{E^t} = T\mathbf{E_0} e^{-j\mathbf{k^t}\cdot\mathbf{r}} = \mathbf{E_0} e^{-j(k_x x + k_y y)} \tag{4.64}$$

where R and T are respectively, the reflection coefficient and the transmitter coefficient.

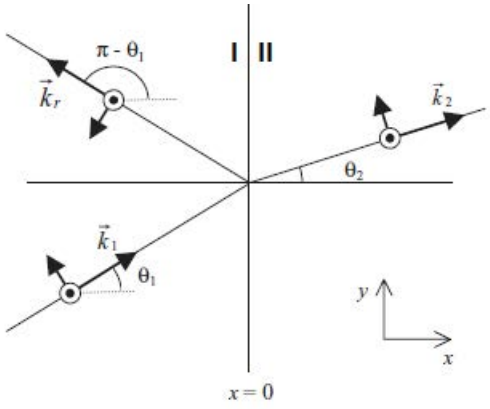

Figure 4.9: Incident, reflected and trasmitted waves

notice that instead of φ in figures appears θ altough both of them refer to the same angle in XY plane, so we will use also θ as denotation in formulation below.

From expressions (4.62) and (4.64) we can observe how $k_{y1} = k_{y2} = k_y$ and $k_{x1} = k_{x2} = k_x$ and it's possible to obtain from (4.54) the wavenumber as function as stretching coordinates,

$$\left(\frac{k_x}{s_x}\right)^2 + \left(\frac{k_y}{s_y}\right)^2 = k^2 = w^2\epsilon\mu \tag{4.65}$$

Realize that (4.65) is like its counterpart in a vacuum, with only k_x replaced with $k_x/\sqrt{s_x s_x^*}$ and k_y replaced with $k_y/\sqrt{s_y s_y^*}$. The following wave numbers satisfy (4.65):

$$k_x = \frac{w}{c}\sqrt{s_x s_x^*}cos\theta \tag{4.66}$$

$$k_y = \frac{w}{c}\sqrt{s_y s_y^*}sin\theta \tag{4.67}$$

Let verify that $k_{y1} = k_{y2} = k_y$,

$$\sqrt{s_{y1} s_{y1}^*}sin\theta_1 = \sqrt{s_{y2} s_{y2}^*}sin\theta_2 \tag{4.68}$$

Then, if $s_{y1} = s_{y2}$ and $s^*_{y1} = s^*_{y2}$, the transverse conductivities σ_y and σ^*_y will be equal, in this case like $\sigma_{y1} = \sigma_{y2} = 0$ the transverse stretching coordinates $s_{y1} = s_{y2} = 1$ (only real part). So to verify (4.68) is necessary that

$$\theta_1 = \theta_2 \tag{4.69}$$

From [5] we obtain the formulation for the reflection coefficient R,

$$R = \frac{\sqrt{\frac{s^*_{x2}}{s_{x2}}}cos\theta_2 - \sqrt{\frac{s^*_{x1}}{s_{x1}}}cos\theta_1}{\sqrt{\frac{s^*_{x2}}{s_{x2}}}cos\theta_2 + \sqrt{\frac{s^*_{x1}}{s_{x1}}}cos\theta_1} \tag{4.70}$$

Using identity (4.69), longitudinal stretching coordinates should be equal ($s_x = s^*_x$) if we need to obtain $R = 0$, that implies $\sigma_x = \sigma^*_x$.

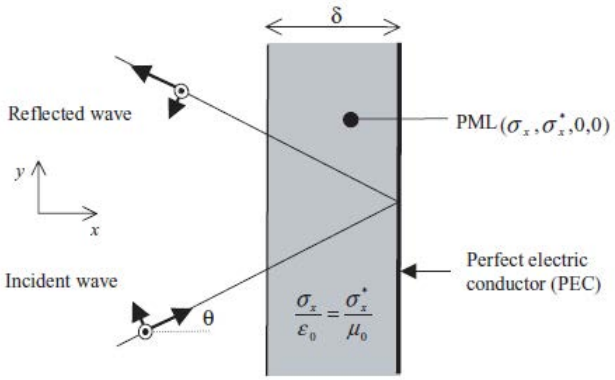

Figure 4.10: The PML ABC on a plane boundary

In conclusion, it's possible to remove reflections between medium-PML for all angle of incidence and for all frequencies, however, if the longitudinal stretching coordinates were not equal, the reflection coefficient would reduce to zero only for some frequencies. Obviously, at an interface between a vacuum and a PML is true $R = 0$ with $(\sigma_x, \sigma^*_x, 0, 0)$.

In actual problems solved by numerical methods, the boundary of the domain is not a plane, as in Fig.4.9, it's a concave surface enclosing a computational domain. The PML media allow such concave ABCs to be realized. This is depicted in Fig.4.11 where the ABC is composed of

various PML media in such a way that the reflection is zero from all the inner interfaces in the domain. This is the case at the vacuum and PML interfaces.

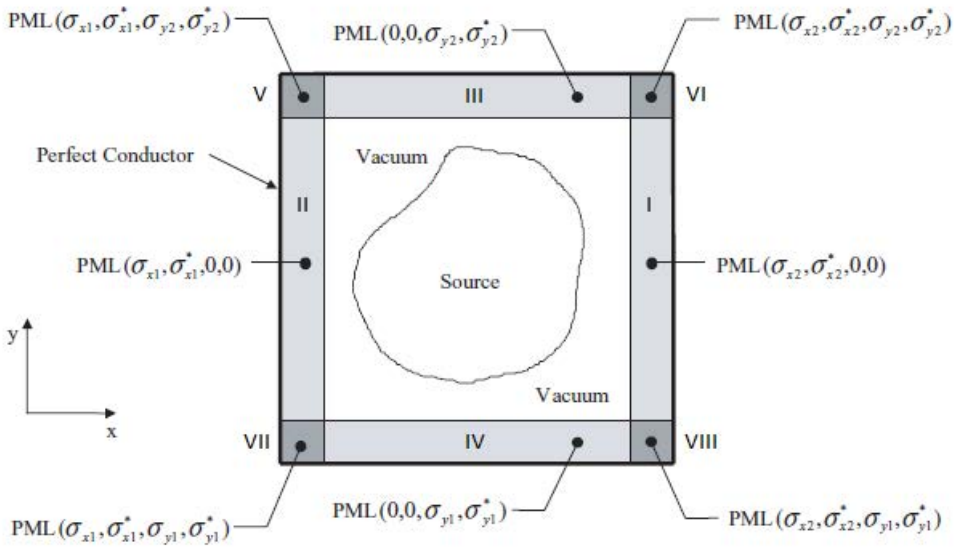

Figure 4.11: Concave surface enclosing the domain

There is a second way to describe the PML problem, it is known as *Anisotropic Formulation* which presents (4.58) and (4.59) as

$$\nabla \times \vec{E}(\vec{r}) = -jw\underline{\underline{\mu}}\vec{H}(\vec{r}) \tag{4.71}$$

$$\nabla \times \vec{H}(\vec{r}) = jw\underline{\underline{\epsilon}}\vec{E}(\vec{r}) \tag{4.72}$$

where

$$\underline{\underline{\epsilon}} = \begin{bmatrix} \epsilon_{xx} & 0 & 0 \\ 0 & \epsilon_{yy} & 0 \\ 0 & 0 & \epsilon_{zz} \end{bmatrix} \qquad \underline{\underline{\mu}} = \begin{bmatrix} \mu_{xx} & 0 & 0 \\ 0 & \mu_{yy} & 0 \\ 0 & 0 & \mu_{zz} \end{bmatrix} \tag{4.73}$$

and these tensors can be expressed as a function of stretching coordinates S_x, S_y and S_z like

$$\underline{\underline{\epsilon}} = \epsilon_o\epsilon_r\underline{\underline{\Lambda}} \qquad \underline{\underline{\mu}} = \mu_o\mu_r\mathbf{\Lambda} \tag{4.74}$$

where

$$\underline{\underline{\Lambda}} = \hat{x}\hat{x}\frac{s_y s_z}{s_x} + \hat{y}\hat{y}\frac{s_x s_z}{s_y} + \hat{z}\hat{z}\frac{s_x s_y}{s_z} \tag{4.75}$$

Now we consider a TM and z polarization, so the Helmholz equations is given by

$$\frac{\partial}{\partial x}\left(\frac{1}{\mu_{xx}}\frac{\partial E_z}{\partial x}\right) + \frac{\partial}{\partial y}\left(\frac{1}{\mu_{yy}}\frac{\partial E_z}{\partial y}\right) - k_o^2 \epsilon_{zz} E_z = -jw\mu_o J_z \tag{4.76}$$

Then, the tensors are defined by

$$\underline{\underline{\epsilon}} = \epsilon_o \epsilon_r s_x s_y \qquad \underline{\underline{\mu}} = \mu_o \mu_r \begin{bmatrix} s_y/s_x & 0 \\ 0 & s_x/s_y \end{bmatrix} \tag{4.77}$$

The next step is how to implement the longitudinal stretching coordinates in each of the possible vacuum and PML interfaces, there are several theories about this object of study. A possibility is given in [7], as the next form,

$$s_x(x) = s_o(x)\left[1 - j\frac{\sigma_x(x)}{w\epsilon'}\right] \qquad with\ \ \epsilon' = \epsilon_r' \epsilon_o \tag{4.78}$$

$$s_o(x) = 1 + s_m\left(\frac{\pi}{\delta}\right)^2 \tag{4.79}$$

$$\sigma_x(x) = sin^2\left(\frac{\pi x}{2\delta}\right) \tag{4.80}$$

where δ is the thickness of the absorber and s_m is a coefficient that depends on the wavelength. Other possibily is given by [1] as

$$s_x(x) = 1 - j\left(\frac{x-\delta}{\delta}\right)^2 \delta_{max} \tag{4.81}$$

$$\delta_{max} = \frac{\sigma_{max}}{w\epsilon_o} \quad or \quad \delta_{max} \approx w^{-1} \tag{4.82}$$

a good choice for the absorber thickness could be $\delta = \lambda/4$.

Finally, we analyze the practical case described in Fig.4.11 which has been implemented during this research work:

1. Region Ω. $s_x = s_x^* = 1 \wedge s_y = s_y^* = 1$
2. Region I. $s_x = (4.81) \wedge s_y = 1$
3. Region II. $s_x = (4.81) \wedge s_y = 1$
4. Region III. $s_x = 1 \wedge s_y = (4.81)$
5. Region IV. $s_x = 1 \wedge s_y = (4.81)$
6. Region V. $s_x = s_y = (4.81)$
7. Region VI. $s_x = s_y = (4.81)$
8. Region VII. $s_x = s_y = (4.81)$
9. Region VIII. $s_x = s_y = (4.81)$

4.7 Assembling FEM Matrix

In Chapter 3 we described how the Forward Problem can be solved measuring the electromagnetic field generated by a set of antennas using the finite element method, to obtain the coefficients that describe the electric field is necessary to solve the matrix equation presented in (3.2), it can be developed according to the formulation described in Section 4.4.2 for scalar problems using nodal basis functions or the formulation described in Section 4.5.1 for vector problems using edge elements. Both of them can be expressed as [1] explain,

$$\underline{\underline{K}}\,\underline{u} = \underline{b} \tag{4.83}$$

where K represents the *Global FEM Matrix*, u is the vector of electric coefficients and b is a vector called as right-hand side formed by the sum of vector f and p. First we analyse the assemble procedure related to nodal basis functions that represent the implementation of our application. In practice, the FEM matrix is computed by assembling contributions from all

elements, this means that compute the local FEM matrix for each element of the total domain Ω is necessary to implement the global matrix.

Matrix expression (4.35) is the general matrix equation for any type of elements used during the domain discretization, in our application the discretization is based on a triangular meshing, so the FEM matrix for a certain element will present the next form

$$K^e = \begin{bmatrix} K^e_{11} & K^e_{12} & K^e_{13} \\ K^e_{21} & K^e_{22} & K^e_{23} \\ K^e_{31} & K^e_{32} & K^e_{33} \end{bmatrix} \tag{4.84}$$

After the assembly of the local matrices, the global numbering scheme is used to build the global FEM matrices. The global matrix K is filled using the following scheme: the first local element $K^e_{i,i}$ in K^e is added to the ith row and the ith column of global matrix K, the second local element $K^e_{i,j}$ is added to the ith row and the jth column of global matrix K, and so on. This is repeated for each triangular element. Assembling contributions from all elements, we obtain

$$K_{ij} = \sum_{e=1}^{Ne} \int_{S_e} \left(\alpha \nabla \varphi^e_i \cdot \nabla \varphi^e_j + \beta \varphi^e_i \varphi^e_j \right) dS \tag{4.85}$$

In Appendix A.1 a detailed analytical evaluation of FEM matrix elements is given for triangular meshing based on nodal basis functions. A very important aspect about the implementation of FEM matrix is the concept of *sparse* matrix, as mentioned in Section 4.1 the main disadvantage of the finite element method against other methods is the cost of computation, sparse matrix is based on processing matrices on the way that only are stored the non-zero values of FEM matrix, this method let us to saves us a considerable cost of time and computation.

For vector problems where edge elements are involved to improve results the FEM matrix is defined by expression (4.47) with $\gamma = 0$. The assembling of Stiffness and Mass matrix is developed in Appendix A.2, formulation obtained in [1].

4.8 Simulations

Finally, this section presents several simulations based on 2D geometries, the purpose is to visualize the results of using FEM to compute the electric field. Due to scalar problems, the basis functions that define our method are the *Nodal Elements*. According to several combinations of current sources, a electric distribution is calculated. In addition, to understand the behaviour of the EM field, different material properties defined by the dielectric parameters will be considered.

4.8.1 Circular Enclosure

In this section we analyse simulations where the PEC enclosure is a circle, that is an essential factor due to wave reflections in PEC interface. The radius of the circular enclosure is equal to 0.1m. It is necessary to comprise that in real biomedical MWI applications, normally the target to analyse presents a "small" size assuming a common tumor. In addition, to minimize the computation cost of simulations is better to implement "small" scenarios. The purpose is to observe different results for different dielectric properties, frecuency and placement for current sources.

Firstly, several dielectric cases are computed with fixed frequency at 500MHz, an essential point, commented during Section 4.2, is the edge length that is implemented as a function of the wavelength, which means that for each permittivity case the number of elements in the corresponding mesh changes. For the next simulations $\epsilon_r' = 20$, so the designed meshing is given by

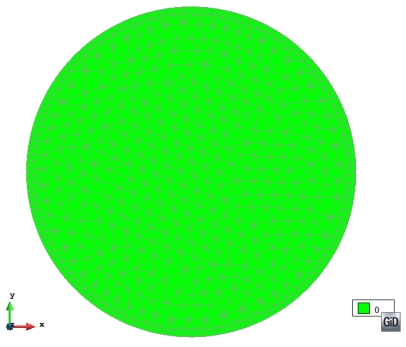

Figure 4.12: 2D meshing for $\epsilon_r' = 20$.

We consider a single current source allocated in cartesian coordinates (Xs,Ys)=(0.5,0) for different values of conductivity.

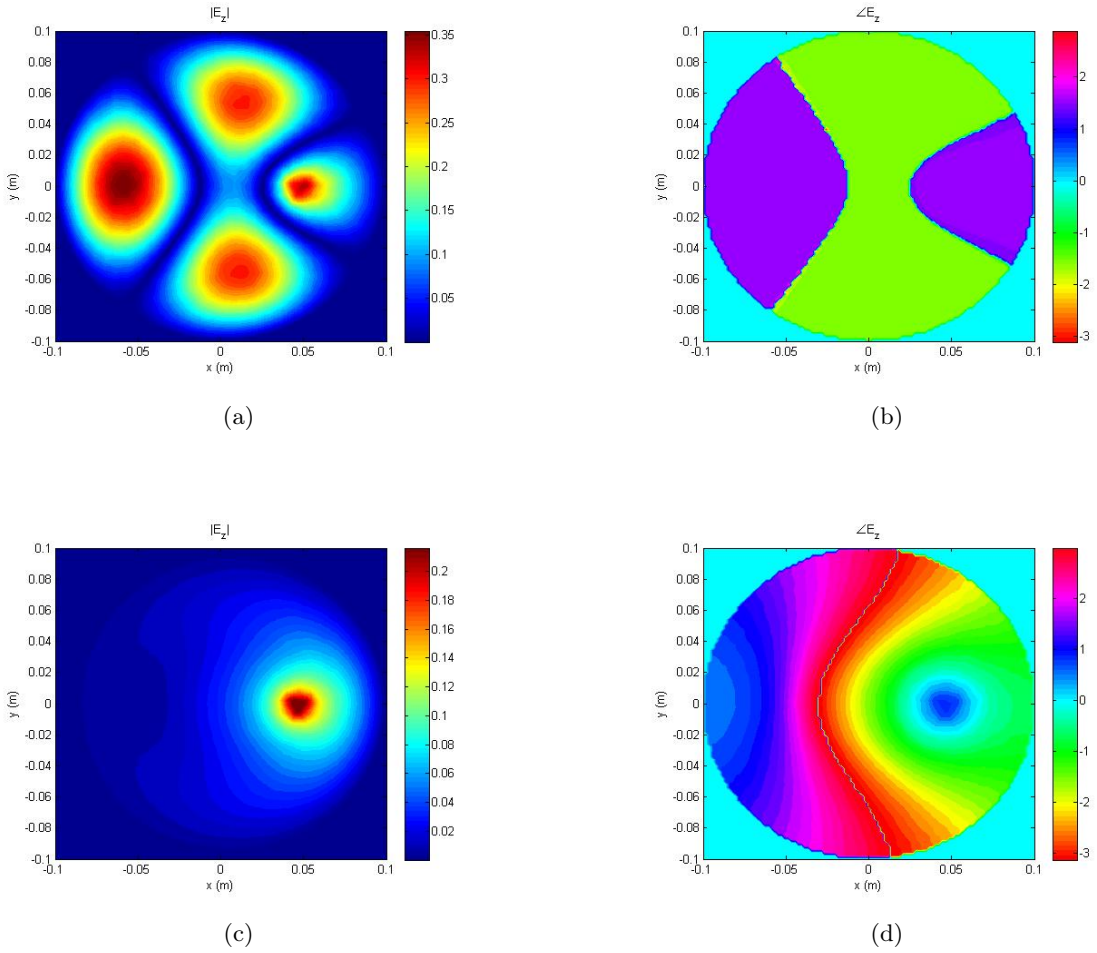

Figure 4.13: Forward Problem solved by FEM using nodal functions: $\epsilon_r' = 20$, (Xs,Ys)=(0.5,0), (a)(b) $|E|$ and $\angle E$ field for $\sigma = 0.0005$ S/m (c)(d) $|E|$ and $\angle E$ field for $\sigma = 0.5$ S/m.

We can extract important information from results above, according to the chosen dielectric properties the number of wave reflections that appear in the computed electric field can be higher or lower. On one hand, when the permittivity and the conductivity are more similar, the peaks of electric intensity are focused at the placement of the given source. On the other hand, if the conductivity is enough small, there will be electric duplicities due to the low attenuation that performs the medium which involves reflections in the PEC.

We talk about lossy mediums (attenuate travel waves) when the conductivity can be considered high. A given medium is a well conductor when the relation $\sigma/(w_o\epsilon') >> 1$ is satisfied.

Now, we present some simulations based on Fig.4.13.(a) with different current source position and different number of sources to understand better the behaviour of the given 2D scenario.

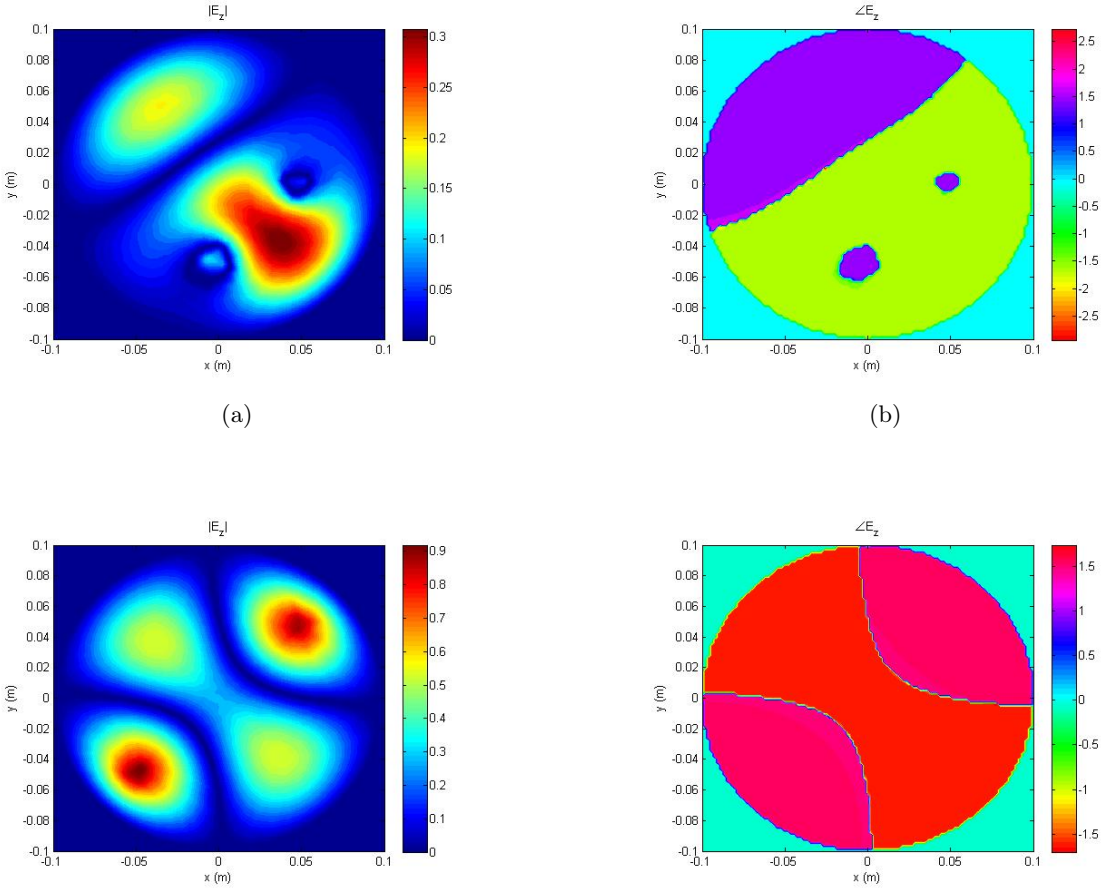

Figure 4.14: Forward Problem solved by FEM using nodal functions: $\epsilon'_r = 20$ (a)(b) $|E|$ and $\angle E$ field for $\sigma = 0.0005$ [S/m] and for current sources (Xs,Ys)=([0.05 0],[0 -0.05]), (c)(d) $|E|$ and $\angle E$ field for $\sigma = 0.0005$ [S/m] and for current sources (Xs,Ys)=([-0.05 0.05],[-0.05 0.05]).

In Fig.4.14.(a) is possible to check that appears an overlap between the two charges due to the s̈mall̈distance among both, this problem has a reason that will be evaluated during the next Chapter 5.

Let's consider a new scenario characterized by a higher permittivity, $\epsilon_r' = 80$, obviously the behaviour of the electric field in the medium will be different. It's not necessary to show the new surface because presents the same structure but with only more number of elements. In Fig.4.15.(a-b), it is possible to observe how the number of performed reflections in PEC has been more numerous. In addition, in Fig.4.15.(c-d) the current source has been placed respectively, farther and nearer to the PEC interface to visualize how the wave reflections decrease or increase because there is more or less space to attenuate the wave propagations.

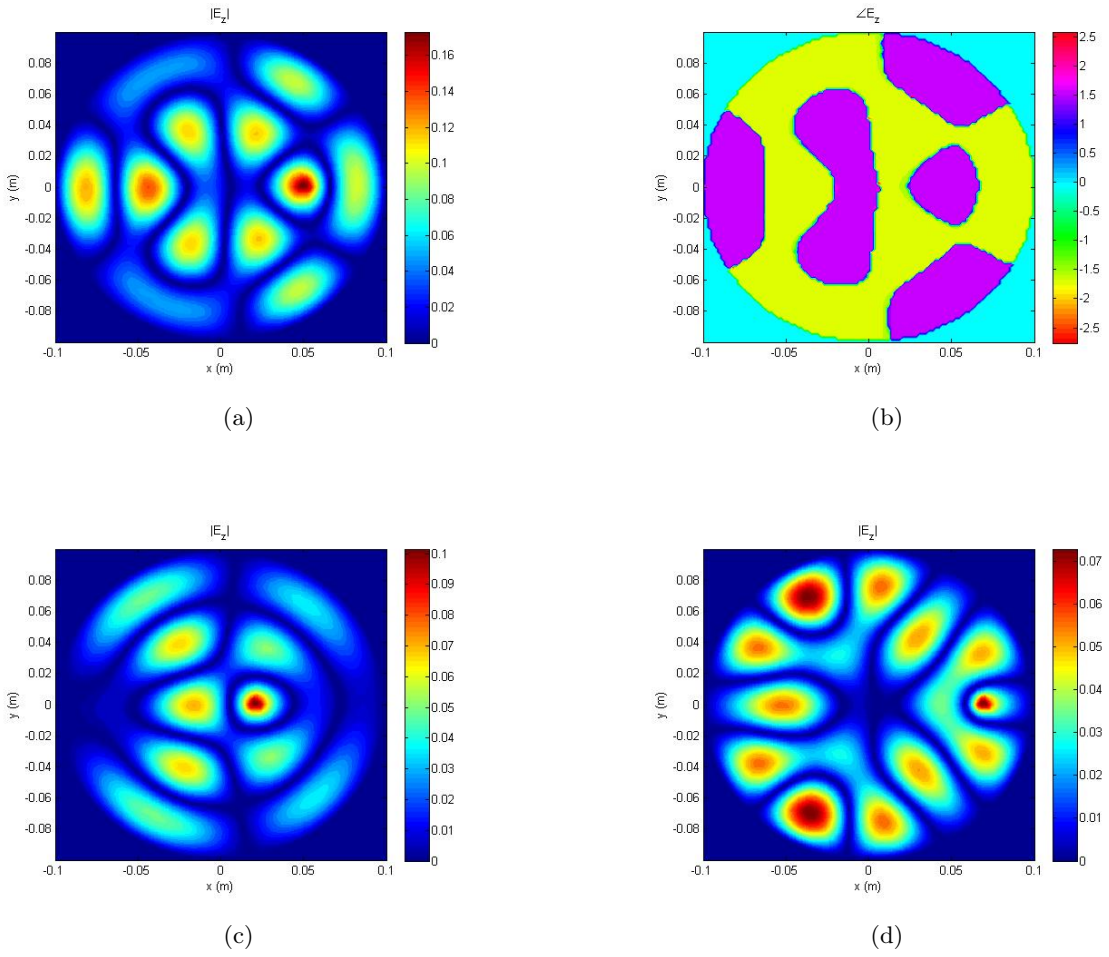

(a) (b)

(c) (d)

Figure 4.15: Forward Problem solved by FEM using nodal functions: $\epsilon_r' = 80$ (a)(b) $|E|$ and $\angle E$ field for $\sigma = 0.0005$ [S/m] and for current sources (Xs,Ys)=(0.05,0), (c)(d) $|E|$ field for $\sigma = 0.0005$ [S/m], current sources (Xs,Ys)=(0.02,0) and (Xs,Ys)=(0.07,0).

We have analysed circular surfaces where the dielectric properties are homogeneous, but in real applications as thomography where the electric field should be computed, dielectric properties variate along the surface, i.e., they are inhomogeneous. In Fig.4.16 inhomogeneous 2D scenarios are presented, they are composed by three different parts, whose permittivities and conductivities are given below the figures.

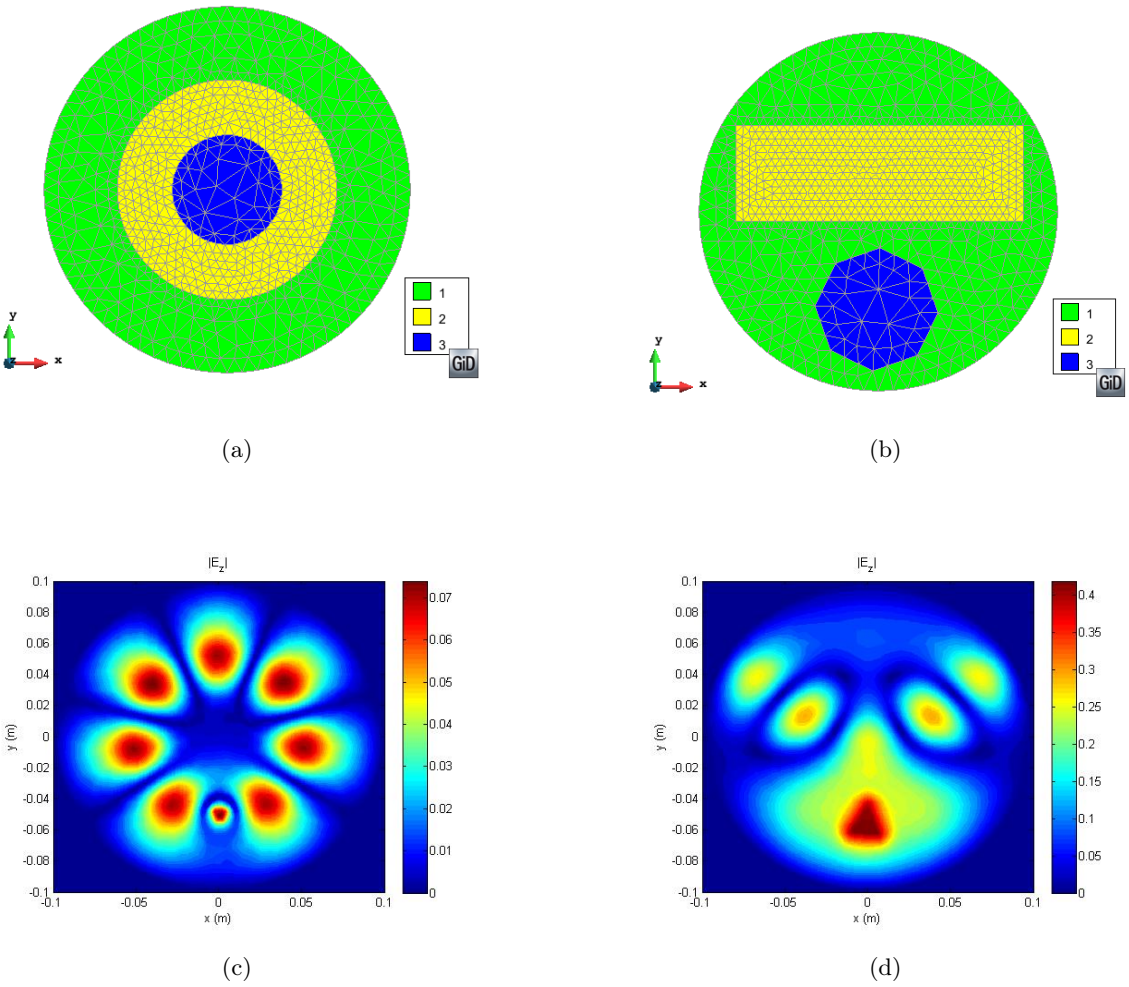

Figure 4.16: (a)(b) Inhomogeneous 2D Scenarios (c)(d) $|E|$ fields for current source at (Xs,Ys)=(0,-0.05).

- Green Surface $\Rightarrow \epsilon_r' = 20$; $\sigma = 0.0005$;
- Yellow Surface $\Rightarrow \epsilon_r' = 80$; $\sigma = 0.02$;
- Blue Surface $\Rightarrow \epsilon_r' = 6$; $\sigma = 0.1$;

We can observe how in Fig.4.16.(a)(c) the reflections appear vividly around the first region where the difference between permittivity and conductivity is greater (low losses), however in blue region no electric intensity is involved due to the high level of losses. The analysis in Fig.4.16.(b)(d) is different because the electric charge is placed in the blue region where the behaviour is similar to Fig.4.13.(c), and the reflections waves are more attenuated.

Now let's fix the dielectric properties to compute some EM results for circular enclosure as a function of the working frequency, thereby we may understand the implications of variations in frequency. Consider a circular enclosure with radius equals to 0.3m, where the surface is homogeneous in terms of dielectric parameters ($\epsilon'_r = 10$,$\sigma = 0.03$), the electric charge is based on a single current source placed in (Xs,Ys)=(0,0.1m).

In Fig.4.17 it is possible to visualize how the increase of the working frequency generates a greater number of field lines, the question that we should arise is why reflections due to PEC interface not appear in the shown results. The reason is double, on one hand, the tangent of losses is lower due to high frequencies. On the other hand, the circular enclosures is three times bigger, so the space to attenuate the wave propagations due to the electric charge is higher.

Then, if the second hypothesis was correct we would obtain more wave reflections in results using a smaller PEC enclosure. In order to perform this experiment, we use the PEC enclosure defined in the first circular scenario (radius=0.1m). In Fig.4.18 two different cases are depycted. The dielectric properties used in Fig.4.17 ($\epsilon'_r = 10$,$\sigma = 0.03$) are considered. Then, we can compare the results against Fig.4.17(a)(d). For a working frequency equals to 700MHz, we obtain a higher level of electric field in the peaks where reflections are focused. With the frequency equals to 2GHz happens the same, so we can conclude that the hypotheis approached above is certain.

Finally, in the next sections other type of enclosures based on triangles or squares are developed briefly, the results will only change due to the new geometry and the corresponding new behaviour of the wave reflections between the medium and the PEC interface. The aim of these simulations is to show some results with different enclosures and compare some computational cost as a function of material and frequency choice.

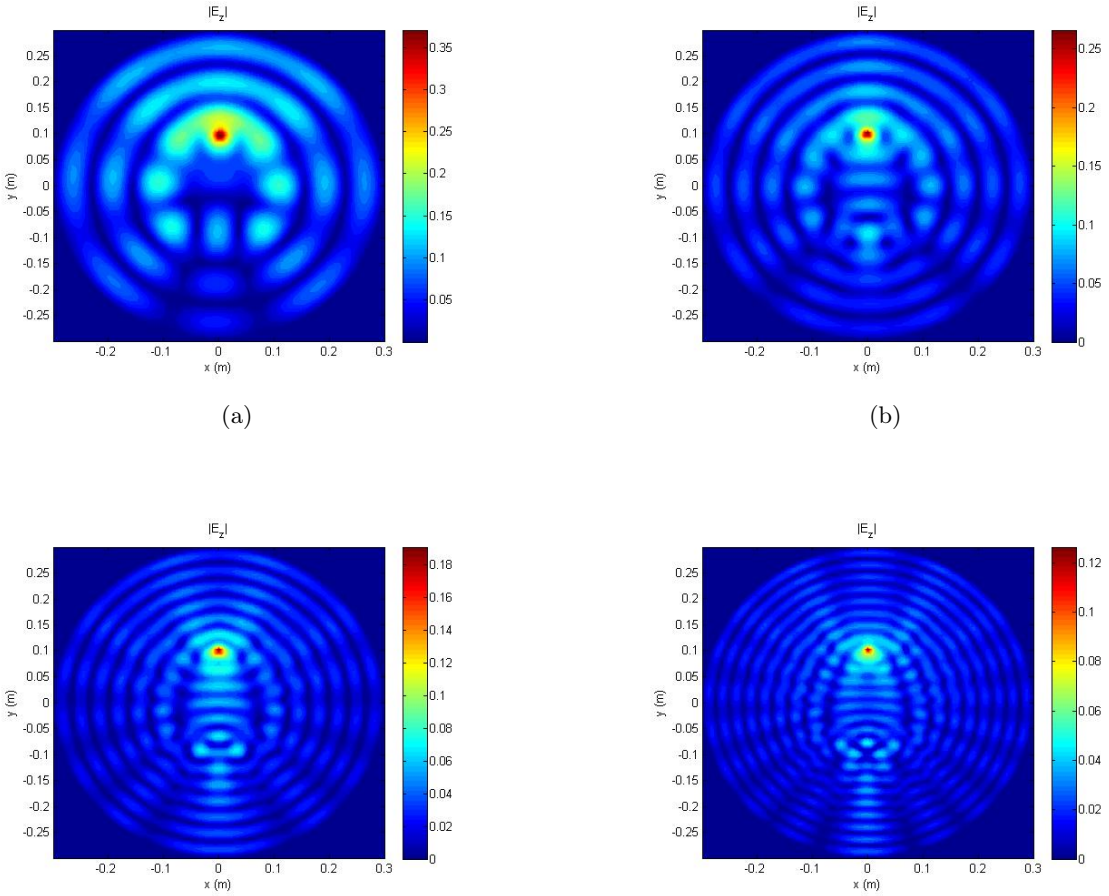

(a) (b)

(c) (d)

Figure 4.17: Forward Problem solved by FEM using nodal functions: $\epsilon_r' = 10$, $\sigma = 0.03$ [S/m], (a) $|E|$ field for $f_o = 700MHz$, (b) $|E|$ field for $f_o = 1GHz$, (c) $|E|$ field for $f_o = 1.5GHz$, (d) $|E|$ field for $f_o = 2GHz$

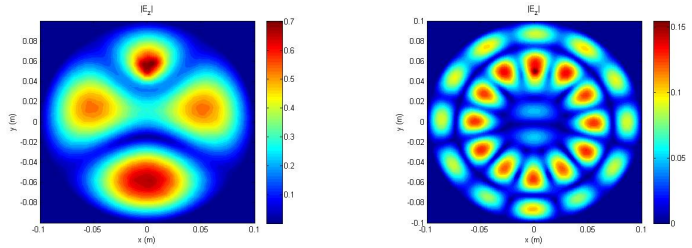

(a) (b)

Figure 4.18: (a)(b) $|E|$ field for $f_o = 700MHz$ and $f_o = 2GHz$ respectively.

4.8.2 Triangular Enclosure

In this section a new 2D scenario is presented, using a triangular enclosure with sides equal to 0.15m we will understand better how the PEC is involved in the corresponding computation. A few examples are described below where the frequency is fixed to 500MHz.

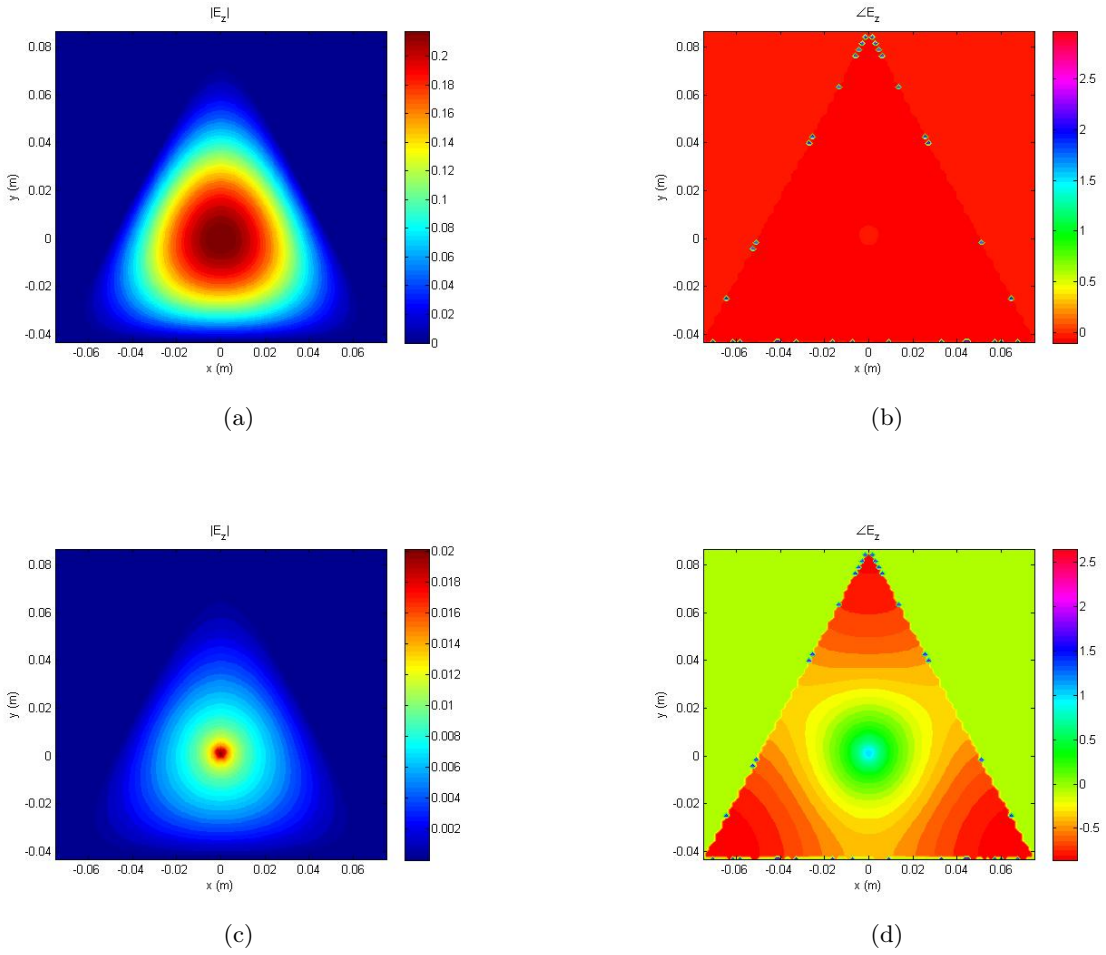

Figure 4.19: Triangular 2D: $\epsilon'_r = 20$, (a)(b) $|E|$ and $\angle E$ for $\sigma = 0.02$ [S/m] and (Xs,Ys)=(0,0), (c)(d) $|E|$ and $\angle E$ for $\sigma = 0.5$ [S/m] and (Xs,Ys)=(0,0)

We can observe in Fig.4.19 the same behaviour respect the dielectric properties than in the case of the circular enclosure, when the relation σ/ϵ'_r decrease, the field intensity is focused on the point where the charge is placed. However, when the relation σ/ϵ'_r increase, the wave propagation is wider, the reason why not appear other peaks of electric field outside the current source placement as in circular enclosure is explained in next figures.

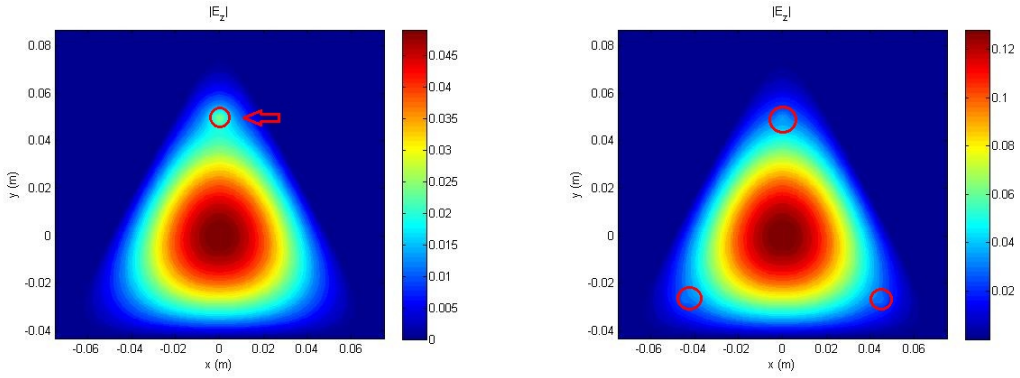

(a) (b)

Figure 4.20: (a) One current source (b) Three current sources

In Fig.4.20.(a) is shown a triangular enclosure with $\epsilon'_r = 20$ and $\sigma = 0.02$ as dielectric parameters, a single current source is placed at (Xs,Ys)=(0,0.05) where the red circular mark has been drawn. We can see how all the electric intensity is focused as in Fig.4.19 in the centre of the triangular scenario, before giving possible reasons to explain this phenomenon, pay attention to Fig.4.20.(b).

In this simulation, three current sources has been allocated in each of the three vertexes that form other smaller triangle inside the triangular enclosure, everyone is indicated with a red circle. The coordinates of each charge are (Xs,Ys)=([0,-0.045,0.045],[0.05,-0.026,-0.026]).

The electric result is the same than in Fig.4.20.(a), all the intensity field is focused on the centre, in this case as there are three charges the field is more intense (compare both numerical results). While in (a) the max value is 0.045V, in (b) the quantity increse over three times, 0.12V.

The conclusion that we can obtain is that the possible wave reflections occurs as in the circular case, however all of them are focused in the centre of the triangular due to the geometric properties of triangles.

4.8.3 Square Enclosure

This section is dedicated to square enclosures, however instead of describing EM results, we will present computational costs to know the difficulty of simulations. As commented in Section 4.2, if the number of elements and nodes related to the domain discretization is very high, the corresponding computation of the *Forward Problem* could present huge costs.

Tabla 4.2: Computational Costs

Frequency [GHz]	Permittivity	Edge Size [m]	Num.Nodes	Num.Elem.	Time [s]
0.4	10	0.0158	210	366	0.220609
0.8	20	0.0056	1534	2922	4.004716
1.5	12	0.0038	3295	6376	15.41539
2	30	0.0018	14356	28266	270.684261
2.5	40	0.0013	27370	54122	1000.769933
3.2	40	9.8821e-004	47375	93940	3349.545703

The scenario is based on a square that is defined by a side equals to 0.2m, and a single charge placed at (Xs,Ys)=(0,0). It is important to indicate that the presented costs in Table.4.2 consider only the computational cost related only to FEM Matrix assembling, nevertheless the visualization process of results involves also considerable costs. The simulations during this research work has been developed by a processor Intel(R) Core(TM) i7-2630QM CPU 2.00GHz with a memory RAM of 6.00GB.

Finally, it's important to claryfy that computational costs depend also of the geometric complexity and the number of current sources. In addition, in *The Inverse Algorithm* that will be described in the next chapter, the FP must be computed for each transmitter, so the total computational cost will be higher.

Chapter 5

Solving Inverse Scattering Problems

This chapter presents the final target of this research work, the Inversion Algorithm. Electromagnetic tomography requires the inversion of a wave equation. Various inversion techniques for wave equations focused on electromagnetic scattering imaging systems have been developed since the early 1980s. The main advantage of full inversion, as opposed to a linearized imaging technique, is that a quantitative inversion of such material parameters as conductivity and permittivity goes a lot further toward solving the clinical identification problem, e.g. tumour or no tumour, and makes the technique much more useful for biomedical applications [10]. Most of these techniques work with Greenś theory implementing these methods with the Greenś function associated with a scatterer located in an unbounded homogeneous region. However, this assumption rarely represents the physical situation for proposed imaging systems. With the use of the Greenś function, the IE is typically solved by the method-of-moments (MoM). If the background medium is inhomogeneous or if the problemś boundary is complicated, the use of Greens function can be a complex, i.e., computationally expensive process. Using partial differential equations (PDE) formulation implementing FEM is possible to solve the problem without Greens function and, thus, the presence of an inhomogeneous background or a complicated boundary can be easily considered without affecting the computational complexity of the numerical solution. As commented in Chapter 3, inversion algorithms require that a forward solver be applied several times at each iteration to calculate the scattered fields associated with each transmitter to determine of the OIs electrical properties.

The inverse method developed during this research work is called as Contrast Source Inversion Method (CSIM), it works iteratively updating two variables: the contrast source and the contrast variables. The update, as we will see later, is based on minimization of a given cost functional. As the method used in EM computation is the FEM instead of IE, the considered algorithm is denoted as FEM-CSIM. During this chapter, the necessary formulation is presented, including the involved operators in the algorithm. Finally, simulations for several 2D scenarios are evaluated.

5.1 The Inversion Algorithm

We consider the 2D TM problem with z-polarized electric field and an exp(jwt) time dependence. The 2D scenario is defined as in Chapter 3 was described, the OI is located within a bounded imaging domain $\mathcal{D}$, this region is surronded by a enclosure presented as a PEC interface and placed into a matching medium known as background (Fig. 3.2). The electric properties of the background medium, which can be inhomogeneous, are known. The permeability of the OI and background are considered as in free-space, μ_o. The corresponding contrast is defined as,

$$\chi(r) = \frac{\epsilon_r(r) - \epsilon_b(r)}{\epsilon_b(r)} \tag{5.1}$$

where $\epsilon_b(r)$ is the complex permittivity of the background, so that, $\chi(r) = 0 \forall r \notin \mathcal{D}$.
As commented in Chapter 3, the Imaging Domain $\mathcal{D}$ is illuminated by one transmitter T from the N transmitters/receivers, the transmitters are assumed to be allocated at 2D point sources with the incident field, E_t^{inc}, produced by transmitter t, modeled by the scalar Helmholtz equation,

$$\nabla^2 E_t^{inc}(r) + k_b^2 E_t^{inc}(r) = jw\mu_o J_t(r) \tag{5.2}$$

where $k_b(r) = w\sqrt{\mu_o \epsilon_o \epsilon_b(r)}$ is the background wavenumber which could be inhomogeneous. In the next step the OI is included in the measure, performing the total electric field, E_t, for each transmitter. The scalar helmholtz equation is satisfied,

$$\nabla^2 E_t(r) + k^2 E_t(r) = jw\mu_o J_t(r) \tag{5.3}$$

In this cases, $k(r) = w\sqrt{\mu_o \epsilon_o \epsilon_r(r)}$. Thus, the scattered field coud be defined as $E_t^{sct}(r) \equiv E_t(r) - E_t^{inc}(r)$, represented as given

$$\nabla^2 E_t^{sct}(r) + k_b^2 E_t^{sct}(r) = -k_b^2(r) w_t(r) \tag{5.4}$$

where the contrast source variable, $w_t(r) = \chi(r) E_t(r)$, describe the contrast variable in terms of the total field perfomed by sources. The incident electric field, E_t^{inc}, and the scattering electric field, E_t^{sct} , must consider the homogeneous Dirichlet BCs related to the PEC surface. From FEM discretization is possible to define the corresponding matrix that describe the behaviour of each node, the next expression relates these FEM matrix to the scattered field,

$$[\mathbf{S} - \mathbf{T_b}]\, E_{t,\Omega}^{sct} = \mathbf{T_b} w_{t,\Omega} \tag{5.5}$$

while $\mathbf{S} \in \mathbb{C}^{N \times N}$, is the Stiffness matrix that depends on the BCs, and $\mathbf{T_b} \in \mathbb{C}^{N \times N}$ is the Mass matrix defined by the background properties, the vectors $E_{t,\Omega}^{sct} \in \mathbb{C}^N$ and $w_{t,\Omega} \in \mathbb{C}^N$ are the nodal values of scattered field and constrast source variables for transmitter t in the total domain Ω.

At this point is necessary to clarify an essential modification developed in FEM matrix assembling. In Chapter 4 the scenario was analysed by linear nodal functions, however the dielectric properties of the medium were allocated element by element. FEM-CSIM needs an assignment based on node by node to define the contrast variable in each point, these modifications in FEM assembling could be observed in [B.1].

5.2 Inversion FEM Matrix Operators

The FEM-CSIM can be described more effectively by introducing several matrix operators. The first operator is denoted as $\mathcal{M}_\mathbf{s} \in \mathbb{C}^{R \times N}$, where R is the number of receivers. This matrix operator lets us to transforms the N nodal scattered field values from the total domain Ω to the R source points. The second operator is denoted as $\mathcal{M}_\mathcal{D} \in \mathbb{C}^{I \times N}$, where I is the number of nodes that are involved in the Imaging Domain $\mathcal{D}$. It selects the field values at the I nodes within the

imaging domain. Both matrix operators are necessary to obtain the contrast source variable in all mesh, becoming $w_t \in \mathbb{C}^I$ at each iteration within Imaging Domain $\mathcal{D}$ to,

$$w_{t,\Omega} = \mathcal{M}_{\mathcal{D}}^T w_t \tag{5.6}$$

using (5.6) in matrix equation (5.5), we obtain a new operator, $\mathcal{L} \in \mathbb{C}^{N \times I}$, given as

$$E_{t,\Omega}^{sct} = \mathcal{L}[w_t] = [\mathbf{S} - \mathbf{T_b}]^{-1} \mathbf{T_b} \mathcal{M}_{\mathcal{D}}^T [w_t] \tag{5.7}$$

5.3 The Contrast Source Inversion Method

As commented at the beginning of the chapter, CSIM is based on updating constrast and contrast source variables on the way that a cost functional is minimized, it is given as

$$\begin{aligned} &\mathcal{F}(\chi, w_t) = \mathcal{F}^S(w_t) + \mathcal{F}^D(\chi, w_t) \\ &= \frac{\sum_t \|f_t - \mathcal{M}_{\mathbf{s}} \mathcal{L}[w_t]\|_S^2}{\sum_t \|f_t\|_S^2} + \frac{\sum_t \left\|\chi \odot E_t^{inc} - w_t + \chi \odot \mathcal{M}_{\mathcal{D}} \mathcal{L}[w_t]\right\|_D^2}{\sum_t \left\|\chi \odot E_t^{inc}\right\|_{\mathcal{D}}^2} \end{aligned} \tag{5.8}$$

Here, $f_t \in \mathbb{C}^R$ is the measured scattered field at R source positions for each transmitter and E_t^{inc} is the incident field vector inside the Imaging Domain $\mathcal{D}$. Remember that we compute the electric field for the total domain Ω, but is easy toy obtain the equivalent measurament inside $\mathcal{D}$ using $E_t^{inc} = \mathcal{M}_{\mathcal{D}} E_{t,\Omega}^{inc}$.

In CSI algorithm, the first step is to update contrast source variables w_t by a conjugate-gradient (CG) method with Polak Ribière search directions, while assuming the contrast variables χ constant. In the second step, w_t is assumed constant, and the domain functional cost $\mathcal{F}^D(\chi, w_t)$ is minimized. Both operations must be executed at each iteration. The first update is

$$w_{t,n} = w_{t,n-1} + \alpha_{t,n} d_{t,n} \tag{5.9}$$

where $\alpha_{t,n}$ is the update step-size for transmitter t at iteration n, $d_{t,n}$ are Polak Ribière search directions.

The update step-size is given as

$$\alpha_{t,n} = \frac{\eta^{\mathcal{S}} \left\langle \rho_{t,n-1}, \mathcal{M}_s \mathcal{L}[d_{t,n}] \right\rangle_{\mathcal{S}} + \eta_n^{\mathcal{D}} \left\langle r_{t,n-1}, d_{t,n} - \chi_{n-1} \odot \mathcal{M}_{\mathcal{D}} \mathcal{L}[d_{t,n}] \right\rangle_{\mathcal{D}}}{\eta^{\mathcal{S}} \left\| \mathcal{M}_s \mathcal{L}[d_{t,n}] \right\|_{\mathcal{S}}^2 + \eta_n^{\mathcal{D}} \left\| d_{t,n} - \chi_{n-1} \odot \mathcal{M}_{\mathcal{D}} \mathcal{L}[d_{t,n}] \right\|_{\mathcal{D}}^2} \tag{5.10}$$

$\eta^{\mathcal{S}}$ and $\eta_n^{\mathcal{D}}$ are the normalization factors given as

$$\begin{aligned} \eta^{\mathcal{S}} &= \left(\sum_t \|f_t\|_{\mathcal{S}}^2 \right)^{-1} \\ \eta_n^{\mathcal{D}} &= \left(\sum_t \left\| \chi \odot E_t^{inc} \right\|_{\mathcal{D}}^2 \right)^{-1} \end{aligned} \tag{5.11}$$

and the error terms $\rho_{t,n-1}$ and $r_{t,n-1}$ are

$$\begin{aligned} \rho_{t,n-1} &= f_t - \mathcal{M}_s \mathcal{L}[w_{t,n-1}] \\ r_{t,n-1} &= \chi \odot E_t^{inc} - w_{t,n-1} + \chi_{n-1} \odot \mathcal{M}_{\mathcal{D}} \mathcal{L}[w_{t,n-1}] \end{aligned} \tag{5.12}$$

The Polak Ribière search directions $d_{t,n}$ are calculated by the following formula

$$d_{t,n} = -g_{t,n} + \frac{\langle g_{t,n}, g_{t,n} - g_{t,n-1} \rangle_{\mathcal{D}}}{\|g_{t,n-1}\|_{\mathcal{D}}^2} d_{t,n-1} \tag{5.13}$$

where $d_{t,0}$ is set to zero and $g_{t,n}$ is the gradient of the cost function $F(\chi, w_t)$ with respect to the contrast sources $w_{t,n}$, which can be approached by the next expression,

$$g_{t,n} = -2\eta^{\mathcal{S}} \mathbf{T}_{\mathcal{D}}^{-1} \mathcal{L}^H \mathcal{M}_s^H \rho_{t,n-1} - 2\eta_n^{\mathcal{D}} \mathbf{T}_{\mathcal{D}}^{-1} \left(\mathbf{I} - \mathcal{L}^H \mathcal{M}_{\mathcal{D}}^T \mathbf{X}_{n-1}^H \right) \mathbf{T}_{\mathcal{D}} r_{t,n-1} \tag{5.14}$$

Here $\mathbf{I} \in \mathbb{R}^{I \times I}$ is an identity matrix and $\mathbf{X}_{n-1}$ is a diagonal matrix whose diagonal entries are the values of χ_{n-1}.

After updating the contrast source variables, χ is evaluated by minimizing $\mathcal{F}^D(\chi, w_t)$ where w_t is considered constant. To obtain χ_n we require the solution of the following sparse matrix equation

$$\left(\sum_t \mathbf{E}_{t,n}^H \mathbf{T}_{\mathcal{D}} \mathbf{E}_{t,n} \right) \chi = \sum_t \mathbf{E}_{t,n}^H \mathbf{T}_{\mathcal{D}} w_{t,n} \tag{5.15}$$

where $\mathbf{E}_{t,n} \in \mathbb{C}^{I \times I}$ is the diagonal matrix defined by the vector $\mathbf{E}_{t,n} = \mathbf{E}_t^{inc} + \mathcal{M}_{\mathcal{D}} \mathcal{L}[w_{t,n}]$.

5.3.1 Norms And Inner Products

In expressions presented above there are some symbols, operators and variables not defined previously. Here, with the unknown variables located at the nodes of the the triangular mesh, the L2 norm and the inner product in $\mathcal{D}$ are calculated as

$$\|x\|^2_{\mathcal{D}} = x^H \mathbf{T}_{\mathcal{D}} x \qquad \text{and} \qquad \langle x, y \rangle_{\mathcal{D}} = y^H \mathbf{T}_{\mathcal{D}} x \tag{5.16}$$

being x and y vectors of size I, and $\mathbf{T}_{\mathcal{D}} \in \mathbb{R}^{I \times I}$ is the mass matrix restricted to nodes lying within the Imaging Domain $\mathcal{D}$, the entries values of the matrix are given by

$$\mathbf{T}_{\mathcal{D}} = \int_{\mathcal{D}} \lambda_i \cdot \lambda_j ds \tag{5.17}$$

Assuming that the receiver locations on the surface S are distributed uniformly, the L2 norm and the inner product on S for vectors of size R are given as

$$\|x\|^2_{\mathcal{S}} = x^H x \qquad \text{and} \qquad \langle x, y \rangle_{\mathcal{S}} = y^H x \tag{5.18}$$

5.3.2 FEM-CSIM Initial Guess

The initial guess for contrast source variables cannot be set to zero because the functional cost would become undefined at the first iteration. From [9] we can extract a formulation for an initial guess. Expression (5.19) is obtained by the method of the steepest descent applied to $\mathcal{F}^S(w_t)$.

$$w_{t,0} = \frac{\mathrm{Re}\left\langle \mathcal{M}_s \mathcal{L}[\mathcal{G}^{\mathcal{S}} f_t], f_t \right\rangle_{\mathcal{S}}}{\|\mathcal{M}_s \mathcal{L}[\mathcal{G}^{\mathcal{S}} f_t]\|^2_{\mathcal{S}}} \mathcal{G}^{\mathcal{S}} f_t \tag{5.19}$$

where the operator $\mathcal{G}^{\mathcal{S}} = -2\eta^{\mathcal{S}} \mathbf{T}_{\mathcal{D}}^{-1} \mathcal{L}^H \mathcal{M}_s^H$. After the inital guess is determined, we can start the iterative algorithm described during this section.

5.4 Simulations

This section presents briefly some results of several simulations based on FEM-CSIM. In this manner, we may obtain the unkown properties of a given OI. This work try to represent a real biomedical application using MWI. All synthetic datasets are created using an FEM forward solver, we can simulate the electromagnetic field that would be generated by real experiment as breast detection. Later, appliying the *Inversion Algorithm*, we obtain the results of interest.
In adittion, we will dicuss about some possible problematic scenarios where the application is not comfortable. Results in terms of error will be presented in order to visualize the effectiveness of the method. All simulations has been executed using MATLAB.

Let's start with a simple scenario, the OI is a circle of radius equals to 0.02m with a complex relative permittimity, $\epsilon_r = 5.0000 - j1.2839$. The OI is illuminated by 16 transmitters at a frequency of $f_o = 700MHz$. The transmitting and receiving points are evenly spaced on a circle of radius 0.3m. The enclosure is a circular PEC of radius equals to 0.36m. The chosen background presents a relative permittivity, $\epsilon_r = 3.0000 - j1.2839$. Due to discretization the number of nodes is 4831 of wich 1352 nodes involved the Imaging Domain.

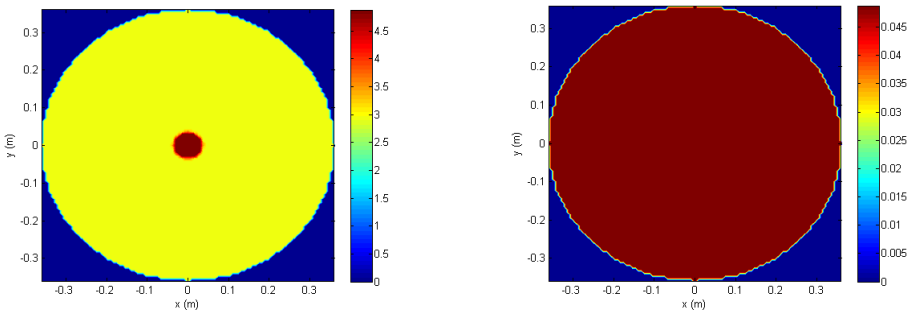

(a) (b)

Figure 5.1: (a) Real relative permittivity ϵ_r' (b) Conductivity σ

FEM-CSIM is an interative method, so that, if we generate enough iterations, the results will be present a low error. However, if the number of iterations is too high, some wrong results may appear. This simulation was based on 400 iterations.

To assess the quality of the synthetic data reconstructions, for each dataset the L_2 error between the exact OI profile and the reconstructed image is calculated. This error is defined as

$$Err = \frac{\|\chi_{exact} - \chi_{reconst}\|^2_{\mathcal{D}}}{\|\chi_{exact}\|^2_{\mathcal{D}}} \tag{5.20}$$

As commented in Section 5.3.2, the inversion algorithm needs a initial step for the contrast variable, $w_{t,0}$, to start the iterative method. In the next figures we can observe the obtained inital guess related to the relative permittivity and conductivity that generates the initial contrast variable, $\chi_{t,0}$.

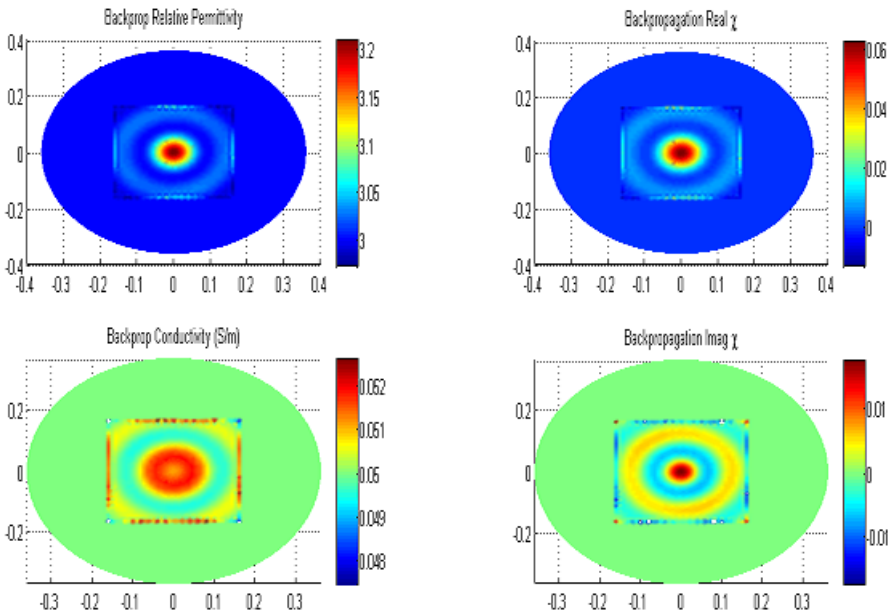

(a) (b)

Figure 5.2: Initial Guess: (a) Diel.Properties (ϵ'_r,σ) (b) Initial Constrast $\chi_{t,0}$

Remember that the initial guess can be based on different criteriums, it is possible to use only the known background dielectric properties or other choice as first step. Obviously each of them involves better or worse results. In our research work the backpropagation method is used with the corresponding advantages and disadvantages that this criterium implies. In Chapter 6 some concepts about backpropagation are described.

In Fig.5.3 results in terms of χ are shown. The exact contrast is compared versus reconstructed contrast variable.

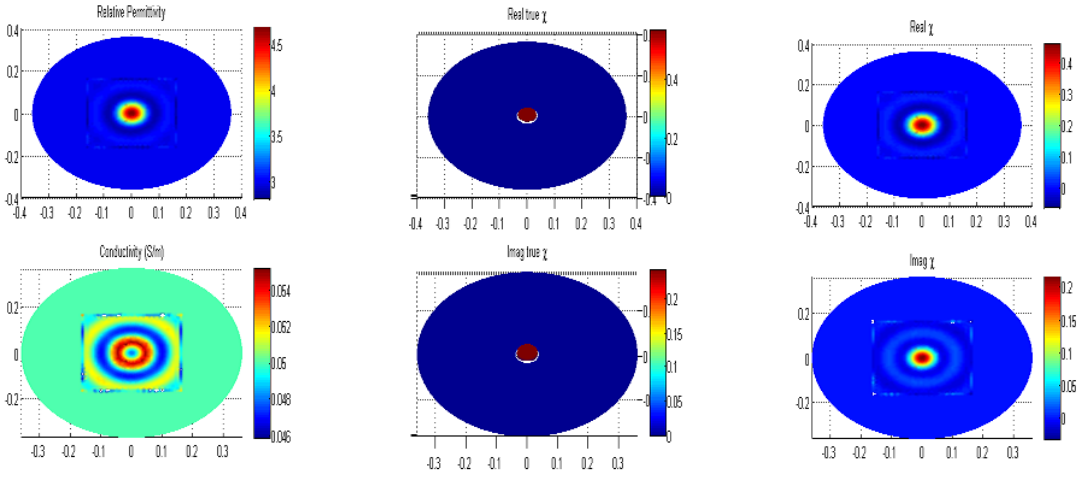

(a) (b) (c)

Figure 5.3: (a) Reconst. diel. properties (b) True Re(χ) and Im(χ) (c) Reconst. Re(χ) and Im(χ)

The reason why the contrast source is so illustrative is due to represents the relation between the OI and background, so we can extract a general vision of the given scenario. We can appreciate that the big problems appears at the boundaries between OI and background due to nodes that are placed in that boundary present a mixed dilectric properties because the corresponding nodal assigment. To estimate better the method performance, in Fig.5.4 the functional cost and the χ error function are shown as a function of the number of iterations. At error over 10^{-5} is the optimal numerical target, we obtain over 10^{-4}. Note that the computational cost is very important to be able to generate a higher number of iterations, so that, the power of the processor used is essential to perform better results.

Let's try to undertstand the importance of the matching medium in results, to get it, we will compare the scenario described above for different contrast χ, we will notice that depending on the kind of values that involve the vector χ the results would present a certain quality in terms of error.

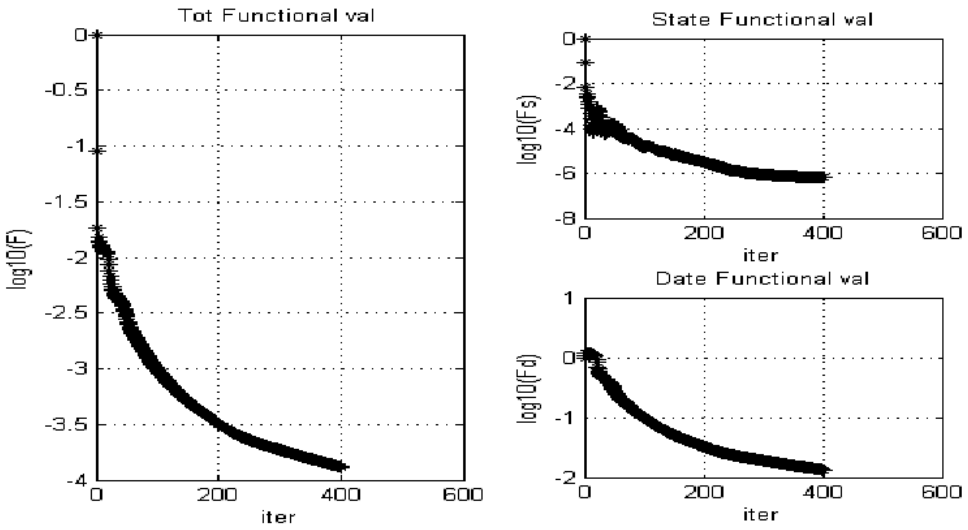

(a)

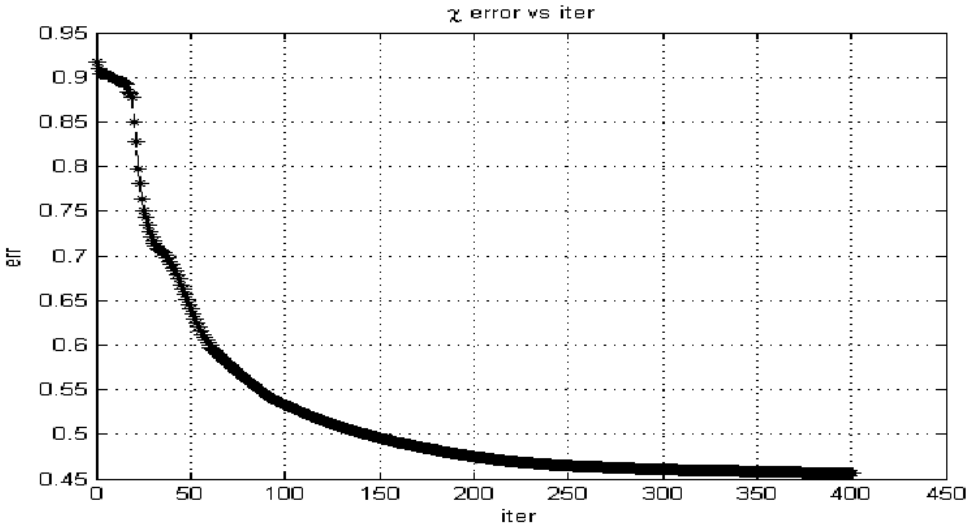

(b)

Figure 5.4: (a) Total, state and domain functional cost (b) Error vs Iterations

While the state functional cost, $\mathcal{F}^S(w_t)$, represents the normalized data-error what implies the quality of the synthetic data against the true ones, $\mathcal{F}^D(\chi, w_t)$ represents the normalized domain-error which implies the level of reconstruction that we have reached during the CSIM performing. It's important to clarify that the data-error function indicates the level of noise in our EM measurament.

Some scenarios depending of the dielectric background properties and scatterers generates bad quality results, even the computation executed by CSI works wrong for some cases obtaining a non legible numerical solutions. A more comprehensive explanation of the reasons why this problem appears is described during Chapter 6 in Contrast Limitations Section.

As commented before, the analyzed scenario is the same than Fig.5.1 but using different dielectric properties for the OI that perform a different contrast source. Firstly, a OI with a complex relative permittivity, $\epsilon_r = 15 - j1.2839$, is described. The number of antennas is also 16 and the same frequency of work. Obviously, due to a higher relative permittivity, the imaging domain $\mathcal{D}$ presents more number of nodes. In the next figures the real contrast is compared to the reconstructed one.

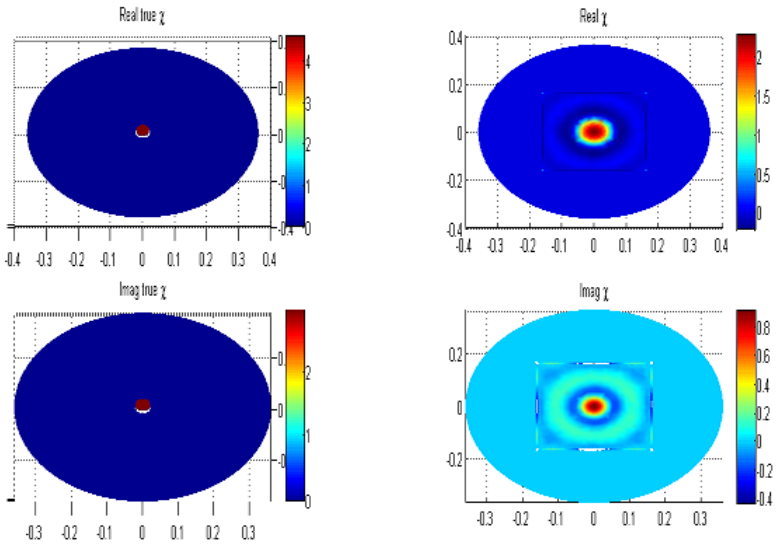

(a) (b)

Figure 5.5: $|\chi| > 1$: (a) True Re(χ) and Im(χ) (b) Reconstructed Re(χ) and Im(χ)

Notice that the contrast source, $\chi \approx 4.603 + j2.955$, then $|\chi| > 1$. Observe that the quality is lower than in Fig.5.3(c). If the OI were bigger, the results would be totally wrong. However the surface related to background is much greater than the scatterer.

The next case is equals to Fig.5.1, with the same dielectric properties, $\epsilon_r = 5 - j1.2839$. However we force the contrast to be negative, $\chi = -0.5634 - j0.24 \Rightarrow Re(\chi) < 0$.

The real and recontructed contrast by CSIM are shown in Fig.5.6.

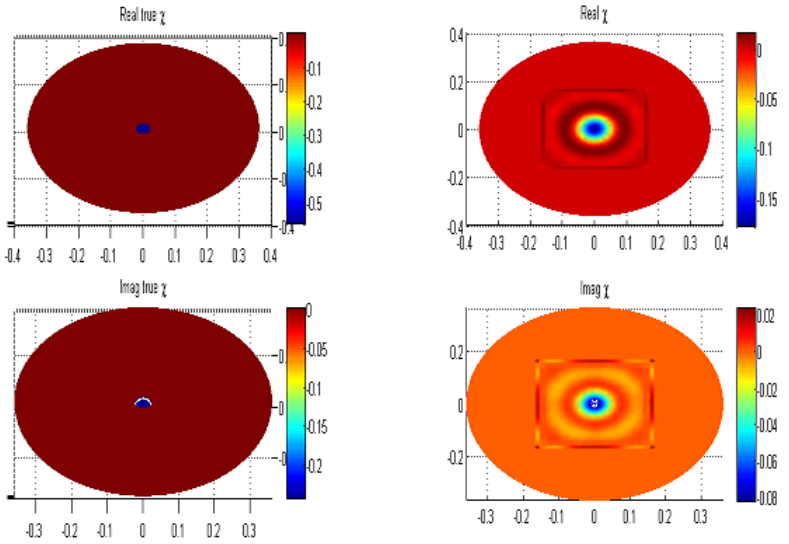

(a) (b)

Figure 5.6: $Re(\chi) < 0$:(a) True Re(χ) and Im(χ) (b) Reconstructed Re(χ) and Im(χ)

Both modified scenarios perform worse results in terms of error, the error related to Fig.5.5 is equals to 0.78 while the error from Fig.5.6 is over 0.73. This growth in error result is due to the contrast variables. This problem increases in scenarios with more complex or bigger OIs (see Section 6.1). From [13] a theoretical study with a experimental demonstration of the possible values for contrast source is developed. This event is explained in Section 6.1.1 but basically to obtain correct results, two contrast condition should be considered:
$|\chi| < 1$ and $Re(\chi) > 0$.

Now we try to estimate the resolution of the inversion method. To perform this target, we create a scenario with a background defined by $\epsilon_{bk} = 6 - j2.876$ bounded by a circular enclosure of radius equals to 0.31m. The OI is based on two circular bodies (radius= 0.025m) separated by a variable distance d. The complex permittivity of both circles is $\epsilon_r = 10 - j1.7975$ at $f_0 = 500MHz$. Firstly, the distance is fixed to d= 0.09m, after simulating this scenario, the distance is reduced to d= 0.02m.

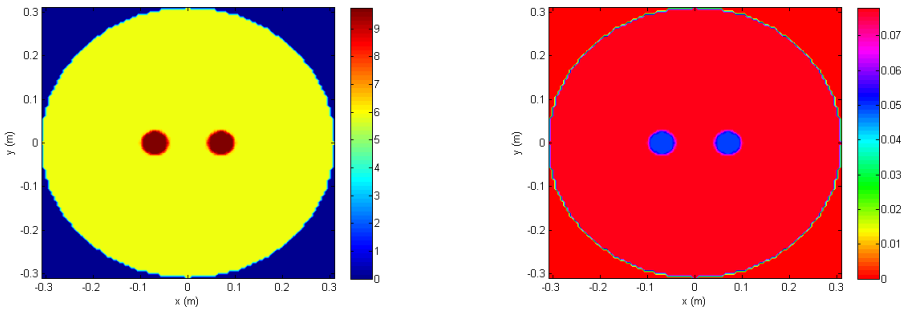

(a) (b)

Figure 5.7: d= 0.09m (a) Real relative permittivity ϵ'_r (b) Conductivity σ

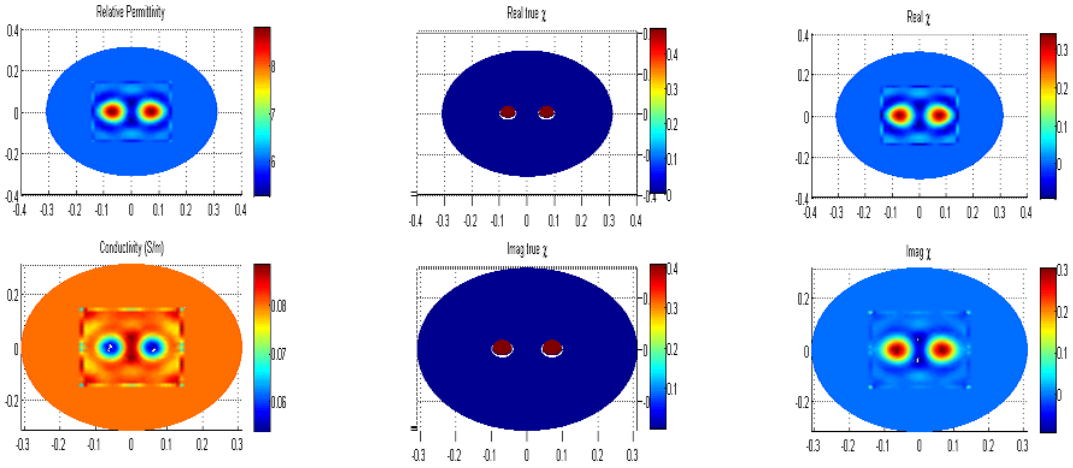

(a) (b) (c)

Figure 5.8: d= 0.09m (a) Reconst. diel. properties (b) True Re(χ) and Im(χ) (c) Reconst. Re(χ) and Im(χ)

During this simulation we don't want to reach an optimal numerical result for error, we are trying to visualize what happens when the distance between two different OIs is lower than the corresponding resolution. That's the reason why we simulate a big scenario instead little problems where the results would be better (see Section 6.1.2). In next figures we can see the results for d= 0.02m, a distance lower than the resolution of the contrast source inversion algorithm, $dmin = \lambda_{bk}/4$, that is the minimun distance to avoid overlap between scatteres as we can see in Fig.5.9.

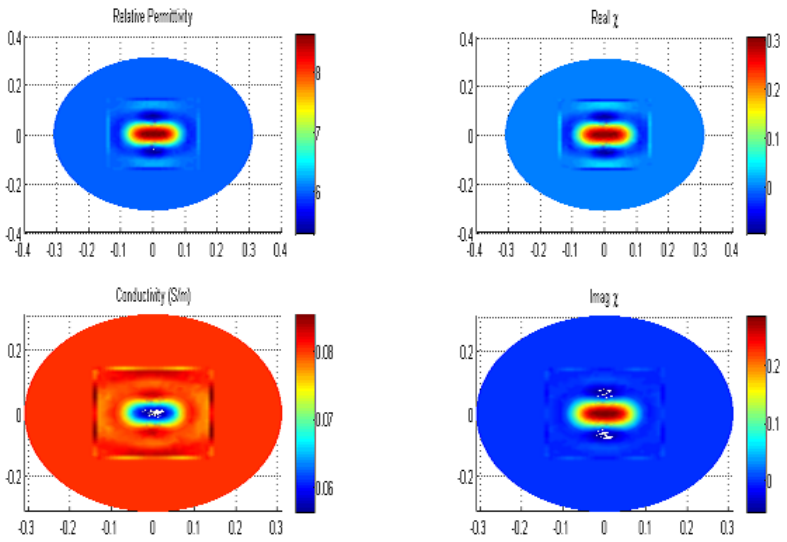

(a) (b)

Figure 5.9: d= 0.02m (a) Reconst. diel. properties (b) Reconst. Re(χ) and Im(χ)

Let's consider a new 2D scenario, in this case, our OI is formed by two circular dielectric surfaces inside a bigger circle. Obviouly, the OI is surrounded by a matching medium that presents a complex permittivity, $\epsilon_b = 8 - j2.246$. A circular PEC of r= 0.312. The first of the scatterers, is based on a circle of r=0.1m, with a permittivity equals to $\epsilon_r = 12 - j0.674$ at 800MHz. The other two circular OIs inside the last one, with a $|\chi| \approx 1$, has a complex permittivity, $\epsilon_r = 16 - j1.573$. The imaging domain is formed by 2853 nodes of the total domain, 8553 nodes. We execute the CSIM during 850 iterations and using 16 antennas placed along a circle of radius 0.25m.

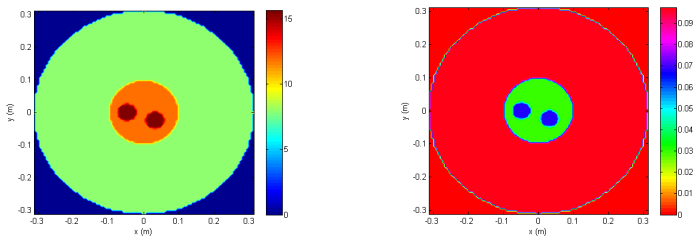

(a) (b)

Figure 5.10: Inhomogeneous Profile (a) Real relative permittivity ϵ_r' (b) Conductivity σ

Here, the CSI results are presented in Fig.5.11,

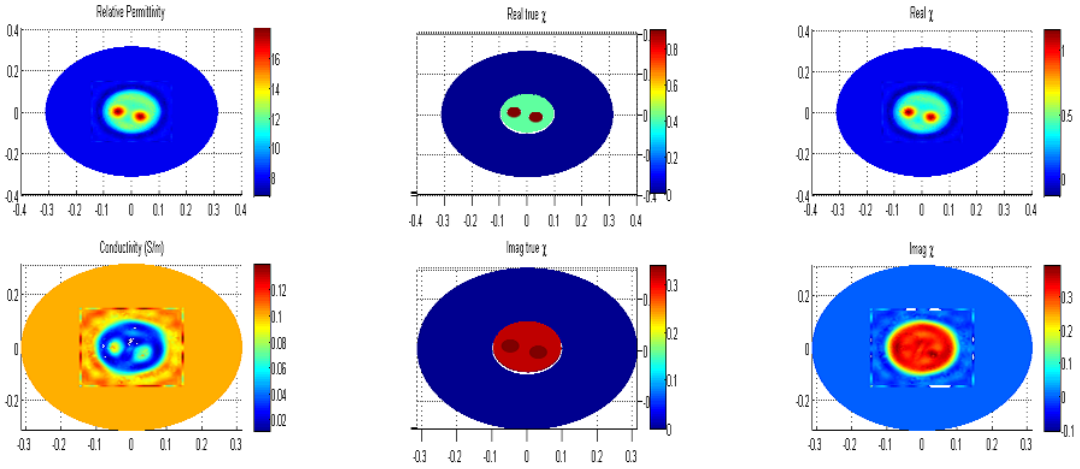

(a) (b) (c)

Figure 5.11: Inhomogeneous Profile (a) Reconst. diel. properties (b) True Re(χ) and Im(χ) (c) Reconst. Re(χ) and Im(χ)

In figures above is possible to observe how the reconstructed values are very near from original ones, the use of a lossy medium that lets to keep the contrast source inside limitations, has performed very good results. We will see in Section 6.3 that medium with considerable losses works better that lossless backgrounds. To analyze easier the obtained numerical results, visualize the error evolution along the CSI in next figure.

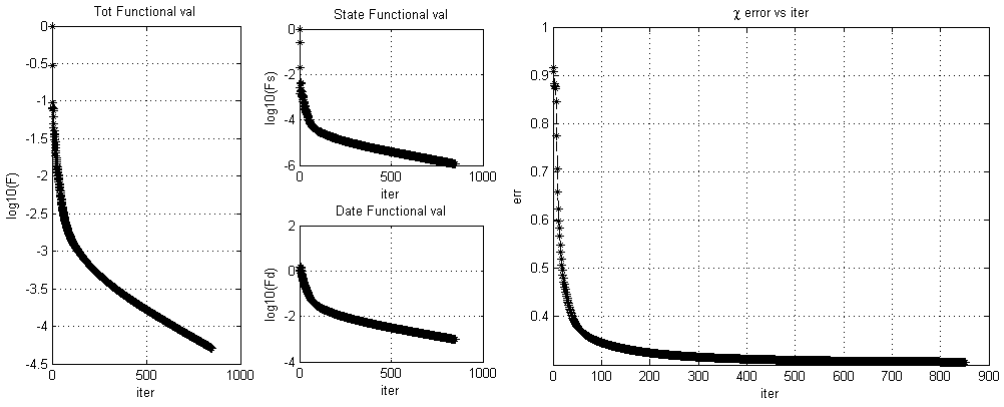

Figure 5.12: Total, state and domain functional cost; Err: Error vs Iterations

The error remains stable at 0.3, so the numerical results after CSI computation have been reached. Due to the successfull simulation, the used initial guess performed by backpropagation method is shown in Fig.5.13.

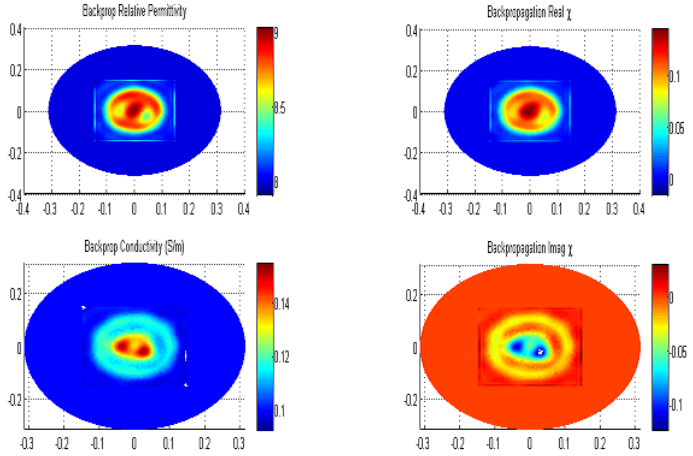

(a) (b)

Figure 5.13: Initial Guess: (a) Diel.Properties (ϵ'_r,σ) (b) Initial Constrast $\chi_{t,0}$

In Section 6.3 more lossy problems will be computated to extract more conclusions about the queality of CSIM in that kind of conditions, comparing it with the problematic related to lossless mediums.

The next simulation is very known in MWI experiments, we consider the Umlaut (Ü) profile whose chosen dielectric properties are depicted in Fig.5.14. In this scenario, the OI consists of several surfaces according to the 'Ü' shape with $\epsilon_r = 24 - j0.9986$ inside a "low-loss" background that presents a complex relative permittivity in this case equals to $\epsilon_{bk} = 16 - j1.7975$ at $f_o =$ 0.9GHz. The data are collected using 16 transmitters/receivers placed in a circle of $r = 0.18$m. The scenario is bounded by a circular enclosure with $r = 0.23$m. The inversion domain $\mathcal{D}$ is based on a square of side equals to 0.2m represented by 2668 nodes. The total number of nodal values considered in this profile is equals to 10441.

The results after 700 iterations let us to identificate an aproximation of the dielectric profile. In Fig.5.15 we can observe the reconstructed dielectric properties: the real relative permittivity and the conductivity. Although, the value of conductivity is not small, for high frequencies

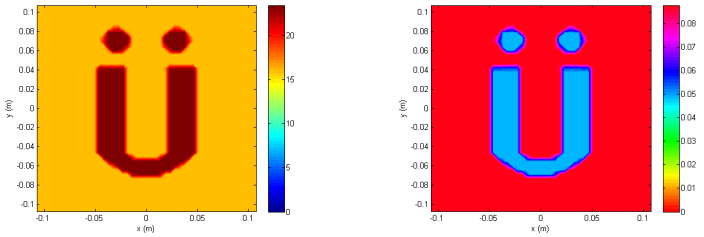

(a) (b)

Figure 5.14: U-Shape profile: (a) Real relative permittivity ϵ'_r (b) Conductivity σ

the losses are lower in background. In images below, the reconstructed conducticity seems non legible, however it happens because conductivities of OI and background are very similar.

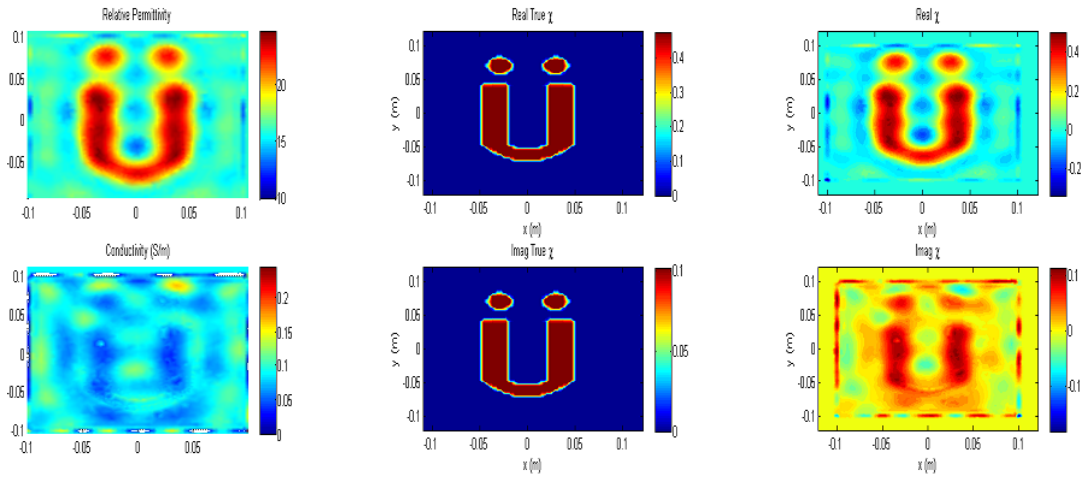

(a) (b) (c)

Figure 5.15: U-Shape profile: (a) Reconst. diel. properties (b) True Re(χ) and Im(χ) (c) Reconst. Re(χ) and Im(χ)

We can observe that in the space between the two little circus and the U shape appear values for relative permittivity and real reacontructed contrast that are greater than the corresponding to background, this occurs because the distance between them is not high in terms of wavelength.

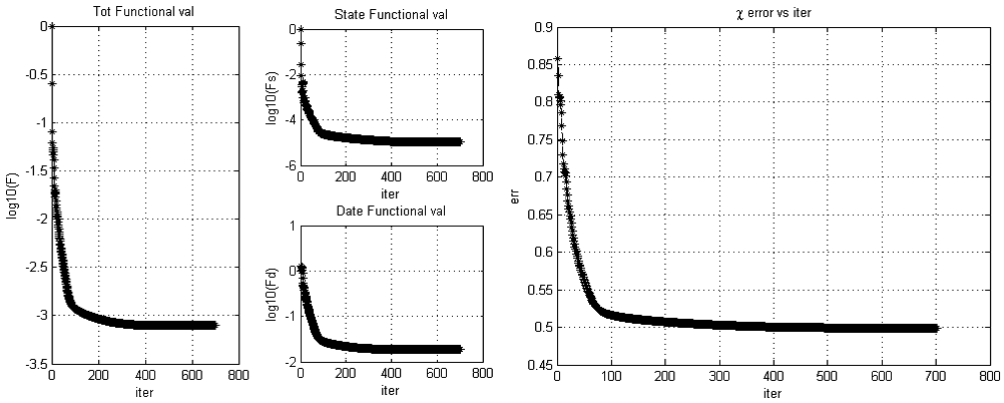

Figure 5.16: U-Shape profile: Total, state and domain functional cost; Err: Error vs Iterations

We reach an error equals to 49% at contrast source for a complex dielectric scenario. Our optimal result would be over 30%. As will be explained before, the medium presents low tangent of losses that performs non optimal results in terms of error. In next chapter, more simulations and experiments will be evaluated in order to define better some properties of inversion algorithm.

Chapter 6

Results And Conclusions

This chapter represents the last part of this research work. While in Chapter 5 a briefly description of a few CSIM simulations were presented to give a clearer picture of the problem, during this chapter we describe deeply a large amount of simulations using the MWI application. Results are classified according to the problem that is analyzed.
Firstly, we will try to establish the conclusions for this research work, to get it the CSIM is evaluated for several 2D problems with the aim of define the constraints of the algorithm, analyze different PEC enclosures and determine the quality of the method for lossy an lossless mediums. Finally, a section where possible future works is presented in order to improve the numerical results and expand the given MWI application to 3D problems.

6.1 Constraints of CSIM

In this section some 2D problems are analyzed with CSIM to observe the behaviour of the inversion algorithm for different situations that performs non optimal inversion result, even non legible. The conclusions that we extract from this study will be applied in future simulations to obtain the best possible results.

6.1.1 Contrast Source Influence

As commented in Section 5.4 one of the main parameters that should be considered in the problem design performed by GiD and MATLAB is the value of the contrast source χ. Then,

we present some CSIM results that works as we conclude from [13] where a interpretation of the numerical results for different backgrounds is developed in CSI applications.

In Section 5.4 a short analysis for contrast limitations was introduced, Fig.5.1 represented a simple scenario with a little circle as OI that was compared against the same geometry problem with different contrast conditions. We extracted some conclusions from commented CSI results. However we noticed that the problem could be more important. Now, we present the same analysis for a more complex 2D scenario according to dielectric properties and dimensions of the background compared with scatterers. A circular enclosure with r= 0.36m is the chosen PEC interface that surrounds the imaging domain, it is based on a square with side length equals to 0.32m and a triangle of l= 0.23m as OI. The permittivities for each region are given by $\epsilon_b = 3 - j0.8988$ and $\epsilon_r = 5 - j0.8988$ at 1GHz. The forward solver measurement was executed by 16 transmitters/receivers placed at a circular distance of 0.3m. The number of nodes involved in the imaging domain, $\mathcal{D}$, is equals to 1963 from the total N= 7994.

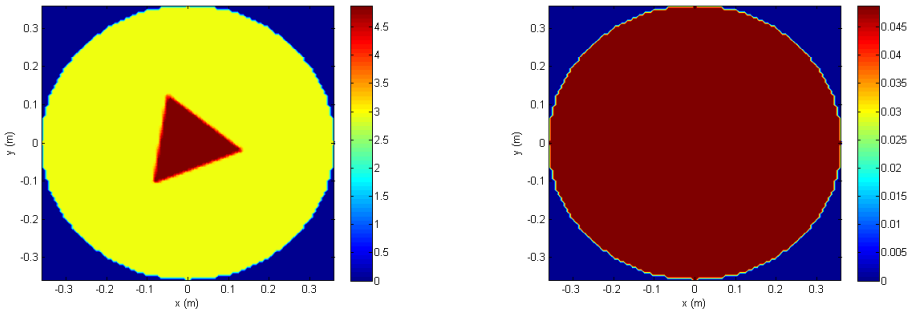

(a) (b)

Figure 6.1: $|\chi| < 1$: (a) Real relative permittivity ϵ_r' (b) Conductivity σ

If we calculate the contrast source using expression (5.1), we can determine that $|\chi| < 1$. Let's compare the results in Fig.6.2 with other possible conditions of χ. In Fig.6.3 we present results for the same scenario where the real part of the contrast has been forced to be lower than zero. We can observe that reconstructed contrast and dielectric results present lower quality than $|\chi| < 1$ and positive sign case. The results in terms of error for both contrast situations can be observed in Fig.6.6 and Fig.6.7. While the error for $|\chi| < 1$ is equals to 30%, the simulation with negative sign in contrast performs an error over 43% at 200 iterations.

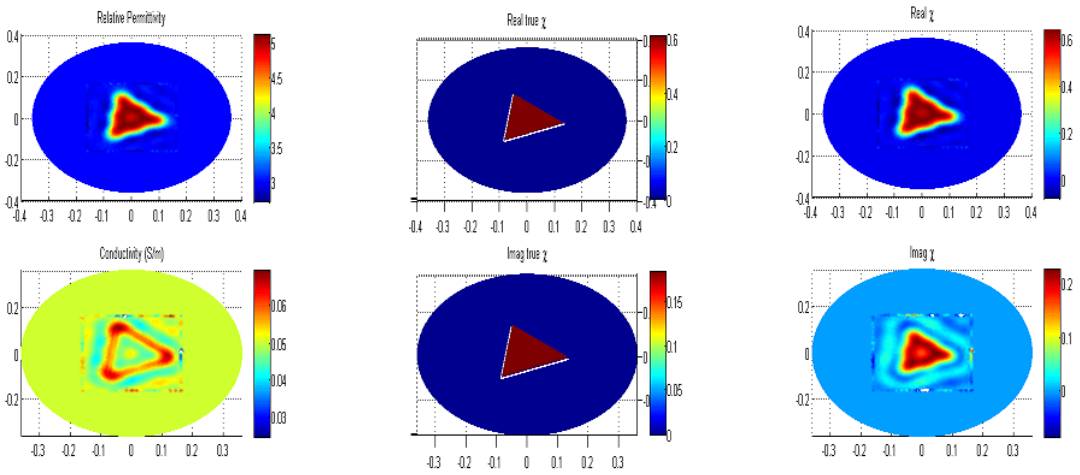

(a) (b) (c)

Figure 6.2: $|\chi| < 1$: (a) Reconst. diel. properties (b) True Re(χ) and Im(χ) (c) Reconst. Re(χ) and Im(χ)

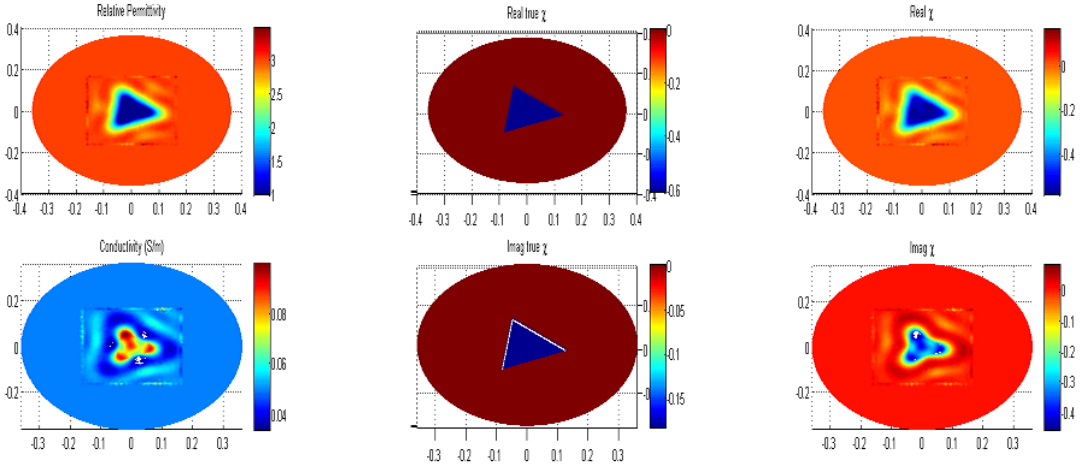

(a) (b) (c)

Figure 6.3: $re(\chi) < 0$: (a) Reconst. diel. properties (b) True Re(χ) and Im(χ) (c) Reconst. Re(χ) and Im(χ)

The next χ case simulation performs worse results than $re(\chi) < 0$ problem. The only difference with last simulations is the chosen dielectric scenario that presents a $|\chi| > 1$. This

condition performs a totally wrong behaviour in CSI computation. The complex permittivity for background is equals to $\epsilon_b = 2 - j0.8988$ and the OI, $epsilon_r = 15 - j0.8988$ at 1GHz. The error in this simulation is over 99% the functional cost decreases slightly less than $10^{-0.7}$ while $|\chi| < 1$ problem minimize the functional cost until $10^{-3.5}$ for the same number of iterations.

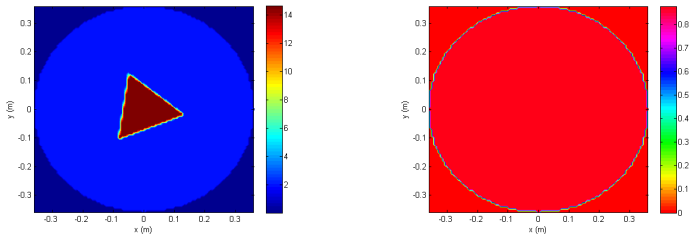

(a) (b)

Figure 6.4: $|\chi| > 1$: (a) Real relative permittivity ϵ_r' (b) Conductivity σ

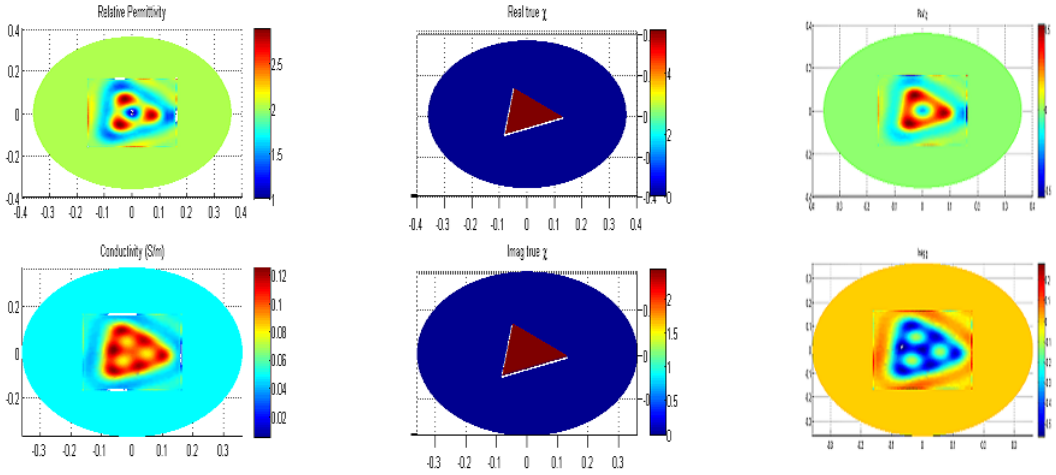

(a) (b) (c)

Figure 6.5: $|\chi| > 1$: (a) Reconst. diel. properties (b) True Re(χ) and Im(χ) (c) Reconst. Re(χ) and Im(χ)

In Fig.6.6 and Fig.6.7 the corresponding errors an cost functional are shown. After this analysis all the future MWI scenarios will consider $|\chi| < 1$ and normally also $re(\chi) > 0.25$ for other reasons.

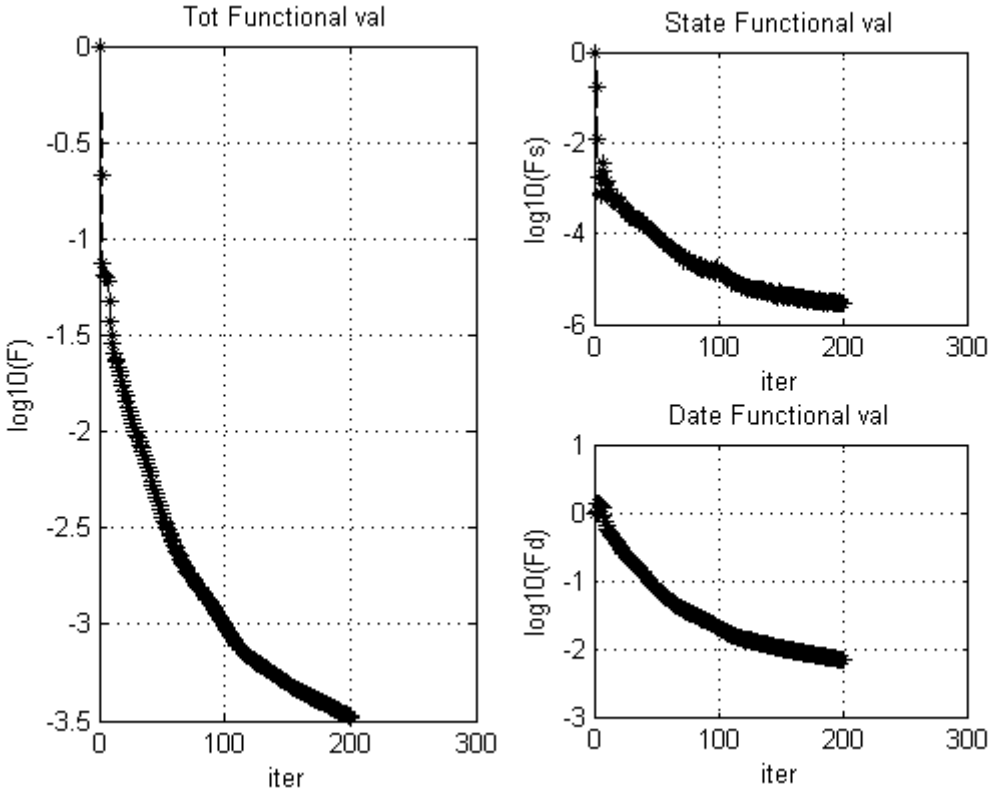

(a)

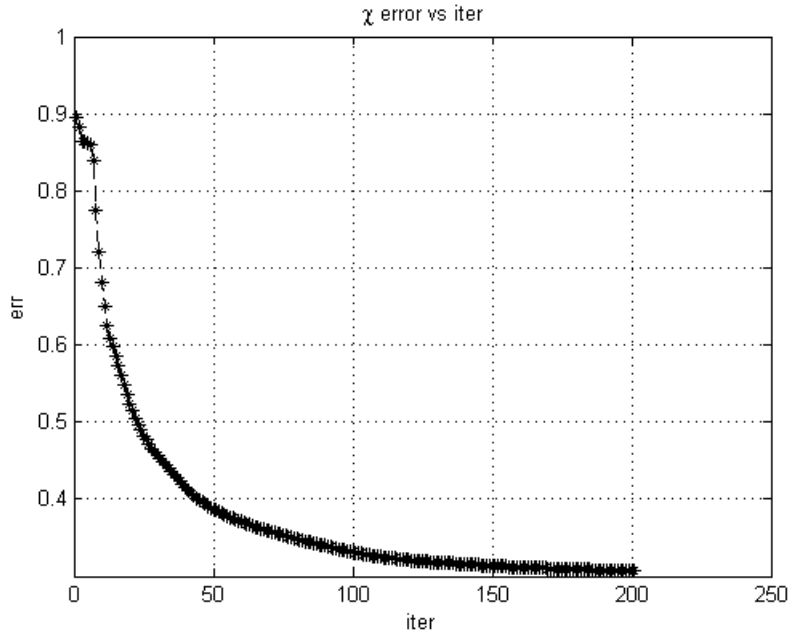

(b)

Figure 6.6: $|\chi| < 1$ (a) Total, state and domain functional cost (b) Error vs Iterations

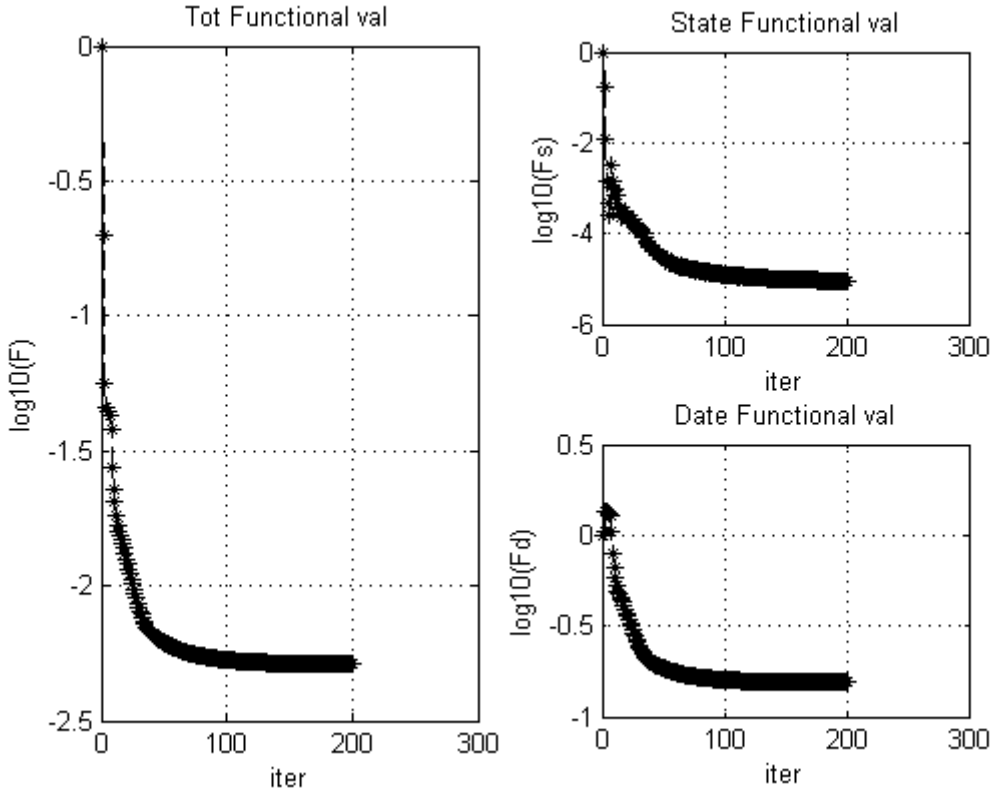

(a)

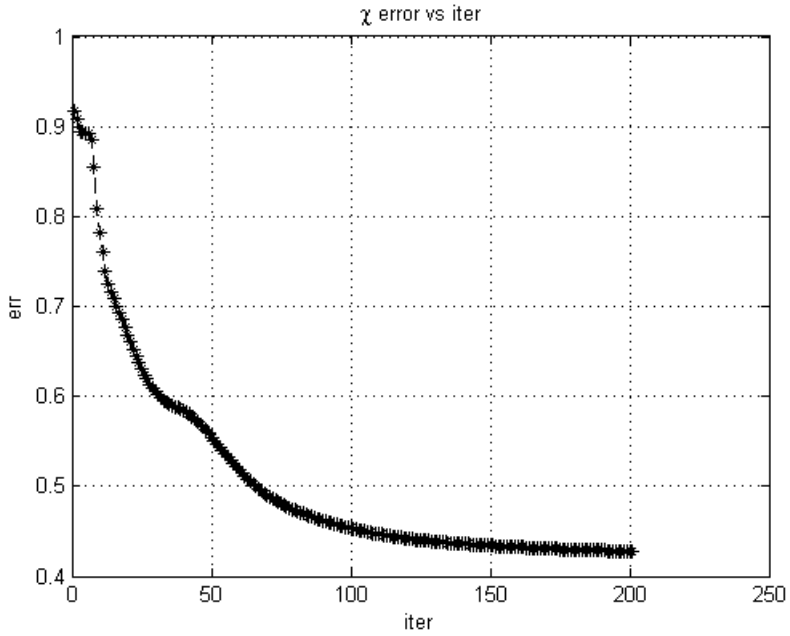

(b)

Figure 6.7: $re(\chi) < 0$ (a) Total, state and domain functional cost (b) Error vs Iterations

Notice that the background choice is essential in CS algorithm due to the contrast limitations, so that, we should match the medium, according to a certain frequency of work, to obtain the most optimal possible results. In addition, other aspects can perform a better or worse CSIM quality. They are the target of study during the next subsection.

6.1.2 Frequency

There are other design parameters to consider in our MWI scenario. The results do not depend only on contrast source that is really the most important constraint, they also depend on other aspects as frequency of work. During Chapter 4, we concluded that FEM working with high frequencies implies higher number of nodes in FEM matrix, which means an increment of the computational cost. This happens also for the inversion algorithm, where more number of nodes means more time to compute a certain number of iterations. If our processor was more powerful, we would have more possibilities to simulate very complex scenarios in a wider bandwidth. However, the problem analyzed here is different, we are focused on the consequences of using a certain frequency for CSI results in terms of error. We will present two different studies.

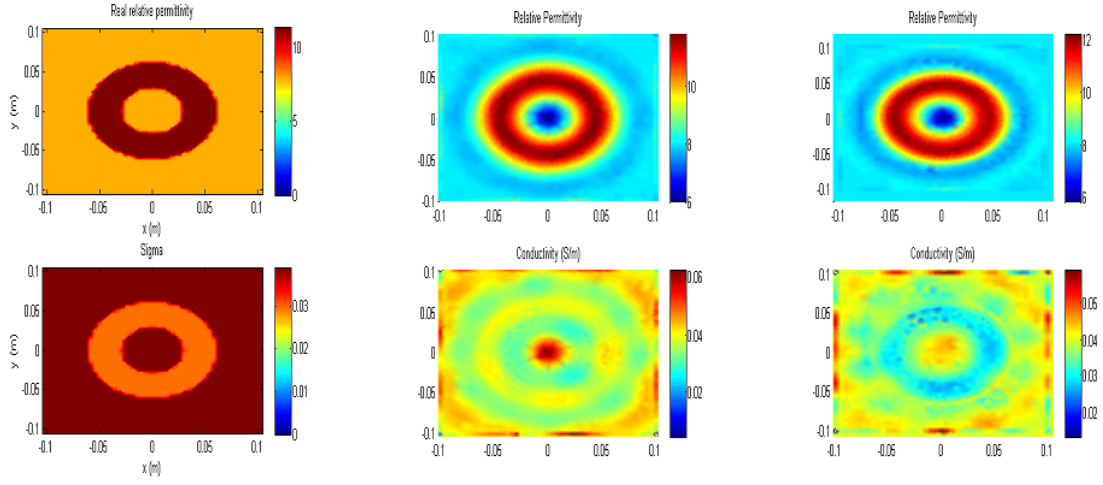

(a) (b) (c)

Figure 6.8: (R/λ_{bk}) analysis (a) Diel.Properties (ϵ'_r,σ) (b) reconst.results r= 0.21m (c) reconst.results r= 0.28m

Firstly, a certain imaging domain is inserted into two different circular enclosures with the same complex dielectric for the background, $\epsilon_b = 8 - j0.719$. The imaging domain is depycted in Fig.6.8(a) where dielectric properties are shown, $\epsilon_r = 11.6 - j0.539$ at $f_o = 1$GHz, and in Fig.6.9(a) where constrast source is represented. First, we computate the inversion algorithm on a PEC interface with radius, r= 0.21m. Second computation, the imaging domain is analyzed with a circular enclosure of r= 0.28m. The aim of this analysis is to determine some differences in numerical error results and discover their possible reasons.

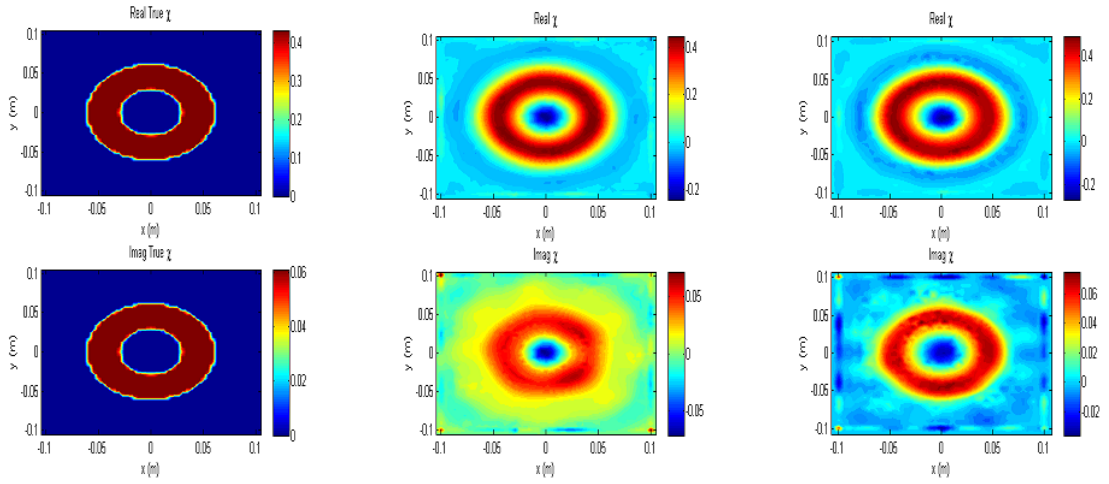

(a) (b) (c)

Figure 6.9: (R/λ_{bk}) analysis (a) True χ (b) Reconst.χ r= 0.21m (c) Reconst.χ r= 0.28m

Notice that the diameter of the circular enclosure, call it as R, in first computation is over $2\lambda_{bk}$ and in the second case it is equals to $2.75\lambda_{bk}$. The reconstructed contrast source for each simulations can be observed in Fig.6.9

Finally, we will perform other analysis about the complex permittivity of the background. In Section 6.1.1 we concluded that the behaviour of the background in a CS problem was an essential point. We need to understand more about the material behaviour of mediums than only the limitations for the contrast source. The imaging domain $\mathcal{D}$ depycted in Fig.6.8(a) continues to be our OI and we use the case of a circular enclosure with r= 0.21m. We compare the simulation results for $\epsilon_b = 8 - j0.719$ and $\epsilon_r = 11.6 - j0.539$ at $f_o = 1$GHz against a new contrast scenario defined by a background,$\epsilon_b = 8 - j1.438$ and $\epsilon_r = 11.6 - j1.0785$ at $f_o = 500$MHz.

Tabla 6.1: Comparision between 3 simulations

f_o [GHz]	$\|\chi\|$	R_PEC [m]	R/λ_{bk}	$\frac{\epsilon_b''}{\epsilon_b'}$	err(%)
1	0.448	0.21	2	0.089	43.8
1	0.448	0.28	2.75	0.089	42
0.5	0.445	0.21	1	0.179	55

Although the two simulations have the same conductivies, the variation of frequency generates a new tangent of losses, $\frac{\epsilon_b''}{\epsilon_b'}$, which implies changes in contrast results as we can observe in Fig.6.10.

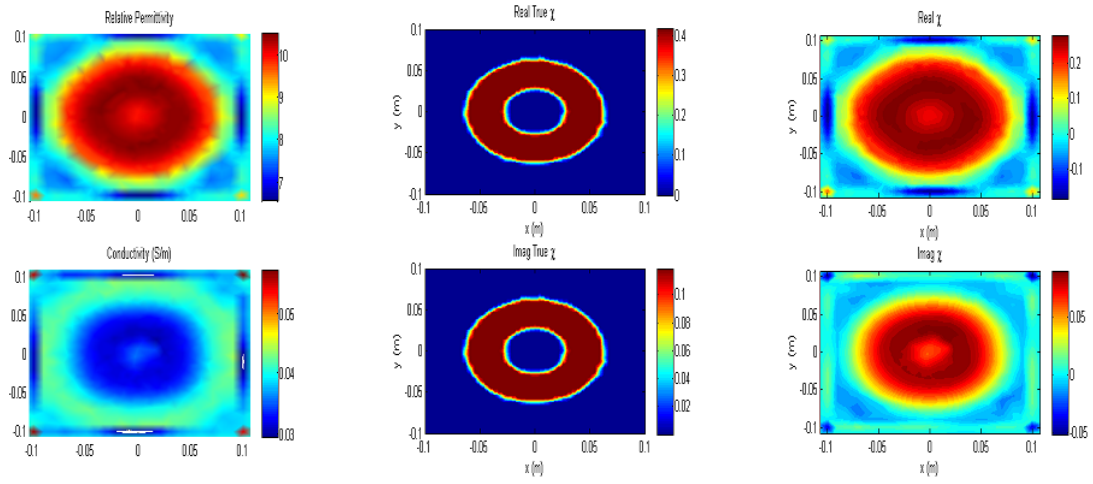

(a) (b) (c)

Figure 6.10: f_o = 500MHz: (a) Reconst. diel. properties (b) True Re(χ) and Im(χ) (c) Reconst. Re(χ) and Im(χ)

Let's to visualize the error terms in Table 6.1 for each simulation after 200 iterations, on this way is easier to understand the solutions of CSIM for each case. We can determine that the simulation number 3 presents the worst results and the number 2 the best results. The contrast limitation is not important in this experiment due to the similar $|\chi|$ for each simulation. The reason for explaining these numerical results is due to the PEC enclosure diameter in terms of background wavelength. On one hand, different frequencies perform different values for tangent of losses. On the other hand, different frequencies imply different wavelengths. This means that

a "low-loss" medium can perform more attenuation than a loss medium because the attenuation lasts more distance in terms of wavelength. On this way, simulation number 3 presents the highest tangent of losses but the lowest ratio R/λ_{bk}, so that, the reflections are less attenuated what is counterproductive to FEM solver. Comparing simulation 1 and 2 happens the same, case 1 present a lower R/λ_{bk} which results to a lower attenuation.

6.1.3 Section Conclusion

Here, we try to collect the possible conclusions that we have extracted from all simulations developed above. We have developed a CS problem based on three different contrast profiles in Section 6.1.1. The results conclude that background medium should match the imaging domain in order to obtain a correct working. Profiles defined by $|\chi| < 1$ work better than $|\chi| > 1$.

Later, an experiment was executed with the aim of visualize the behaviour of inversion algorithm according to the frequency of work used in FP. Three different scenarios were compared. Two of them at the same frequency but with different ratio R/λ_{bk}, being R the radius of the circular PEC enclosure. The other one, presents the same dielectric properties but the losses were higher in background due to a lower frequency. Then, we were comparing three scenarios with different ratio R/λ_{bk} and the same dielectric profile. The numerical results conclude that the simulation with highest dimensions in terms of wavelength generates a better solution, this means that losses depend on both, dielectric properties and frequency of work.

6.2 PEC Enclosures

During this section we will discuss about the most benefit PEC enclosure that we can design for a certain MWI application based on CSIM. We will present a profile for different shapes. On this way, we may know which of them would be the most suitable for our experiment. In enclosure analysis we must consider the distance from the PEC interface to the OI, and the possible reflections that could happen for different shapes.

Imagine that we have three cylinders with equal dimensions but with different material properties. The identity of each of them are unknown. To identificate each cylinder, we perform the CSIM for every cross section of all targets at the same measurament, placing them at the

same distance between each other. We will compare the results for three different PEC enclosure shapes. Notice that all images refers only to the imaging domain $\mathcal{D}$.

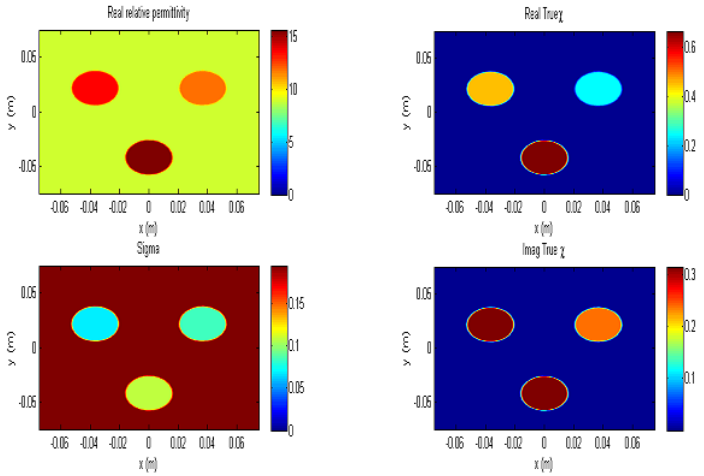

(a) (b)

Figure 6.11: PEC study profile: (a) Dielec.Properties (b) True Contrast Source

Firstly, the profile for dielectric properties and contrast source are depycted in Fig.6.12 for the imaging domain $\mathcal{D}$. The complex relative permittivity for each OI surface is: $\epsilon_{sc1} = 14 - j0.8988$; $\epsilon_{sc2} = 12 - j1.0913$; $\epsilon_{sc3} = 16 - j1.4123$ at $f_o = 1.4$GHz. In next figures the CS results are shown for each simulation:

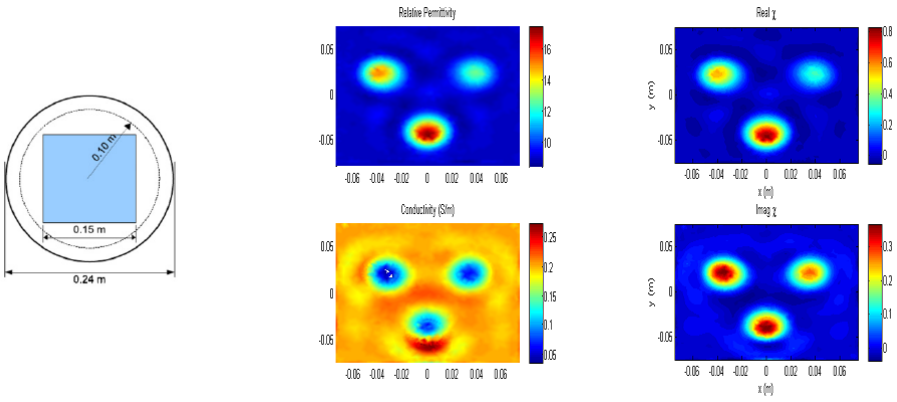

(a) (b) (c)

Figure 6.12: Circle: (a) Enclosure shape (b) reconst.dielectric prop. (c) reconst.contrast source

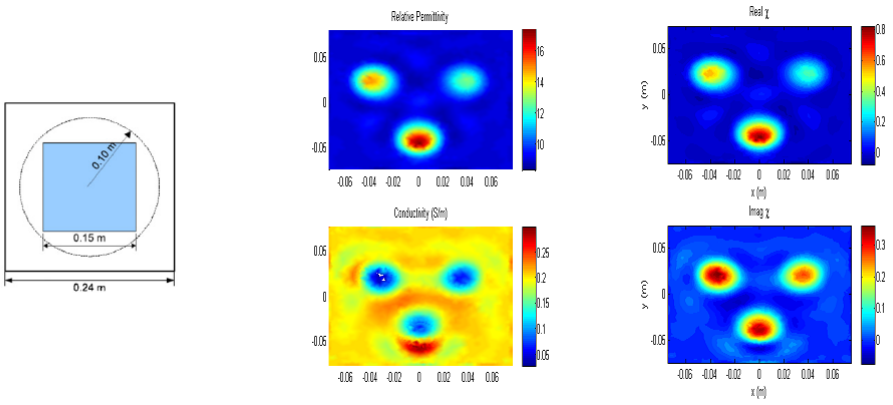

(a) (b) (c)

Figure 6.13: Square: (a) Enclosure shape (b) reconst.dielectric prop. (c) reconst.contrast source

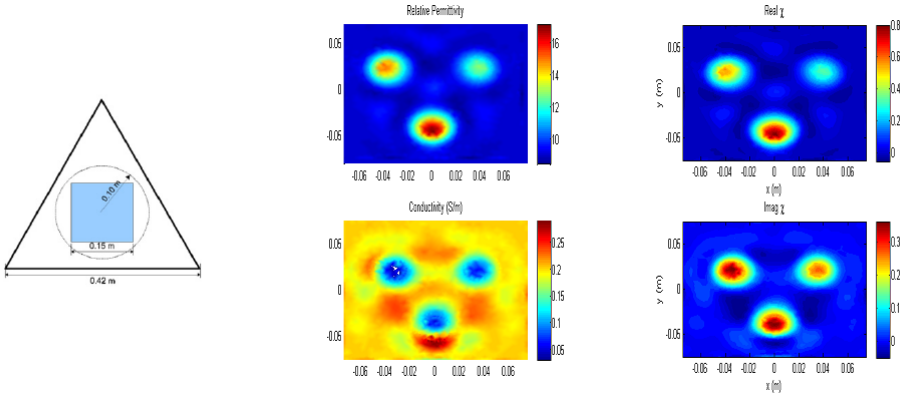

(a) (b) (c)

Figure 6.14: Triangle: (a) Enclosure shape (b) reconst.dielectric prop. (c) reconst.contrast source

As commented above, the imaging domain is centered within three different PEC enclosures of different shapes: a circle of radius 0.12m, a square with side of 0.24m and an equilateral triangle of side length equals to 0.42 m. The dimensions of each enclosure are depicted in figure 6.13(a), 6.14(a) and 6.15(a) (images obtained from [9] beside CS results).

Tabla 6.2: Comparision between PEC shapes

Simulation	err(%)	$log_{10}(F)$	$log_{10}(F_s)$	$log_{10}(F_d)$
Circle	51	-3.61	-5.5	-1.8
Square	52	-3.375	-5.4	-1.7
Triangle	52.5	-3.65	-5.7	-1.5

In all enclosures, the OI is surrounded by a lossy background medium of relative permittivity, $\epsilon_b = 9 - j2.568$ for $f_o = 1.4$GHz. The OI is interrogated by 24 antennas. For all enclosures, the transmitting and receiving points are evenly spaced and located on a circle of radius 0.1m.

The inversion domain $\mathcal{D}$ is a square centered in the middle of the enclosures with the square's side length equal to 0.15 m. The number of unknowns in the total computational domain are between 5000-6000 nodes for all cases. For any enclosure, the unknowns are positioned on the vertices of triangles in an unstructured arbitrary mesh.

The reconstructed results for each enclosure shape are very similar, so we can understand that there are not consequences in shape choice. To be totally sure, we identificate the error between true and reconstructed contrast source at the last iteration, number 550. The lowest error and functional cost for each simulations are presented in Table 6.2. We can observe that the circular shape performs better results that the others two cases. However the difference in terms of error is very small, so we can conclude that all shapes perform very similar CS results. This means that the attenuation of reflections are similar in each background.

6.3 Background Choice

As commented in Section 6.1 the background presents a huge influence in CSI behaviour. The choice of this region should be chosen considering the contrast limitations and the relation between dimensions and frequency. In addition, assuming certain losses in background, our scenario would be limited to a shorter or wider possiblities. During the described simulations developed in this section we will observe how for a higher losses in the medium the results will be better, however, in lossless mediums appears some problems in CSI computation due to the

quality of synthetic data.

6.3.1 Lossy Mediums

A new inhomogeneous scenario is presented, based on a square OI of side equals to 0.07m inside a bigger one of l= 0.12m. The smallest scatterer presents a complex permittivity, $\epsilon_r = 12 - j0.449$, and the bigger, $\epsilon_r = 8 - j1.123$. The biggest OI is surrounded by a circular PEC with radius, r=0.28m, and background permittivity, $\epsilon_b = 6 - j1.7975$ at 800MHz. The measurement was performed by 16 antennas allocated along a circle of radius 0.22m. The imaging domain, $\mathcal{D}$, has a number of nodes equals to 1590, while the total domain is formed by 6759 nodes. In Fig.6.15(a) the profile is shown. In the same figure reconstructed dielectric properties and the initial guess are also included.

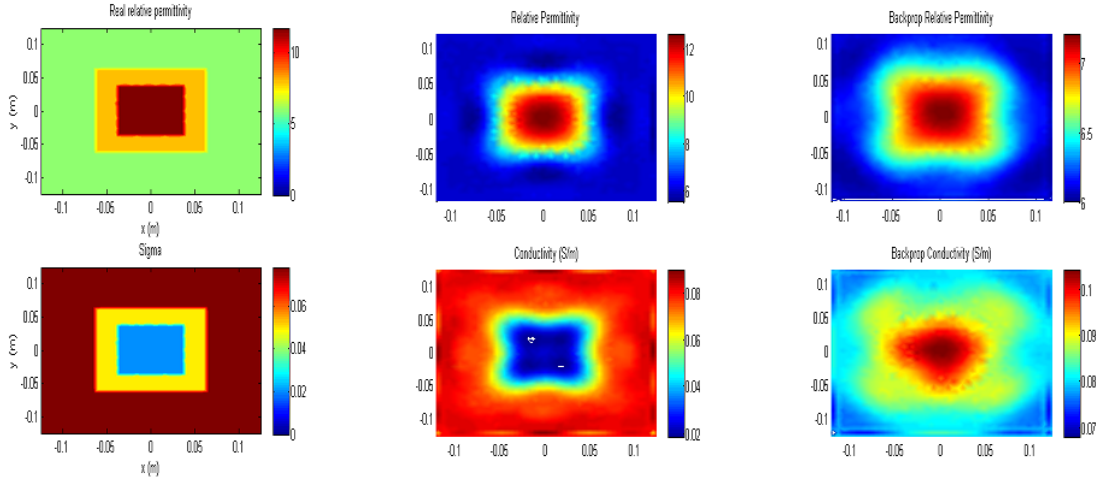

(a) (b) (c)

Figure 6.15: Squares: a) True diel. properties (b) Reconst. diel. properties (c) Initial guess

The results after 220 iterations are optimal, with an error over 25%. This means that the error has descreased very fast from inital guess and reconstructed solution. In Fig.6.16 the results related to the real and imaginary part of contrast source, χ, are depycted. Like other simulations, the worst results appears in boundary interfaces due to the mix of different dielectric properties. In numerical terms, quality of given results can be determined in Fig.6.17 where cost functional and error as a function of performed iterations are depycted.

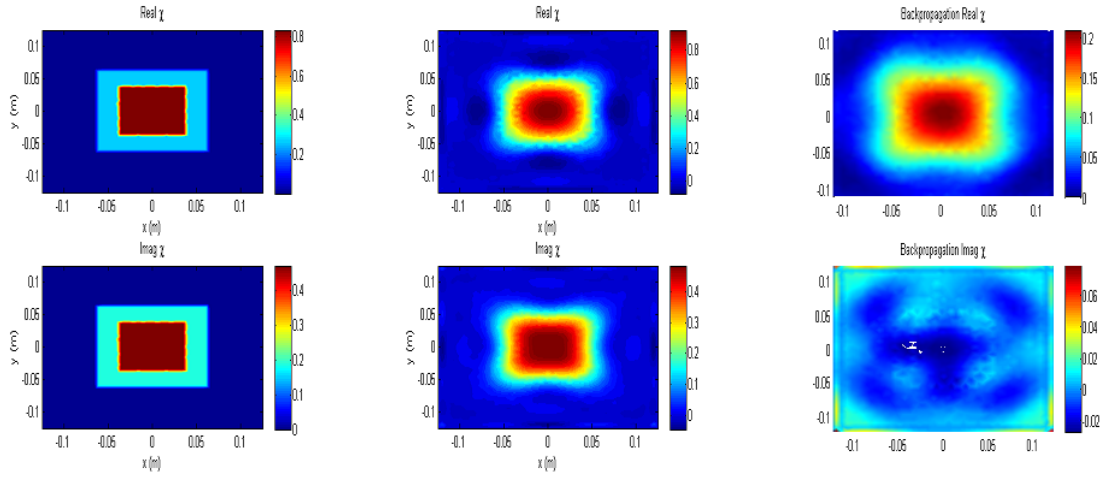

(a) (b) (c)

Figure 6.16: Squares: a) True χ (b) Reconstructed χ (c) Initial guess

In next figure, the error and functional costs are presented. The minimization of functional cost arrives at $10^{-4.5}$. So we are very near from the optimous target of obtain 10^{-5} as result.

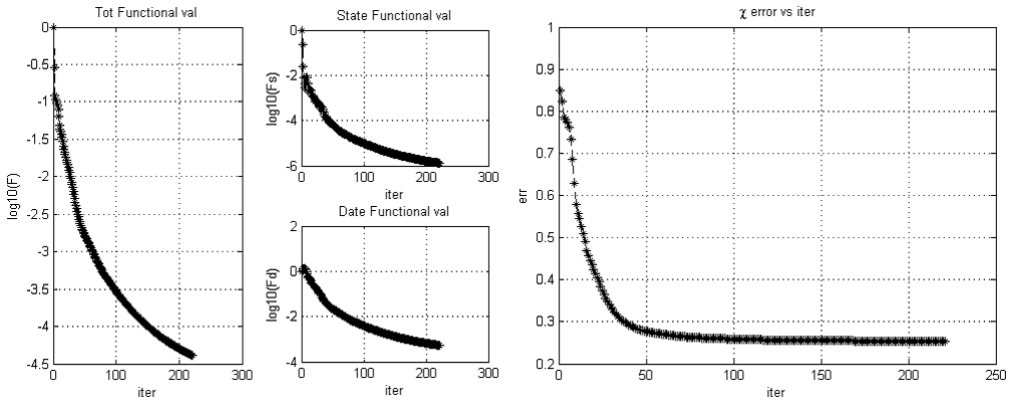

Figure 6.17: Squares: Total, state and domain functional cost; Err: Error vs Iterations

Now we present a very popular profile known as E-phantom, in this case we consider a low lossy background with a complex relative permittivity, $\epsilon_b = 16 - j1.8$ at $f_o = 1.2GHz$. The background and OI are inside a circular enclosure with r= 0.17m. The E-phantom is based on an inhomogeneous dielectric properties, the big part, $\epsilon_r = 33 - j2$ at $f_o = 1.2GHz$ and for the inclusion and the right-most feature of the OI at $f_o = 1.2GHz$ is $\epsilon_r = 33 - j8.33$.

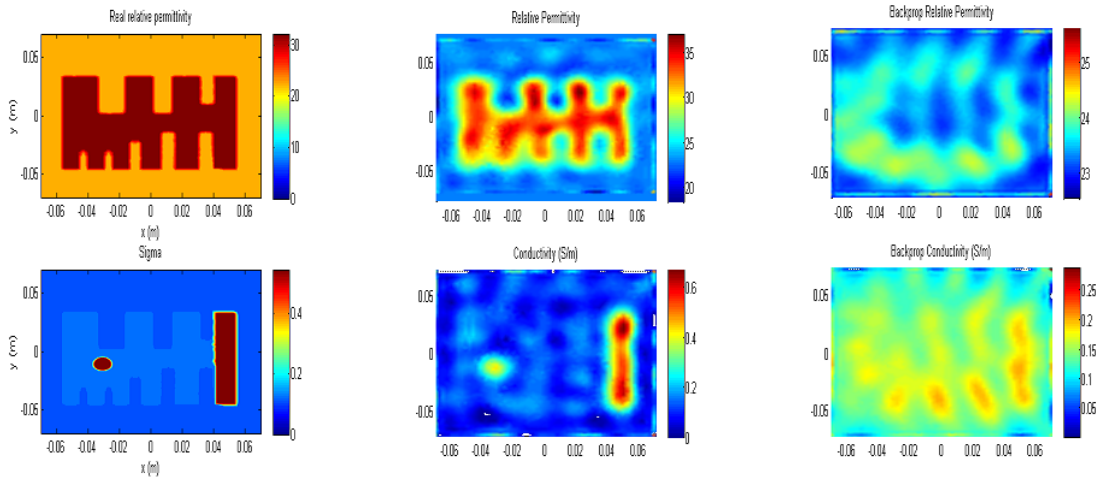

(a) (b) (c)

Figure 6.18: E-phantom: a) True diel. properties (b) Reconst. diel. properties (c) Initial guess

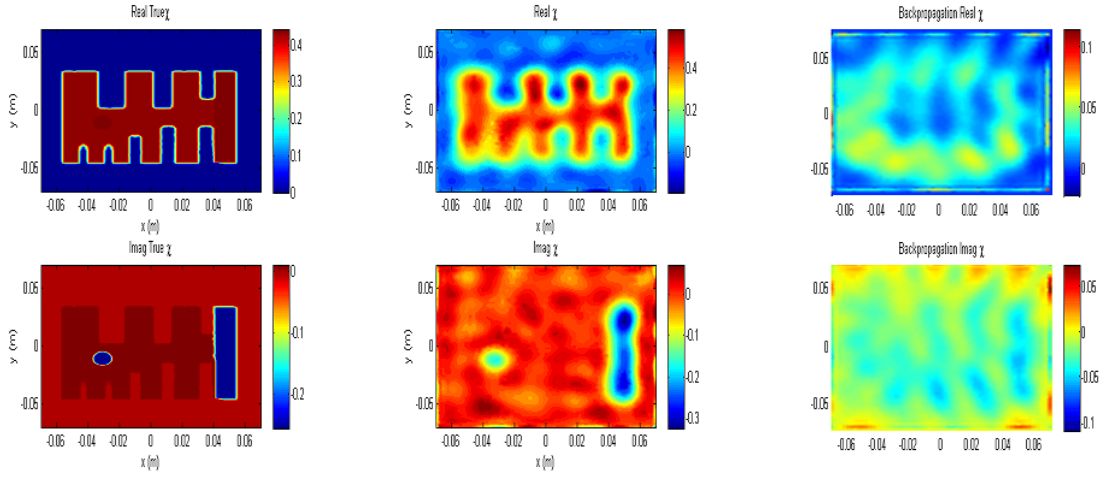

(a) (b) (c)

Figure 6.19: E-phantom: a) True χ (b) Reconstructed χ (c) Initial guess

The imaging domain is based on a square with side equals to 0.14m with a total of 2936 nodes while the total domain Ω has 13051. This scenario is illuminated by 16 antennas in a circle of r=0.12m. The true, reconstructed dielectric properties and the corresponding initial guess are

shown in Fig.6.18. The true, reconstructed contrast source and the corresponding initial guess are depycted in Fig.6.19. We can identificate each of the two regions that form the e-phantom OI, this means that the CS solution presents a high level of quality, obtaining an error of 38.1% after 751 iterations including the initial step that can be analyzed in Fig.6.20. If we observe reconstructed results, in the part of the profile were the lines are closer, the resolution does not let us to identificate the different lines, showing them as an unique part.

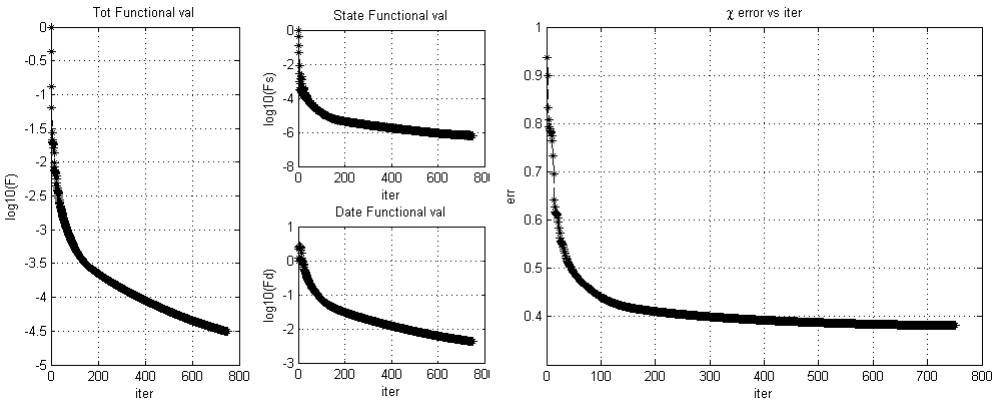

Figure 6.20: E-phantom: Total, state and domain functional cost; Err: Error vs Iterations

6.3.2 Lossless Mediums

Now, we present CS results using lossless mediums. We will observe how the quality of reconstructed profile decreases. As commented other times, a lossless background does not present losses, this implies that the number of reflections that happen in PEC interface, are not attenuated or removed along their propagation. This situation doesn't let inversion algorithm to work on the correct way. The problem is related to synthetic data processing, namely, the *Forward Problem* solved using FEM. The simulated electric field along the total domain Ω is not a real solution due to the great number of reflections that illuminate the imaging domain $\mathcal{D}$. Then, CSIM reconstructs a certain target that does not represent the OI.

Notice that this research work tries to explain how a inversion method based on MWI lets us to discover the material properties of an unknown target. In real applications, the *Forward Problem*, as commented in Chapter 3, is solved by MWI instruments. However, in our case, the data are synthetic what implies some limitations.

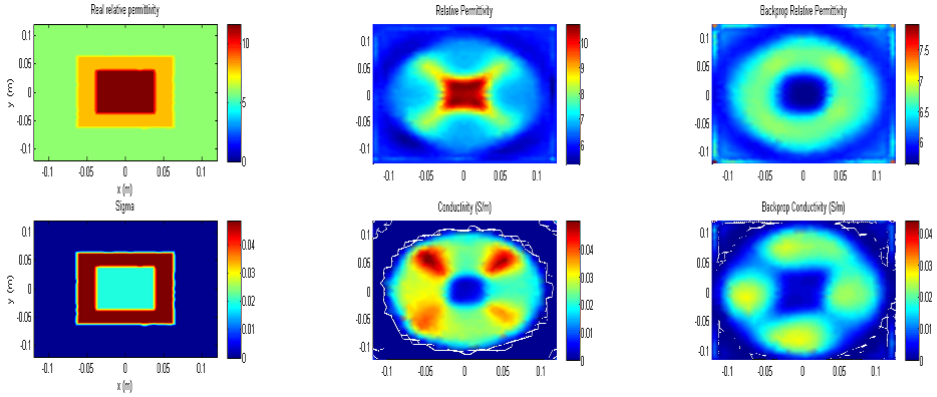

(a) (b) (c)

Figure 6.21: Lossless I: a) True diel. properties (b) Reconst. diel. properties (c) Initial guess

Firstly, we present the same dielectric profile than in Fig.6.15(a) but inside a lossless background with complex permittivity, $\epsilon_b = 6$ at 800MHz. Remember that the inhomogeneous OI is based on a little square with side equals to 0.07m and complex permittivity, $\epsilon_r = 12 - j0.449$ at 800MHz, inside a bigger square of side 0.12m, and $\epsilon_r = 8 - j1.123$ at 800MHz. The imaging domain $\mathcal{D}$ is a square with a side, l= 0.24m. We can observe how the reconstructed dielectric properties identifies approximate values for each of the two scatterers regions but the placement and shape of them are not correctly defined. Let's depyct the contrast results in order to stablish more conclusions.

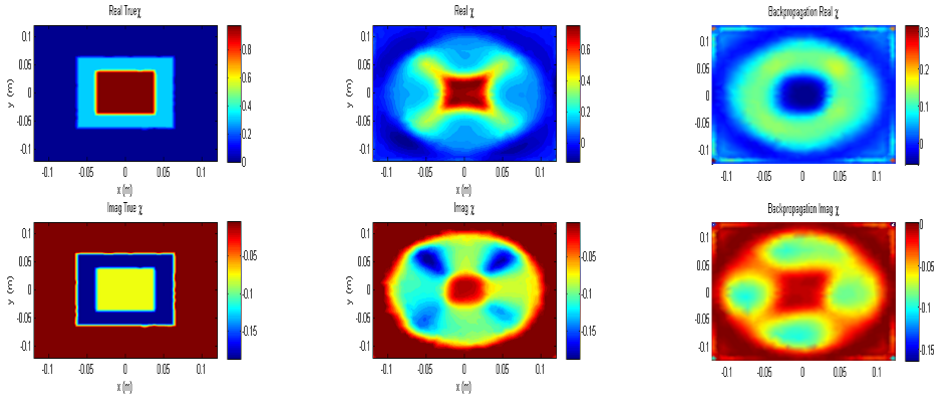

(a) (b) (c)

Figure 6.22: Lossless I: a) True χ (b) Reconstructed χ (c) Initial guess

The results for reconstructed contrast work in the same way, the contrast error is not too high because the numerical results don't differ greatly from true values. However appear strange shapes inside the imaging domain due to the strong reflections that are involved in electric illumination. This phenomenon implies errors in measuraments during FP solver procedure. So that, the reconstructed imaging domain does not represent the real target. The numerical error after 70 iterations is equals to 49%. In Fig.6.23 the error functions can be observed.

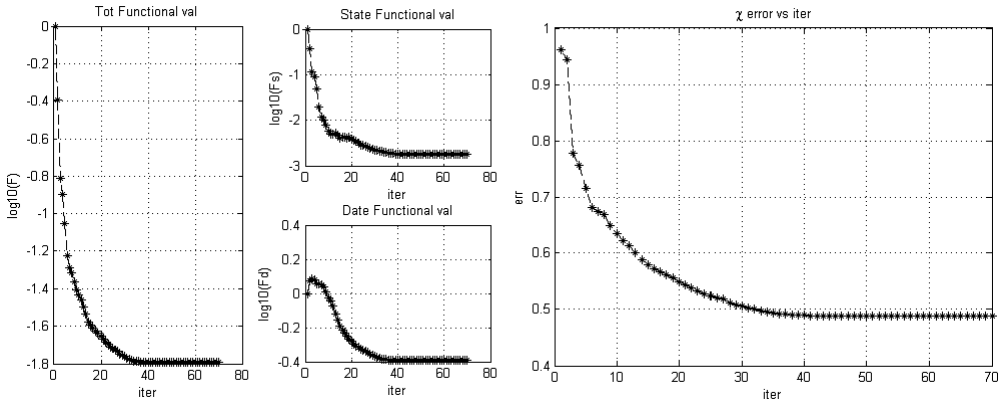

Figure 6.23: Lossless I: Total, state and domain functional cost; Err: Error vs Iterations

With the next simulation we can compare the results between E-phantom profile defined in Fig.6.18(a) against the same shape inside a lossless medium. In this case, we have chosen a homogeneous OI with a complex permittivity equals to $\epsilon_r = 5.9 - j1.7975$ at $f_o = 800$MHz, and a background permittivity, $\epsilon_b = 4.2$ at $f_o = 800$MHz. Obviously the number of nodes involved in the total domain has descreased due to a low frequency and permittivity value: 4480 nodes.

In Fig.6.24 is possible to conclude that using the same enclosure and Tx/Rx antennas placement, the reconstructed results have descreased greatly from lossy case. Due to the resolution ($\lambda_b/4$ is too high) the target shape and placement is not identify well. As happens in first lossless simulation, the contrast error could be considered acceptable, however, detect correclty the placement and patterns of the OI is a main target for MWI applications as tomography. The constast error reachs a value of 49.5% after 400 iterations.

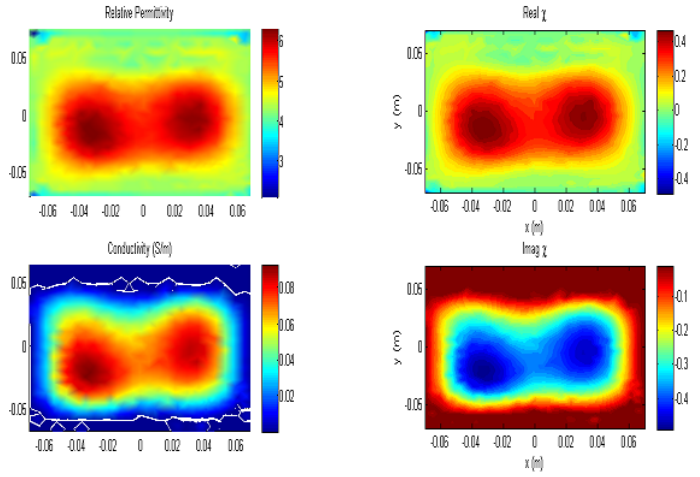

(a) (b)

Figure 6.24: Lossless II: (a) Reconst.Dielectric Properties (b) Reconst.Contrast Source

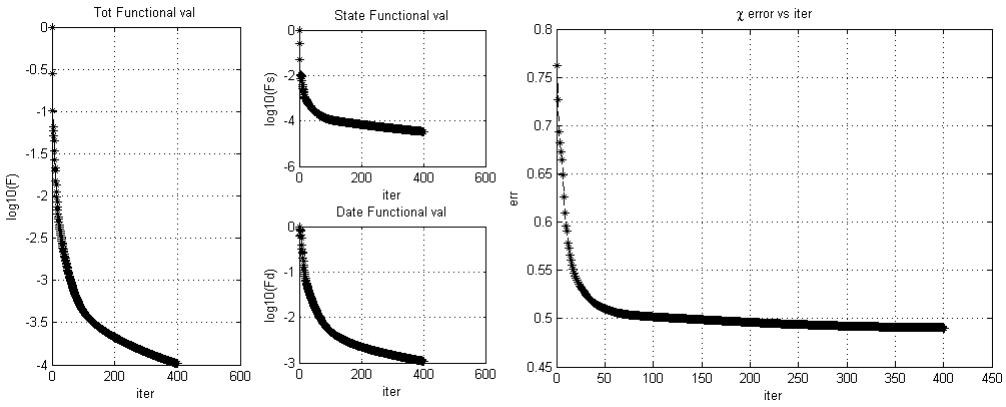

Figure 6.25: Lossless II: Total, state and domain functional cost; Err: Error vs Iterations

6.4 Biomedical Issues

During this section several simulations related to possible real biomedical experiments are computed. We will show CS results for two complex scenarios that represent two different biomedical MWI applications. The high wavelength value for each dielectric region that are part of the imaging domain $\mathcal{D}$ implied a huge computation in terms of time due to the number of nodes generated after meshing. The aim of these experiments is to analyze if our method can

Tabla 6.3: Forearm properties

Skin	Muscle	bones
$46 - j15$	$55 - j16$	$13 - j2.3$

reconstruct real 2D scenarios using the techniques developed during this research work.

Firstly, a bone issue is performed. Imagine that we want to determine the health of a certain forearm in a medical bone diagnosis. The forearm is based on different parts. In Table 6.3 different dielectric properties are shown. The Imaging Domain $\mathcal{D}$ is a square od side equals to 0.1m inside a background with $\epsilon_b = 76.56 - j15$ at 1GHz. This imaging domain is surrounded by a circular enclosure with r= 0.14m. A total of 16 antennas are interrogating the imaging domain at a frequency of 1GHz. The total domain Ω is based on 19707 nodes, 3984 are involved in $\mathcal{D}$. Dielectric properties of the imaging domain are depycted in Fig.6.26.

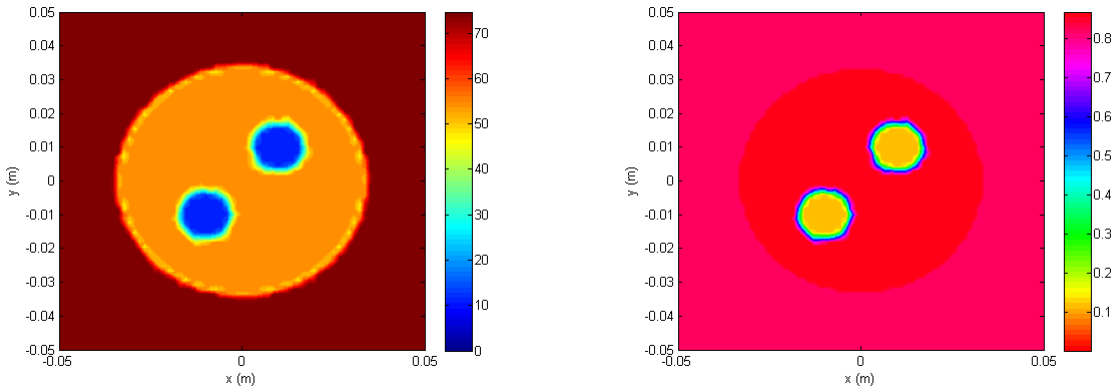

(a) (b)

Figure 6.26: Forearm: (a) Real relative permittivity ϵ_r' (b) Conductivity σ

In Fig.6.27 reconstructed constrast is compared against the true ones. We can observe how the bones are localized, however, the skin is not detected. Surely, it is due to errors in FP solver due to the close region of skin. In next figure we can determine the quality of results in terms of error a functional cost minimization. We obtain an error equals to 0.338 after 415 iterations. Then, the experiment has performed very good results.

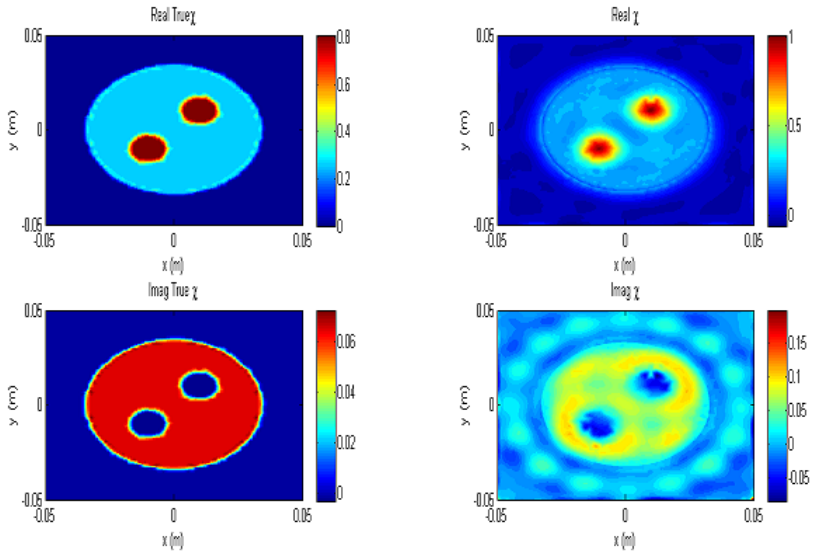

(a) (b)

Figure 6.27: Forearm: (a) True Contrast (b) Reconst.Contrast

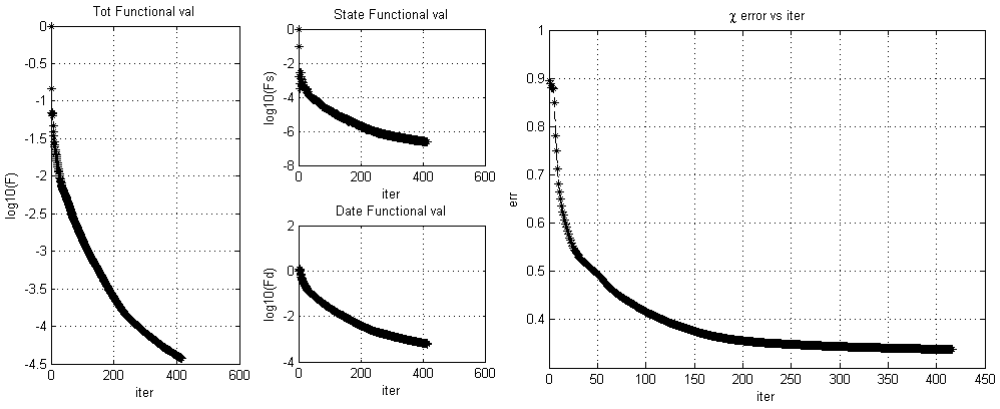

Figure 6.28: Forearm: Total, state and domain functional cost; Err: Error vs Iterations

The second experiment is more complex. We try to analyze a model of a brain exhibiting symptoms of a stroke. It consists of an outer skin region followed by the skull, the cerebral-spinal fluid (CSF), the gray matter (GM) and the white matter (WM). A stroke region representing a blood clot is located on the left side of the white matter region. The dielectric properties of each region are described in Table 6.4 at $f_o = 1$GHz. The imaging domain is based on 6171 nodes from the total 26858 nodes that form the computational domain. Furthermore, the imaging

Tabla 6.4: Brain Model

Skin	Skull	CSF	GM	WM	Stroke
$46 - j15$	$40 - j2.4$	$69.3 - j42.8$	$52.8 - j16.9$	$38.6 - j9$	$61.1 - j28.5$

domain is illuminated by 16 antennas placed in a circle of r= 0.16m inside a background with $\epsilon_b = 35 - j13$ at 1GHz. The PEC enclosure is also a circle of radius equals to 0.28m. Profiles for dielectric properties and contrast are depycted in Fig.6.29.

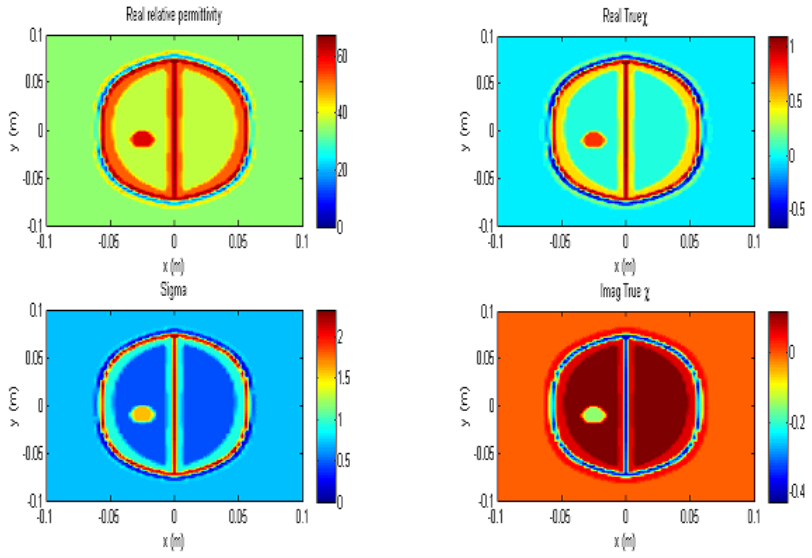

(a) (b)

Figure 6.29: Brain: (a) Dielectric properties (b) True Contrast

In next figures, the reconstructed results and error terms are showm. It is easy to observe how the quality of reconstruction is not acceptable. The different regions are not identificated, and they appear mixed between each other. In addition, the stroke has not been detected, this means that the MWI application does not work for this biological experiment. If we analyze the error, we can determine that the error after 500 iterations is equals to 0.9465 and the cost functional related to the data is over $10^{-0.1}$ while our optimal result is 10^{-6}.

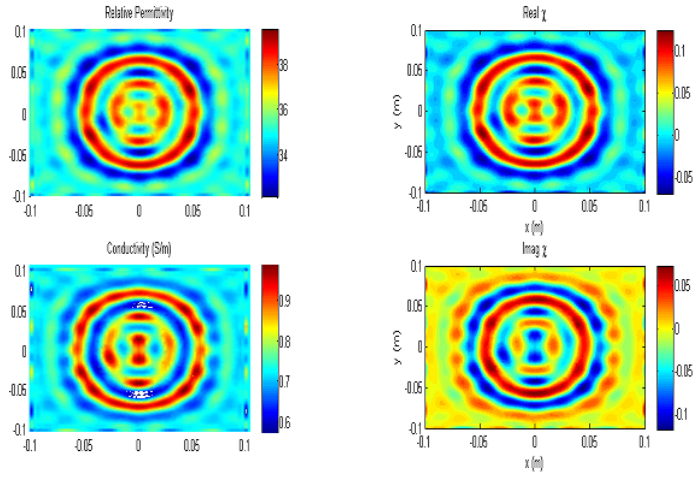

(a) (b)

Figure 6.30: Brain: (a) Reconst.Diel.Properties (b) Reconst.Contrast

We can conclude that we only are visualizing noise because the reconstructed parameters has not described the original true electric results. If we observe the state functional cost, we see how the function is not decreasing, this means that the inversion algorithm is working only with noise. Then, this complex biomedical issue can not be performed by our CSIM. In addition, due to the limitations of our processor, we can not generates a correct number of nodes because the computational cost would be too huge (the actual simulation lasted 8 hours for solving the FP and 14 hours to finish the CSIM), this implies problems in accuracy as commented in Chapter 4 that are greater in very complex scenarios like this.

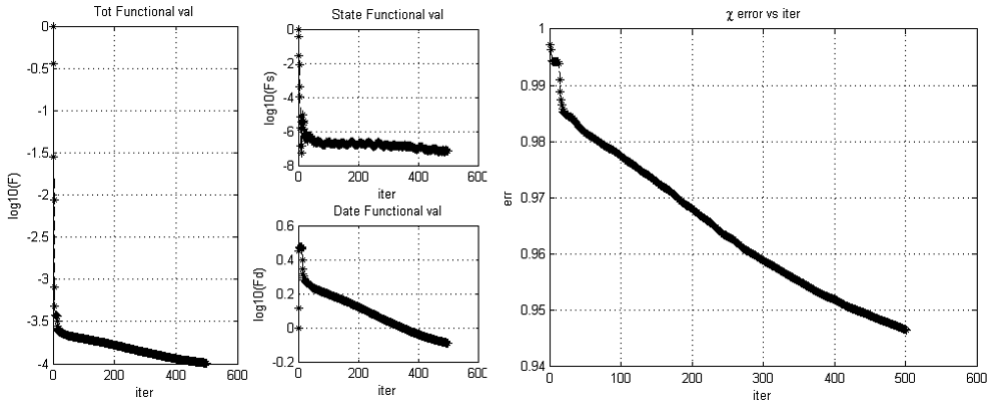

Figure 6.31: Brain: Total, state and domain functional cost; Err: Error vs Iterations

6.5 Conclusions

Here, we summaryze all the main conclusions that we have obtained along this research work. Both, the Forward Problem and Inversion algorithm are considered in this section.

We have shown how the Helmholtz equations that describe the behaviour of electromagnetics can be solved using several techniques, one of these techniques is the *Finite element Method*, that provide several advantages as accuracy in complex scenarios or problems related to enclosure shapes. However we observed that FEM implies a very high computational cost that may perform limitations in some simulations.

During assembling matrix description, we concluded that for scalar problems the nodal basis functions works corretly, however, when the considered problem is based on vector ones, nodal functions perform spurious solutions that can be solved using edge functions.

We analyzed results of FP for different situations, comparing different PEC shapes, several dielectric properties, current source placements and consequences of frequency. We concluded that if the dielectric properties and frequency involve a low losses along the background, the results will be non acceptable due to the great number of reflections that illuminate all the imaging domain. In addition, frequency implies a huge or low computational cost, so that, to perform this MWI applications is necessary to work with powerful processor to consider a wider bandwith.

In real MWI applications the measureament electric field is determined by engineering instruments. In our case we have used synthetic data, so we need to take into account the limitations in FEM to use the FP results as an input for the inversion algorithm.

CSIM is the inversion algorithm that we have developed to reconstruct the unknown dielectric properties of different imaging domains that were placed into a certain enclosure. The different matrix operators and norms that define the algorithm were described. In addition, we talked about initial guess based on backpropagation method, we explained that this procedure is obtained by the method of the steepest descent applied to functional cost. Backpropagation criterium lets us to determine the global minimum value of an error function instead of local minima values as using other methods. However some disadvantages exist: The convergence obtained from backpropagation learning is very slow and this convergence is not guaranteed.

Tabla 6.5: CSIM Results

Simulation	N nodes	I nodes	Iterations	err(%)	$log_{10}(F)$	$log_{10}(F_s)$	$log_{10}(F_d)$
Circle $\|\chi\| < 1$	4831	1352	400	45.5	-3.9	-6.1	-1.9
Inhomogeneous circ.OI	8553	2853	850	30	-4.25	-6	-3.1
Ü profile	10441	2668	700	49	-3.1	-4.9	-1.85
Triangle $\|\chi\| < 1$	7794	1963	200	31	-3.5	-5.5	-2.1
Lossy Squares	6759	1590	250	25	-4.4	-5.98	-3.6
Lossy E-phantom	13051	2936	750	38.1	-4.5	-6	-2.85
Lossless Squares	4988	1146	70	49	-1.8	-2.85	-0.4
Lossless E-phantom	3480	818	400	49	-4	-4.5	-3
Bio. Issue: Forearm	19707	3984	415	33.8	-4.45	-6.4	-3.25

We have tried to analyze the CSIM in order to understand its behaviour and possible limitations. An experiment for determining the resolution of the method was performed, we concluded that the minima distance to identificate two different OIs is equals to $\lambda_b/4$. We simulated several experiments to obtain the limitations of inversion algorithm as constrast constraints, results mained that the method works on the correct way when the condition $|\chi| < 1$ is considered. In addition, we analyzed the consequences of frequency in reconstructed results, we concluded that beside computational cost, the frequency is involved in background dimensions in terms of wavelength where the attenuation of reflections are performed. Later, we compared lossy and lossless mediums, this experiment is related also to losses in background, while for lossy medium the results are very optimal because the reflections in PEC interface are very attenuated, for lossless mediums the results are bad or even wrong because the lack of losses implies that reflections are not attenuated and as commented above, the FEM calculates an irreal solution for the scattered field.

Finally, some biomedical experiments were developed in order to visualize possible error in very complex profiles. The forearm simulation worked very good, obtaining very optimal numerical error. However, the brain model due to discretization constraints performed non acceptable results. In Table 6.5 we can observe a summary of many of the simulations developed.

6.6 Future Works

CSIM has been analyzed for a great quantity of simulations, obtaining the expected results for synthetic data performed by FEM. However, there are more advanced techniques that could improve the CS results in terms of error, reducing it to levels over 20%, some of these new techniques are known as *Multiplicative Regularization* (MR FEM-CSIM) or *Balanced Multiplicative Regularization* (BMR FEM-CSIM) that works with the same inversion algorithm but including some new operators. Using these improvements, more complex and biomedical experiments could be anlyzed in better conditions

We may develop more experiments: Backpropagation compared versus different criteriums for inital guess, or FEM-CSIM could be compared against other methods as IE-CSIM, analyzing wich of them perform better results for different situations.

In addition, under the topic of this thesis, we could extend the experiments to 3D scenarios where the edge basis functions should be implemented in order to obtain correct results. Then, the problem would be presented as a vector problem and the meshing would be built using other type of subelements as tetrahedra.

Finally, real experiments could be solved using the necessary MWI intruments as FP solver and the inversion algoritm to reconstruct the experimental data.

Appendix

Appendix A

Assembly of FEM Global Matrices

A.1 Scalar Problems

The main purpose of this section is to derive analytically the expressions for the entries of all element matrices that are present in the linear system of equations given by (4.30). These entry values depend on the type of interpolation functions used in the finite element method, in our application we consider linear triangular elements. To obtain the values of the FEM matrix elements we divide the FEM matrix into Mass matrix and Stiffnes matrix as in (4.30), we develop matrix for each element and later the contributions of each of them must be performed to obtain the *Global FEM Matrix*, first we analyse M^e matrix given, according to (4.31),by

$$M_{ij}^e = -\int\int_{\Omega_e} \left[\alpha_x \left(\frac{\partial N_i}{\partial x} \right) \left(\frac{\partial N_j}{\partial x} \right) + \alpha_y \left(\frac{\partial N_i}{\partial y} \right) \left(\frac{\partial N_j}{\partial y} \right) \right] dxdy \tag{A.1}$$

A linear interpolation function based on a triangle must be linear in two orthogonal directions defined by the natural coordinates ξ and η. A triangle or arbitrary shape (Fig.A.1(a)) could be mapped to the master triangle (Fig.A.1(b)). According to Section 4.3.1 each linear interpolation function relates to a triangle node. We can denote each of them as $N_1(\xi, \eta)$, $N_2(\xi, \eta)$ and $N_3(\xi, \eta)$. Shape functions present the next form

$$N_i(\xi, \eta) = c_1 + c_2\xi + c_3\eta \tag{A.2}$$

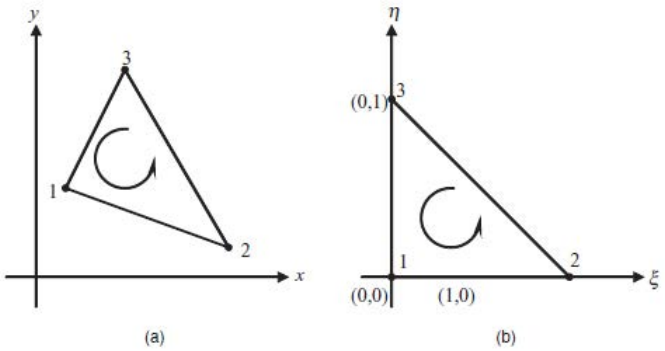

Figure A.1: (a) Linear triangular element in the xy-plane. (b) Linear triangular element (master element) in the $\xi\eta$-plane

In [4] interpolation functions are analysed, then expression (A.2) for each function results

$$N_1(\xi,\eta) = 1 - \xi - \eta \tag{A.3}$$

$$N_2(\xi,\eta) = \xi \tag{A.4}$$

$$N_3(\xi,\eta) = \eta \tag{A.5}$$

$$\Rightarrow N_1 + N_2 + N_3 = 1 \tag{A.6}$$

For isoparametric elements, the same functions used in interpolation inside an element are also used to interpolate the space coordinates x and y,

$$x = x_1^e N_1 + x_2^e N_2 + x_3^e N_3 = \sum_{i=1}^{3} x_i^e N_i \tag{A.7}$$

$$y = y_1^e N_1 + y_2^e N_2 + y_3^e N_3 = \sum_{i=1}^{3} y_i^e N_i \tag{A.8}$$

Substituting function N_i into (A.7) and (A.8) yields

$$x = x_1^e + \bar{x}_{21}\xi + \bar{x}_{31}\eta \tag{A.9}$$

$$y = y_1^e + \bar{y}_{21}\xi + \bar{y}_{31}\eta \tag{A.10}$$

Using rule of differentiation, we can write that

$$\begin{aligned}\frac{\partial N}{\partial \xi} &= \frac{\partial N}{\partial x}\frac{\partial x}{\partial \xi} + \frac{\partial N}{\partial y}\frac{\partial y}{\partial \xi} \\ \frac{\partial N}{\partial \eta} &= \frac{\partial N}{\partial x}\frac{\partial x}{\partial \eta} + \frac{\partial N}{\partial y}\frac{\partial y}{\partial \eta}\end{aligned} \tag{A.11}$$

These equation can be written as

$$\begin{Bmatrix} \frac{\partial N}{\partial \xi} \\ \frac{\partial N}{\partial \eta} \end{Bmatrix} = [J] \begin{Bmatrix} \frac{\partial N}{\partial x} \\ \frac{\partial N}{\partial y} \end{Bmatrix} \tag{A.12}$$

where [J] is the Jacobian matrix of the transformation, using expressions (A.9) and (A.10) [J] is given by

$$[J] = \begin{bmatrix} \frac{\partial x}{\partial \xi} & \frac{\partial y}{\partial \xi} \\ \frac{\partial x}{\partial \eta} & \frac{\partial y}{\partial \eta} \end{bmatrix} = \begin{bmatrix} \bar{x}_{21} & \bar{y}_{21} \\ \bar{x}_{31} & \bar{y}_{31} \end{bmatrix} \tag{A.13}$$

Note that $|J| = \bar{x}_{21}\bar{y}_{31} - \bar{x}_{31}\bar{y}_{21} = 2A^e$, using (A.12) is possible to obtain the partial difference of interpolation functions

$$\begin{Bmatrix} \frac{\partial N_i}{\partial x} \\ \frac{\partial N_i}{\partial y} \end{Bmatrix} = \frac{1}{2A^e} \begin{bmatrix} \bar{y}_{31} & -\bar{y}_{21} \\ -\bar{x}_{31} & \bar{x}_{21} \end{bmatrix} \begin{Bmatrix} \frac{\partial N_i}{\partial \xi} \\ \frac{\partial N_i}{\partial \eta} \end{Bmatrix} \tag{A.14}$$

In other words,

$$\begin{aligned}\frac{\partial N_1}{\partial x} &= \frac{\bar{y}_{23}}{2A^e} \\ \frac{\partial N_1}{\partial y} &= \frac{\bar{x}_{32}}{2A^e}\end{aligned} \tag{A.15}$$

$$\begin{aligned}\frac{\partial N_2}{\partial x} &= \frac{\bar{y}_{31}}{2A^e} \\ \frac{\partial N_2}{\partial y} &= \frac{\bar{x}_{13}}{2A^e}\end{aligned} \tag{A.16}$$

$$\begin{aligned}\frac{\partial N_3}{\partial x} &= \frac{\bar{y}_{12}}{2A^e} \\ \frac{\partial N_3}{\partial y} &= \frac{\bar{x}_{21}}{2A^e}\end{aligned} \tag{A.17}$$

To evaluate the double integral in (A.1), is necessary to change the variables of integration from x and y to ξ and η. The transformation of a double integral from the regular coordinate system to the natural coordinate system is given by

$$\int\int_{\Omega^e} f(x,y)\,dxdy = \int_0^1 \int_0^{1-\eta} f(x(\xi,\eta), y(\xi,\eta))\,|J|\,d\xi d\eta \tag{A.18}$$

Using expressions (A.15)-(A.17) and the Jacobian transformation (A.18) we can obtain the entries of element matrix M^e,

$$M^e_{11} = -\left[\alpha_x \frac{(\bar{y}_{23})^2}{4A^e} + \alpha_y \frac{(\bar{x}_{32})^2}{4A^e}\right] \tag{A.19}$$

$$M^e_{12} = M^e_{21} = -\left[\alpha_x \frac{\bar{y}_{23}\bar{y}_{31}}{4A^e} + \alpha_y \frac{\bar{x}_{32}\bar{x}_{13}}{4A^e}\right] \tag{A.20}$$

$$M^e_{13} = M^e_{31} = -\left[\alpha_x \frac{\bar{y}_{23}\bar{y}_{12}}{4A^e} + \alpha_y \frac{\bar{x}_{32}\bar{x}_{21}}{4A^e}\right] \tag{A.21}$$

$$M^e_{22} = -\left[\alpha_x \frac{(\bar{y}_{31})^2}{4A^e} + \alpha_y \frac{(\bar{x}_{13})^2}{4A^e}\right] \tag{A.22}$$

$$M^e_{23} = M^e_{32} = -\left[\alpha_x \frac{\bar{y}_{31}\bar{y}_{12}}{4A^e} + \alpha_y \frac{\bar{x}_{13}\bar{x}_{21}}{4A^e}\right] \tag{A.23}$$

$$M^e_{33} = -\left[\alpha_x \frac{(\bar{y}_{12})^2}{4A^e} + \alpha_y \frac{(\bar{x}_{21})^2}{4A^e}\right] \tag{A.24}$$

Now the second term of K FEM matrix is evaluated, the Mass matrix, T^e given by (4.32),

$$T^e_{ij} = \int\int_{\Omega_e} \beta\, N_i\, N_j\, dxdy \tag{A.25}$$

It's necessary to apply the Jacobian transformation to (A.25), however there is a simple generic formula that can be used

$$\int\int_{\Omega_e} (N_1)^l (N_2)^m (N_3)^n \, dxdy = \frac{l!m!n!}{(l+m+n+2)!} 2A^e \tag{A.26}$$

then, the remaining entries of matrix T^e are given by

$$T^e_{11} = \int\int_{\Omega_e} \beta \, (N_1)^2 \, dxdy = \beta \frac{2!0!0!}{(2+0+0+2)!} 2A^e = \frac{\beta A^e}{6} \tag{A.27}$$

$$T^e_{12} = T^e_{21} = \frac{\beta A^e}{12} \tag{A.28}$$

$$T^e_{13} = T^e_{31} = \frac{\beta A^e}{12} \tag{A.29}$$

$$T^e_{22} = \frac{\beta A^e}{6} \tag{A.30}$$

$$T^e_{23} = T^e_{32} = \frac{\beta A^e}{12} \tag{A.31}$$

$$T^e_{33} = \frac{\beta A^e}{6} \tag{A.32}$$

In addition, for simplicity we consider the homogenous Neumann boundary condition, that is, the special case of (4.15) with $\gamma = q = 0$, that means

$$b^e_i = f^e_i + p^e_i = f^e_i = \int\int_{\Omega_e} N_i \, g \, dxdy \tag{A.33}$$

that can be written as

$$b^e_i = \frac{A^e}{3} g \tag{A.34}$$

Finally, we define the area for each element,

$$A^e = \frac{1}{2} \begin{bmatrix} 1 & x^e_1 & y^e_1 \\ 1 & x^e_2 & y^e_2 \\ 1 & x^e_3 & y^e_3 \end{bmatrix} = \frac{1}{2} \left(b^e_1 c^e_2 - b^e_2 c^e_1 \right) \tag{A.35}$$

with b^e_i and c^e_i being defined in Section 4.3.1.

A.2 Vector Problems

To assemble the FEM matrix for vector problems is necessary to introduce the formulation derived from Edge basis funtions. Stiffnes and Mass matrix are given by

$$S_{ij}^{e} = \int\int_{\Omega_e} (\nabla \times \mathbf{N_i^e}) \cdot \left(\nabla \times \mathbf{N_j^e}\right) d\Omega \tag{A.36}$$

$$M_{ij}^{e} = \int\int_{\Omega_e} \mathbf{N_i^e} \cdot \mathbf{N_j^e}\, d\Omega \tag{A.37}$$

for triangular elements the Stiffness matrix elemets can be evaluated as

$$S_{ij}^{e} = \frac{l_i^e l_j^e}{\Delta^e} \tag{A.38}$$

while the integration for (A.37) is more complex, but using the expression (A.26) is possible to obtain for each element of the matrix

$$\begin{aligned}
M_{11}^{e} &= \frac{(l_1^e)^2}{24\Delta^e}\,(f_{22} - f_{12} + f_{11}) \\
M_{22}^{e} &= \frac{(l_2^e)^2}{24\Delta^e}\,(f_{33} - f_{23} + f_{22}) \\
M_{33}^{e} &= \frac{(l_3^e)^2}{24\Delta^e}\,(f_{11} - f_{13} + f_{33}) \\
M_{12}^{e} &= \frac{l_1^e l_2^e}{48\Delta^e}\,(f_{23} - f_{22} - 2f_{13} + f_{12}) \\
M_{13}^{e} &= \frac{l_1^e l_3^e}{48\Delta^e}\,(f_{21} - 2f_{23} - f_{11} + f_{13}) \\
M_{23}^{e} &= \frac{l_2^e l_3^e}{48\Delta^e}\,(f_{31} - f_{33} - 2f_{21} + f_{23})
\end{aligned} \tag{A.39}$$

where $f_{ij} = b_i^e b_j^e + c_i^e c_j^e$ with b_i^e and c_i^e being defined in Section 4.3.1.

Appendix B

FEM-CSIM

B.1 Scalar Problems: Two-Dimensional Case

The contrast variable, χ, is defined for each node due to the behaviour of the inversion algorithm, FEM-CSIM. According to this requirement is necessary to introduce some variations in FEM matrix assembling. The dielectric parameters that describe the physical properties of the computational domain Ω can be assigned for each element by,

$$\beta^e = \sum_{i=1}^{3} \beta_i^e \varphi_i^e \tag{B.1}$$

In addition, the electric field of interest is the scattered one which performs a new Helmholtz equation in terms of the scattered field, $\vec{E}^{sct}$.

$$\nabla^2 E^{sct} + k_b^2 \left(\chi + 1\right) E^{sct} = -k_b^2 \chi E^{inc} \tag{B.2}$$

Assuming this variation of the Helmholz equation and applying the Garlerkin's method, we obtain the Stiffness and Mass matrix that assemble the FEM matrix.

$$S^e = \int_{\Omega^e} \begin{bmatrix} \nabla\lambda_1^e \cdot \nabla\lambda_1^e & \nabla\lambda_1^e \cdot \nabla\lambda_2^e & \nabla\lambda_1^e \cdot \nabla\lambda_3^e \\ \nabla\lambda_2^e \cdot \nabla\lambda_1^e & \nabla\lambda_2^e \cdot \nabla\lambda_2^e & \nabla\lambda_2^e \cdot \nabla\lambda_3^e \\ \nabla\lambda_3^e \cdot \nabla\lambda_1^e & \nabla\lambda_3^e \cdot \nabla\lambda_2^e & \nabla\lambda_3^e \cdot \nabla\lambda_3^e \end{bmatrix} ds \tag{B.3}$$

$$T^e = \int_{\Omega^e} \begin{bmatrix} \lambda_1^e \lambda_1^e \beta^e & \lambda_1^e \lambda_2^e \beta^e & \lambda_1^e \lambda_3^e \beta^e \\ \lambda_2^e \lambda_1^e \beta^e & \lambda_2^e \lambda_2^e \beta^e & \lambda_2^e \lambda_3^e \beta^e \\ \lambda_3^e \lambda_1^e \beta^e & \lambda_3^e \lambda_2^e \beta^e & \lambda_3^e \lambda_3^e \beta^e \end{bmatrix} ds \tag{B.4}$$

Using expression [A.26], we obtain the next values entries for Mass matrix

$$T^e = \frac{A^e}{60} \begin{bmatrix} 6\beta_1^e + 2\left(\beta_2^e + \beta_3^e\right) & \beta_3^e + 2\left(\beta_1^e + \beta_2^e\right) & \beta_2^e + 2\left(\beta_1^e + \beta_3^e\right) \\ \beta_3^e + 2\left(\beta_2^e + \beta_1^e\right) & 6\beta_2^e + 2\left(\beta_1^e + \beta_3^e\right) & \beta_1^e + 2\left(\beta_2^e + \beta_3^e\right) \\ \beta_2^e + 2\left(\beta_3^e + \beta_1^e\right) & \beta_1^e + 2\left(\beta_3^e + \beta_2^e\right) & 6\beta_3^e + 2\left(\beta_1^e + \beta_2^e\right) \end{bmatrix} ds \tag{B.5}$$

B.2 Incident Field in Conductive Enclosures

To perform the FEM-CSIM is necessary to calculate the incident electric field inside bounded problem, $Einc$, for recording the synthetic data. For 2D TM scalar problems, the zpolarized scalar incident field E_z^{inc}, bounded by a conductive enclosure, is governed by the Helmholtz equation

$$\nabla^2 E_z^{inc}(\vec{r}) + k_b^2 E_z^{inc}(\vec{r}) = jw\mu_o J_z \tag{B.6}$$

The incident field must satisfies the Dirichlet BCs at enclosure interface, $E_z^{inc}(\vec{r}) = 0 \forall \vec{r} \in \Gamma$. We assume that the current source at each point present the next behaviour,

$$J_z(\vec{r}) = \frac{-1}{jw\mu_o} \delta\left(\vec{r} - \vec{r_t}\right) \tag{B.7}$$

where $\vec{r_t}$ is the vector position of current source placement. A solution for this equation that satisfies the homogeneous Dirichlet BC is given as

$$E_z^{inc}(\vec{r}) = E_z^{inc,fs}(\vec{r}) + p_t(\vec{r}) \tag{B.8}$$

Here $E^{inc,fs}$ is the incident field in free-space conditions that is calculated as,

$$E_z^{inc,fs}(\vec{r}) = \frac{1}{j4} H_o^2 \left(k_b \left|\vec{r} - \vec{r}_t\right|\right) \tag{B.9}$$

where H_o^2 is the zerothorder Hankel function of second kind. The last step is to determine p_t function, to perform this is necessary to set the next BVP

$$\begin{aligned} \nabla^2 p_t(\vec{r}) + k_b^2 p_t(\vec{r}) &= 0 \\ p_t(\vec{r}) &= 0 \qquad \text{on}\,\Gamma \end{aligned} \tag{B.10}$$

Bibliography

[1] Jianming Jin, *The Finite Element Method in Electromagnetics.*
A Wiley-Interscience Publication, John wiley & Sons, Inc. 2nd Edition, 2002.

[2] A.Bondenson, T.Rylander, P.Ingelström, *Computational Electromagnetics.* Springer.
June 27,2005.

[3] Amer Zakaria, *The Finite-Element Contrast Source Inversion Method for Microwave Imaging Applications.* A Thesis submitted to the Faculty of Graduate Studies of The University of Manitoba. 2012.

[4] Anastasis C.Polycarpou, *Introduction to the Finite Element Method in Elecromagnetics.*
Morgan & Claypool Publishers. First Edition, 2006.

[5] Jean-Pierre Berenger, *Perfectly Matched Layer (PML) for Computational Electromagnetics.*
Morgan & Claypool Publishers. First Edition, 2007.

[6] Elia A.Attardo, *Computational Methods for Microwave Imaging: Biomedical Applications.*
PhD Thesis, Politecnico di Torino. May 2011.

[7] Jiayuan Fang, Zhonghua Wu, *Generalized Perfectly Matched Layer-An Extension of Berenger's Perfectly Matched Layer Boundary Condition.*
IEEE Microwave And Guided Wave Letters, VOL. 5, NO. 12. December 1995.

[8] David M.Pozar, *Microwave Engineering.*
John wiley & Sons, Inc. Second Edition, 1998.

[9] A.Zakaria, C.Gilmore and J.LoVetri, *Finite-Element Contrast Source Inversion Method for Microwave Imaging.*
Article IOPscience. September 2010.

[10] C.Gilmore and J.LoVetri, *Enhancement of Microwave Tomography Through The Use of Electrically Conducting Enclosures.*
Article IOPscience. April 2008.

[11] International Center for Numerical Methods in Engineering, http://gid.cimne.upc.es/support/manuals
CINME,UPC.

[12] Microwave Imaging Laboratory Website, http://www.ece.umanitoba.ca/EM_Imaging_Lab/index.html
University of Manitoba.

[13] M.D'Urso, T.Isernia, and Andrea F.Morabito, *On the Solution of 2-D Inverse Scattering Problems via Source-Type Integral Equations.*
IEEE TRANSACTIONS ON GEOSCIENCE AND REMOTE SENSING, VOL.48, NO.3, March 2010.

[14] A.Zakaria and J.LoVetri, *Application of Multiplicative Regularization to the Finite-Element Contrast Source Inversion Method.*
IEEE TRANSACTIONS ON ANTENNAS AND PROPAGATION, VOL. 59, NO. 9, September 2011.

[15] C.J.Reddy, Manohar D.Deshpande, C.R.Cockrell, and Fred B.Beck *Finite Element Method for Eigenvalue Problems in Electromagnetics.*
NASA Technical Paper 3485, December 1994.

[16] Jianming Jin and W.C. Chew *Combining PML and ABC for Finite Element Analysis of Scattering Problems.*
Article of University of Illinois at Urbana-Champaign,

[17] J.Fang and Z.Wu *Generalized Perfectly Matched Layer for the Absorption of Propagating and Evanescent Waves in Lossless and Lossy Media.*

IEEE TRANSACTIONS ON MICROWAVE THEORY AND TECHNIQUES, VOL. 44, NO.12 December 2012

[18] P.Mojabi and J.LoVetri *Eigenfunction Contrast Source Inversion for Circular Metallic Enclosures.*

IOP PUBLISHING. INVERSE PROBLEMS. 12 January 2010